Magneto-Optical and Multiferroic Oxide Thin Films, Integrated Nonreciprocal Photonic Devices and Multiferroic Memory Devices

by

Mehmet Cengiz Onbaşlı

B.S., Electrical and Electronics Engineering, 2010
Bilkent University, Ankara, Turkey

Submitted to the DEPARTMENT OF MATERIALS SCIENCE AND ENGINEERING
In Partial Fulfillment of the Requirements for the Degree of

DOCTOR OF PHILOSOPHY IN MATERIALS SCIENCE AND ENGINEERING
at the
MASSACHUSETTS INSTITUTE OF TECHNOLOGY
June 2015

Signature of Author: _____
Department of Materials Science and Engineering
May 11th, 2015

Certified by : _____
Caroline A. Ross
Toyota Professor of Materials Science and Engineering
Thesis Advisor

Accepted by : _____
Donald R. Sadoway
Chair, Departmental Committee on Graduate Students

I dedicate this thesis to

my great grandfather dear Prophet Mohammad ﷺ

Magneto-Optical and Multiferroic Oxide Thin Films, Integrated Nonreciprocal Photonic Devices and Multiferroic Memory Devices

by

Mehmet Cengiz Onbaşlı

Submitted to the Department of Materials Science and Engineering on April 27, 2015 in Partial Fulfillment of the Requirements for the Degree of Doctor of Philosophy in Materials Science and Engineering

Abstract

Complex oxide thin films offer unique functionalities which can potentially extend the utility of current storage, processing and optical isolator technologies. In this thesis, we present three categories of studies on complex oxide growth using pulsed laser deposition (PLD) and structural, magnetic, magneto-optical and ferroelectric characterization. We first focused on enhancing integrated magneto-optical isolator performance by improving the growth method of magneto-optical $Ce_1Y_2Fe_5O_{12}$ (Ce:YIG) films. The spectral and substrate orientation dependence of the magneto-optical figure of merit of epitaxial Ce:YIG on GGG substrates show very high magneto-optical figure of merit (379-400 ° dB^{-1} at λ = 1550 nm for all substrate orientations). The thermal budgets of Ce:YIG growth on Si_3N_4 (2 high temperature PLD steps and a rapid thermal anneal, RTA), silicon-on-insulator substrates (a high and a low temperature PLD step and a RTA) and optical resonator chips (one PLD step, one RTA, YIG seed layer from the top) were progressively reduced to achieve improved integrated optical isolators with low insertion loss of 7.4 ± 1.8 dB and an isolation ratio of 13.0 ± 2.2 dB. We demonstrated that the ferrimagnetic insulator YIG thin films ($Y_3Fe_5O_{12}$) epitaxially grown on GGG substrates achieve ultralow Gilbert damping of spin waves (α = 2.2-7 × 10^{-4}), which enable cm-long in-plane propagation of spin waves. This demonstration enables researchers to fabricate near-dissipationless magnon-based logic computers. Finally, we present a substitutionally-doped perovksite, STCo30 ($SrTi_{0.70}Co_{0.30}O_{3-\delta}$) integrated on Si, STO (100), and on Nb:STO substrates. This perovskite oxide has been found to exhibit ferroelectricity and magnetism at room temperature. Experimental results on magnetism, ferroelectricity and structure were reproduced using density functional theory simulations.

Thesis Supervisor: Caroline A. Ross
Title: Toyota Professor of Materials Science and Engineering

Table of Contents

List of Publications

[1] J. M. Florez, Shyue Ping Ong, **M. C. Onbasli**, C. A. Ross and G. Ceder, **"First-Principles Simulations of Structural and Magnetic Properties of Cobalt-Doped $SrTiO_3$",** Applied Physics Letters **100**, 252904 (2012).

[2] Taichi Goto, **M. C. Onbasli**, Caroline A. Ross, **"Magneto-optical properties of cerium substituted yttrium iron garnet films with reduced thermal budget for monolithic photonic integrated circuits"**, Optics Express, **20**, 28517 (2012).

[3] L. Bi, J. Hu, P. Jiang, H. S. Kim, D. H. Kim, **M. C. Onbasli**, G. F Dionne, C. A Ross, **"Magneto-Optical Thin Films for On-Chip Monolithic Integration of Non-Reciprocal Photonic Devices"**, Materials **6**, 5094 (2014).

[4] M. Lang, M. Montazeri, **M. C. Onbasli**, et al., **"Proximity Induced High Temperature Magnetic Order in Topological Insulator-Ferrimagnetic Insulator Heterostructure"**, Nano Letters **14**, 3459 (2014).

[5] A. Kehlberger, G. Jakob, **M. C. Onbasli**, D. H. Kim, C. A. Ross, M. Kläui, **"Investigation of the magnetic properties of insulating thin films using the longitudinal spin Seebeck effect"**, J. Appl. Phys. **115**, 17C731 (2014).

[6] T. Goto, **M. C. Onbasli**, D. H. Kim, V. Singh, M. Inoue, L. C. Kimerling, C. A. Ross, **"A nonreciprocal racetrack resonator based on vacuum-annealed magnetooptical cerium-substituted yttrium iron garnet"**, Optics Express **22**, 19047 (2014).

[7] **M. C. Onbasli**, A. Kehlberger, D. H. Kim, G. Jakob, M. Kläui, A. V. Chumak, B. Hillebrands, C. A. Ross, **"Pulsed laser deposition of epitaxial yttrium iron garnet films with low Gilbert damping and bulk-like magnetization"**, APL Materials **2**, 106102 (2014).

[8] **M. C Onbasli**, T. Goto, X. Sun, N. Huynh, C. A. Ross, **"Integration of bulk-quality thin film magneto-optical cerium-doped yttrium iron garnet on silicon nitride photonic substrates"**, Optics Express **22**, 25183 (2014).

[9] X. Sun, C. Zhang, N. M Aimon, T. Goto, **M. C. Onbasli**, D. H. Kim, H. K. Choi, C. A. Ross, "**Combinatorial Pulsed Laser Deposition of Magnetic and Magneto-optical $Sr(Ga_xTi_yFe_{0.34-0.40})O_{3-\delta}$ Perovskite Films**", ACS Combinatiorial Science **16**, 640 (2014).

[10] W. Liu, L. He, Y. Xu, K. Murata, **M. C. Onbasli**, M. Lang, N. Maltby, S. Li, X. Wang, C. A. Ross, P. Bencok, G. van der Laan, R. Zhang, Rong; K. Wang, **"Enhancing Magnetic Ordering in Cr-doped Bi_2Se_3 using High-T_C Ferrimagnetic Insulator"**, Nano Letters **15**, 764 (2015).

[11] X. Sun. M. Veis, J. Kousal, E. Jesenska, C. Zhang, N. Aimon, T. Goto, **M. C. Onbasli**, D. H. Kim, H. K. Choi, C. A. Ross, **"$SrGa_{0.7}Co_{0.3}O_{3-\delta}$ perovskite-cobalt oxide-metal nanocomposite films: magnetic and optical properties"**, Nanotechnology **26**, 115701 (2015).

[12] M. Veis, M. Zahradnik, L. Ohnoutek, L. Beran, M. Kucera, X. Sun, C. Zhang, N. Aimon, T. Goto, **M. C. Onbasli**, D. H. Kim, H. K. Choi, and C. A. Ross, **"Magneto-optical studies of $SrGa_{0.7}Co_{0.3}O_{3-\delta}$ perovskite thin films with embedded cobalt nanoparticles"**, Journal of Applied Physics, *(accepted)* (2015).

[13] M. B. Jungfleisch, A. V. Chumak, A. Kehlberger, V. Lauer, D. H. Kim, **M. C. Onbasli**, C. A. Ross, M. Kläui, and B. Hillebrands, **"Thickness and power dependence of the spin-pumping effect in $Y_3Fe_5O_{12}$/Pt heterostructures measured by the inverse spin Hall effect"**, Physical Review B **91**, 134407 (2015).

[14] **M. C. Onbasli**, D. H. Kim, L. Bi, G. F. Dionne, C. A. Ross, **"Oxygen stoichiometry dependence of the magnetic and magnetooptical properties of epitaxial $SrTi_{1-x}Co_xO_{3-\delta}$ films"**, *(accepted), Optics Express*

[15] A. Kehlberger, U. Ritzmann, D. Hinzke, R. Röser, G. Jakob, **M. C. Onbasli**, D. H. Kim, C. A. Ross, M. B. Jungfleisch, B. Hillebrands, U. Nowak, M. Kläui, **"Lengthscale of the spin Seebeck effect"**, *(under review)*

[16] A. Kehlberger, K. Richter, G. Jakob, **M. C. Onbasli**, D. H. Kim, T. Goto, C. A. Ross, G. Götz, G. Reiss, T. Kuschel, M. Kläui, **"Enhanced magnetooptic Kerr effect and magnetic properties of epitaxial CeYIG thin films"**, *(under review)*

[17] M. Montazeri, P. Upadhyaya, **M. C. Onbasli**, G. Yu, K. L. Wong, M. Lang, Y. Fan, P. K. Amiri, R. N. Schwartz, C. A. Ross, K. L. Wang, **"Microscopy of spin-orbit torques in metallic and insulating magnetic structures"**, *(under review)*

[18] X. Sun, Q. Du, T. Goto, **M. C. Onbasli**, D. H. Kim, N. M. Aimon, H. K. Choi, J. Hu, C. A. Ross, **"One-step-deposition of cerium substituted yttrium iron garnet on an integrated optical isolator"**, *(under review)*

[19] T. Goto, D. H. Kim, X. Sun, N. M Aimon, **M. C. Onbasli**, J. M. Florez Uribe, K. Ackland, P. Stamenov, M. Inoue, M. Coey, G. F Dionne, C.A. Ross, **"Magnetism and Faraday rotation in polycrystalline and single-crystal iron-substituted strontium titanate films deposited at different base pressures"**, *(manuscript prepared)*

[20] **M. C. Onbasli**, J. M. Florez, X. Sun, E. Lage, Shyue Ping Ong, T. Goto, G. Ceder, C. A. Ross, **"Room temperature multiferroic and magnetoelectric $SrTi_{0.70}Co_{0.30}O_{3-\delta}$ films on silicon"**, *(manuscript prepared)*

[21] J. M. Florez, **M. C. Onbasli**, Shyue Ping Ong, G. Ceder, C. A. Ross, **"Density functional theory insights on multiferroic and magnetoelectric switching in $SrTi_{0.70}Co_{0.30}O_{3-\delta}$ films on Strontium Titanate and Silicon substrates"**, *manuscript in preparation*

[22] **M. C. Onbasli**, L. Beran, M. Veis, C. A. Ross, **"Wavelength and substrate orientation dependence of the permittivity tensor, Faraday and Kerr rotation spectra of epitaxial Cerium-doped Yttrium iron garnet films on $Gd_3Ga_5O_{12}$ substrates",** *manuscript in preparation*

[23] F. Casola, H. Zhang, **M. C. Onbasli**, T. van der Sar, Amir Yacoby, **"Magnon-assisted on-chip quantum teleportation of individual nitrogen-vacancy center spins"**, *manuscript in preparation*

[24] T. Goto, T. Yoshimoto, R. Isogai, **M. C. Onbasli**, C. A. Ross, H. Takagi, P. B. Lim, Y. Nakamura, M. Inoue, **"Fabrication of Cerium Substituted Yttrium Iron Garnets on Dielectric Mirrors Using Sputtering and Vacuum Annealing"**, *manuscript in preparation*

[25] Joel Yuen-Zhou, **M. C. Onbasli**, M. Baldo, V. Bulovic, C. A. Ross, **"Time-reversal symmetry breaking in topologically protected and surface plasmon polariton enhanced excitons in porphyrin thin films"**, *manuscript in preparation*

List of Tables

List of Figures

Acknowledgements

بِسْمِ اللهِ الرَّحْمٰنِ الرَّحِيْمِ
اَشْهَدُ انْ لّآ اِلهَ اِلَّا اللّٰهُ وَ اَشْهَدُ اَنَّ مُحَمَّدً اعَبْدُه وَرَسُولُه
لا إله إلا الله محمد رسول الله
سُبْحَان اللهِ وَ الْحَمْدُ لِلّٰهِ وَ لآ اِلهَ اِلّا اللّٰهُ، وَ اللّٰهُ اَكْبَرُ وَلا حَوْلَ وَلاَ قُوَّةِ الَّا بِاللّٰهِ الْعَلِىّ الْعَظِيْم
لا الهَ اِلَّا اللّٰهُ وَحْدَهُ لا شَرِيْكَ لَهْ، لَهُ الْمُلْكُ وَ لَهُ الْحَمْدُ يُحْى وَ يُمِيْتُ بِيَدِهِ الْخَيْرُ وَهُوَ عَلى كُلِّ شَئ قَدِيْرٌ
أَسْتَغْفِر اللَّهَ الْعَظِيمَ الَّذِي لَا إِلَهَ إِلَّا هُوَ الْحَيَّ الْقَيُّومَ وَأَتُوبُ إِلَيْهِ

لَوْ أَنزَلْنَا هَٰذَا الْقُرْآنَ عَلَىٰ جَبَلٍ لَّرَأَيْتَهُ خَاشِعًا مُّتَصَدِّعًا مِّنْ خَشْيَةِ اللَّهِ ۚ وَتِلْكَ الْأَمْثَالُ نَضْرِبُهَا لِلنَّاسِ لَعَلَّهُمْ يَتَفَكَّرُونَ
هُوَ اللَّهُ الَّذِي لَا إِلَٰهَ إِلَّا هُوَ ۖ عَالِمُ الْغَيْبِ وَالشَّهَادَةِ ۖ هُوَ الرَّحْمَٰنُ الرَّحِيمُ
هُوَ اللَّهُ الَّذِي لَا إِلَٰهَ إِلَّا هُوَ الْمَلِكُ الْقُدُّوسُ السَّلَامُ الْمُؤْمِنُ الْمُهَيْمِنُ الْعَزِيزُ الْجَبَّارُ الْمُتَكَبِّرُ ۚ سُبْحَانَ اللَّهِ عَمَّا يُشْرِكُونَ
هُوَ اللَّهُ الْخَالِقُ الْبَارِئُ الْمُصَوِّرُ ۖ لَهُ الْأَسْمَاءُ الْحُسْنَىٰ ۚ يُسَبِّحُ لَهُ مَا فِي السَّمَاوَاتِ وَالْأَرْضِ ۖ وَهُوَ الْعَزِيزُ الْحَكِيمُ
سُبحَانَ اللهِ وَ بِحَمْدِهِ ، سُبحَانَ اللهِ الْعَظِيمِ الحمد لله الله أكبر لا إله إلا الله

اللَّهُمَّ أَنْتَ رَبِّي لّا إِلَهَ إِلَّا أَنْت، خَلَقْتَنِي وَأَنَا عَبْدُكَ، وَأَنَا عَلَى عَهْدِكَ وَوَعْدِكَ مَا اسْتَطَعْت، أَعُوذُ بِكَ مِنْ شَرِّ مَا صَنَعْت، أَبُوءُ لَكَ بِنِعْمَتِكَ،عَلَيَّ، وَأَبُوءُ بِذَنْبِي فَاغْفِر لِي فَإِنَّهُ لَا يَغْفِرُ، الذُّنُوبَ إِلَّا أَنْتَ

اللهم صلِّ علـى سيدنا محمد،
رَضِينَا بِاللهِ رَبًّا وَبِالْإِسْلَامِ دِينًا وَبِمُحَمَّدٍ رَسُولًا

اللَّهُمَّ صَلِّ عَلَى مُحَمَّدٍ بِعَدَدِ مَنْ صَلَّى عَلَيْهِ وَصَلِّ عَلَى مُحَمَّدٍ بِعَدَدِ مَنْ لَمْ يُصَلِّ عَلَيْهِ وَصَلِّ عَلَى مُحَمَّدٍ كَمَا أَمَرْتَ بِالصَّلاَةِ عَلَيْهِ وَصَلِّ عَلَى مُحَمَّدٍ كَمَا تُحِبُّ أَنْ يُصَلَّى عَلَيْهِ وَصَلِّ عَلَى مُحَمَّدٍ كَمَا تَنْبَغِي الصَّلاَةُ عَلَيْهِ.

فصلى الله على نبينا محمد كلما ذكره الذاكرون وغفل عن ذكره الغافلون وصلى عليه في الأولين والآخرين أفضل وأكثر وأزكى ما صلى على أحد من خلقه وزكانا وإياكم بالصلاة عليه أفضل ما زكى أحداً من أمته بصلاته عليه السلام عليه ورحمة الله وبركاته وجزاه الله عنا أفضل ما جزى مرسلاً عمن أرسل إليه
(The Arabic text that I included above is a summary of my thanks to God.)

I am grateful to my mother, father, sister, brother-in-law for their help and kindness while I was working to get my PhD. I am grateful to Mr. Ahmet Mahmut Unlu and Dr. E. Gokce Gun for their moral support. I am grateful to God for giving me the chance to study and learn from people at MIT.

I am grateful to my PhD advisor Prof. Caroline A. Ross, for her support and guidance. She guided me through a lot of dark times of my PhD and helped me be successful. I am grateful to her for her support and for sharing her hard-earned wisdom.

I am grateful to my thesis committee members Prof. Geoff Beach and Prof. Lionel C. Kimerling for their helpful comments and suggestions. The courses they taught were very helpful in my PhD both in terms of getting the essential knowledge and in terms of becoming an insightful and independent researcher.

I thank my co-workers in the lab, in particular, Prof. Taichi Goto, whose help was essential for me to learn how to succeed in the lab. I also thank Dr. Gerald F. Dionne, Dr. Nicolas Aimon, Prof. Dong Hun Kim, Jae Jin Kim, Dr. Di Chen, Prof. Juan Manuel Florez, Dr. Umut Eser, Melih Okan, Ahmet Demir, Oguz Ahsen, Prof. Ali K. Okyay, Wubin Bai, Dr. Adam Hannon, Dr. Kevin Gotrik, Dr. Carlos Garcia, Dr. Jean Anne Currivan Incorvia, Jinshuo Zhang, Frank Liu, Astera Tang, Shuchi Ojha, Dr. Lara Tryputen, Dr. Pin Ho, Dr. Enno Lage, Kun-Hua Tu, Dr. Xueyin Sun, Chen Zheng, Dr. Hong Kyoon Choi, Dr. Karim Aissou, Dr. Jeong Gon Son, Prof. Lei Bi, Prof. Juejun Hu, Prof. Polina Anikeeva, Alex Manick, Annia Pan, Nathalie Huynh, Andy Cruz and my collaborators including Dr. Murong Lang, Dr. Mohammad Montazeri, Prof. Kang Wang, Prof. Joel Juen, Andreas Kehlberger, Prof. M. Kläui, Dr. Toeno van der Sar, Dr. Francesco Casola, Dr. Huiliang Zhang, Prof. Amir Yacoby, Dr. Andrii Chumak, Prof. Burkard Hillebrands and other collaborators who I may have missed.

I acknowledge the support from S3TEC, National Science Foundation as well as Samsung Advanced Institute of Technology.

I thank MIT staff, especially the DMSE staff at headquarters, Angelita Mireles and Elissa Haverty for their support. I also acknowledge the support from MIT facilities and other offices which helped us at some point. I am thankful for the support of Mr. David Bono on Faraday rotation setup. I acknowledge the help of the current or former MIT CMSE staff Dr. Scott Speakman, Dr. Charles Settens, Dr. Josh Guske, Dr. Shaoyan Chu, Dr. Elisabeth L. Shaw, Tim McClure for their training and assistance on the characterization equipments. I thank Prof. Karl Berggren for allowing me to use the NanoStructures Laboratory, and Mr. Jim Daley, Mr. Mark Mondol and Mr. Tim Savas for their help on the NSL facilities. I also thank Dr. Kurt Broderick for training me and helping with processing and measurements in the MTL.

March 24, 2015

Mehmet Cengiz Onbaşlı

Chapter 1. Introduction

1.1 Changing nature of computation and data storage

The first quarter of the twenty-first century indicates that semiconductor industry is approaching a series of fundamental and revolutionary technological changes in transistor and electronic chip designs, data storage media and devices and even computer achitectures. These changes are driven by two categories of driving forces:

1. Growing consumer and business demand for mobile devices and real-time data processing (and associated demand on cloud data storage and processing)
2. Fundamental technological limits that prevent device, bandwidth, energy consumption and data storage density scaling.

The consumer demand for mobile devices is a major driver for efficient use of telecommunication bandwidth, battery, and chip real estate allocated for data storage and processing. In 2014, about 90 million traditional cameras and 2 billion smartphones and tablets with cameras were sold [1]. According to the same report, more photos will be taken in the next year or two [with smartphone cameras] than were taken on film ever [1]. As camera resolution increases and mobile video streaming volume grows at an almost exponential rate [2], the need for energy-efficient and fast-accessible data storage on servers (‘the cloud’) grows.

The second category of driving forces is the fundamental technological limitations on materials and devices used for data storage, processing, battery and display technologies. For personal mobile and commercial server data storage, storage devices need to be able to offer high speed access to data (for reading, writing and erasing), with minimum 10 year data retention, high endurance, high security, high density, power efficiency, manufacturability and ideally merging the volatile and nonvolatile storage capabilities into a single device architecture. On the data processing side, further transistor and chip scaling along Moore’s

Law [3] is no longer the most effective direction, as power consumption per area starts exceeding feasible on-chip thermal management solutions and operation at higher frequencies, clock distribution across chips/boards becomes uneven due to jitter, skew or RC delays, and transistor ON/OFF ratios are as low as 10 and gate oxide leakage starts imposing reliability issues [4]. The nonvolatile data storage devices, in particular hard disk drives, are also scaling magnetic bit densities faster than the scaling rate of transistors guided by Moore's Law, as shown on Fig. 1-1(a). Fig. 1-1(a) shows the areal density scaling of the bit patterned media and compares with transistor densities over the past 5 decades. As hard disk grains shrink, the magnetic grain sizes approach the superparamagnetic size limit (~ 8-10 nm), below which storing data is not possible due to thermal instabilities. Therefore new *methods and materials of storing data are needed*. In addition, the read-head of the magnetic hard disk drive is a major component of the total data storage power consumption and reduces the reliability of the data storage unit. In order to meet the growing market demand for high throughput data processing, a fundamentally more efficient and scalable data processing method needs to be established (i.e. by avoiding electron transport, eliminating read head, reducing power consumption and operation frequency).

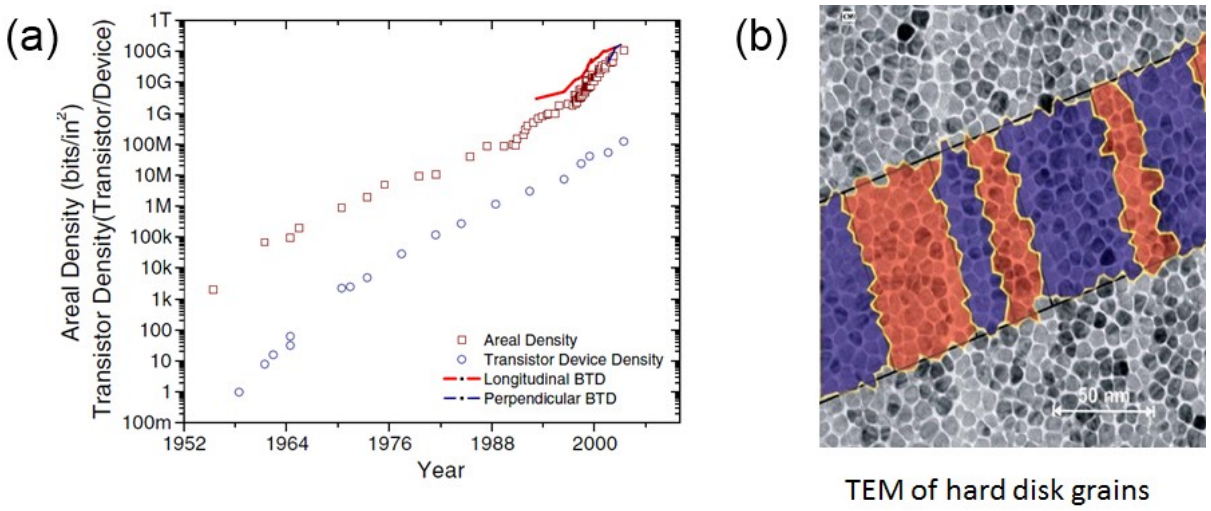

Fig. 1-1. Traditional magnetic hard disk drives are reaching their limits of bit density. (a) The transistor scaling rate is compared with areal density of bits (bits/in^2) [5]. (b) The bit sizes used for hard disk drives is approaching the superparamagnetic size limit of magnetic materials (t < 10 nm) [6].

On the interconnection side, while significant development and engineering on the Group III-V laser, photodetector and silica fiber technologies enabled high transmission rates for long-haul communications [7,8], communication rate on board and chips are significantly limited by RC time delays and other limitations of electrical interconnects [4]. In order to circumvent the limitations of electrical interconnects, board-to-board and chip-to-chip photonic interconnects can offer to meet the projected demand for data throughput and processing speed. On the other hand, optical components are still premium elements that continue to cost a greater fraction of the data communication link budget for every new generation of systems. In order to keep manufacturing costs manageable (i.e. similar cost per chip), scalability and cost studies were done [9] and monolithic photonic integration has been found to be the only viable solution, especially beyond 1 Tbps communication rate. Other manufacturing or integration methods such as flip-chip bonding or wire bonding of photonic and electronic chips are only solutions for the shorter term [9] and do not meet the cost requirements for scalable chip designs. Figure 1-2 is a scaling chart for photonic industry prepared by Photonic Systems Manufacturing Consortium [9] in order to meet the energy, bandwidth and distance trade-offs of the future projected demand in communications infrastructure. Photonic components are integrated to maximize the available bandwidth, physical density of components, and input and output port count while reducing latency, power consumption (i.e. insertion loss for passive devices and heat dissipation in active devices) and overall cost.

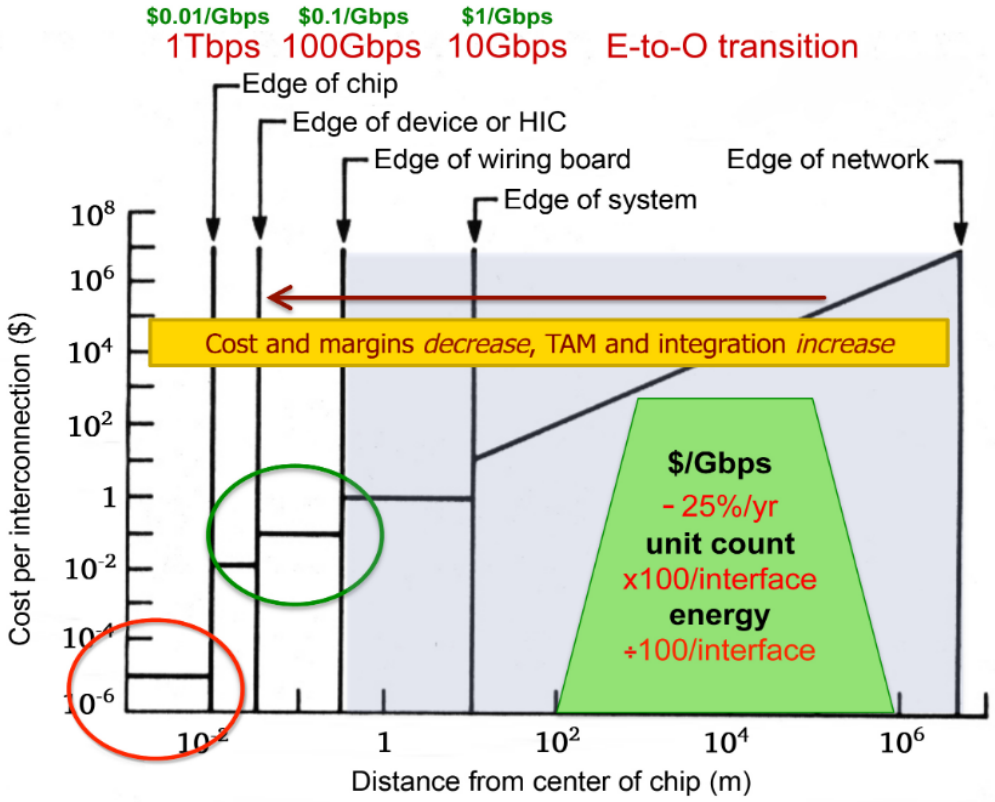

Fig. 1-2. Design rule for the deployment of optical interconnections: The systems cost per Gbps bandwidth needs to decrease by about 25% annually; the unit count needs to increase and energy consumed per component needs to decrease by two orders of magnitude for every major generation of integration (vertical black lines) (Image courtesy of Prof. L. C. Kimerling and Photonic Systems Manufacturing Consortium) [9]

As each aspect of the technology is driven to undergo fundamental changes, a range of useful data storage methods, materials and architectures were proposed. In Section 1.2, a summary of solutions to the aforementioned technological limitations are presented, together with proposed solutions for each issue.

In Section 1.3, photonic/electronic integration is summarized and previous studies on a key missing element, integrated optical isolators, have been discussed with respect to optical isolation ratio, bandwidth, insertion loss, footprint, thermal budget, Si complementary metal-oxide semiconductor (CMOS) compatibility and power consumption (if optical isolation requires active control) requirements.

In Section 1.4, previous studies on multiferroic materials are discussed with respect to

strength of ferroelectricity and magnetism, magnetoelectric coupling and Si CMOS compatibility for nonvolatile magnetic/multiferroic random access memory (MRAM) with ternary logic.

In Section 1.5, magnonic materials and devices are discussed, as their operation frequencies are beyond 5 GHz upto 7 THz (1st Brillouin Zone of $Y_3Fe_5O_{12}$) and power consumption can potentially be as low as a $60k_BT$/switching. In Section 1.6, a short summary of the thesis is presented.

1.2 Emerging solutions for the new demands and constraints on computation and data storage

Ideal nonvolatile data storage elements store information with low cost, high manufacturability, high bit density per area, high read/write/erase rates, at least 10 years of data retention, no leakage current and consistent voltage and current specifications over the lifetime of the component [2]. In order to meet these needs, magnetic data storage has been developed. Since data access times of magnetic hard disk drives have been long (~10 ms), computer architectures in the past two decades had to include a solid state random access memory (RAM) based on semiconductors. As a result, DRAM (dynamic random access memory, 1 transistor/1 capacitor) and SRAM (static random access memory, 6 transistors/2 capactiors) were developed. Although these RAM architectures are volatile memory elements (information is lost when power is switched OFF), they are indispensable elements of computers. In state-of-the-art computation infrastructures, DRAM dominates the RAM space of desktop personal computers while SRAM's are used for more specialized applications such as cache memories and small embedded systems [2]. SRAM is a static volatile memory (written once while power is ON and accessed many times without having to refresh). DRAM's however require periodic refreshing of the bits. SRAM's provide fast access, ease of control and better integration (no bus needed unlike DRAM's). DRAM's are simpler, cheaper and they operate at lower power than SRAM. One issue with DRAM's is they are

slower than SRAM. Despite the major functional advantages of SRAM with respect to DRAM, DRAM became the dominant volatile memory due to its lower cost [2].

In early 1990's, Flash memory (nonvolatile floating gate) was developed to reduce device footprint and power requirements. NOR and NAND Flash memories are the first major breakthroughs to combine nonvolatile data storage with high-speed access (writing an entire page in a small cell size). The current trend in data storage industry is to vertically integrate NAND flash memory elements to save chip real estate. Nonvolatile NAND Flash has gradually been taking over larger market share of the solid state data storage space of computers from DRAM and SRAM and 3D integration has extended the scaling of these memory elements. Complexities associated with the fabrication of 3D vertical stacks of NAND flash memories limits the number of generations of 3D NAND flash memory elements. In addition, NAND flash memories have problems with random access time, bit alterability and write cycles. As a result of these limitations, new nonvolative memory (NVM) materials and architectures have started emerging. These NVM elements, such as a ferroelectric RAM (nonvolative), have already started being commercialized in niche applications such as Texas Instruments MSP430 microcontrollers [10] due to nonvolatile and reliable data storage (over 100 trillion read/write cycles), fast write times like SRAM (1000x faster than Flash) and low power requirements (1.5V to write and erase, $V_{write} > 10V$ for Flash) and after year 2020, these elements are expected to take over DRAM and SRAM altogether.

Table 1-1. Emerging solutions to the limitations of data storage, interconnection and processing devices.

Device type	Functionality	Current Problem	Proposed solutions	Relevant materials solutions in this thesis	Relevant solutions in this thesis	Major achievements
Random Access Memory (RAM)	Volatile data storage	volatile storage, chip real estate	Nonvolatile RAM architectures	$SrTi_{0.70}Co_{0.30}O_{3-\delta}$ (STCo30)	Multiferroic material switching (STCo30)	STCo30/Si room temperature multiferroic switching.
Electrical Interconnects	Data transfer	RC delays, reliability	Optical interconnection	Si CMOS integration of Ce:YIG	Integrated optical waveguides and isolators	Optical isolators (Isolation ratio: 13.0± 2.2 dB), (insertion loss: 7.4 ± 1.8 dB)
Transistors	Data processing	Scalability, power consumption, operation frequency limits processing constraints	Spin-based computation (magnonics)	$Y_3Fe_5O_{12}$ (YIG), $Ce_1Y_2FeO_{12}$ (Ce:YIG), $Tm_3Fe_5O_{12}$ (TmIG)	(not included in the thesis, to be published by collaborators)	Ultra-low damping magnon transport, low-energy nonvolatile switching.

Table 1-1 summarizes the three major components (RAM, interconnects, transistors) and their limitations. Volatile RAM memory technologies have matured over the past three decades as a result of the learning curve and production volume demanded by the semiconductor industry. As transistors no longer scale in feature sizes or operation frequencies, RAM technologies also started slowing in scaling. The real estate that RAM occupies on chip and volatile storage make motivate further research into new memory element architectures. As a result, more fundamental materials and device architectures have started being explored.

This thesis brings multiple materials solutions that help resolve some of the limitations of new nonvolatile memory technologies, optical interconnects and optical isolators and magnetic and spin logic elements. $SrTi_{0.70}Co_{0.30}O_{3-\delta}$ (STCo30) films were grown on Si and

demonstrated to have magnetic and ferroelectric switching. By accessing ferroelectric and magnetic states separately, one can double the number of bits per cell. For improving optical interconnects and isolators, methods for growing good quality magneto-optical garnet films on Si-based substrates were explored. An improved deposition method of $Ce_1Y_2Fe_5O_{12}$ (Ce:YIG) on Si enables enhanced optical isolator performance characteristics. For improving transistors (and ultimately replacing them with logic gates), epitaxial growth methods for $Y_3Fe_5O_{12}$ (YIG) films with ultra-low Gilbert damping values were developed. This development enables the demonstrations of magnonic logic gates, ultra-low energy switching magnetoelectric devices such as Bi_2Se_3/YIG heterostructures [11].

Table 1-2 summarizes a few major classes of emerging NVM are presented below. Ferroelectric RAM, magnetic RAM, spin-torque transfer (STT) RAM, Phase-change RAM are compared on Table 1-2 in terms of read time, write/erase time, endurance, power consumption and maturity of the technology. These devices merge the best of RAM (volatile memory with fast access) and hard disk drive storage (nonvolatile memory with longer access time). Since each of these new memory achitectures depend critically on the unique electronic or magnetic switching properties of resistive oxides, phase change materials, ferroelectric materials or magnetic tunnel junctions, establishing Si CMOS compatibility of these materials is essential. Once the materials compatibility issue is resolved, devices can be engineered to high spatial density and scalability (larger cell sizes), high read/write speed and lower power consumption.

Table 1-2. Comparison of emerging nonvolatile memory technologies [2].

Features	FeRAM (Ferroelectric RAM)	Magnetic RAM (MRAM)	Spin-torque transfer RAM (STT-RAM)	Phase Change memory (PCM)
Cell size (F^2)	Large (~ 40)	Large (~25)	Small (~6-20)	Small (~8)
Storage mechanism	Permanent polarization of a ferroelectric material (PZT or SBT)	Permanent magnetization of a ferromagnetic material in a magnetic tunnel junction	Spin-polarized current applies torque on the magnetic moment	Amorphous/polycrys. Phases of chalcogenide alloy
Read time (ns)	20 to 80	3 to 20	2 to 20	20 to 50
Write/erase time (ns)	50/50	3 to 20	2 to 20	20/30
Endurance	10^{12}	$> 10^{15}$	$> 10^{16}$	10^{12}
Write power	Mid	Mid to high	Low	Low
Nonvolatility	Yes	Yes	Yes	Yes
Maturity	Limited production	Test chips	Test chips	Test chips
Applications	Low density	Low density	High density	High density

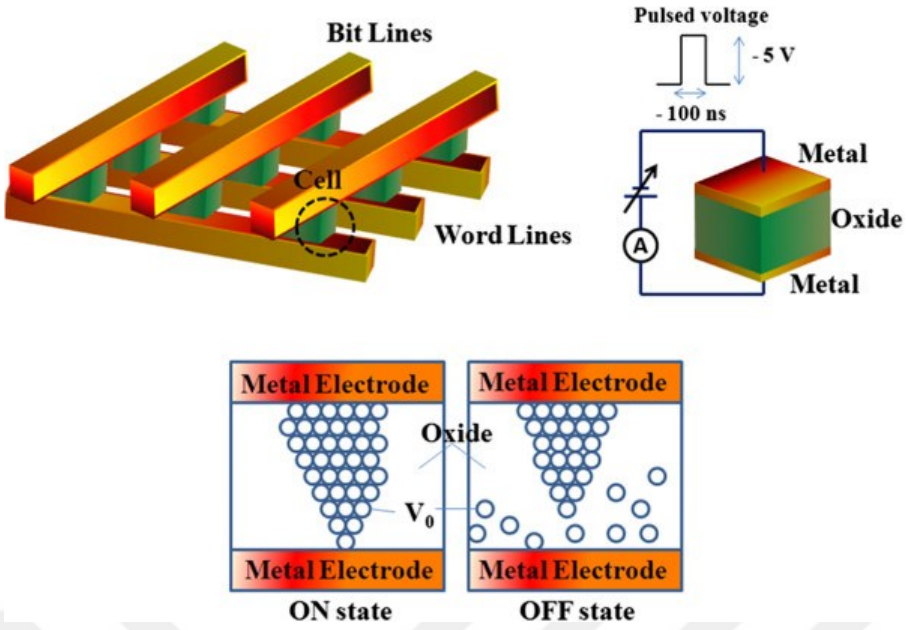

Fig. 1-3. Resistive RAM architecture and working principle [2].

A basic resistive RAM architecture is presented in Fig. 1-3. An oxide resistive layer is sandwiched between two metal contacts. ON state of the device is when the resistance of the oxide is low due to filaments that form between top and bottom electrodes. When a high voltage and short ERASE pulse is applied, the filament is broken and the increase in the resistivity of the oxide is read out as OFF state. Similarly, a write pulse can also be applied to restore the ON state (with filament microstructure). The device performance depends on the reliability of the resistive material (oxide or metal) microstructure.

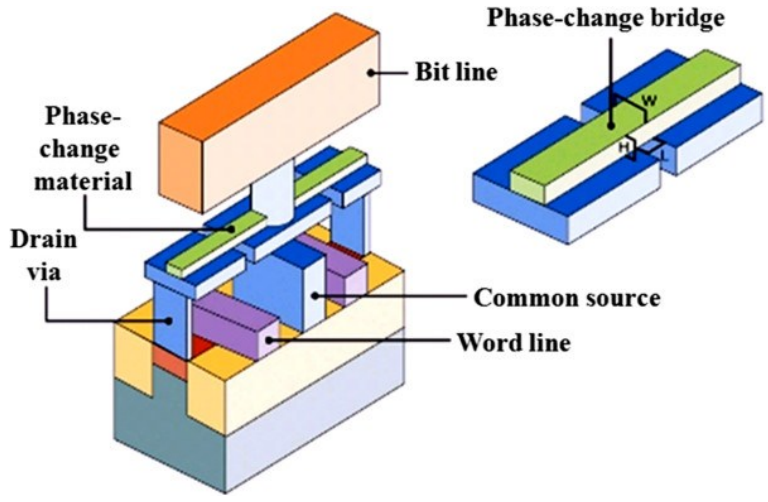

Fig. 1-4. Phase-change RAM architecture and working principle [2].

The basic phase-change RAM architecture is presented in Fig. 1-4. The microstructure of

the phase-change material is toggled between crystalline or amorphous states, corresponding to low or high resistances, respectively. Most phase-change materials contain at least one element from group 6 of the periodic table. The most promising phase-change materials are GeSbTe alloys (pseudobinary compositions between GeTe and Sb_2Te_3), which are already in use as the data layer in rewritable compact disks and digital versatile disks (CD-RW and DVD-RW). Intel, STMicroelectronics and Samsung have been working on these materials and RAM architectures.

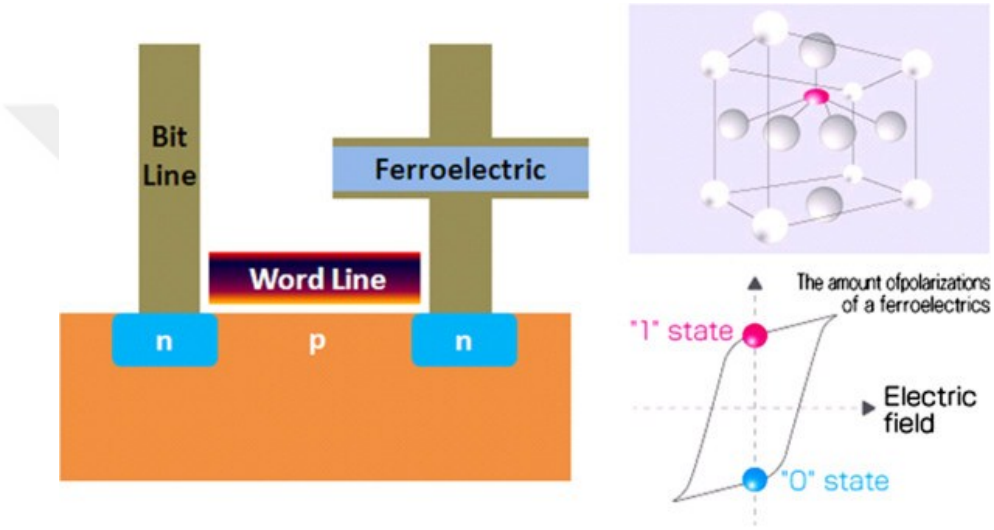

Fig. 1-5. Ferroelectric RAM architecture and working principle [2].

Fig. 1-5 shows the basic structure of a ferroelectric RAM. The device consists of a transistor and a capacitor where the dielectric of the capacitor is a ferroelectric oxide such as PZT (lead zirconium titanate, exact compositions vary). The transistor applies different voltages on the ferroelectric capacitor and cycles over the ferroelectric consistutive relationship of the capacitor dielectric. This cycling requires very low energy to switch and it is nonvolatile since the remanent state of the ferroelectric oxide is retained without power. FeRAM's offer fast and low-energy nonvolatile storage compared with today's NAND Flash, but FeRAM's are still slower than DRAM.

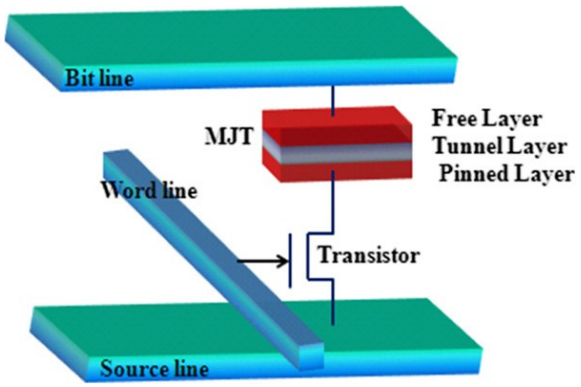

Fig. 1-6. Spin-torque transfer RAM (STT RAM) architecture and working principle [2].

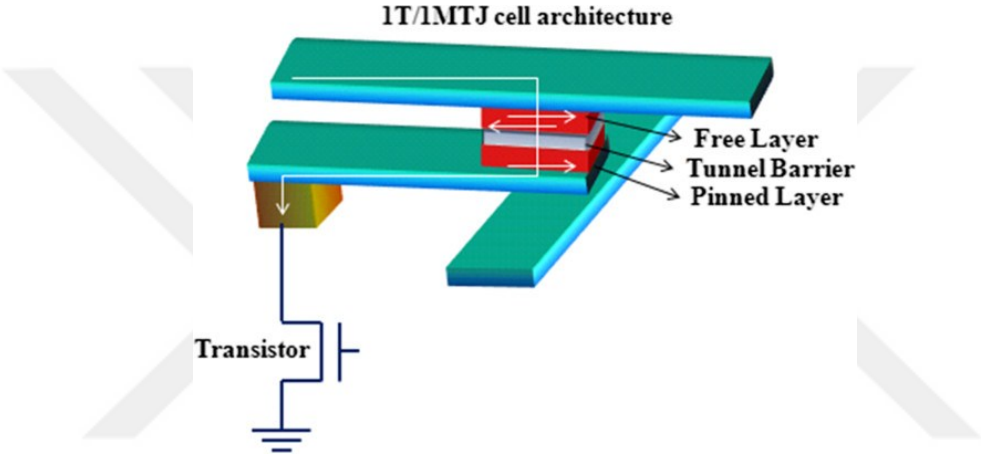

Fig. 1-7. Magnetic RAM (MRAM) architecture and working principle [2].

Fig. 1-6 and Fig. 1-7 show spin-torque transfer RAM and magnetic RAM architectures, respectively. MRAM and STT-RAM have similar reading mechanism across the tunnel barrier: When the free magnetic layer and the pinned magnetic layer have (anti) parallel magnetic moments, the total resistance state is low (high) and a high (low) current output is read out as electrons are going to be able to tunnel through the barrier. In order to write and erase bits on MRAM cells, a current is passed through the write line to induce a magnetic field across the cell. Samsung. IBM, Hitachi, TSMC and Toshiba are actively developing MRAM memory elements. In STT RAM's, an electric current is polarized by aligning the spin direction of the electrons flowing through a magnetic tunnel junction. Data writing is achieved by using spin polarized current to change the magnetic orientation of the information storage layer in the tunnel junction via spin-transfer torque. The resistance difference of the tunnel junction is read-out. STT-RAM's are developed by Everspin, Grandis,

Hynix, IBM, TDK, Toshiba and Samsung. One major challenge of STT-RAM's is achieving low write power and thermal stability at the same time.

As each of these device architectures utilize a unique functionality of an oxide or a resistive layer which are not conventionally integrated with CMOS circuits, methods of growing oxides on Si-based substrates need to be established for demonstrating useful oxide switching behavior. In this thesis, we focus on integrating magneto-optical oxides (garnet) or multiferroic perovskites on Si or other substrates (Si waveguide chips, thick SiO_2, Quartz or other chips). After achieving integration of magneto-optical or multiferroic oxides, one can start engineering CMOS control and device architecture for high performance. Integrated magneto-optical oxides may enable monolithic integration of photonic/electronic chips, while multiferroic (perovskite-based materials) and magnonic (YIG-based materials) oxides may enable novel data storage behavior similar to the devices shown above. The focus of this thesis is the fundamental materials science behind the materials which are ultimately going to enable high performance device architectures proposed for meeting the demands of computation and data storage.

1.3 Integrated nonreciprocal photonic devices

Lasers are destabilized by reflections coming back into gain region. As a result, optical isolators are used in order to prevent any backreflections into the lasers. Preventing these reflections is essential for stable and reliable operation of lasers. This optical isolation functionality can only be reliably achieved when the optical isolator is a nonreciprocal photonic element, i.e. time-reversal symmetry is broken. When time-reversal symmetry is broken, backreflected light has to travel along a different path than its forward path due to the difference between forward and backward effective refractive indices. High performance optical isolators are commercially available as discrete bulk components for operation near wavelength of $\lambda = 1550$ nm.

As presented in part 1.1, optical interconnection and cost reduction per bandwidth and distance requires monolithic integration of optical components. These components, including lasers [12], waveguides, modulators and photodetectors [13] have started being developed as monolithic elements of a single chip. One missing element in this monolithic integration has been optical isolators. The integration of the optical isolator element has been a major processing problem because of differences between crystal structures, lattice parameters and thermal expansion coefficients of magneto-optical (MO) thin films typically used for nonreciprocity and silicon. The performance of MO thin films is poorer than that of the bulk MO material and these films require high thermal budget for growth [14].

Several important demonstrations of on-chip optical isolators made out of $Ce_1Y_2Fe_5O_{12}$ (Ce:YIG) by several groups [14-19] indicated that on-chip optical isolation is not impossible, but it is essential that the integration technology for MO material/device and MO film quality (in terms of MO figure of merit) are further improved to fulfill the demanding requirements of photonic integration. The MO figure of merit is defined as:

$$FoM = \frac{\theta}{\alpha} = \frac{Faraday\ rotation\ (^\circ\ cm^{-1})}{Optical\ Loss\ (dB\ cm^{-1})}$$

One critical materials engineering challenge in the demonstration of high-performance on-chip isolators is the integration of high FoM MO garnet oxides on waveguide/resonator chips while not damaging the waveguide structures. High FoM MO garnet oxides typically require high thermal budget of growth, and too much annealing can damage Si waveguides. Therefore, the trade-off between achieving high FoM MO garnet oxides and retaining low insertion loss waveguides must be balanced. In this thesis, we focus on developing MO garnet oxide growth and integration method on Si-based photonic substrates in order to demonstrate reduced insertion loss and enhanced isolation ratio by establishing a garnet growth method with enough thermal budget for protecting the waveguide chips and achieving high MO FoM. By reducing the insertion loss of optical isolators, the ultimate goal of

energy-efficient and less expensive bandwidth and component costs discussed in Part 1.1 becomes possible.

1.4 Multiferroic Materials and Devices

Materials that exhibit multiple ferroic (hysteretic) properties such as ferroelectricity, ferromagnetism or ferroelasticity are called multiferroic materials. There has been significant research interest in these materials as these materials have the possibility of voltage controlled low-energy switching and fabrication in two-dimensional addressable and dense planar arrays. Multiferroic single phase or composite materials can be designed for enhanced functionality and design flexibility. As many of the multiferroic materials are complex oxides, pulsed laser deposition method is the most useful and appropriate means for growing high quality multiferroic thin films [20-25]. Using different mechanisms substitutional doping, oxygen vacancy doping, or by using substrate strain, an otherwise regular dielectric material can be made ferroelectric by distorting the unit cell of the material from cubic to tetragonal, as in the case of epitaxial $SrTiO_3$ on Si [26].

Many magnetic perovskites have been shown to exhibit (anti)ferromagnetic and/or ferroelectric switching, and magnetoelectric coupling [20-25]. Magnetoelectric coupling is the electrical control of magnetic polarization and this coupling is observed in strong ferromagnetic materials. Among many classes of oxides, perovskites (ABO_3) are among the best known materials systems. Engineering the defect density on the A, B or oxygen vacancy sites open up separate handles for tuning material conductivity, optical absorption, magnetism, ferroelectricity, dielectric constant and chemical reactivity. For data storage and processing applications, perovskites offer many unique capabilities that most other materials systems cannot offer. For instance, one can substitutionally dope A and B sites separately to independently engineer magnetic, optical and magneo-optical or ferroelectric properties.

While perovskites are promising materials for magnetism, ferroelectricity and related

applications, a previous study indicated that magnetism and ferroelectricity in single-phase perovskites are in competition, as ferroelectricity requires d^0 (completely filled or depleted d-shell) and ferromagnetism requires a nonzero d electron valence state to yield a net magnetic moment [27]. While this fundamental tradeoff prevents achieving room temperature multiferroic oxides with simultaneously strong magnetic and ferroelectric response, one can circumvent this tradeoff by breaking the cubic symmetry of perovskites via oxygen vacancy doping and B-site cation substitution. Independent tunability of conductivity and magnetism can be achieved for insulating magnetic perovskites as well. Ultimately, any functional perovskite oxide may also need to be integrated on silicon based chips. Magnetic perovskites enable room-temperature ferromagnetic, room-temperature multiferroic switching mechanisms for more energy-efficient switching and possibly magneto-optical isolators integrated on silicon based optical chips. Such films are going to be discussed in chapter 5.

1.5 Magnonic Materials and Devices

Magnon is the collective spin oscillations in a material. Magnons are quantized spin-wave oscillations associated with the flip of a single spin. Magnons bosons and they obey Bose-Einstein statistics [28,29]. The field magnonics has started emerging as researchers started understanding ways to convert charge currents into spin currents (and vice versa), transport spins on chip with low cross-talk and low power consumption over wide frequency ranges such as beyond 5 GHz and upto 7 THz that are not available to Si CMOS. Two major types of spin wave oscillations were identified: strong but short-distance exchange interaction and relatively weak long-range dipole-dipole interactions. The properties of the short wavelength ($\lambda < 1$ μm) waves are governed by exchange interactions. Long-wavelength interactions are dipolar or magnetostatic waves [2,3]. For data processing using dipolar magnons, four groups of materials are found to be useful: polycrystalline metallic permalloy ($Ni_{81}Fe_{19}$), ferromagnetic Heusler compounds (high-spin polarization, high saturation magnetization, high Curie temperature and low Gilbert damping) [30], CoFeB composites [31] and nanometer-thick YIG insulating ferrimagnetic thin films with ultra-low Gilbert

damping [32]. Recent progress in exciting, transporting and detecting magnons and converting magnons on these functional thin films have opened up the field of magnonics.

To excite a desired frequency or wavelength and phase of the magnons, an electromagnetic signal is applied to a microwave antenna and this antenna excites the magnetization precession in the magnetic material via an alternating Oersted field induced around the antenna. Other spin injection methods include ultra-short optical pulsing, parametric amplification of spin waves from thermal fluctuations, magnetoelectric cell in which an electric field controls exchange bias or magnon injection by spin-transfer torque. Each method has its own advantage: The classical microwave antenna excitation interfaces electromagnetic waves and spin waves, while STT-based magnon injection enables the direct coupling of spin waves with a spin-polarized DC electric current (i.e. bridge between magnonics, charge-based spintronics and electronics) [33-39].

Several advantages distinguish magnon-based data processing with respect to conventional methods:

1) **Eliminating Joule heat dissipation:** Since one can use insulating magnetic materials for information transport and data processing, i.e. using YIG thin films that can transport magnons over cm-long distances, Joule heat dissipations are eliminated for the spin transport stage (for spin excitation and detection, there is still transient and Joule heat dissipation).

2) **Wide operation frequency ranges not available to CMOS:** The magnon spectrum can reach from GHz to a few THz, where the first magnonic Brillouin zone in YIG lies at about 7 THz [40].

3) **Contactless wiring**: Since magnons can be excited with an electromagnetic antenna, most of the wiring can be eliminated to simplify circuits. A global microwave field can drive a number of separate and local spin-wave oscillators and avoid today's clock skew or distribution problems while simplifying wiring [41].

4) **Wave-based computation**: Since magnons are waves, data processing logic gates can operate on the phase of the waves rather than just intensity. This capability enables the implementation of non-Boolean algorithms that can scale easier with simpler hardware [42].

5) **Nonlinear data processing techniques**: Concepts in nonlinear photonics also apply analogously to magnons. Many nonlinear effects such as spin-wave solitons, four-wave mixing, power limiting, wave front reversal can be demonstrated [43].

6) **Room temperature macroscopic quantum phenomena**: Using magnons, a form of Bose-Einstein condensate (a coherent ground state) can be demonstrated at room temperature. A magnon supercurrent (a collective motion of magnons driven by a phase gradient of a condensate wavefunction) can be used for low-loss information transfer [44].

In order achieve these advantages, growth methods for magnetic insulator thin films such as $Y_3Fe_5O_{12}$ (YIG) need to be established. The magnetic moment of these films must achieve the saturation and remanent moments of the bulk YIG crystal. In addition, the films coercivities must be comparable to the coercivities of the bulk crystal. These key materials challenges motivate the growth studies presented in chapter 4. In chapter 4 of this thesis, we focus on experimental preparation methods for the most critical element that enables all of these advantages of magnonics: the YIG thin film with bulk-like magnetic and damping properties.

1.6 Overview and layout of the thesis

Chapter 2 covers the oxide powder and thin film preparation and characterization methods. In addition, simulation methods used for guiding experimental work are also summarized. Chapter 3 focuses on the fundamental materials science and engineering of magneto-optical

garnet and perovskite oxide films for integrated nonreciprocal photonic device applications. In the second part of chapter 3, experimental and simulation work on nonreciprocal isolator demonstrations, optical filters and modulators are presented. Chapter 4 covers new classes of magnetic device architectures to enable data processing at low-power and at operation frequencies that CMOS architectures cannot offer. In chapter 5, a rational multiferroic oxide design and an experimental demonstration of a promising room temperature multiferroic oxide is presented. The final chapter covers the conclusions, applications enabled after this thesis and future research opportunities.

References

[1] B. Evans, "The explosion of imaging," http://ben-evans.com/benedictevans/2014/6/24/imaging, date accessed: March 16, 2015.

[2] J. S. Meena, S. M. Sze, U. Chand, and T.-Y. Tseng, Nanoscale Research Letters, **9**:526 (2014).

[3] G. E. Moore, Electronics, **38**, 8, April 19, (1965).

[4] D. A. B. Miller, Int'l J. Optoelectronics **11** (3), 155 (1997).

[5] T. W. McDaniel, *J. Phys.: Condens. Matter*, **17**, R315 (2005).

[6] C. A. Ross, "Data Storage - Lecture Slides of 3.45 Magnetic Materials Course", Chapter 17, Slide 5, (2012).

[7] Infinera, "Photonic Integration", http://www.infinera.com/pdfs/whitepapers/Infinera-WP-Photonic_Integration.pdf, date accessed: April 15, 2015.

[8] D. Dyer and D. Gross, "The Generations of Corning: The Life and Times of a Global Corporation," Oxford University Press, 2001, New York.

[9] B. Pfahl, L. C. Kimerling, J. McElroy, "High Volume Photonics Manufacturing, INEMI, Webcast 2-19-15", <http://photonicsmanufacturing.org/>, date accessed: 4/15/2015.

[10] Texas Instruments MSP430 microcontrollers, <http://software-dl.ti.com/trainingTTO/trainingTTO_public_sw/MSP430_LaunchPad_Workshop/v3/MSP430_Workshop_v3_02a.pdf>, date accessed: 4/15/2015.

[11] M. Lang, M. Montazeri, M. C. Onbasli, et al, *Nano Lett.* **14**, 3459 (2014).

[12] J. Liu, X. Sun, R. Camacho-Aguilera, L. C. Kimerling, and J. Michel, Opt. Lett. **35** (5), 679–681 (2010).

[13] E. Onaran, M. C. Onbasli, A. Yesilyurt, H. Y. Yu, A. M. Nayfeh, and A. K. Okyay, Opt. Express **20** (7), 7608–7615 (2012).
[14] T. Goto, M. C. Onbasli, and C. A. Ross, *Opt. Express* **20**, 28507 (2012).
[15] T. Mizumoto, R. Takei, and Y. Shoji, *IEEE J. Quantum Electronics* **48**, 252 (2012).
[16] M. C. Onbasli, T. Goto, X. Sun, N. Huynh, C. A. Ross, *Opt. Express* **22**, 25183 (2014).
[17] M.-C.Tien, T. Mizumoto, P. Pintus, H. Kromer, and J. E. Bowers, *Opt. Express* **19**, 11740 (2011).
[18] Y. Shoji, M. Ito, Y. Shirato, T. Mizumoto, *Opt. Express* **20**, 18440 (2012).
[19] S. Ghosh, S. Keyvavinia, W. Van Roy, T. Mizumoto, G. Roelkens, R. Baets, *Opt. Express* **20**, 1839 (2012).
[20] N. A. Spaldin, M. Fiebig, *Science* **309**, 391 (2005).
[21] L. W. Martin, S. P. Crane, Y.-H. Chu, M. B. Holcomb, M. Gajek, M. Huijben, C.-H. Yang, N. Balke, and Ramesh, R.; *J. Phys.: Condens. Matter* **20** 434220 (2008).
[22] H. Schmid, *Ferroelectrics* **162**, 317 (1994).
[23] R. Ramesh, and N. A. Spaldin, *Nat. Mater.* **6**, 21, (2007).
[24] W. Eerenstein, N. D. Mathur, J. F. Scott, *Nature* **442**, 759, (2006).
[25] J. van den Brink, and D. I. Khomskii, *J. Phys.: Condens. Matter*. **20**, 434217 (2008).
[26] J. H. Haeni, P. Irvin, W. Chang, R. Uecker, P. Reiche, Y.L.Li, S. Choudhury, W. Tian, M. E. Hawley, B. Craigo, A. K. Tagantsev, X. Q. Pan, S. K. Streiffer, L. Q. Chen, S. W. Kirchoefer, J. Levy and D. G. Schlom, *Nature* **430**, 758 (2004).
[27] N. A. Hill, *J. Phys. Chem. B*, **104**, 6694 (2000).
[28] A. G. Gurevich and G. A. Melkov, *Magnetization Oscillations and Waves* (CRC, 1996).
[29] D. D. Stancil and A. Prabhakar, *Spin Waves: Theory and Applications* (Springer, 2009).
[30] T. Kubota et al., *Appl. Phys. Lett.* **94**, 122504 (2009).
[31] H. Ulrichs, B. Lenk, M. Munzenberg, *Appl. Phys. Lett.* **97**, 092506 (2010).
[32] M. C. Onbasli et al., *APL Mater.* **2**, 106102 (2014).
[33] V. Vlaminck, and M. Bailleul, *Science* **322**, 410 (2008).
[34] T. Brächer, *Appl. Phys. Lett.* **105**, 232409 (2014).
[35] S. Dutta, D. E. Nikonov, S. Manipatruni, I. A. Young, and A. Naeemi, *IEEE Trans. Magn.* **50**, 1300411 (2014).
[36] V. E. Demidov, S. Urazhdin, and S. O. Demokritov, *Nature Mater.* **9**, 984 (2010).
[37] M. Madami, *et al. Nature Nanotech.* **6**, 635 (2011).
[38] V. E. Demidov, *et al. Nature Mater.* **11**, 1028 (2012).
[39] A. Hamadeh, *et al. Phys. Rev. Lett.* **113**, 197203 (2014).
[40] V. Cherepanov, I. Kolokolov, V. L'vov, *Phys. Rep.* **229**, 81–144 (1993).
[41] Y. Au, *et al. Appl. Phys. Lett.* **100**, 182404 (2012).
[42] S. Khasanvis, M. Rahman, S. N. Rajapandian, & C. A. Moritz, *2014 IEEE/ACM International Symposium on Nanoscale Architectures (NANOARCH),* 171-176 (2014).
[43] B. A. Kalinikos, N. G. Kovshikov, & A. N. Slavin, *Phys. Rev. B* **42**, 8658 (1990).
[44] S. Takei, & Y. Tserkovnyak, *Phys. Rev. Lett.* **112**, 227201 (2014).

Chapter 2. Experimental and Simulation Methods

This chapter focuses on the experimental and simulation methods used for fabricating and testing oxide powders, films and devices. Ceramic targets were prepared using furnaces provided by Prof. Harry Tuller and bulk powder processing techniques. The multiferroic, magnonic and magneto-optical oxide films were grown using pulsed laser deposition. Growth conditions (base pressure, substrate temperature, growth rate, oxygen pressure, whether or not there is post-growth rapid thermal annealing, and other project-specific recipes) for samples used for each project are presented in the respective chapters. For a few projects, a molecular beam epitaxy setup of our collaborators in Prof. Kang Wang's group was used for epitaxially growing Bi_2Se_3 on Yttrium iron garnet ($Y_3Fe_5O_{12}$) films on GGG ($Gd_3Fe_5O_{12}$) (111) substrates [1].

For characterizing the phase purity, in-plane and out-of-plane lattice parameters, film thickness, substrate quality and mosaicity of the samples, x-ray diffraction methods (powder ω - 2θ, rocking curves, x-ray reflectivity, reciprocal space maps, 2D x-ray scans) were used. Atomic force microscopy was also used for measuring surface topography and for quantifying surface roughness. For epitaxial films thinner than 100 nm, x-ray reflectivity was used and for all films thicker than 100 nm, dektak and surface profilometer were used. Magnetic properties (saturation moment, coercivity, saturation field, magnetic anisotropy) of the samples were measured using vibrating sample magnetometry (VSM) at room temperature and using superconducting quantum interference device (SQUID) for below

room temperature [2]. In order to distinguish and quantify the effects of oxygen vacancies, B-site cation substitutions and strain effects in multiferroic oxide crystals, first-principles simulations using density functional theory (DFT) were done [3]. Optical transmission, refractive index and extinction coefficient spectra were characterized using UV-visible spectrophotometry and ellipsometry [4-13]. Faraday rotation of the samples were characterized using custom-built Faraday measurement setup [4-13]. Metallic contacts for ferromagnetic resonance and ferroelectric measurements were sputtered or e-beam evaporated [1, 14-23]. Ferroelectric hysteresis loops of the films were measured using a probe station and specialized commercial electronics and software provided by Prof. Sang-Gook Kim. Optical resonator chips have been fabricated using optical or e-beam lithography [6,11,13]. Optical transmittance measurements were carried out on optical waveguides and resonators [6,11,13].

2.1 Thin Film and Photonic Device Fabrication

Pulsed-laser deposition (PLD) is a deposition technique most commonly used for growing high-quality thin film complex oxides. PLD enables researchers to grow bulk-quality complex oxide thin films with good control of stoichiometry and sub-monolayer level control of film growth upto about 500 nm thickness range. PLD systems are much less expensive and easier to maintain than molecular beam epitaxy systems [24]. In this subsection, thin film and device fabrication methods are discussed.

2.1.1 Pulsed-laser deposition (PLD)

PLD is a vacuum deposition method that combines the advantages of evaporation and sputtering. PLD deposition system consists of a laser, a growth chamber with computer-controlled heaters, vacuum pumps, substrate and target rotation control motors. Thin films are grown by first focusing laser pulses on a ceramic target disk (1 inch diameter, 0.2-0.7 inches thick) that has the desired stoichiometry of the film and then plume ejected from PLD target gets deposited on substrates. Lighter elemental species (Bi, Li, oxygen etc.) in PLD plume may have slight differences in stoichiometry when transferred to film. The

chamber is typically under vacuum or oxygen atmosphere at high temperature (up to 1000°C) or room temperature. Substrates are rotated during deposition to ensure low roughness for film surfaces. PLD targets are rotated and rastered during laser ablation and deposition in order to consume the targets uniformly and preserve their stoichiometry uniform. The window of the chamber through which the laser beam entered is also cleaned before each deposition in order to maintain constant pulse energy at the surface of the target.

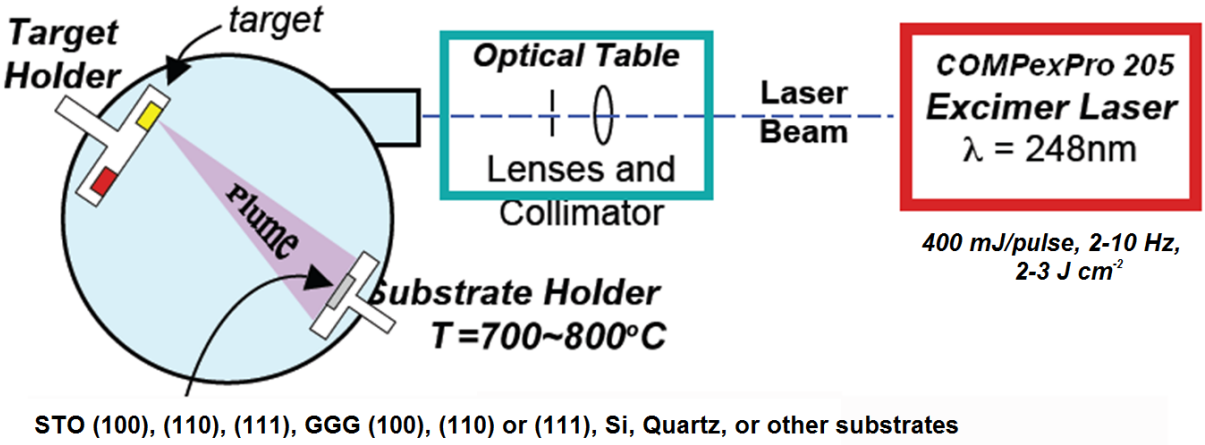

Fig. 2-1. A schematic plot of the pulsed-laser deposition system [25]

As indicated on Fig. 2-1, a PLD system consists of the laser (a Coherent COMPexPro 205 KrF with λ = 248 nm excimer laser was used for the experiments for this thesis), the optics, the chamber, the target and the substrate. Typically KrF (λ=248nm) with pulse duration of 25 nanoseconds are used at 2-30 Hz pulse rate in most PLD systems. Most materials are absorptive in these wavelengths. Inelastic collisions of the laser pulses with the target surface causes momentum transfer from the pulse to the PLD target and plumes are generated. The laser optics (beamsplitters with no loss, lenses with high focusing power, mirrors with high reflectivity at the operation wavelength) guides and focuses light onto the PLD target. Laser pulses are focused to a high energy density (typically 2~3 $J \cdot cm^{-2}$) on the target. Soon after laser pulse reaches the surface of the target (0.1~20ns after pulse exits the laser), the laser pulse is absorbed by the target. The target starts ejecting plume (atomic, di-atomic, molecular and ionic) near 1μs after pulse exits the laser. At t~1-4 μs, the plume travels towards the substrate in vacuum/oxygen ambient and thin films form around t~4 μs. A

schematic cartoon and a photo of the pulsed laser deposition process and the plume are shown on Fig. 2-2.

The following advantages of PLD make this crystal growth method attractive for the films grown described in chapters 3-5:

1) **Good stoichiometry transfer from ceramic targets to films:** Complex oxides are functional materials which can be engineered to have piezoelectric, magnetic, ferroelectric, magnetoelectric, thermoelectric and/or many other useful properties. These functionalities of complex oxides are very sensitive to ionic ratios (A:B ratio in a ABO_3 perovskite or Re:Fe ratio in $Re_3Fe_5O_{12}$ garnets). Chemical vapor deposition or simple evaporation methods cannot form the desired material phases on areas large enough to be useful for devices, because the efficiencies of surface reactions to form the desired phase during growth are never perfect (either due to kinetic or even thermodynamic limitations).

   One way to increase the repeatability of growing correct single-phase complex oxides is to avoid surface reactions on the surface altogether and simply transfer a preexisting oxide plume with the desired stoichiometry onto substrates. Researchers working on growing functional magnetic, ferroelectric or functional oxides have found this method quite useful particularly useful since early 1990's and widespread academic adoption of PLD method has started in early 2000's with improved commercial instrumental control. After being able to reproducibly grow single-phase complex oxide thin films, researchers could explore new effects resulting from substrate-induced strain which induces strains in thin films that cannot otherwise be achieved in bulk form of the crystals.

2) **Unique to PLD, one can grow composite or combinatorial composition gradients** of complex oxides from multiple ceramic targets at the same time in the same deposition chamber. Depending on the growth conditions, a full compositional

gradient can be achieved as well as complete immiscibility between two or more different material phases. This functionality enables researchers to explore a wide range of substitutional dopants and compositional gradients between two different simple oxides that would not otherwise form in bulk form. Researchers who could stabilize non-equilibrium phases in complex thin film material found new composite thin film structures with unique multiferroic and magnetoelectric properties this way.

3) **Flexibility of PLD deposition enables the growth of thin films with a wide range of functionalities using most elements of the elements from the periodic table.** Using PLD, one can grow films that can be used for solid oxide fuel cells, magnetic and ferroelectric data storage, perovskite photovoltaic materials, superconducting layers, memristors, resistive oxides, batteries to name a few applications. Thicker films (0.7 nm upto 400 nm) are grown by ablating the PLD targets with higher number of laser pulses. Deposition rate (2-50 $Å \cdot min^{-1}$) can be increased by reducing target-substrate distance (5-12 cm). Deposition rate can also be reduced by reducing the laser pulse rate (1-30 Hz). Typically, slower depositions yield a better crystalline quality if the substrate or the device underneath can withstand the prolonged high temperature process. Increasing substrate temperature during growth often improves long-range crystalline quality of the films grown, but some materials have an upper limit of growth temperature where the complex oxide starts breaking down into secondary phases. Lower cooling rate of PLD improves the likelihood of getting single crystals and avoiding secondary phases such as CoO, Co_3O_4 or CeO_2. A low base pressure (1 μTorr or lower) helps clean the chamber from any elemental or molecular residual gas (N_2, trace amounts of inert gases from the atmosphere or outgassing) which might end up entering film lattice and modify electrical and magnetic properties. A low base pressure (1 μTorr or lower) is desirable for minimizing the concentration of unintentional dopants inside film lattice.

4) **PLD systems are modular.** These systems decouple the growth chamber and the laser (the initiator of growth) unlike a molecular beam epitaxy system where the

growth chamber and the effusion cells are integrated. One can use different lasers of different wavelengths on the same chamber or use the same chamber to grow films at different chambers at the same time. The ability to use different lasers with different wavelengths, powers, pulse widths and repetition rates allow enables the PLD growth of different classes of materials, such as organic compounds.

5) **Control of oxygen pressure during growth enables ionic p-type doping for oxide thin films:** One major advantage of growing oxides using PLD is that PLD enables the control of oxygen vacancy concentration in a perovskite film. Growing oxide films in an oxygen deficient environment can lead to the formation of $ABO_{3-\delta}$ instead of ABO_3. The deficiency of oxygen in the perovskite lattice causes formation of ionic holes with 2+ charges. In addition, deposition rates of films decrease significantly when oxygen partial pressure during growth is increased. This difference affects growth kinetics and vacancy distribution too. For instance growing a perovskite of ABO_3 under 10 mTorr and 1 μTorr pressures can make a difference of conducting ($\rho \sim$ a few 10's of Ω·cm) and optically absorptive (reflecting and gray color) or a highly insulating ($\rho \sim 10^7$-10^{14} Ω·cm) and transparent film of the same material. Two specific examples will be covered regarding these cases in Chapter 3 (Magneto-optical and optical properties of $SrTi_{0.70}Co_{0.30}O_{3-\delta}$ films) and in Chapter 5 (multiferroic $SrTi_{0.70}Co_{0.30}O_{3-\delta}$ films). In addition, since the oxygen bonds are not strong (compared with Ti or Co bonds), one can reversibly cycle between oxygen-poor and oxygen-rich states by annealing. A voltage-controlled cycling between oxygen-poor and oxygen-rich states is enhanced when oxygen vacancy concentration is increased.

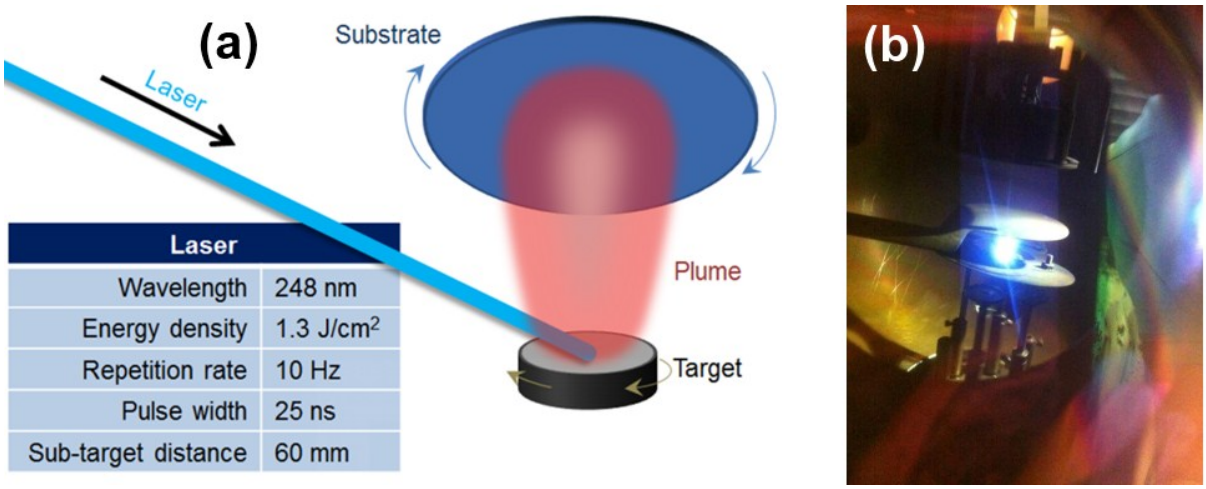

Fig. 2-2. (a) The PLD process (b) A plume generated in a PLD chamber.

Precursor powders with the stoichiometric element ratios of the final target compositions were mixed and ball milled with YSZ (yttrium stabilized zirconia) grinding media for 24 hours in ethanol. The mixture was then dried and calcinated in a tube furnace in air to form the desired phase. Then the calcinated powders were uniaxial and cold isostatic pressed (CIP) at 40,000 psi for 2 min into a 1.1" diameter pellet. Finally, the pellet was transferred to a tube furnace and sintered to form the final target.

Oxygen or vacuum conditions were adjusted after reaching the base pressure and then the substrates were heated to the desired deposition temperature at a speed of $10^{\circ}C \cdot min^{-1}$. After heating the chamber, the process chamber outgasses and for some projects that require high concentrations of oxygen vacancies, the chamber is pumped down again to the base pressure at high temperature (different from the previous PLD recipes used in Ross Group [25]). Next, the laser runs to complete the deposition. After the deposition, the samples are cooled down to room temperature at a speed of $5^{\circ}C \cdot min^{-1}$ in vacuum or under high oxygen pressure for oxygen stoichiometry. The specific fabrication conditions for different materials systems are summarized in the respective chapters since the number of critical processing steps are different for each project. Deposition conditions are determined by taking a few desired end results into account, such as the material stoichiometry, the valence state of ions, and the strain state of the film due to substrate.

One limitation of PLD technique is that one can observe a low surface density of μm-scale particulates on the film. Due to the distribution of grain sizes inside PLD targets, μm-scale might get transferred on to films and alter the film properties. In addition, the current designs of most of the state-of-the-art PLD chambers are not engineered for high throughput. The PLD recipes used for growing films in low throughput (a few 10 x 10 cm^2 substrates per day) also need to be modified for growing films at high throughput (a few tens of 4 inch wafers or more per hour or more).

Pulsed laser deposition is an advantageous method for fabricating complex oxides, because the stoichiometry of a complex oxide can be transferred with high fidelity from a ceramic target to thin films. In a typical reactive thin film growth method such as chemical vapor deposition, fabricating stoichiometric complex oxides across reasonably large areas for electronic chips is not possible. Therefore, PLD technique heavily depends on fabricating good quality ceramic targets which are single-phase and stoichiometric.

2.1.2 Fabrication of Ceramic targets for PLD

Fabricating single-phase targets is possible by starting with simple oxide precursor powders which can react easily with other oxide precursors to form the desired stoichiometry and crystal structure at elevated temperatures such as 1400°C. The desired stoichiometry of targets is achieved by mixing the correct amounts of oxide powders based on the reaction equation of the calcination and sintering processes. Three garnet targets and one perovskite stoichiometric target were fabricated using conventional mixed oxide sintering method for ceramics and the furnaces and the labs of Prof. Harry Tuller were used. The targets of yttrium iron garnet ($Y_3Fe_5O_{12}$, YIG), thulium iron garnet ($Tm_3Fe_5O_{12}$, TmIG) and cerium substituted yttrium iron garnet ($Ce_1Y_2Fe_5O_{12}$, Ce:YIG) were prepared. For YIG and Ce:YIG, a conventional mixed oxide sintering method from powders (Alfa Aesar) of Y_2O_3 and Fe_2O_3 for YIG, with CeO_2 added for the CeYIG target. For TmIG, the precursor powders were Tm_2O_3 and Fe_2O_3. These compounds were calcined at 1150°C for 5 hours, pressed into a 1 inch diameter, 0.5 inch thick cylinder shape, then sintered at 1400°C for 10 hours in air, which

resulted in pure garnet phase targets identified by x-ray diffraction (XRD).

In order to fabricate a perovskite target of $SrTi_{0.70}Co_{0.30}O_{3-\Delta}$, (oxygen deficiency of the target: Δ), precursor powders of $SrCO_3$, TiO_2 and CoO were mixed at the stoichiometric cation ratios of the final target composition. After mixing, the powder was ball-milled with alumina grinding media for 24 hours in ethanol. The mixture was then dried and calcinated for 12 hours in a tube furnace at 1400°C in air. Next, the calcinated powder was cold isostatically pressed (CIP) at 40,000 psi for 2 min into a 1" diameter disk. Finally, the disk was transferred to a tube furnace and sintered at 1400°C for 18 hours to form the final STCo30 target. Pure perovskite phase target with the desired stoichiometry was achieved based on the XRD ω-2θ results that match a previous reference XRD pattern with very similar stoichiometry (powder diffraction reference number: 00-053-1216) [12].

2.1.3 E-beam lithography

Electron beam (E-beam) lithography facility of Nanostructures Laborator (NSL) was used for fabricating resonator structures (Elionix, ELS-F125). E-beam lithography is a resist patterning technique in which electron beams are used to expose resist patterns (instead of photons). The e-beam lithography system does not require a physical mask unlike optical lithography. In addition, due to the shorter wavelength of electrons (compared to photons), e-beam lithography can achieve higher spatial resolution. The resonator fabrications were done by Dr. Taichi Goto for the most part and with help from Mehmet C. Onbasli.

Figure 2-3 shows the fabrication process for a resonator structure used for integrated magneto-optical resonator and isolator experiments [6]. Using a silicon-on-insulator (SOI, Soitec) wafer with Si(250 nm)/SiO_2(3 μm)/Si, a 80 nm-thick hydrogen silsesquioxane (HSQ) negative resist (Dow Corning XR-1541 6%) was spin-coated on the wafer for 1 minute at 5000 rpm. The e-beam pattern was designed using e-beam software. The features were then defined by electron beams exposure with acceleration voltage of 125 kV, current 10 nA,

aperture of 120 μm, 6×10^4 pixels in a 600×600 μm^2 area, at a dose time of 0.20 μsec. The waveguide width is 450 nm, radius of curvature of the racetrack is 45 μm, and the straight line portion of the racetrack is 200 μm. After e-beam exposure, the resist was developed using using tetra-methyl-ammounium hydroxide (TMAH, MF-CD-36) at 25°C with ultra-sonication for 3 minutes and a rinse with deionized water. Next, the reactive ion etching system (RIE, PlasmaTherm SLR) was used to etch the Si film part that is not covered by e-beam resist under 10 mTorr HBr gas (1.0×10^{-5} Torr base pressure, 200 W forward power, etch rate of 1.0 nm $\cdot$ sec^{-1}. The top cladding of 1 μm-thick SiO_2 was then deposited onto the sample using plasma-enhanced chemical vapor deposition (PECVD) with a deposition rate of 28.9 nm $\cdot$ min^{-1} ($T_{substrate}$ = 250°C, P_{base} = 10 mTorr, $P_{working}$ = 500 mTorr, gases used during deposition: 150 sccm 5% SiH_4 in He and 600 sccm N_2O, input power: 25W). The quality factor (Q-factor) of the unloaded resonator was then characterized on a Newport Auto Align workstation using an optical vector analyzer (LUNA Technologies OVA-5000) with a built-in tunable laser. The laser light was coupled into and out of the devices using tapered lens-tip fibers to improve coupling efficiency. The transmitted light was analyzed with an optical vector analyzer (LUNA Technologies). The sample was placed onto a thermostat stage kept at 25°C to decrease the effects of the temperature-dependent index of silicon. The unloaded Q-factor of the resonator was measured to be ~ 34,000 with a free spectral range of 0.90 nm (FSR, wavelength separation between two adjacent resonance dips in the transmission spectra) [6].

After fabricating the waveguide and resonator structure, one arm of the resonator needs to be covered with a magneto-optical Ce:YIG layer so that the degeneracy of the transmission resonance spectra for forward and backward propagating light are going to be different. In order to deposit Ce:YIG layer onto one arm of the racetrack resonator (20×200 μm^2 area), a window in the top SiO_2 cladding was etched using a 1 μm-thick positive resist (ZEP520A), which was spin coated for 1 minute at 5000 rpm and baked at 180°C for 3 minutes on a hot plate. The resist was exposed by e-beam lithography with the e-beam parameters described above, except that the current was 2 nA, aperture 120 μm and a dose time 0.2 μsec after aligning the e-beam gun at the appropriate location of the racetrack resonator. In order to

achieve alignment of the rectangular e-beam exposure with the arm of the resonator, two cross-shaped alignment marks were formed on the 3 μm-thick SiO_2 layer at the edge of the SOI substrate (during first e-beam exposure) and covered with polyimide tapes during the SiO_2 deposition and the ZEP coating so they would be visible. After the second e-beam exposure, the pattern was developed with o-xylene (ZED-WN) for 1 minute at room temperature (RT) without ultra-sonication followed by rinsing with IPA for 1 minute at RT and nitrogen blowing. Next, the SiO_2 on the resonator and under the exposed positive resist was etched by RIE in 200 mTorr (20 sccm) CHF_3 gas with a substrate temperature of 200°C, base pressure of 1 μTorr, and input power of 100 W. The etching rates for the resist and SiO_2 were ~ 21 nm· min^{-1} for both. SiO_2 claddings (from HSQ) were left intentionally on the sides of the resonator arm to prevent Ce:YIG from covering the sides of the waveguide (and essentially canceling the magneto-optical effect) [6]. Finally, the magneto-optical garnet layers were deposited and annealed.

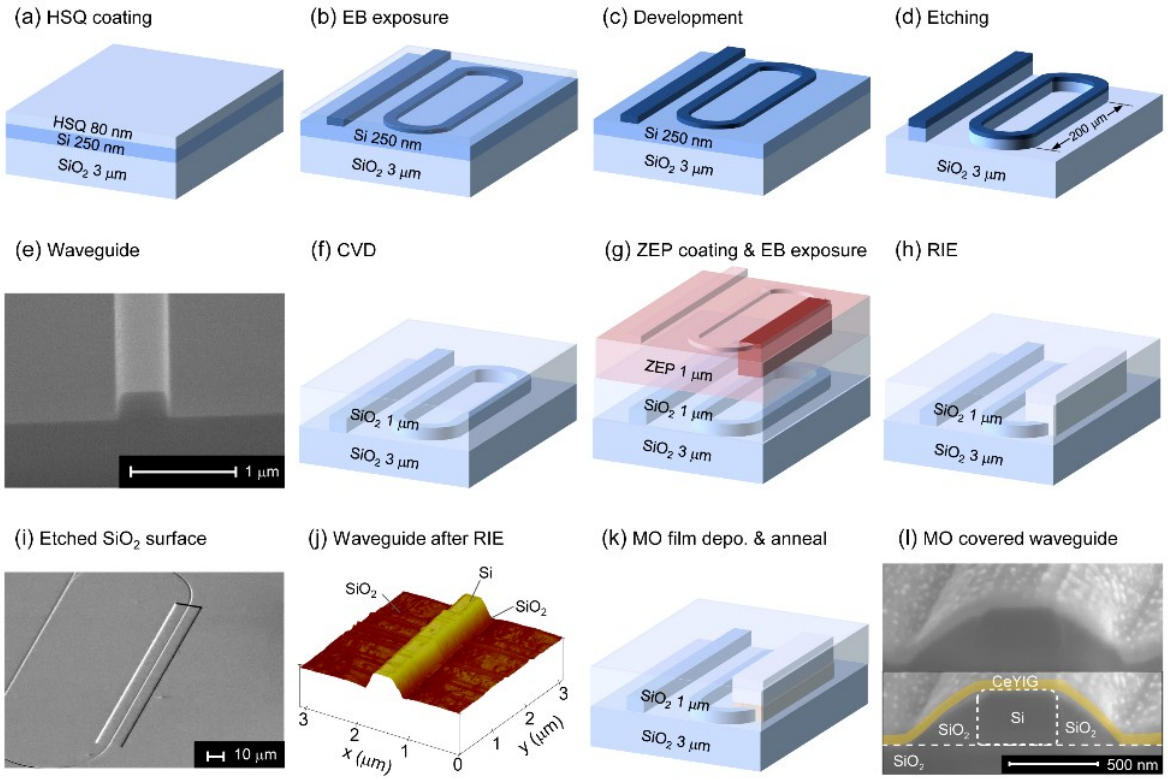

Fig. 2-3. A schematic plot of the fabrication process using e-beam lithography [6]

2.2 Characterization

2.2.1 X-ray diffraction

In order to probe the phases and phase purity, out-of-plane and in-plane lattice parameters, to measure film thickness and to analyze the film texture (different orientations of the same crystal in the film), x-ray diffraction (XRD) was used. The specific XRD methods used include 1DXRD (ω - 2θ), 2DXRD, XRD pole figures, reciprocal space maps (RSM) and X-ray reflectometry (XRR). For all 1DXRD measurements, PANalytical X'Pert PRO (MPD in ω-2θ mode with Cu K_α radiation source at a wavelength of 0.1541 nm) instrument at MIT Center for Materials Science and Engineering (CMSE) was used. For 2DXRD, pole figures, RSM and XRR measurements, Rigaku SmartLab multipurpose diffractometer was used with Ge(022) monochromator attachment that improved angular resolution.

1DXRD and 2DXRD

Ewald sphere is used to describe the XRD from a crystal. All diffraction patterns from a crystal would be collected at the same if the x-ray detector covered the 4π solid angle. Due to small angular coverage of the x-ray detector however, some specific conventions such as 1DXRD and 2DXRD were defined. Regular ω-2θ diffraction patterns are collected by x-ray detectors in the coupled scan configuration shown on Fig. 2-4. While running an ω-2θ scan, the source angle and the detector angle ($\omega = \theta$) are fixed to be equal to each other and the x-ray source and the detector both move to higher angles at the same time to collect higher diffraction orders during a measurement. A coupled scan can be used to detect any mosaicity (different orientations of the same crystal inside the same film) and a coupled scan was used to study the mosaicity of $SrTi_{0.70}Co_{0.30}O_{3-\delta}$ films on $SrTiO_3$ (STO) substrates (chapter 3). 1DXRD scans are useful in extracting the out-of-plane lattice parameters of films.

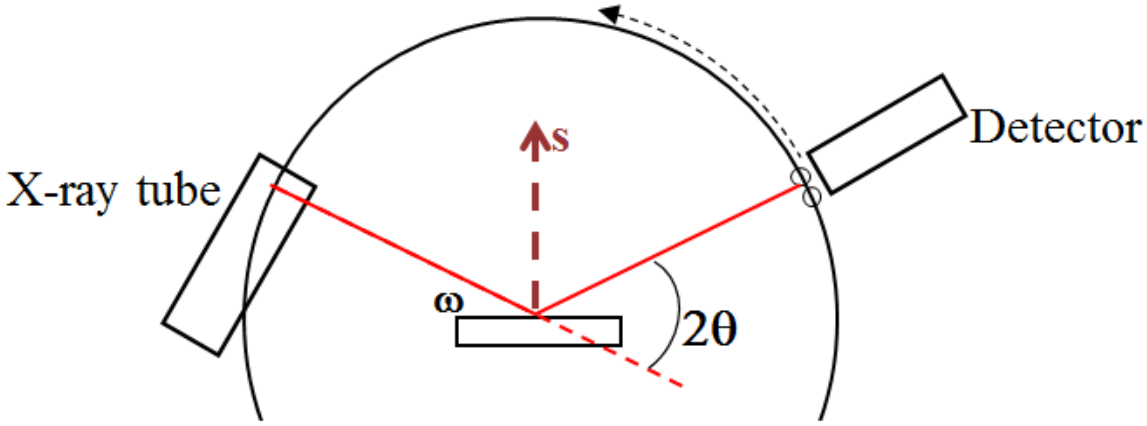

Fig. 2-4. Definition of 1DXRD a ω-2θ scan. In a coupled scan, ω and 2θ are increased gradually (x-ray source and the detector move towards higher angles at the same time) to collect diffraction peaks [26].

In order to measure the substrate quality and the sample strain, *a rocking curve* is also measured (especially before RSM measurements). A rocking curve is a plot of x-ray intensity as a function of ω (either the detector or the substrate stage is rotated during measurement, while the detector position is fixed). A double-axis rocking curve measurement produces both film and substrate peaks since the detector can see several different angles of 2θ and these peaks can also be used later to extract the film thickness from a diffraction model.

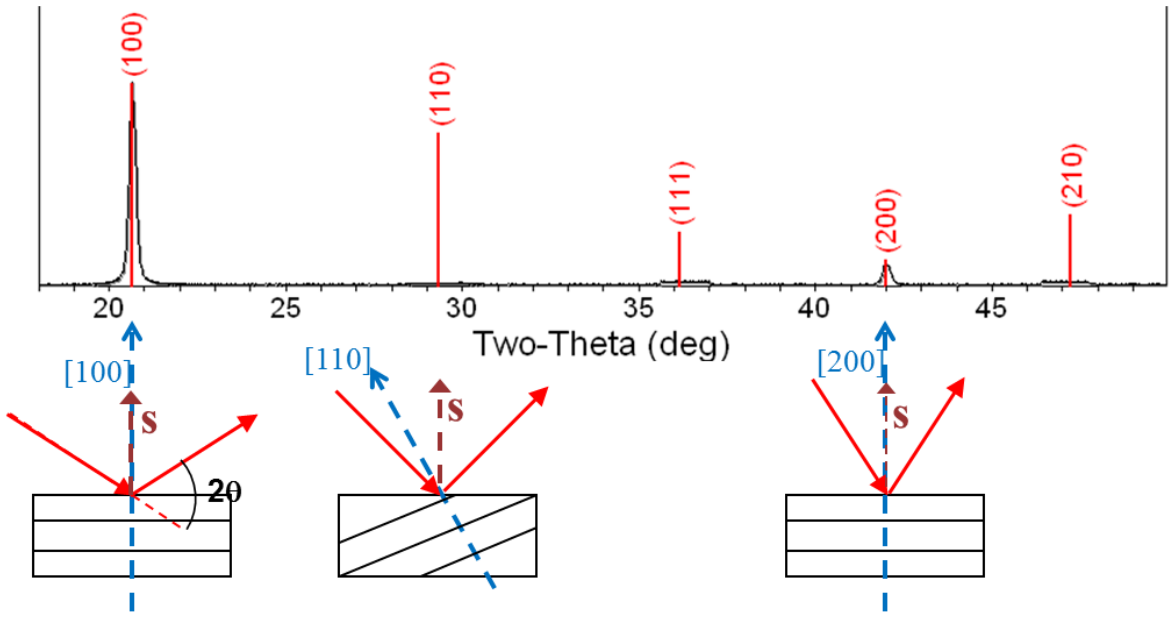

Fig. 2-5. The way 1DXRD (ω-2θ scan) can be used to identify if the sample can yield the same crystal with multiple orientations such as (100) and (110). For $SrTi_{0.70}Co_{0.30}O_{3-\delta}$ films, first, the ω-2θ scans were

acquired. Pole figures for the samples that had (110) or (111) peaks in their ω-2θ scans were acquired.

X-ray pole figures, X-ray reflectometry and X-ray reciprocal space mapping

X-ray pole figure, as shown on Fig. 2-6 (a), is a plot of XRD intensity with respect to the sample orientations in three dimensions. X-ray pole figures are useful in identifying the mosaicity of the film, i.e. whether different orientations such as (100), (110) or (111) of the same material phase are present. Two-dimensional XRD (pole figures) scans about a peak, i.e. typically 101 peak, was conducted on perovskite films using the Rigaku Smartlab Multipurpose Diffractometer and In-plane Pole Figure (medium resolution PB) Preinstalled Package in the Smartlab Guidance software.

X-ray reflectometry (XRR), as shown on Fig. 2-6(b), is an x-ray measurement of grazing incidence scattering intensity of x-rays at low 2θ range (0-7°). After XRR measurement, an XRR model based on the electron densities of the layers (related to the numbers of electrons of each layer) is constructed to fit the XRR measurement results. The model parameters (the thicknesses and surface roughnesses of layers) are varied to fit the experimental pattern. This non-invasive measurement technique allows extracting the film thicknesses and surface roughnesses to with 0.1 nm.

An RSM, as shown on Fig. 2-7, is essentially a collection of multiple ω-2θ scans, but each coupled scan is collected with a slightly different offset (tilt) in the ω direction (2θ = 2ω + tilt). Typically, relative ω is varied and multipled ω-2θ coupled scans are collected. A single coupled asymmetric scan yields enough data to extract in-plane and out-of-plane lattice parameters of both films and substrates. An RSM plot is typically presented in terms of reciprocal space parameters (proportional to inverse of lattice constants, in units of $Å^{-1}$) and yields in-plane and out-of-plane lattice constants. In addition, the broadening of the RSM peaks indicates defects. Especially for garnet crystals presented in chapter 4, the GGG substrates have both mosaic spread (lattice constant gradient for out-of-plane directions) and lateral correlation (lattice constant gradient for in-plane directions). The advantage of an

RSM measurement is that both the film and substrate diffraction patterns can be collected simultaneously and the film and substrate lattice parameters (both in-plane and out-of-plane), strain state and defect densities can be extracted quantitatively [1, 26].

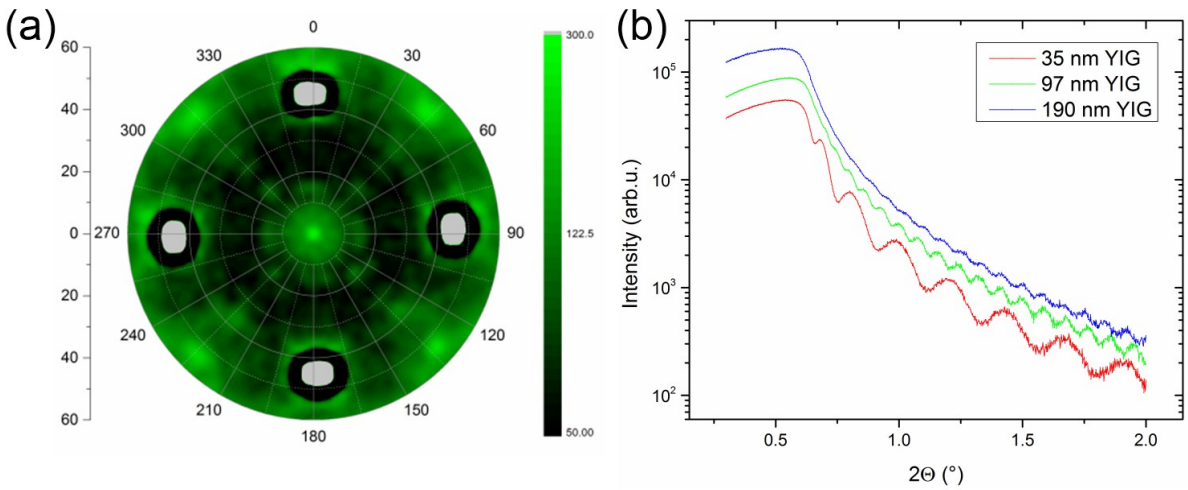

Fig. 2-6. (a) A pole figure of a $SrTi_{0.70}Co_{0.30}O_{3-\delta}$ film on $SrTiO_3$ substrate (indicates the prescence of $SrTi_{0.70}Co_{0.30}O_{3-\delta}$ with (100), (110) and (111) orientations [12]. (b) High-resolution XRR plot for 34, 97 and 190 nm thick YIG films. The period of the oscillations decreases for thicker films [1].

The reciprocal space map (RSM) given in Fig. 2-8 belongs to the (248) peak of 79 nm thick YIG film on GGG (substrate) measured at grazing incidence configuration. The strong peak near $(q_x, q_z) = (0.3610, 0.647)$ $Å^{-1}$ belongs to the (248) peak of the GGG (100) substrate. The peak near $(q_x, q_z) = (0.3610, 0.646)$ $Å^{-1}$ belongs to the (248) peak of the YIG (100) film. The RSM demonstrates that the q_x of both film and the substrate are identical, while the q_z of the film and the substrate are different. Since q_z (film) < q_z (substrate), the film is in tetragonal lattice form.

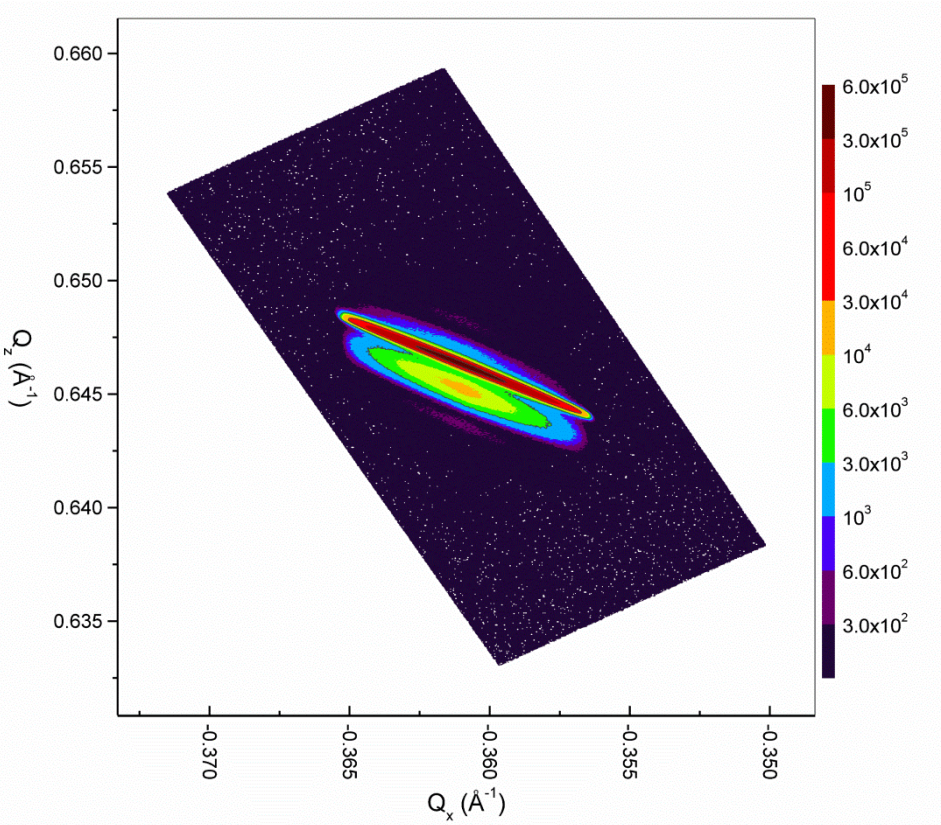

Fig. 2-7. Reciprocal space map for 79 nm thick YIG film on GGG (100) near the (248) peak measured in grazing incidence configuration [1].

2.2.2 Vibrating sample magnetometry (VSM)

The VSM is a method for measuring room temperature and/or high-temperature magnetic properties of samples as a function of applied magnetic fields using inductive coils. A sample is placed in between two electromagnetic coils. During measurement, the sampleholder is vibrated at a constant frequency while magnetic field is applied. The oscillation of the sample and the change in the sample's magnetization causes change in the magnetic flux going through the pick up coil of the VSM. As a result of Faraday's law of electromagnetic induction (the electromotive force generated the pickup coil is proportional to the time variation of the magnetic flux), a voltage output at the pickup coil is read out. From calibration measurements, the amount of magnetic moment that the voltage output of pickup coils corresponds to is already recorded by the data acquisition software. Therefore, the software automatically converts the voltage read out (as a function of applied magnetic field) to magnetic moment hysteresis loops as a function of applied magnetic field.

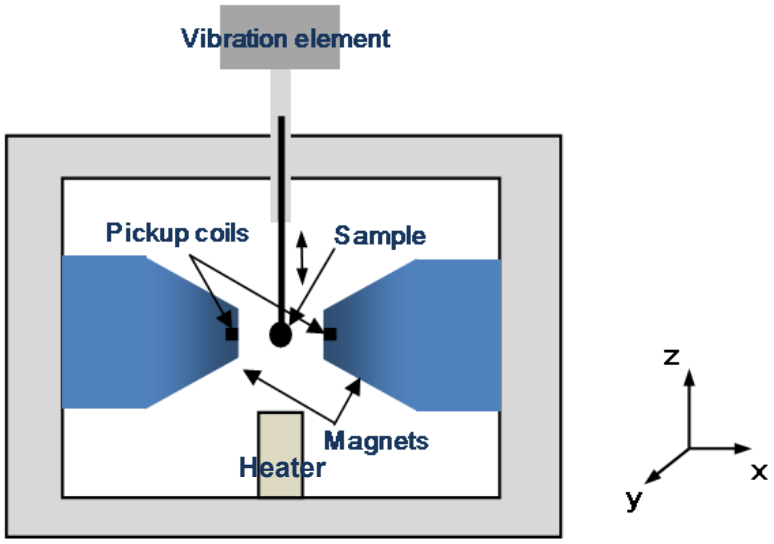

Fig. 2-8. A schematic plot of a vibrating sample magnetometer [25].

Fig. 2-8 shows a schematic plot of a typical VSM. The sample is loaded onto a diamagnetic sample holder (pyrex glass or quartz) and vibrated along the z direction. A homogeneous magnetic field of up to 1.3 Tesla can be applied along the x direction. The VSM used for the projects described in the subsequent chapters is a Digital Measurement Systems Torque/Vibrating Sample Magnetometer Model 1660 Signal Processor (ADE Technologies VSM Model 1660). In typical experiments, room temperature magnetic hysteresis loops are measured by applying a cycle of magnetic fields -1 T to +1 T (and back) on the samples. VSM can achieve a magnetization resolution of a few 10^{-6} emu, samples and sampleholders are always cleaned thoroughly before measurements. The calibration sample is always positioned with a similar geometry (in-plane vs. out-of-plane) as the sample to be measured for quantitative accuracy and minimum shape effect. For all thin film results, the paramagnetic contribution of the GGG substrates was removed by subtracting a linear function from the raw magnetic hysteresis loop data and then the remaining signal was divided by the film volume.

For some of the experiments, the heater was also used. In those experiments, magnetic moments of the samples were measured at saturation as a function of temperature (up to 700 ˚C). The heater element heats the samples with Argon flow which are heated inside the

instrument. By flowing Argon at lower temperatures than the sample, one can measure magnetization change as a function of temperature under field-cooling configuration (or zero-field cooling if field is switched OFF). The temperature-dependent magnetic moment measurements specifically focus on finding the Curie temperature of the films as well as investigating whether the film behaves as a ferromagnet with a Brillouin-function decay of its saturation moment with temperature. If the decay does not follow a perfect Brillouin function (i.e. a linear decrease for $SrTi_{0.70}Co_{0.30}O_{3-\delta}$ which will be discussed later [25]), the film is a spin-glass. VSM decouples typical environmental noise (low frequency mechanical vibrations, 50-60 Hz electrical noise) from measurements.

2.2.3 Superconducting quantum interference device (SQUID)

SQUID magnetometry is a sensitive magnetization measurement method based on the phase shift on the Josephson junctions due to the magnetic flux change from the sample. It is the most sensitive magnetic flux measurement method ever known (field resolution at the 10^{-17} T). For every magnetic field point, sample is scanned vertically across the SQUID loop and the magnetic flux of the sample is measured by a ring of superconductor interrupted by one or more Josephson junctions (superconductor separated by a thin normal resistor). Below the superconducting critical temperature (superconductor T_c), the loop has no resistance upto a critical current density. Beyond the critical current density, the superconductor behaves as a regular resistor. The current-voltage curve of the SQUID is shown on Fig. 2-9. Before measurement, the SQUID is biased at a current I to stay in between the resistive and superconducting states. When a sample with magnetization is passed through the device, a flux change occurs. Current flows in such a way in superconductors that the total **B-**field inside the superconductor is zero (Meissner effect). As a result, the SQUID shifts in the I-V curve. Since flux is quantized with very small intensity for superconductors, a read-out circuit counts the voltage oscillations induced due to changes in the flux [25].

Temperature dependence of magnetization (both M vs. T at for saturated films and M vs. H

hysteresis loops at different temperatures) for $Sr(Ti_{0.70}Co_{0.30})O_{3-\delta}$ and Ce:YIG ($Ce_1Y_2Fe_5O_{12}$) films were measured using MIT CMSE's Quantum Design SQUID magnetometer [7]. The SQUID is cooled using liquid He, and the saturation magnetization is recorded at different temperature points while enough magnetic field is applied to saturate the films at all times (field cooling, FC).

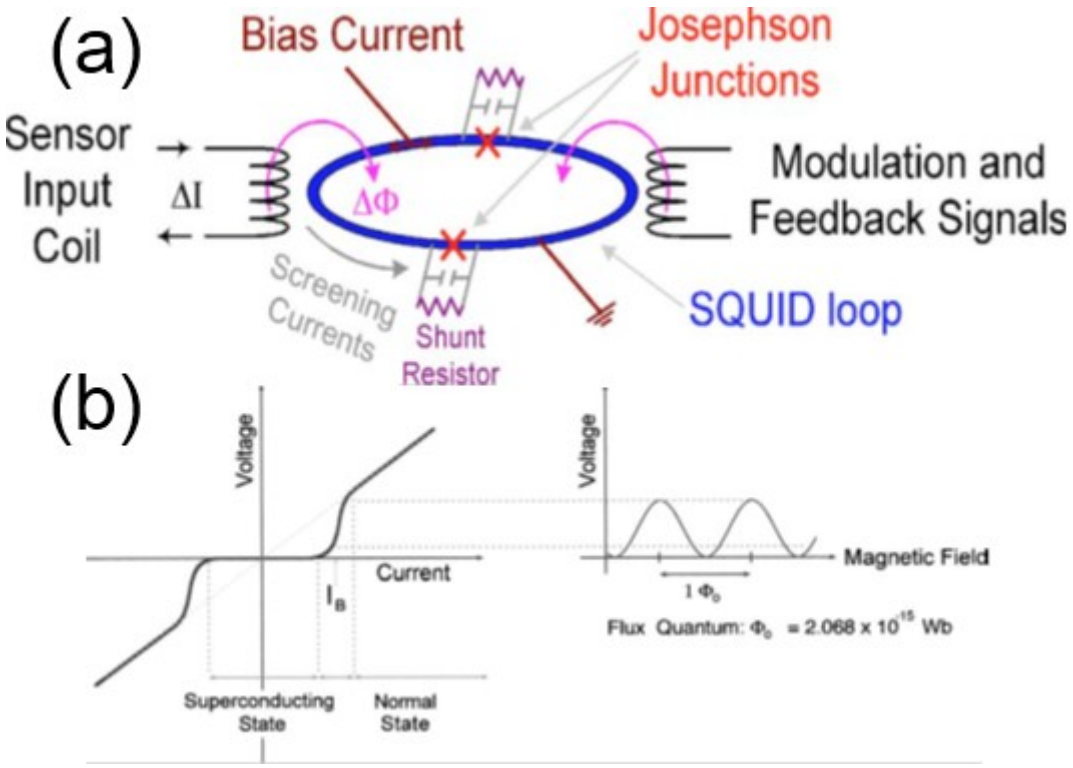

Fig. 2-9. (a) A superconductor pickup coil with Josephson Junctions used in SQUID measurements. (b) The current-voltage and voltage-magnetic field curve of the SQUID shown in (a) [25].

2.2.4 Faraday rotation

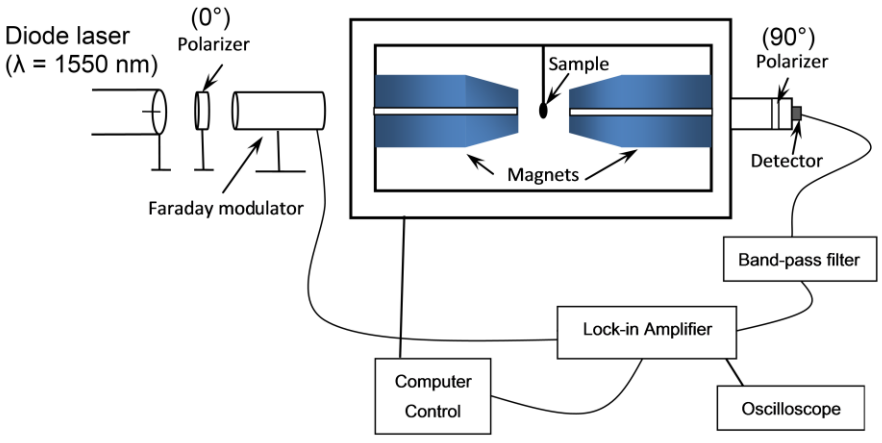

Fig. 2-10. Faraday rotation measurement setup [25].

Faraday rotation is rotation of the electric field polarization of a propagating wave inside a magneto-optical material. This rotation occurs due to the non-zero off-diagonal element in the permittivity tensor of the magneto-optical material. Fig. 2-10 shows the schematic of a custom-built Faraday rotation setup in Ross group at MIT. Faraday rotation hysteresis loops magneto-optical thin films were measured as a function of applied magnetic field (field applied perpendicular to film surface) using this setup at λ = 1550 nm. A diode laser that operates at 1550 nm wavelength emits a continuous wave signal and the electromagnetic wave first passes through a linear polarizer. The linearly polarized light is then modulated at 1000 Hz by a voltage controlled electro-optic modulator controlled by the lock-in amplifier. The light then passes through the middle of the first electromagnetic coil, through the sample and then through the middle of the second electromagnetic coil. The light then passes through another polarizer aligned perpendicular to the first polarizer between the laser and the modulator. After passing through the polarizer, the light is detected and converted to current at a Ge detector. The Ge detector output is fed into a band pass filter that transmits only 1000 Hz (the modulator frequency) and helps isolate the Faraday rotation measurement system from mechanical vibrations. The signal coming out of the filter is fed into the lock-in amplifier, the oscilloscope and the LabView interface that controls the Faraday rotation setup. The 90° difference between the polarizers ensures that only rotated polarization component of light reaches the photodetector. The LabView interface controls and sweeps the magnetic field applied from the electromagnetic coils (between -1T to 1T in a full loop) and reads out the Faraday rotation hysteresis signal (voltage) of the sample. The Faraday rotation voltage vs. H-field information is converted to Faraday rotation angle vs. H-field by multiplying with the calibration factor (in terms of mV induced per ° rotation). To measure this calibration factor, first, the polarizer between the modulator and the laser is rotated to 1°. Then the sample is placed between the electromagnetic coils. Then, the lock-in amplifier voltage due to 1° read out. This reading is entered in the LabView interface that controls the Faraday rotation measurement setup. For thin films with small rotation angles, the rotation angle is assumed to be linearly proportional to the signal intensity.

2.2.5 UV-Vis-NIR spectrophotometry

MIT CMSE's Cary 500i UV-Vis-NIR Dual-Beam Spectrophotometer with a range from 175 nm to 2000 nm was used to measure the optical and near-infrared transmission spectra of the films. For UV measurements, a deuterium discharge lamp was used. For visible and NIR measurements**,** a tungsten-halogen lamp was used as the light source. A monochromator scans the wavelengths from UV to NIR range in 1 nm steps, which was guided by the spectrophotometer optics to simultaneously pass through an air reference and a sample. Transmission intensities are collected and compared to the case of baseline (no samples in the optical path) to determine the transmission of sample.

For transmittance measurements, thin film samples are compared to their uncoated substrates (STO, GGG, Si etc.) as their native standard samples. The transmission measurement yields the optical bandgap and absorption tails (i.e. whether the films are direct or indirect gap materials) of the films. Any absorption peak in the transmission spectra corresponds to an electronic transition (described later for Ce:YIG samples in Chapter 3). Sometimes, the optical transmission of a sample (film and the substrate) is higher than the transmission of a bare similar substrate since the film can serve as a refractive index matching layer between air and the substrate (antireflection effect).

2.2.6 Ellipsometry

Refractive indices (n) and extinction coefficients (k) of the magneto-optical films were extracted as a function of near-infrared and visible wavelengths from spectroscopic ellipsometry measurements [12]. Ψ and Δ were measured using a Woollam Vase Spectroscopic ellipsometer in UNAM in Bilkent University in Ankara, Turkey. Ψ and Δ are defined as $\tan(\Psi)\cdot e^{i\Delta} = R_p/R_s$ where $R_p = |E_{reflected}(p)/E_{incident}(p)|e^{i\delta p}$ and $R_s = |E_{reflected}(s)/E_{incident}(s)|e^{i\delta s}$. Ψ and Δ are the amplitude ratio and phase difference (in radians) parameters to quantify the change in polarization of an incoming light upon reflecting off the

sample surface. R_p and R_s are Fresnel reflection coefficients for the p and s polarizations as shown on Fig. 2-11. The film thicknesses were measured using a KLA Tencor P16 Profilometer at MIT CMSE. Optical dielectric thin film models were constructed with Lorentzian oscillators to fit the Ψ and Δ spectra obtained using the ellipsometer. Once these models fit the Ψ and Δ spectra, the n and k spectra are also found. The mean square error in each fit has been typically less than 10^{-3}.

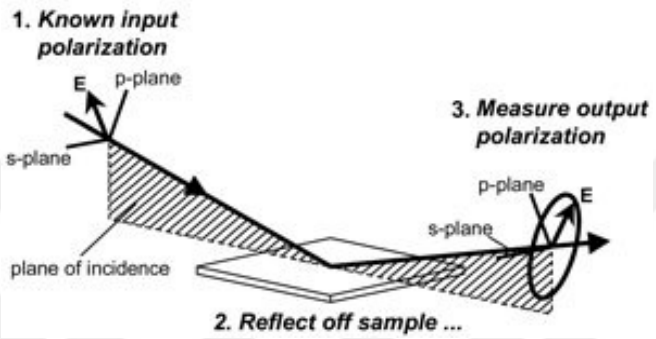

Fig. 2-11. A schematic plot of the ellipsometry measurement setup [25].

2.2.7 Optical waveguide and resonator characterization

The transmission spectra of the optical isolators were analyzed on a Newport Auto Align workstation coupled with an optical vector analyzer (LUNA Technologies OVA-5000). Fig. 2-13(a) shows the measurement stage with the alignment lens. First, the waveguide chips were cleaved to form flat and sharp end facets. Then, they are placed on a thermostat stage and kept at 25˚C using a temperature controller. Near-infrared laser light was coupled in and out of the chip through tapered lens-tip fibers. The infrared detector shown on Fig. 2-13(a) was then used to align the fiber by imaging the guided mode from the output facet. Next, the infrared detector was moved aside and another fiber was aligned to the output facet to couple the light from the waveguide into the detector fiber. An automatic alignment system with a spatial resolution of 50 nm was used for minimizing human errors and coupling light reproducibly. Transmission spectra were measured between 1470nm to 1560nm wavelengths for all devices [25].

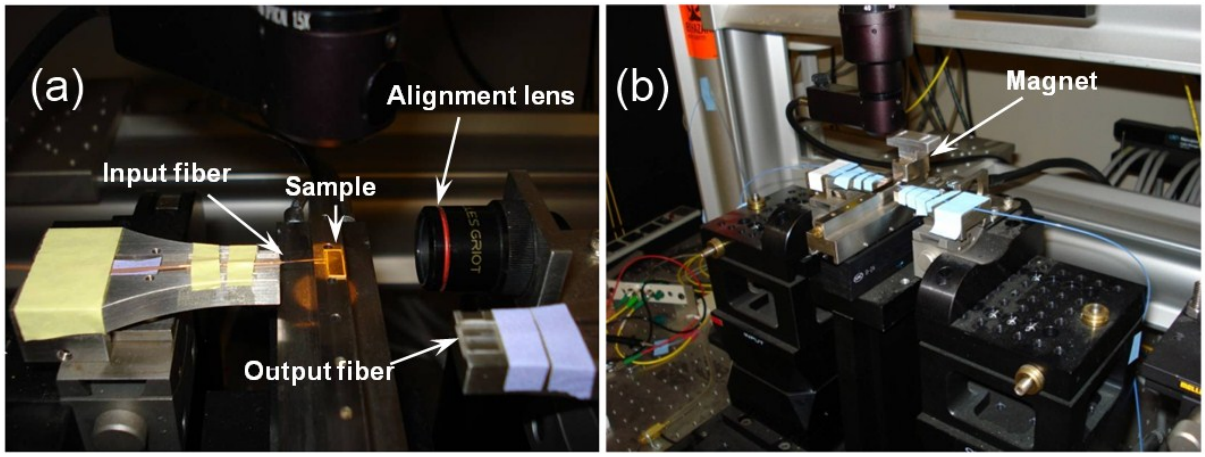

Fig. 2-12. (a) Optical waveguide and resonator transmittance measurement stage with the infrared detector to assist fiber-to-waveguide coupling. (b) The nonreciprocal transmission measurement setup with both fibers [25].

This setup was used to measure nonreciprocal phase shift and resonance shifts of the waveguide/resonator samples. A permanent magnet, as shown on Fig. 2-13(b), was placed by the side of sample to produce ~1000 Oe magnetic field in-plane and perpendicular to the racetrack waveguide section in the window region during the measurement. Optical isolation performance of the device was tested by reversing the magnetic field direction while maintaining the same light propagation direction, which is equivalent to reversing the light propagation direction. In order to mitigate the effect of temperature fluctuations which can lead to spurious resonance shift, the transmission measurement was repeated multiple times with the magnetic field directions reversed. The interval between each measurement is about two minutes.

2.2.8 X-ray photoelectron spectroscopy (XPS)

XPS was used to probe into the ion valence states of $SrTi_{0.70}Co_{0.30}O_{3-\delta}$ films on MIT CMSE's Kratos Axis Ultra spectrometer with a monochromated Al K_α source and a hemispherical analyzer. The high resolution spectrum at the Co *K*-edge was measured with a pass energy of 20 eV and an energy resolution of 0.3 eV. XPS probes into the valence states of all ions on the surface with a beam spot size of less than 700 × 300 μm^2 area. XPS was also used to quantify if there is Sr deficiency, as one might expect that some of Cobalt ions can go into Sr sites. The XPS results related to the elemental fractions in the films as well as valence states

of Co ions are presented in chapter 3. Since XPS probes into a few nm of the surface of the films, the ions deep inside the films need a separate investigation. This investigation was done using cross-section transmission electron microcopy and elemental mapping of each ion [12, 17].

2.2.9 Ferromagnetic resonance and radiofrequency reflection measurements

When an external applied magnetic field is applied on a magnetic material, the spin vector of a magnetized magnetic material goes through a precession motion since the external field exerts a torque on the sample magnetization. Gilbert damping parameter α is defined as a measure of how fast the precession decays. High α means fast decay, low α means very slow decay and longer propagation distance for coupled spin waves. Typical damping constants for bulk permalloy ($Ni_{80}Fe_{20}$ alloys) and $Y_3Fe_5O_{12}$ (YIG) are $\sim 10^{-2}$ and $3 \cdot 10^{-5}$, respectively [1,16]. For propagation of spin waves (magnons) over long distances (a few hundred μm's) via dipolar coupling, an ideal material would exhibit no or negligible damping with extremely sharp ferromagnetic resonance peaks. One material that can achieve close-to-ideal behavior is $Y_3Fe_5O_{12}$ (YIG) and $Ce_1Y_2Fe_5O_{12}$ (Ce:YIG) crystal, which will be discussed in more detail in chapter 4 [1].

Ferromagnetic resonance (FMR) is a spectroscopic probing technique for sample magnetization resulting from the magnetic moments of dipolar-coupled but unpaired electrons. The ferromagnetic resonances of YIG and Ce:YIG thin film epitaxial crystals were measured between frequencies in the 7-13 GHz range, in order to extract the Gilbert damping parameters α of the garnet films. FMR linewidths of absorption peaks can be affected both by dipolar-narrowing and exchange-broadening effects depending on the materials.

The Gilbert damping parameters were measured by FMR using a Vector Network Analyzer (VNA) attached to a grounded coplanar waveguide (GCPW). The YIG film is placed facing the signal stripe on the GCPW. Signal stripe and external magnetic field were

applied parallel to the in-plane [100] direction of the films. The measurements were performed by recording absorption of the S_{21} signal (reflection) emitted by the VNA over the frequency range of 7-13 GHz. For one measurement the frequency was swept over 7-13 GHz, while the applied magnetic field was kept constant. More details are presented in chapter 4. A Lorentz fit model is applied to determine the frequency linewidth Δf from these signals. Assuming no magnetic anisotropy terms other than shape anisotropy, as indicated by the hard-axis saturation field, we converted the obtained frequency linewidth Δf into the corresponding ΔH H-field linewidth by using the Kittel formual $f_{Kittel} = \left({}^{\gamma\mu_0}/_{2\pi}\sqrt{H^2 + H\,M_S}\right)$ without an anisotropy term [23]

$$\Delta H = \left({}^{\partial f_{Kittel}}/_{\partial H}\right)^{-1} \Delta f = \Delta f\left(2\sqrt{H^{\,2} + H\;\; M_S}\right) / \left({}^{\gamma\mu_0}/_{2\pi}(2H\;\; + M_S)\right), \qquad (1)$$

where H is the magnetic field during the measurement and ${}^{\gamma}/_{2\pi} \widehat{=} 28\ (\mathrm{GHz/10\ kOe})$ is the gyromagnetic ratio [1]. The value for M_S was extracted from the resonance frequency as function of the applied field by fitting the Kittel equation [1]. Only the shape anisotropy is considered. Magnetocrystalline or magnetoelastic anisotropy terms are neglected. Using the ΔH obtained from those measurements, we extracted the Gilbert damping parameter α as the slope of ΔH vs. the applied driving frequency. In the Landau-Lifshitz model the relation between ΔH and excitation frequency is given by $\Delta H = \Delta H_0 + \frac{4\pi\alpha}{\gamma} f$, where ΔH_0 describes the inhomogeneous broadening for zero frequency. The values derived are given in chapter 4.

2.3 First-principles simulation using Density Functional Theory (DFT)

In order to predict the structural properties (lattice parameter, c/a ratio, ionic distribution, formation energies, stable phases), electronic properties (valence states of ions, spin-resolved electronic band structures, band gap), magnetic properties (net magnetic moment per unit cell), ferroelectric polarization and charge ordering mechanisms, density functional theory

modeling of $SrTi_{0.75}Co_{0.25}O_{2.875}$ and $SrTi_{0.75}Co_{0.25}O_3$ crystals were done in collaboration with Dr. Juan Manuel Florez. In order to get reliable structural and band structure information including band gap and ferromagnetic moment, Heyd-Sceseria-Ernzerhof (HSE06) hybrid functionals were used. For ferroelectric results, GGA (generalized gradient approximation) +U (Liechtenstein's implementation) was sufficient [3]. For 3d transition metal ions, electrons are highly localized and correlated. As a result, electronic interactions must be taken into account with Coulomb repulsion +U methods (which adds on-site electron interaction and exchange energy terms)

Hohenberg and Kohn were the first to propose the density functional theory in 1964. This theory assumes that a functional (a function of functions) describes the relation between the ground state electron density and its external potential and this functional relates the ground state energy of the electrons to the electron density. This statement was formulated by Kohn-Sham equations as a sum of kinetic, Coulomb and exchange energies.

The Kohn-Sham equation relating the electron density and the electron wavefunction is:

$$\left\{-\frac{\nabla_1^A}{2}-\left(\sum_{A=1}^{M}\frac{Z_A}{r_{1A}}\right)+\int\frac{\rho(\mathbf{r}_2)}{r_{12}}d\mathbf{r}_2+V_{XC}[\mathbf{r}_1]\right\}\varphi_i(\mathbf{r}_1)=\varepsilon_i\varphi_i(\mathbf{r}_1)$$

The first term is the non-interacting electron kinetic energy. The second term is a potential energy due to electron-nucleus interaction. The third is a Coulomb energy term which is a spatial integral of electrostatic interaction energy at a certain electron density level ρ. The last term is the exchange correlation (related to the interaction of electrons) and this term cannot be accurately determined but it is approximated by various approximations, including GGA. For LDA (local density approximations), the exchange energy at each point in space is approximated by the exchange-correlation energy of a homogeneous electron gas with the same electron density, while for GGA this approximation is further improved by also considering the electron density gradient [25].

For $SrTi_{0.75}Co_{0.25}O_{2.875}$ and $SrTi_{0.75}Co_{0.25}O_3$ crystals simulations [3], Vienna Abinitio Simulation Package was used to perform spin-polarized calculations. A planewave energy

cutoff of 500 eV was used. The following k-point grids were used:

- 6 × 6 × 6 for single unit cells of cubic STO and SCO (HSE06),
- 8 × 8 × 8 for a comparison calculation of STO using GGA, and
- 2 × 2 × 2 for the larger STCO unit cells (HSE06).

Cubic perovskite supercells with 40 ($\delta = 0$) and 39 atoms ($\delta = 0.125$) were considered. The lattice structures, formation energies and electronic structures were modeled and the results are described in chapter 5.

References

[1] M. C. Onbasli, A. Kehlberger, D. H. Kim, G. Jakob, M. Kläui, A. V. Chumak, B. Hillebrands, C. A. Ross, *APL Mater.* **2**, 106102 (2014).

[2] M. C Onbasli, T. Goto, X. Sun, N. Huynh, C. A. Ross, *Opt. Express* **22**, 25183 (2014).

[3] J. M. Florez, Shyue Ping Ong, M. C. Onbasli, C. A. Ross and G. Ceder, *Appl. Phys. Lett.* **100**, 252904 (2012).

[4] Taichi Goto, M. C. Onbasli, C. A. Ross, *Opt. Express*, **20**, 28517 (2012).

[5] L. Bi, J. Hu, P. Jiang, H. S. Kim, D. H. Kim, M. C. Onbasli, G. F Dionne, C. A Ross, *Materials* **6**, 5094 (2014).

[6] T. Goto, M. C. Onbasli, D. H. Kim, V. Singh, M. Inoue, L. C. Kimerling, C. A. Ross, *Opt. Express* **22**, 19047 (2014).

[7] M. C Onbasli, T. Goto, X. Sun, N. Huynh, C. A. Ross, *Opt. Express* **22**, 25183 (2014).

[8] X. Sun, C. Zhang, N. M Aimon, T. Goto, M. C. Onbasli, D. H. Kim, H. K. Choi, C. A. Ross, *ACS. Comb. Sci.* **16**, 640 (2014).

[9] X. Sun. M. Veis, J. Kousal, E. Jesenska, C. Zhang, N. Aimon, T. Goto, M. C. Onbasli, D. H. Kim, H. K. Choi, C. A. Ross, *Nanotechnology* **26**, 115701 (2015).

[10] M. Veis, M. Zahradnik, L. Ohnoutek, L. Beran, M. Kucera, X. Sun, C. Zhang, N. Aimon, T. Goto, M. C. Onbasli, D. H. Kim, H. K. Choi, and C. A. Ross, "Magneto-optical studies of $SrGa_{0.7}Co_{0.3}O_{3-\delta}$ perovskite thin films with embedded cobalt nanoparticles", *J. Appl. Phys., (accepted)* (2015).

[11] X. Sun, Q. Du, T. Goto, M. C. Onbasli, D. H. Kim, N. M. Aimon, H. K. Choi, J. Hu, C. A. Ross, "One-step-deposition of cerium substituted yttrium iron garnet on an integrated optical isolator", *(under review)*

[12] M. C. Onbasli, D. H. Kim, L. Bi, G. F. Dionne, C. A. Ross, "Oxygen stoichiometry dependence of the magnetic and magnetooptical properties of epitaxial $SrTi_{1-x}Co_xO_{3-\delta}$ films", *(under review)*

[13] T. Goto, D. H. Kim, X. Sun, N. M Aimon, M. C. Onbasli, J. M. Florez Uribe, K. Ackland, P. Stamenov, M. Inoue, M. Coey, G. F Dionne, C.A. Ross, "Magnetism and Faraday rotation in polycrystalline and single-crystal iron-substituted strontium titanate films deposited at different base pressures", *(manuscript prepared)*

[14] M. B. Jungfleisch, A. V. Chumak, A. Kehlberger, V. Lauer, D. H. Kim, M. C. Onbasli, C. A. Ross, M. Kläui, and B. Hillebrands, *Phys. Rev. B* **91**, 134407 (2015).
[15] A. Kehlberger, U. Ritzmann, D. Hinzke, R. Röser, G. Jakob, M. C. Onbasli, D. H. Kim, C. A. Ross, M. B. Jungfleisch, B. Hillebrands, U. Nowak, M. Kläui, "Length scale of the spin Seebeck effect", *(under review)*
[16] A. Kehlberger, K. Richter, G. Jakob, M. C. Onbasli, D. H. Kim, T. Goto, C. A. Ross, G. Götz, G. Reiss, T. Kuschel, M. Kläui, "Enhanced magnetooptic Kerr effect and magnetic properties of epitaxial CeYIG thin films", *(under review)*
[17] M. C. Onbasli, J. M. Florez, X. Sun, E. Lage, Shyue Ping Ong, T. Goto, G. Ceder, C. A. Ross, "Room temperature multiferroic and magnetoelectric $SrTi_{0.70}Co_{0.30}O_{3-\delta}$ films on silicon", *(manuscript prepared)*
[18] M. C. Onbasli, J. M. Florez, X. Sun, E. Lage, Shyue Ping Ong, T. Goto, G. Ceder, C. A. Ross, "Room temperature oxygen vacancy-assisted multiferroic and magnetoelectric switching in $SrTi_{0.70}Co_{0.30}O_{3-\delta}$ films on Niobium-doped Strontium Titanate substrates", *manuscript in preparation*
[19] J. M. Florez, M. C. Onbasli, Shyue Ping Ong, G. Ceder, C. A. Ross, "Density functional theory insights on multiferroic and magnetoelectric switching in $SrTi_{0.70}Co_{0.30}O_{3-\delta}$ films on Strontium Titanate and Silicon substrates", *manuscript in preparation*
[20] M. C. Onbasli, J. M. Florez, X. Sun, E. Lage, T. Goto, C. A. Ross, "Substrate orientation dependence of room temperature ferroelectricity, magnetism and magnetoelectric coupling of epitaxial $SrTi_{0.70}Co_{0.30}O_{3-\delta}$ films on Strontium Titanate substrates", *manuscript in preparation*
[21] M. Montazeri, M. Lang, M. C. Onbasli, et al., "Room temperature ultra-low power spin-torque transfer switching in topological insulator/magnetic insulator (Bi_2Se_3/YIG) heterostructures", *manuscript in preparation*
[22] M. Lang, M. Montazeri, M. C. Onbasli, et al, *Nano Lett.* **14**, 3459 (2014).
[23] W. Liu, L. He, Y. Xu, K. Murata, M. C. Onbasli, M. Lang, N. Maltby, S. Li, X. Wang, C. A. Ross, P. Bencok, G. van der Laan, R. Zhang, Rong; K. Wang, "Enhancing Magnetic Ordering in Cr-doped Bi_2Se_3 using High-T_C Ferrimagnetic Insulator", *Nano Lett.* **15**, 764 (2015).
[24] R. Eason ed., *Pulsed Laser Deposition*, Wiley-Interscience publication, 2007
[25] L. Bi, PhD Thesis, Magneto-Optical Oxide Thin Films and Integrated Nonreciprocal Photonic Devices, Massachusetts Institute of Technology, 2011
[26] S. Speakman, "Introduction to High-resolution X-ray Diffraction of Epitaxial Thin Films," <prism.mit.edu/xray/oldsite/3%20Introduction%20to%20HRXRD.pptx> Date accessed: April 19, 2015.

Chapter 3.
Magneto-optical Oxides and Devices

Integrated optical isolators, which protect the gain media of lasers [1], need to include a magneto-optical (MO) material layer which breaks time-reversal symmetry and enables nonreciprocal photonic transmission. The most commonly used MO layers for optical isolators are cerium- or bismuth-substituted yttrium iron garnet (Ce:YIG or Bi:YIG, (Ce or Bi)$_x$Y$_{3-x}$Fe$_5$O$_{12}$ with x usually ~1) which have high MO figure of merit (given in ° dB^{-1}, is defined as Faraday rotation, in ° cm^{-1}, over optical loss, in dB cm^{-1}) [1]. These materials have high visible and optical transmission as well as strong Faraday rotation [2-6]. In addition, recently, magnetic and magneto-optical perovskite oxide thin films have also started getting attention due to their potential for extending Faraday rotation functionality over wavelengths other than 1550 nm, such as 780 nm.

In this chapter, we study epitaxial magneto-optical iron garnet thin films, polycrystalline iron garnet thin films on Si-based photonic substrates, substitutionally-doped perovskite oxides and their magneto-optical behavior. In the first section, we first study the structural, optical, magneto-optical and magnetic properties of epitaxial Ce:YIG films on GGG (100), (110) and (111) substrates. We then extract the spectral dependence of MO figure of merit of Ce:YIG on each different substrate orientation. The spectral dependence of MO figure of merit of epitaxial Ce:YIG films define an upper limit for how much Faraday rotation and optical loss that one can expect from Ce:YIG films grown on nongarnet substrates. By comparing the Faraday rotation and absorption of Ce:YIG on GGG substrates and on nongarnet substrates (such as Si photonics or III-V substrates) one can also identify the steps needed to improve the MO figure of merit of Ce:YIG films on nongarnet substrates. In the second half of the chapter, we present an optical isolator application where we demonstrate a new way of crystallizing Ce:YIG layer directly on top of Si waveguides. Device fabrications done by Dr. Taichi Goto, device characterizations done by Qingyang Du, ellipsometry fits done by Martin Veis & Enes Battal, deposition help from Dr. Xueyin Sun are acknowledged.

3.1 Magneto-optical Oxides

3.1.1 Garnet films epitaxially-grown on garnet substrates

Integrated optical isolators are the missing critical and useful components for fabricating a fully-integrated optical signal processor. In order to fabricate a passive magneto-optical isolator, one needs to be able to achieve low insertion loss and high isolation ratio, which requires the integration of a magneto-optical material such as Ce:YIG, on common useful nongarnet substrates such Si, SOI, SiO_2, Si_3N_4, InP, InGaAsP and other Si-based or III-V-based substrates and films [2-7]. Earlier studies indicated that there are major processing issues of MO iron garnet films in integrating optical isolators onto photonic circuits. MO thin films have significant lattice parameter and thermal expansion coefficient mismatch with typical photonic substrates [8-11]. When these differences are not considered in processing, direct growth of these garnet layers are either not going to yield good nonreciprocity (garnet does not properly crystallize as a single phase) or the optical waveguides crack (due to extensive thermal cycling). To address this problem, new optimized processing techniques have been developed [12-22]. Using these techniques, new nonreciprocal photonic devices such as isolators and sensors have started being demonstrated [23-27].

Ce:YIG integration with photonic devices is a materials engineering challenge in which the figure of merit of Ce:YIG layer in each study is iteratively improved with respect to the previous attempts of Ce:YIG/photonic device integration. There is a need for establishing the "gold-standard" bulk-quality Ce:YIG films and measuring their optical properties across the photonic bands of interest (the tensor as a function of wavelength across visible and near-infrared). This "gold-standard" for Ce:YIG films is ultimately going to define the upper limit for the MO figure of merit achievable through materials engineering and eventually guide photonic device engineers on the available room for improving optical isolator topology and mechanism. Since the polycrystalline Ce:YIG films grown on Si-based

photonic devices have lower Faraday rotation and higher optical absorption compared with epitaxial Ce:YIG on GGG substrates, one can identify and alleviate the sources of reduced MO figure-of-merit. In addition, materials engineers working on improving MO films other than Ce:YIG or working for nonreciprocal photonics for different applications such as lasers operating at different wavelengths are going to have a reference catalogue of wavelength-dependent MO figure of merit for Ce:YIG, which is going to eventually help develop higher figure of merit MO materials. In this part, we present the structural and magnetic properties and spectral dependence of Faraday rotation, optical loss and magneto-optical of thin film MO Ce:YIG ($Ce_1Y_2Fe_5O_{12}$) films on Gadolinium Gallium Garnet ($Gd_3Ga_5O_{12}$, GGG) substrates over visible and near infrared bands as a reference for future optical isolator studies. Among commercially available substrates, GGG (a = 12.376 Å) was preferred because it has the closest lattice parameter to Ce:YIG (a = 12.57 Å) [28]. Bulk-like MO and magnetic properties are therefore expected for Ce:YIG, when grown on GGG.

Previous reports of Ce:YIG films include figure of merit measurement results only for a single wavelength or only for a few sample wavelengths representative of an entire photonic band [1-7,13,22,24,25,29,30-32]. This limits the applicability of the films for other wavelengths as well as reproducibility of the results. A previous study by Gomi et al. [33] presents wavelength-dependent Faraday rotation and optical absorption within 1-3 eV photon energy (λ = 413 – 1240 nm) but does not include any data on near-infrared, which is the most interesting band for integrated photonics and fiber optical communications. Despite the previous research interest in using garnet-based films for nonreciprocal photonic devices, to the best of our knowledge, there has been no study which presents optical properties and magneto-optical figure of merit completely as a function of wavelength. We grew Ce:YIG films with thicknesses of 14 nm (from XRR) and 80 nm (from ellipsometry) on GGG (100), (110) and (111) substrates and characterized the structural, magnetic hysteresis, magnetic anisotropy and optical properties (n, k and Faraday rotation) of the films.

The films were grown on GGG (100), (110) and (111) double-side polished substrates using pulsed laser deposited (PLD) method using the Ce:YIG oxide targets fabricated as described in chapter 2. During PLD, the base and oxygen pressure used for Ce:YIG growth were $5 \cdot 10^{-6}$ Torr and 5 mTorr, respectively. In the first deposition run, Ce:YIG films of 80 nm thicknesses (measured using ellipsometry) were deposited with the laser pulse rate of 10 Hz at 650°C substrate temperature, with a deposition rate of 18 Å·min^{-1}. Ce:YIG was deposited at the same time inside the same chamber on all three substrate orientations. The cooling rate of the chamber after deposition was 10°C·min^{-1}. Peak-to-peak surface roughness of Ce:YIG films is within 1 nm. Control of oxygen pressure and substrate temperature can preserve the stoichiometry and prevent the formation of secondary phases such as ceria. After the deposition of films, no further rapid thermal anneal (RTP) step was necessary. When designing garnet growth recipes, RTP steps are generally not preferred on Ce:YIG films (unless essential for crystallizing the garnet) since RTP may not necessarily yield thermodynamically-stable phases.

The crystalline phase content of the films was characterized using XRD and the XRD peaks of all samples indicated purely Ce:YIG and GGG phases, within the resolution of the diffractometer. Ce:YIG and GGG lattice parameters are close and hence the Ce:YIG and GGG phases were distinguishable within less than 0.2-0.5°. The ω-2θ plots in Fig. 3-1(a) indicate the Ce:YIG/GGG (100) films with 80 nm thickness and GGG (100) substrate with no film. The substrates were not tilted during measurement in order to pick up the substrate peaks with full intensity. A silicon zero-background holder was used to reduce background noise and avoid spurious peaks from sample stage. The film and the substrate peaks for (400) planes were labeled on Fig. 3-1(a) and these signals are sharpest and strongest peaks, as expected from typical reference patterns for Ce:YIG and GGG. Although the remaining peaks were not labeled on the figure, they belong to the substrates. Fig. 3-1(b) shows the ω-2θ scan for the Ce:YIG films grown on GGG (110). The substrate guides the film formation during growth and hence the (440) planes yield the strongest XRD peaks for (110) substrate. All of the peaks belong to the substrate and the film. Intensity offset is due to variations among different substrates. Fig. 3-1(c) shows the ω-2θ scan for the Ce:YIG films

grown on GGG (111) and (444) peaks are labeled. The patterns in Fig. 3-1(c) are similar to the garnet film pattern on GGG (111) reported previously [34].

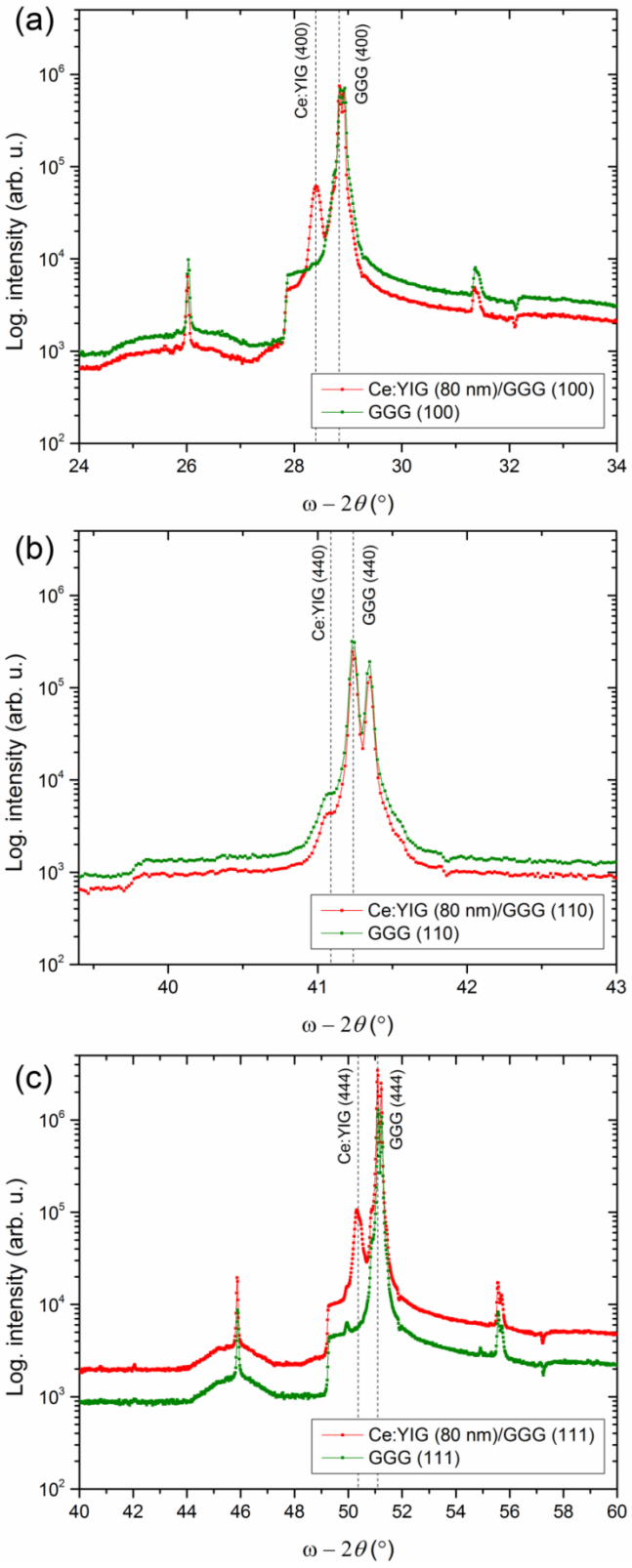

Fig. 3-1. XRD patterns of Ce:YIG (80 nm) films on (a) GGG (100), (b) GGG (110), and (c) GGG (111)

substrates. Y_2O_3 or CeO_2 peaks were not found. Each plot contains an XRD pattern for a similar substrate without film. All films are single garnet phase. Major substrate peaks are indicated with dashed lines.

Magnetic properties of Ce:YIG films were measured with magnetic fields applied parallel to the film surface plane (in-plane configuration, IP) or perpendicular to the film surface plane (OP) at room temperature (RT) using a vibrating sample magnetometer (VSM). IP magnetization hysteresis loops for Ce:YIG (80 nm)/GGG (100), Ce:YIG (80 nm)/GGG (110) and Ce:YIG (80 nm)/GGG (111) films are shown in Fig. 3-2(a). OP magnetization hysteresis loops for Ce:YIG (80 nm)/GGG (100), Ce:YIG (80 nm)/GGG (110) and Ce:YIG (80 nm)/GGG (111) films are shown in Fig. 3-2(b). The films saturate near $M_s = 150\pm15$ emu·cm^{-3}, slightly higher than M_s values reported previously [31].

Although GGG has lattice parameter very close to that of Ce:YIG, one disadvantage of GGG substrates is these substrates have very high paramagnetic background signal. A small background noise can amplify to distort the overall signal especially during high field measurements ($|H_{applied}| > 6000$ Oe). This disadvantage is not present for magneto-optical or transmission measurements, since the setups used for these measurements are much more robust to the background noise than the VSM available for our study.

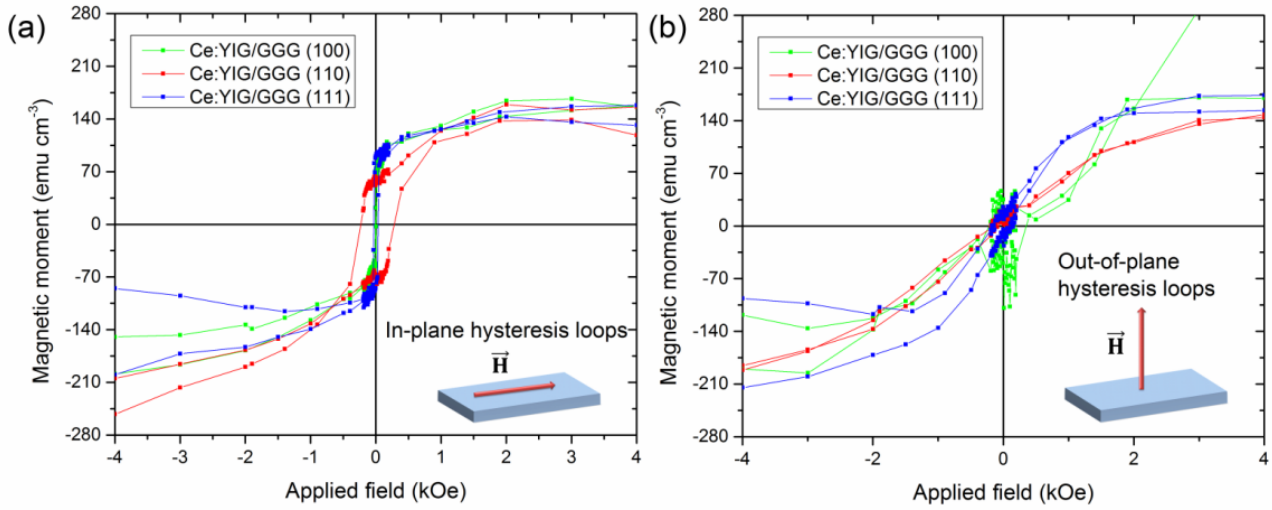

Fig. 3-2. Room temperature magnetic hysteresis loops of Ce:YIG (80 nm) films on GGG (100), GGG (110), and on GGG (111) substrates with magnetic field applied (a) in plane and (b) perpendicular to the film plane. All films have in-plane magnetic easy axis.

All of the films had their easy axes in-plane regardless of the substrate type and they saturate around 2000 Oe when magnetized in-plane. OP saturation fields of the Ce:YIG samples on GGG (100), GGG (110) and GGG (111) are around 8000 Oe, 5000 Oe, and 2000 Oe, respectively. Shape anisotropy ($4\pi M_s$), magnetocrystalline and magnetoelastic anisotropy drive the total anisotropy of the films. Total anisotropy energy includes a magnetoelastic anisotropy contribution due to the difference between the lattice parameters of bulk Ce:YIG and bulk GGG and a c/a ratio ~ 1.015. The saturation field difference originates from the differences in crystal fields imposed on Ce:YIG by different orientations of GGG substrates.

In addition to OP hysteresis loop measurements, a more extensive study of the IP magnetic anisotropy of Ce:YIG on GGG substrates is presented in Fig. 3-3. IP room-temperature magnetic hysteresis loops were measured for each Ce:YIG (80 nm) film on the GGG substrates for every 10°. Field direction was fixed and the substrate was rotated 10° around an axis perpendicular to the film plane for each IP hysteresis measurement. Angular dependence of IP coercivity (Hc) for Ce:YIG (80 nm) on GGG (100), (110), and (111) are in Fig. 3-3 (a, c, e), respectively.

Angular dependence of in-plane squareness (defined as magnetic remanence/saturation; M_r/M_s) for Ce:YIG (80 nm) on GGG (100), (110), and (111) are in Fig. 3-3 (b, d, f), respectively. Squareness is a measure of anisotropy normalized to the saturation moment. Ce:YIG on GGG (100) exhibits 4-fold cubic symmetry and IP <011> are the magnetic easy directions, which show up along 45, 135, 225 and 315° IP on Fig. 3-3(a, b). These directions are also the expected easy directions in a previous study of Ce:YIG/GGG (100) [28]. Ce:YIG on GGG (110) exhibits a clear 2-fold symmetry. Ce:YIG on GGG (111) exhibits 4-fold and 6-fold symmetry as a result of the projection of the (111) plane of garnet substrate. The 6-fold symmetry is consistent with the earlier measurements in [28]. In addition, the 4-fold symmetry is also consistent with the observations in the anisotropies between 0, 45 and 135° IP directions.

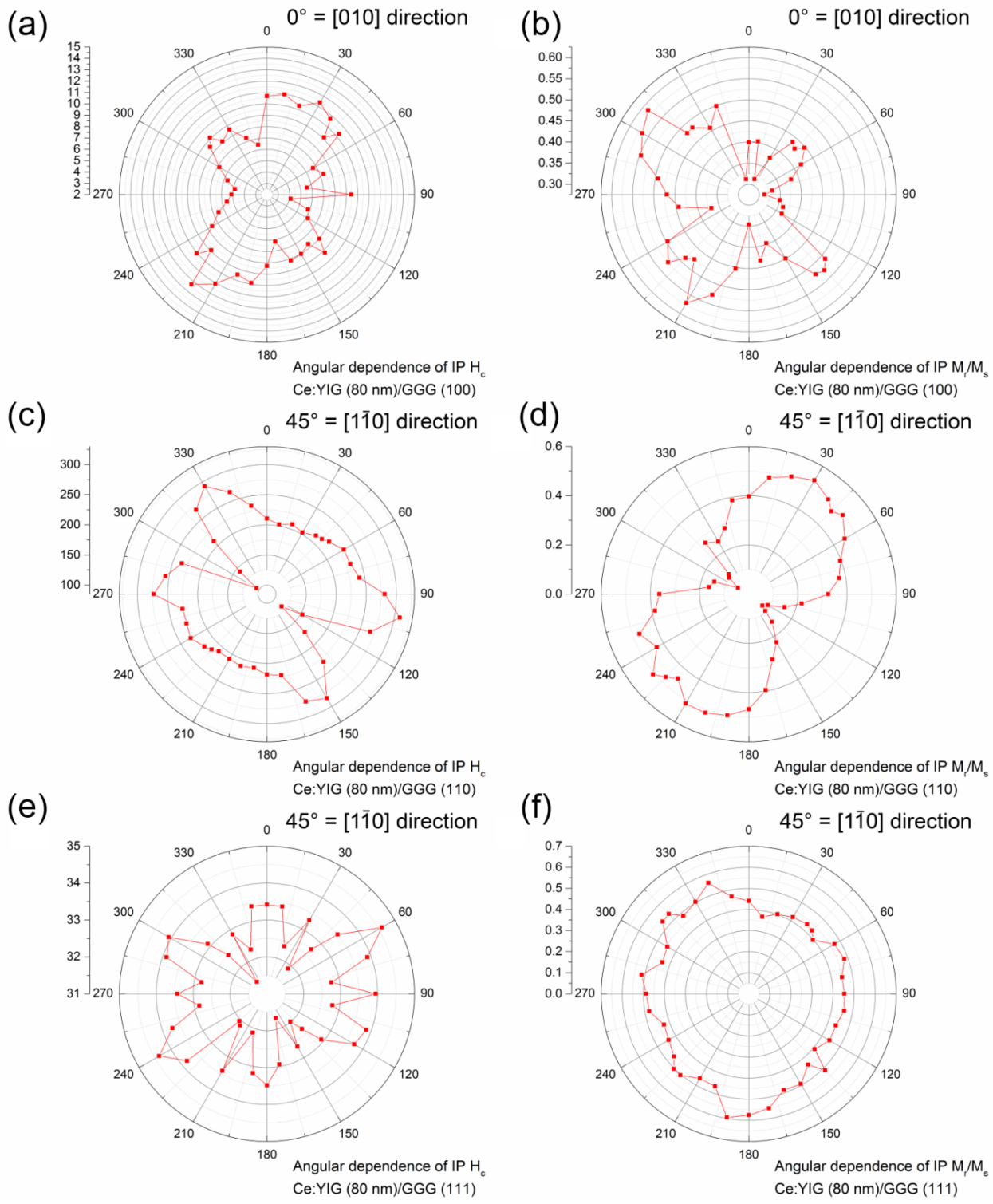

Fig. 3-3. Angular dependence of in-plane coercivity (Hc) for Ce:YIG (80 nm) on GGG (100), (110), and (111) are in (a, c, e), respectively. Angular dependence of in-plane squareness (defined as magnetic remanence/saturation; Mr/Ms) for Ce:YIG (80 nm) on GGG (100), (110), and (111) are in (b, d, f), respectively. Films on GGG (100) show 4-fold cubic symmetry, films on GGG (110) show 2-fold symmetry, and the films on GGG (111) show both 6-fold and 4-fold symmetries.

After establishing the structural and magnetic properties of Ce:YIG films on GGG (100), (110) and (111) substrates, optical (n,k) and magneto-optical properties (Faraday rotation, ellipticity, Kerr rotation) of the films are presented as a function of wavelength and substrate orientation. First, the electronic band gap and optical transmission of the films and uncoated substrates were measured and presented on Fig. 3-4. GGG has a band edge at λ_g = 232 nm (E_g (GGG) = 5.336 eV) for all substrate orientations. GGG also has a band tail that extends from 232 nm to 750 nm, with sharp absorption peaks at λ = 275.3 nm, 307.3 nm, 313.2 nm due to intrinsic electronic transitions inside the GGG lattice. 275.3 nm (36320 cm^{-1}), 307.3 nm (32510 cm^{-1}) and 313.2 nm (31930 cm^{-1}) transitions belong to the 4f transitions of Gd^{3+} ions from ^8S ground state to ^6I, $^6P_{5/2}$ and $^6P_{7/2}$, respectively [35,36]. These energy transitions originate from spin-orbit and crystal field splitting. The transmission spectra for 80 nm-thick films shown on Fig. 4 indicates that Ce:YIG has an indirect band-gap similar to GGG, but with an absorption tail reaching into the visible and infrared indicating that $E_{g\,(Ce:YIG)} < 0.6$eV. There is also a weak but non-zero refractive index difference between the substrates with different orientations.

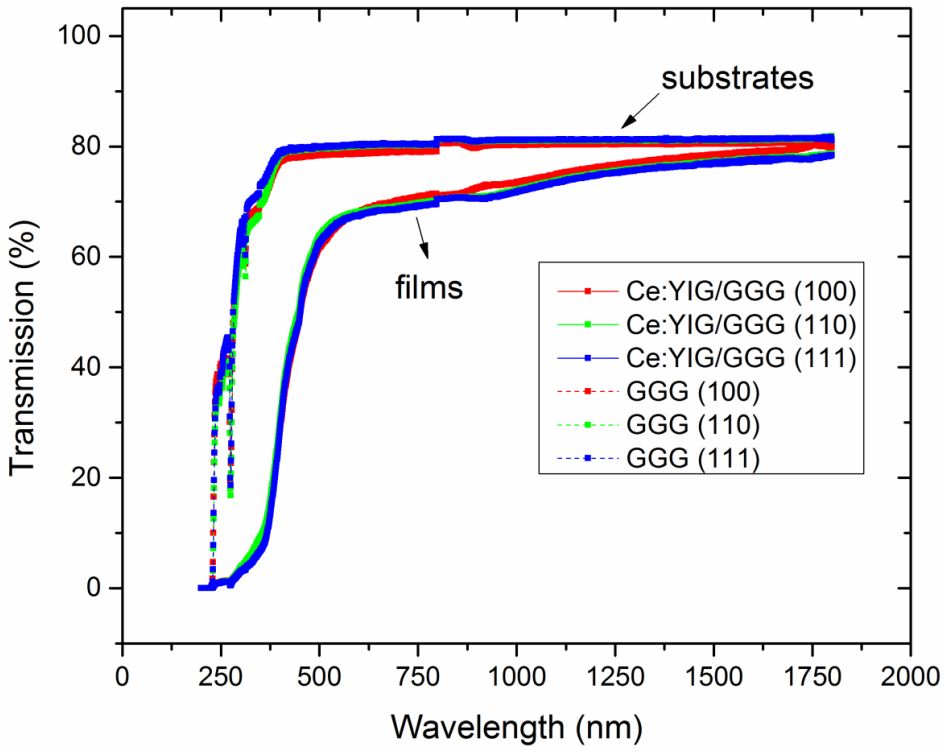

Fig. 3-4. Room temperature optical and near-infrared transmission of Ce:YIG (80 nm) films on GGG substrates.

Next, we characterize the dielectric permittivity (ε tensor), refractive index (n) and extinction coefficients (k). The permittivity tensor of magnetic material in magnetic field perpendicular to its surface can be written in the form (with restriction to linear magneto-optical effects):

$$\varepsilon = \begin{pmatrix} \varepsilon_1 & -i\varepsilon_2 & 0 \\ i\varepsilon_2 & \varepsilon_1 & 0 \\ 0 & 0 & \varepsilon_1 \end{pmatrix}, \quad (1)$$

where ε_1 and ε_2 are complex numbers describing optical and magneto-optical response of the material. We assumed that there is no birefringence. This tensor form can be used for theoretical description of Faraday and polar Kerr magneto-optical effects since the magnetization points in the same direction. The ellipsometry measurements and fits were done by Prof. Martin Veis group at Charles University of Prague at Czech Republic. In order to be able to obtain the film properties, first, the optical properties of GGG were determined from measurements done on uncoated substrates. Fig. 3-5 shows the ε_1 values (real and imaginary parts) extracted from fitting the Ψ and Δ results from spectroscopic ellipsometry measurements done on Ce:YIG films on GGG (100), (110) and (111) substrates.

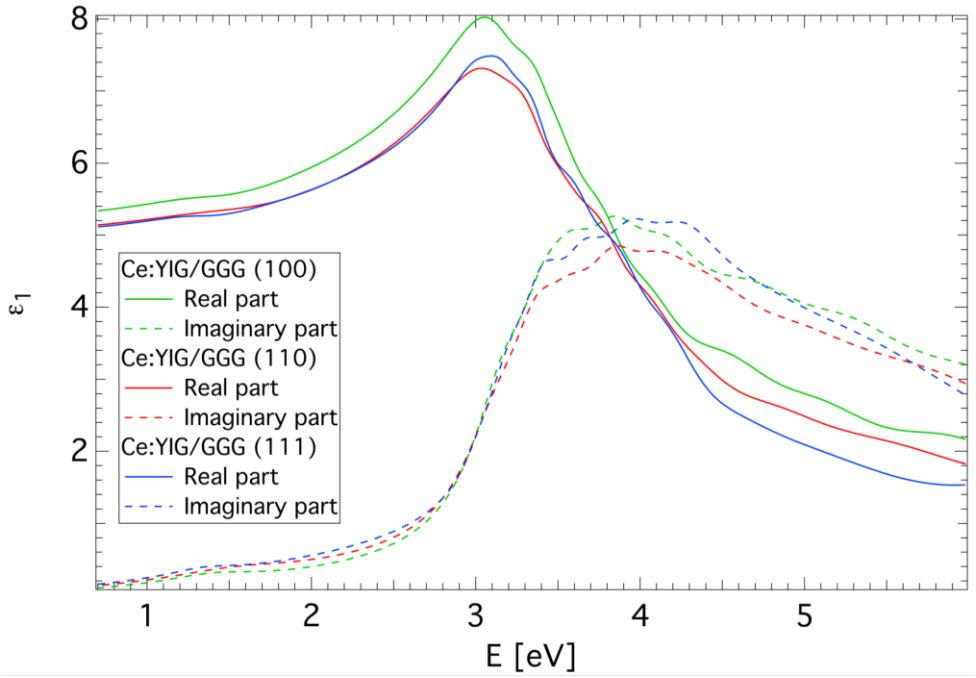

Fig. 3-5. Spectral dependence of diagonal permittivity elements, ε_1, of investigated Ce:YIG films (80 nm).

(results provided by Prof. Martin Veis group)

An optical thin film model was designed to fit the measured Ψ and Δ spectra of Ce:YIG films. This model consists of a homogenous single layer on GGG substrate and takes surface roughness of the layers into account. A summation of 10 Lorentz oscillators were used in the thin film model dielectric function ε_1 to fit most of the spectral features in the Ψ and Δ spectra. The spectral dependence of ε_1, shown in Fig. 3-5, is similar to that of YIG single crystals and thin films [37-40]. The main difference between ε_1 spectra of Ce:YIG and YIG is in the energy region between 1 and 2 eV, driven mainly by the absorption peak near 1.4 eV in the spectra of the imaginary part of ε_1. The absorption near 1.4 eV (λ = 885.6 nm) arises from electrical dipole transitions among substituted-Ce^{3+} ions. This absorption can also be seen in the transmission spectra in Fig 3-4. The thickness fits match with the thickness results of XRR.

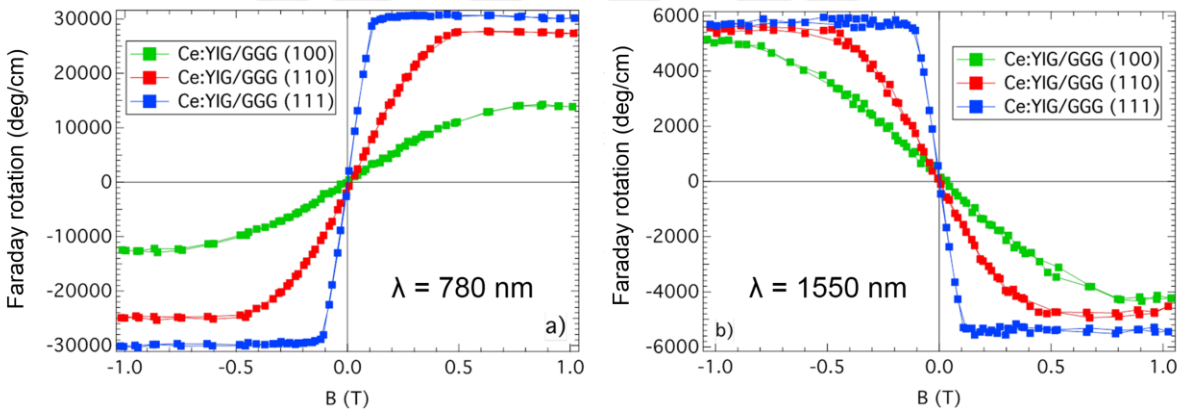

Fig. 3-6. Room temperature Faraday rotation hysteresis loops of Ce:YIG films (80 nm) at (a) λ = 780 nm, (b) λ = 1550 nm. (results provided by Prof. Martin Veis group)

Faraday rotation spectra and hysteresis loops were obtained on a spectrometer based on azimuth modulation technique (rotating polarizer). Faraday loops at λ = 780 nm and 1550 nm are shown on Fig 6(a) and 6(b), respectively. The loops are consistent with OP VSM measurements shown in Fig. 3-2(b), confirming the saturation magnetization around 8000 Oe, 5000 Oe and 2000 Oe for (100), (110) and (111) GGG substrates respectively. The value of 2000 Oe for the sample on (111) GGG substrate is close to the saturation magnetization of YIG crystals (1780 Oe) [41]. To the best of our knowledge, Faraday rotation values as high

as -5750 °·cm^{-1} as in Fig. 3-6 were not reported for PLD-grown magneto-optical oxides thinner than 100 nm.

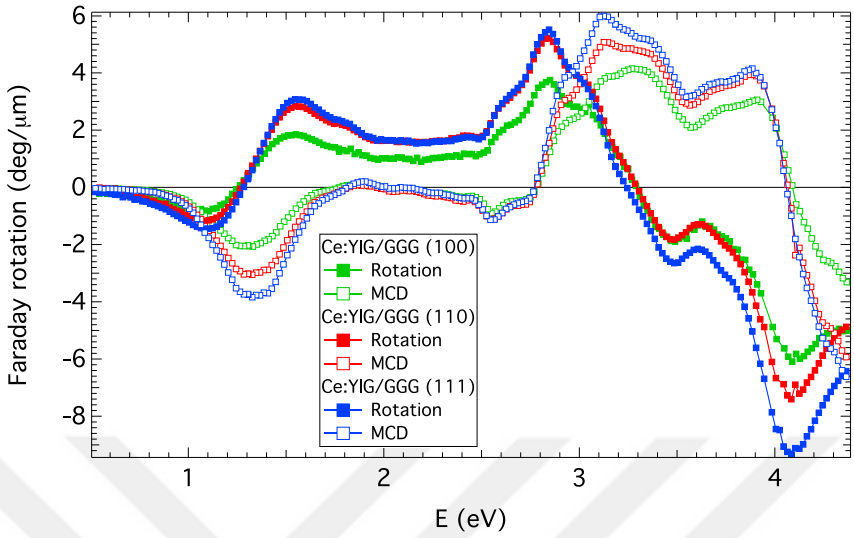

Fig. 3-7. Room temperature Faraday rotation and MCD spectra of 80 nm thick Ce:YIG films on GGG (100), (110) and (111) substrates. (results provided by Prof. Martin Veis group)

The spectral dependence of saturation Faraday rotation and MCD (magnetic circular dichroism, i.e. Faraday ellipticity) are shown on Fig. 3-7. For micrometer-thick Ce:YIG layers with high Ce^{3+} content, similar spectral dependence was reported [42-44]. A strong increase of Faraday ellipticity (MCD) is observed near 1.4 eV (similar to the 1.4 eV feature in optical transmission and ε_1 spectra). This increase originates from 4f-5d transition in Ce^{3+} ions [45,46] and is the origin of strong enhancement of magneto-optical properties in Ce:YIG compared to YIG. The strong peaks near 3.1 and 3.9 eV on the MCD curves originate from Fe^{3+} crystal-field transitions discussed in literature [47]. From the saturation Faraday rotation amplitudes shown on Fig. 3-7, one can conclude that Ce:YIG on GGG (111) is the highest quality sample.

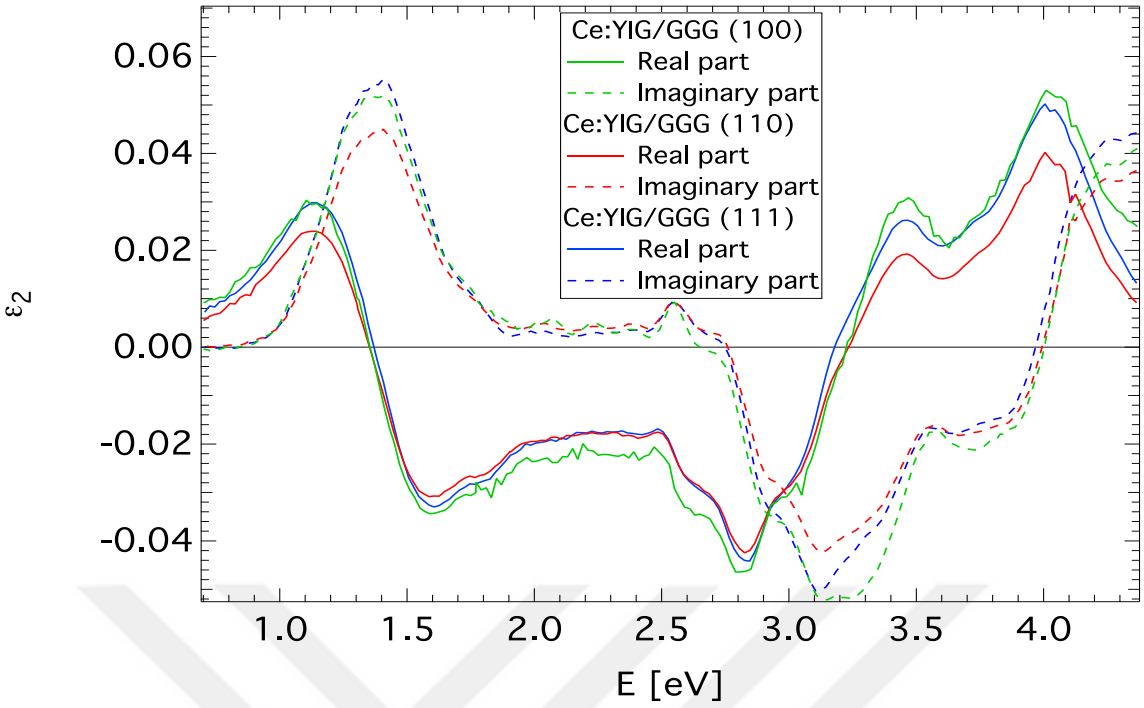

Fig. 3-8. Spectral dependence of off-diagonal permittivity element, ε_2, of Ce:YIG films on GGG. (results provided by Prof. Martin Veis group)

Faraday rotation spectra shown in Fig. 3-7 were used to calculate the spectral dependence of ε_2 (off-diagonal element of permittivity tensor shown in Eq. 1). The real and imaginary parts of the ε_2 are coupled by Kramers-Kronig relations. Therefore simply analyzing either the real part or the imaginary is sufficient to describe the band transitions of Ce:YIG. The dominant features on the imaginary part of ε_2 spectra are around 1.4 eV and above 2.6 eV. The low energy (1.4 eV) magneto-optical feature is related to electrical dipole transitions among Ce^{3+} ions. For energies above 3 eV, the magneto-optical properties of Ce:YIG are mainly driven by charge transfer transitions of involving Fe^{3+} ions [47].

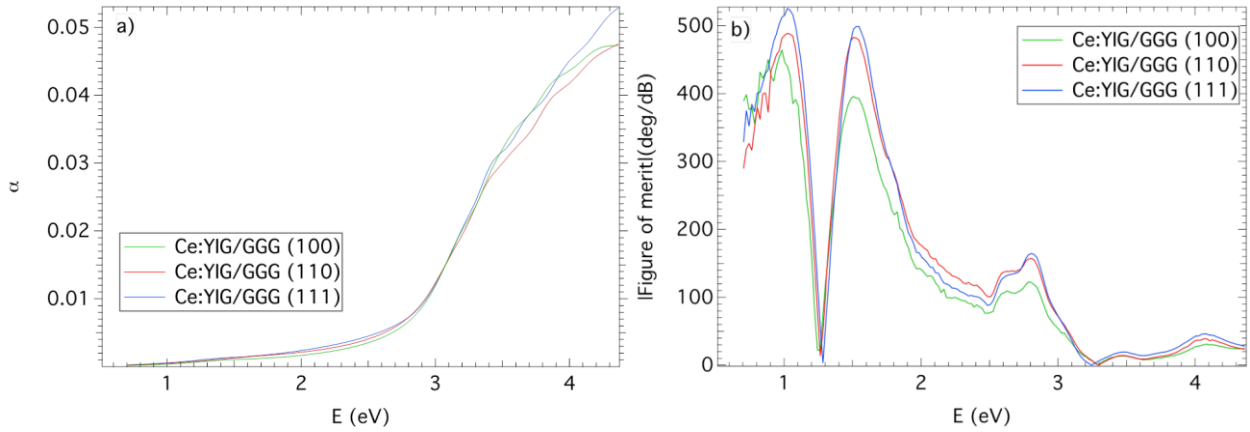

Fig. 3-9. (a) Spectral dependence of absorption coefficient of investigated Ce:YIG films on GGG substrates. (b) Spectral dependence of Figure of merit of investigated Ce:YIG films on GGG substrates. (results provided by Prof. Martin Veis group)

Fig. 3-9(a) shows the spectral dependence of absorption coefficients ($\alpha = 4\pi k/\lambda$) of Ce:YIG films. Fig. 3-9(b) shows the calculated magneto-optical figure-of-merit of Ce:YIG films. Since the absorption coefficients of the Ce:YIG films in IR region (especially near 0.8 eV or λ = 1550 nm) are low, the figures of merit at the telecommunication wavelength 1550 nm are found to be as high as *379, 380, and 401 deg · dB*$^{-1}$ for Ce:YIG films on GGG (100), (110) and (111) substrates, respectively. These thin film epitaxial Ce:YIG figures of merit are higher than the previous reports of 340 deg · dB^{-1} figure-of-merit for single-crystal MO thin films on garnet substrates [32]. From Fig. 3-9, we also conclude that using the same deposition conditions for Ce:YIG on GGG substrates, the best film quality is obtained when the substrate has (111) orientation. The figure of merit values were calculated for 80 nm thickness. The figures-of-merit presented above serve as upper limits for MO quality for garnet films on GGG. In the next section, we investigate two different methods for growing MO garnets on Si-based substrates (Si and Si_3N_4) and compare the resulting figures of merit with those of the epitaxial Ce:YIG films.

3.1.2 Polycrystalline garnet films on non-garnet substrates

In this section, we present two studies. The first study is the growth of good-quality Ce:YIG films on Si_3N_4. The second study is the growth of Ce:YIG on Si. The first study focuses on first growing a YIG seed layer, doing a rapid thermal anneal to crystallize YIG and then growing Ce:YIG on the YIG polycrystalline seed to get good magneto-optical properties. That study highlights the importance of growth temperature and seed layer quality (and growth rate) for achieving good quality garnet. The second study focuses on growing Ce:YIG with a YIG seed layer that is deposited at room temperature on Si. The second study focuses on reducing the thermal budget by eliminating high temperature steps as much as possible while retaining a high enough figure-of-merit for garnet films grown.

Growth of Ce:YIG films on Si_3N_4

In this part, we focus on growing Ce:YIG on Si_3N_4. Silicon nitride is interesting because it is a common cladding layer for Si integrated microphotonics and an integrated optical isolator may need to be integrated with nitride claddings. Growth of MO thin films on Si-based substrates has been a difficult materials processing issue because of the differences between crystal structures, lattice parameters and thermal expansion coefficients of MO thin films and silicon. Specific to silicon nitride, silicon nitride is also less stable when an MO garnet layer is grown on nitride claddings. Additionally, even when MO films are grown, their performance is typically poorer than that of the bulk MO material, and their growth requires high thermal budgets [1,5]. An improved integration method for MO films on Si-based substrates including silica and silicon nitride is therefore necessary for enabling on-chip optical isolation and modulation.

The most commonly used MO materials are iron garnets based on yttrium iron garnet (YIG, $Y_3Fe_5O_{12}$), in particular cerium- or bismuth-substituted YIG (Ce:YIG or Bi:YIG, $(Ce \text{ or } Bi)_xY_{3-x}Fe_5O_{12}$ with x usually ~1) has been demonstrated as a candidate material for

optical isolators [2, 5]. YIG has a large unit cell with lattice parameter a = 12.376Å and space group $Ia\bar{3}d$) [9], much larger than that for any of the common photonic substrates including Si (a = 5.431Å), GaAs (a = 5.6533Å) and InP (a = 5.8696Å) [9-11]. The thermal expansion coefficient for garnet films is much larger than that of non-garnet substrates (YIG: 10.4 x 10^{-6} K^{-1}, Si: 3 x 10^{-6} K^{-1}, GaAs and InP: 5 x 10^{-6} K^{-1}) [8]. The garnet phases also require a large thermal budget for growth on photonic substrates, and for some garnet compositions, the processing route must avoid the formation of unwanted phases such as ceria in the growth of Ce:YIG.

Previously, YIG and substituted garnet films have been obtained on non-garnet substrates using wafer bonding [13], metal-organic chemical vapor deposition (MOCVD) [14], rf sputtering [15-22] and pulsed laser deposition (PLD) [1,2,3,5,29,48,49]. Wafer-bonding of bulk garnet crystals to non-garnet substrates produces devices with excellent MO properties but this approach is not easily scalable and issues with alignment and contamination need to be addressed. MOCVD growth requires surface reactions in order to form stoichiometric oxides, narrowing the processing window for single phase growth. Garnet films have been grown by sputtering or PLD on a range of non-garnet substrates including Si, ceria, MgO and quartz, but the growth requires high deposition or annealing temperature which can lead to cracking [16,24]. Despite this, sputtered Bi:YIG films with magnetization (M_s) of 135 emu cm^{-3} and coercivity (H_c) of 80 Oe on Si substrates [17], Ce:YIG with M_s = 120 emu cm^{-3} and H_c = 15 Oe on silica and Si [22] and YIG films with M_s = 100 emu cm^{-3} and H_c = 35 Oe on MgO and quartz [18] have been grown.

We have previously presented a three-step fabrication process consisting of growth of a YIG seedlayer, a rapid thermal anneal, then growth of Ce:YIG or Bi:YIG by pulsed laser deposition [1,2,5] to give well-crystallized Ce:YIG or Bi:YIG films on silica, silicon on insulator (SOI) or Si. The polycrystalline YIG seed layer acts as as a virtual substrate, templating the growth of the Ce:YIG.

This study demonstrates the integration of YIG and Ce:YIG on silicon nitride, including the effect of growth temperature and deposition rate of the YIG layer, to achieve bulk or near bulk magnetization and Faraday rotation at 1550 nm wavelength. Silicon nitride is commonly used in Si CMOS (complementary metal oxide semiconductor) and photonic circuits and the growth of magneto-optical Ce:YIG on nitride is an important contribution to fully integrated photonic circuits. Silicon nitride is less stable than silicon oxide or Si, because the silicon nitride can oxidize (i.e. become $SiON_x$ or even react with garnet along the interface) during the high-temperature YIG deposition under an oxygen atmosphere. This complication affects the YIG stoichiometry and requires a separate process development for growing YIG on silicon nitride films. The quality of YIG template can be optimized for the silicon nitride layer by changing the growth temperature and deposition rate. The structural and magnetic quality of YIG has significant impact on the quality of Ce:YIG grown subsequently. The process presented here will be useful in making structures for the investigation of nonreciprocal photonic phenomena and integrated photonic devices [27].

Samples consisted of Si with nitride of 760 nm thickness deposited by plasma enhanced chemical vapor deposition. First, YIG seed layers were grown. During PLD growth of films, the base and oxygen pressure used for YIG growth were 5 x 10^{-6} Torr and 5 mTorr, respectively. YIG films of 40±5 nm thicknesses were first deposited at a slow laser pulse rate of 2 Hz at 500, 560 and 640 °C substrate temperature for the first sample batch and at 10 Hz pulse rate at 500, 560 and 640 °C for the second sample batch. The YIG deposition rates were 5 Å min^{-1} and 25 Å min^{-1} for 2 Hz and 10 Hz respectively. Next, the YIG films were rapid thermal annealed (RTA) at 850 °C for 300 s. After RTA, Ce:YIG films were grown on top of the annealed YIG at 640 °C substrate temperature, 160±10 nm thickness, at 10 Hz. Each deposition and recrystallization step was carried out in an oxygen ambient. Control of oxygen pressure and substrate temperature can preserve the stoichiometry and prevent the formation of secondary phases such as ceria [1,5,24]. After Ce:YIG deposition, no further RTA step was necessary, because Ce:YIG grew as a large grained polycrystalline phase on the lattice-matched polycrystalline YIG layer.

A properly crystallized and single phase YIG template is desired for forming good quality Ce:YIG on top of YIG layer. The structural quality and phases present in Ce:YIG 160 nm/YIG 40 nm films were characterized using x-ray diffraction (XRD), transmission electron microscopy (TEM) and atomic force microscopy (AFM). Ce:YIG and YIG lattice parameters are very similar (lattice parameters for Ce:YIG and YIG are about 12.41 Å and 12.376 Å, respectively) [50,51], so within the resolution of the x-ray diffractometer, the Ce:YIG and YIG phases were not distinguishable.

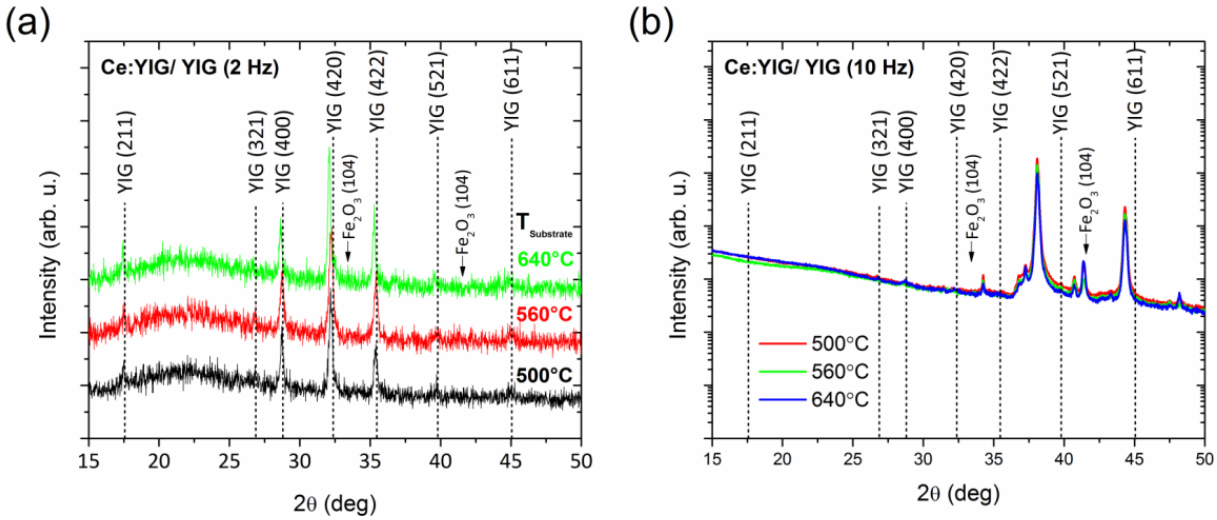

Fig. 3-10. XRD patterns of Ce:YIG (160 nm)/YIG (40 nm)/Si_3N_4/Si films grown at substrate temperatures of 500°C, 560°C, and 640°C when YIG was deposited at (a) 2 Hz pulse rate and (b) 10 Hz pulse rate. Dashed lines indicate the 2θ positions of the corresponding peaks of YIG. The peaks at 2θ = 38° and 2 θ = 44° correspond to Y_2O_3 (024) and Y_2O_3 (015), respectively. All Ce:YIG layers had the same deposition conditions, 640°C and 10 Hz.

The ω-2θ plots on Fig. 3-10(a) indicate the Ce:YIG/YIG films in which the YIG was deposited at 500, 560 and 640°C substrate temperature and 2 Hz pulse rate. In the measurement of the ω-2θ scan, the samples were tilted by 1° to avoid strong peaks from the Si substrate. In addition, a zero-background holder was used to avoid spurious signals. Si_3N_4 peaks are absent since the nitride layer is amorphous. Peaks for YIG (211), (400), (420), (422) and (611) planes were present with no other detectable phases. Peak locations for Fe_2O_3 are also indicated to demonstrate that the Ce:YIG layers did not contain detectable iron oxide phases. The garnet peaks became stronger and narrower with higher deposition temperature.

This transition indicates that the crystal size and quality improve with higher temperature deposition.

Fig. 3-10(b) shows the ω-2θ scan for the Ce:YIG films grown on YIG which was grown at 500, 560 and 640°C substrate temperature and pulse rate of 10 Hz. This higher deposition rate of YIG led to dramatically different growth. At 10 Hz, the YIG did not crystallize at any of the temperatures investigated, and iron oxide and yttrium oxide phases appear in each Ce:YIG film. The peaks are identified on both Fig. 3-10(a) and (b), as well as on the figure caption. Based on this observation, a slow growth rate (2 Hz pulse rate) is necessary for obtaining sufficient surface diffusion to crystallize the YIG needed to template the Ce:YIG.

Fig. 3-11 (a)-(d) and 3-11(e) show the TEM images and AFM surface profile of the Ce:YIG (160 nm)/YIG (40nm, 2 Hz)/Si_3N_4 layers, respectively. Fig. 3-11(b) confirms that the silicon nitride is amorphous, and YIG is crystalline with the expected lattice parameter. The nitride-YIG interface, marked 1, is diffuse whereas the YIG-Ce:YIG interface is sharp. The Ce:YIG shown in Fig. 3-11(c) was not crystallized, but the magnetic data (described below) is characteristic of crystalline Ce:YIG and we therefore assume that the focussed ion beam preparation of the TEM sample led to amorphization. Fig. 3-11(d) shows the Ce:YIG-Au interface (the Au is added during sample preparation). Fig. 3-11(e) is a representative surface profile of a 160 nm Ce:YIG layer on YIG (40 nm, 2 Hz) grown at 625°C. The image is notable for the large ~8 μm diameter grains with radial patterns and occasional 1-2 μm wide voids assumed to represent the early stages of dewetting, or from resputtering of the film. Based on their depth (up to 15 nm), these voids are present only at the top of the Ce:YIG layer. This suggests that the Ce:YIG growth conditions favor significant surface diffusion, and a lower growth rate or temperature for this layer may improve the surface morphology (all Ce:YIG was grown at 640°C and 10 Hz).

The grain size of the Ce:YIG films increased with the growth temperature of the YIG, and the root-mean-square roughness of the Ce:YIG was 9.6 nm, 3.6 nm and 2.7 nm, for YIG 2 Hz grown at 500, 560 and 625°C respectively. Thus in these experiments the YIG grown at

lower deposition rate and higher temperature produced Ce:YIG with the best crystallinity, but the Ce:YIG deposition conditions need to be further improved to reduce voiding and roughness.

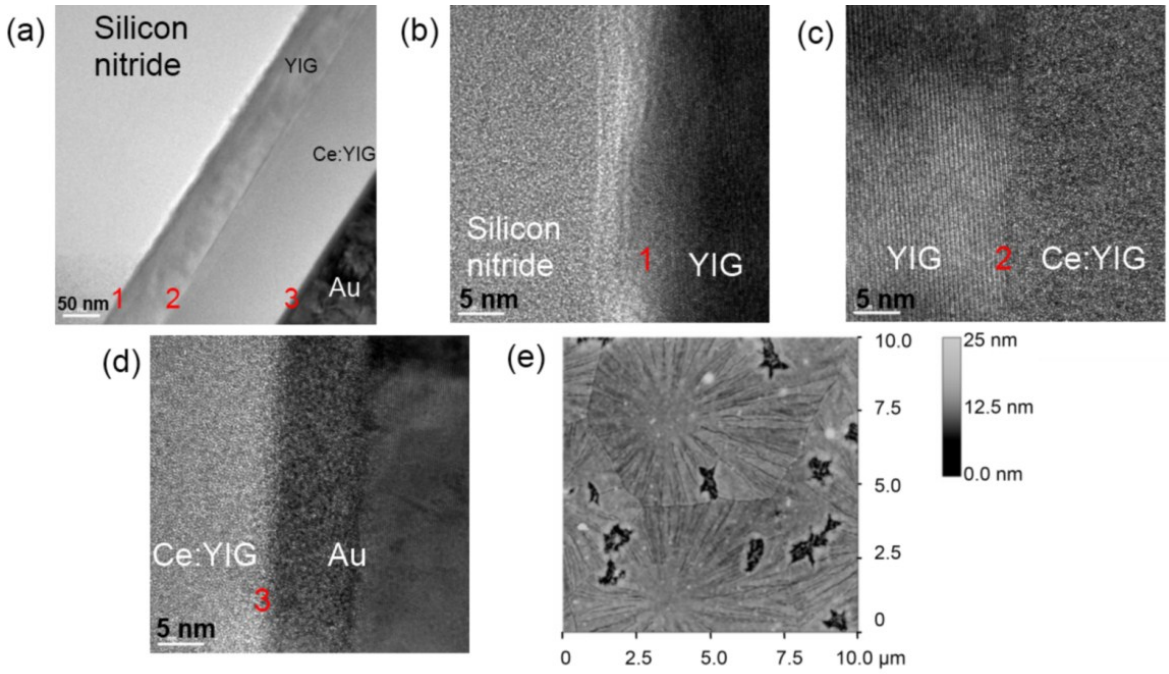

Fig. 3-11. TEM and AFM scan of the surface topography of Ce:YIG (160 nm)/YIG (40 nm)/Si_3N_4/Si films in which the YIG was grown at a substrate temperature of 640°C and at 2 Hz pulse rate. Grain sizes are around 8 µm in diameter, and rms roughness is 2.7 nm. (a) TEM image of Ce:YIG/YIG/Si3N4 layers (scale bar: 50 nm). high resolution TEM image of the interfaces between (b) silicon nitride and YIG, labelled 1, (c) YIG and Ce:YIG, labelled 2, (d) Ce:YIG and Au, labelled 3. Scale bars for (b) – (d): 5 nm, (e) AFM surface profile over 10 µm x 10 µm area. (TEM imaging done by Dr. Xueyin Sun).

Fig. 3-12 shows the elemental mapping of Fe, O, Ce, Y, N and Au from the scanning transmission electron microscope sample together with a bright field TEM image. Ce is detected inside the Ce:YIG layer, and Y and Fe ions in the YIG and Ce:YIG layers. Comparing the depth of the Y-rich and Fe-rich regions with that of the O-rich region, it appears that oxygen is present in the upper ~10 – 15 nm of the nitride substrate. This is consistent with the diffuse interface observed in Fig. 3-11(b) and suggests partial oxidation of the nitride during the YIG growth.

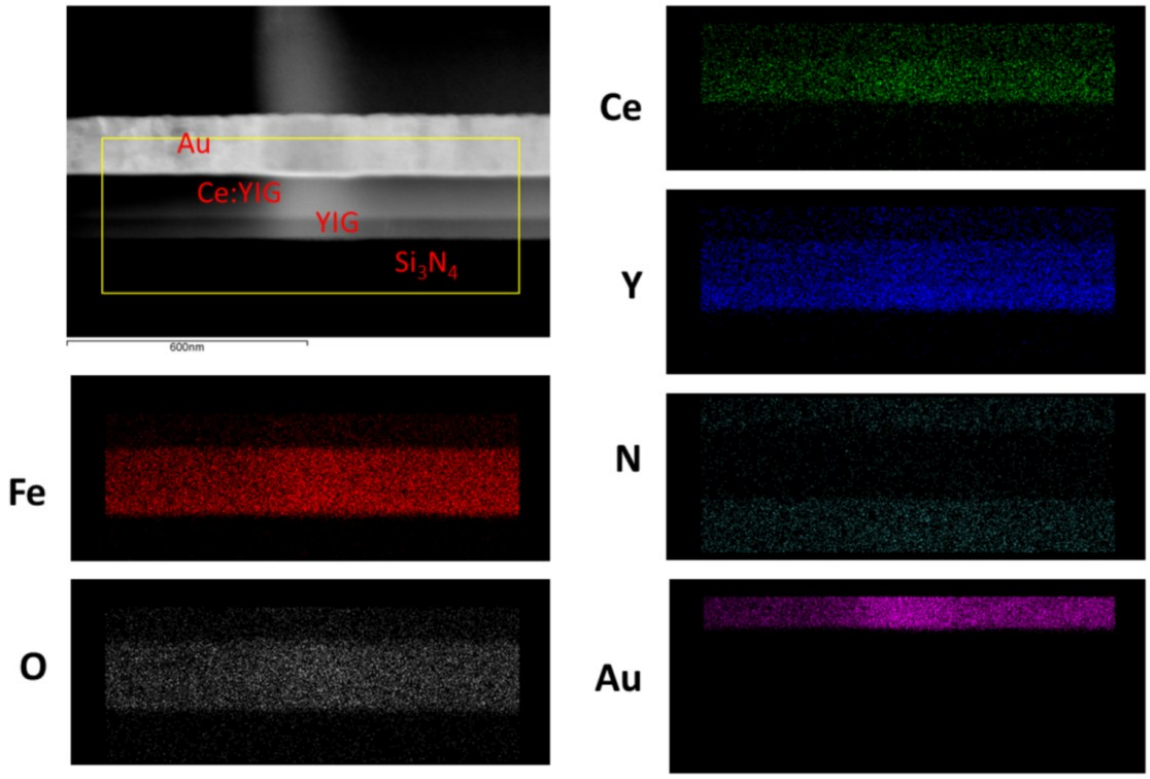

Fig. 3-12. STEM-EDX elemental mappings for Fe, O, Ce, Y, N, Au ions. The scale bar (shown below TEM image) is 600 nm. Cerium has not diffused into YIG or nitride layers, but there is oxygen interdiffusion in the top surface of the nitride. (TEM imaging and elemental mapping done by Dr. Xueyin Sun).

Magnetic properties of Ce:YIG films were measured with magnetic fields applied perpendicular to the film plane (out-of-plane, OP, configuration, along Si [001] direction) or in the film plane (IP, along Si [010] direction) at room temperature (RT) using a vibrating sample magnetometer (VSM), and measured at 50 K and 200 K using a superconducting quantum interference device (SQUID) magnetometer. IP magnetization hysteresis loops for Ce:YIG/YIG are shown in Fig. 3-13(a). Fig. 3-13(b) shows a narrower magnetic field range to more clearly indicate the remanent magnetization and coercivity of the samples. For Ce:YIG 160 nm/YIG 40 nm in which the YIG was deposited at 2 Hz, the M_s was 125, 134 and 142 emu cm^{-3} (with ~5% error estimate) and coercivity H_c was 76, 81, and 76 Oe for YIG films grown at 500, 560 and 625°C, respectively.

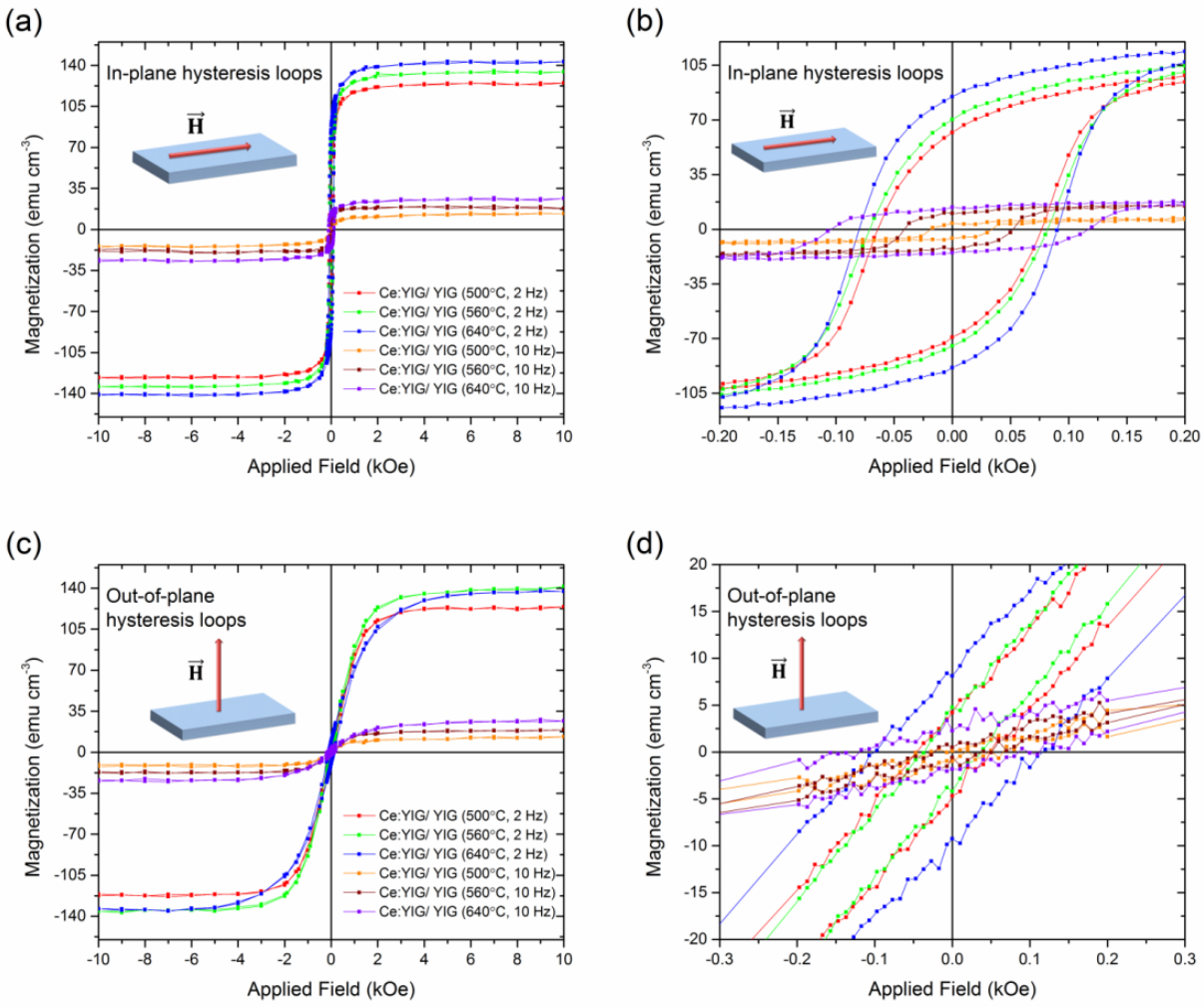

Fig. 3-13. Room temperature hysteresis loops of Ce:YIG/YIG/Si3N4/Si with magnetic field applied (a,b) in plane, (c,d) perpendicular to the film plane. Growth temperatures and PLD pulse repetition rates for the YIG layer for each film are shown in the legend. All Ce:YIG layers had the same deposition conditions, 640°C and 10 Hz.

For YIG deposited at 10 Hz, the M_s was 13, 19, and 25 emu cm^{-3} and H_c was 33, 53, and 119 Oe for YIG films grown at 500, 560 and 625°C, respectively. The M_s presented is the average over both garnet layers, and these M_s values were calculated by first subtracting the linear diamagnetic substrate contribution and then dividing the signal by the film volume (0.85 cm x 0.85 cm x 200 nm). The RT bulk saturation moment of YIG is about 140 emu cm^{-3} [51] and for Ce:YIG it is similar, 120 emu cm^{-3} [31]. The coercivity of single layer YIG is typically a few Oe, so the measured coercivities of up to 80 Oe are attributed to the magnetically harder Ce:YIG layers. We therefore see that the YIG growth rate profoundly affects the magnetic properties as well as the microstructure of the Ce:YIG.

Fig. 3-13(c) and (d) show the corresponding OP magnetic hysteresis loops. The IP and OP measurements of M_s for each sample were within 5% of each other. The OP coercivities were 45, 37, and 100 Oe for 2 Hz deposited YIG and 23, 23, and 120 Oe for 10 Hz deposited YIG grown at 500, 560 and 625°C, respectively. All of the films had their easy axes in-plane, regardless of growth temperature and YIG deposition rate. Out of plane saturation fields of around 2 kOe for the samples with 2 Hz grown YIG are consistent with a shape anisotropy of $4\pi M_s$ indicating shape anisotropy is the major contributor to the film anisotropy.

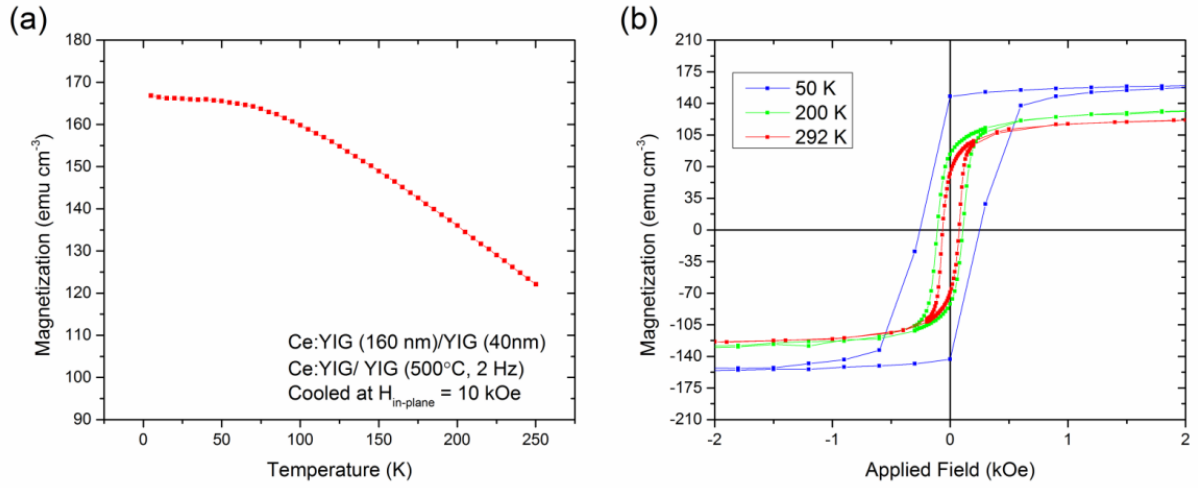

Fig. 3-14. Temperature dependence of magnetic properties of Ce:YIG film grown on YIG grown at 500°C and at 2 Hz. (a) Temperature dependence of saturation magnetization when the film is cooled under 10 kOe in plane bias field. (b) In plane magnetic hysteresis loops of the same film at 50, 200 and 292K. Inset shows the remanent magnetization and coercivities at 50, 200 and 292K.

The temperature dependence of magnetization of a Ce:YIG film on YIG (2 Hz, 500°C) was measured using a SQUID magnetometer, Fig. 3-14. Fig. 3-14(a) shows the temperature dependence of M_s for this film (after substrate subtraction) when cooled at 10 kOe magnetic field applied in the film plane. The M_s was 125 emu cm^{-3} at RT and increased to 135 and 165 emu cm^{-3} at 200 K and 50 K, respectively. The substrate contribution to the magnetization was found by fitting a linear diamagnetic signal to the hysteresis loop at 200 K and evaluating its magnitude at 10 kOe. The same linear diamagnetic contribution was subtracted for all temperatures. Fig. 3-14(b) shows the IP magnetic hysteresis loops at 50, 200 and 292 K, with

the diamagnetic Si signal subtracted. The coercivity was 76 Oe at RT, and increased to 107 Oe and 246 Oe at 200 K and 50 K respectively. The films are ferrimagnetic without any phase transitions at low temperatures. Previous measurements of temperature dependence of magnetism in YIG [52] gave M_s at 50K, 200K and 292K of 189.4 emu cm^{-3}, 166 emu cm^{-3} and 140 emu cm^{-3}, respectively, which are close to the experimental values measured here for Ce:YIG on YIG (2 Hz) films.

In comparison to these results for YIG/Ce:YIG, in single layer Ce:YIG films grown directly on nitride, the Ce:YIG did not crystallize and M_s never exceeded 3 emu cm^{-3}. A lattice-matched YIG virtual substrate for Ce:YIG is therefore necessary to achieve the garnet structure with bulk saturation magnetization. Given the difference in structural and magnetic properties of Ce:YIG on YIG grown at 2 Hz and 10 Hz, growing YIG at low growth rates is also important.

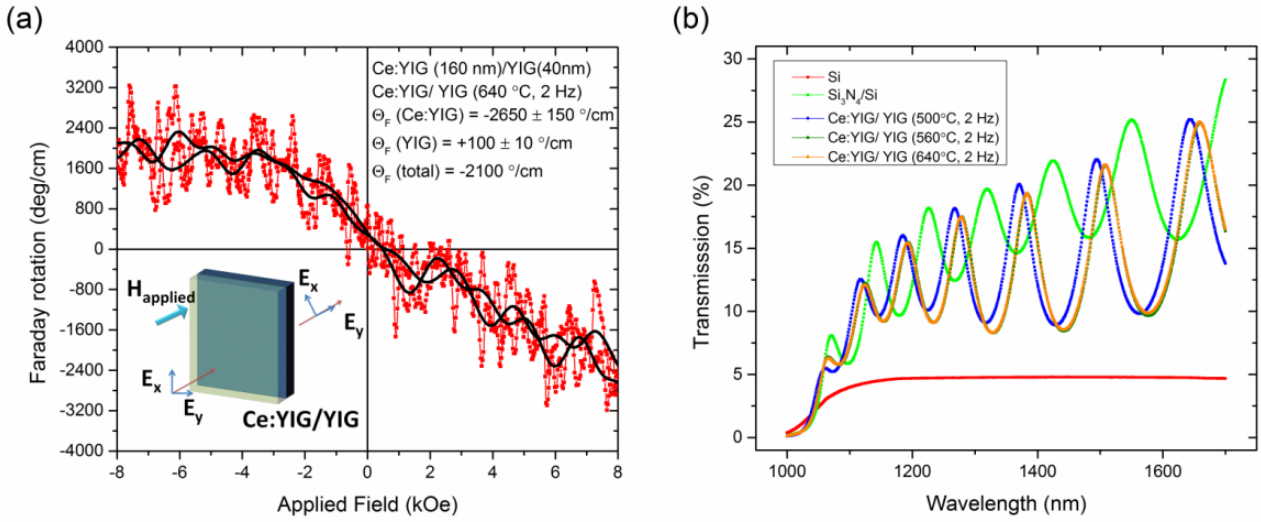

Fig. 3-15. (a) Faraday rotation of Ce:YIG (160 nm)/YIG (40 nm)/Si3N4/Si films grown at 640°C show around -2100 °cm^{-1} total Faraday rotation. Since YIG has opposite sign of Faraday rotation (+100 ° cm^{-1}, measured but not shown here), the Ce:YIG layer has about -2650 ± 150 ° cm^{-1} Faraday rotation. The solid line shows smoothed data. All Faraday rotation loops were measured at 1550 nm wavelength. Backsides of Si substrates were not polished, which reduced the overall transmission of the samples. (b) Near-infrared transmission spectra of the Ce:YIG/YIG films grown at different YIG substrate temperatures. The fringes in the transmission spectra occur due to Fresnel reflections between the top and bottom surfaces of the films.

Magneto-optical and optical properties of the films were measured using a custom-built Faraday setup and a spectrophotometer in transmission mode. Faraday rotation of the films was measured for near-infrared light (λ_0 = 1550 nm) passing perpendicularly through the film, while sweeping the magnetic field perpendicular to the film plane from -10 kOe to 10 kOe in a full loop. Fig. 3-15(a) shows the total Faraday rotation (FR) loop of Ce:YIG (160 nm)/YIG (40 nm) with 2 Hz rate and 625°C growth temperature for the YIG. The total Θ_F was -2100 ° cm^{-1}. We extract the saturation Θ_F (Ce:YIG) by subtracting the contribution of YIG based on the thicknesses of the layers, i.e. Θ_F (total) = {160 × Θ_F (Ce:YIG) + 40 × Θ_F (YIG)}/200. Since Θ_F (YIG) in our samples is about +100 °cm^{-1} [1], Θ_F (Ce:YIG) = -2650 ± 150 °cm^{-1}. The Θ_F (Ce:YIG) obtained in films on silicon nitride was 20% lower than a value of Θ_F reported for bulk Ce:YIG, which was around -3300°cm^{-1} [32]. The Θ_F for Ce:YIG/YIG/nitride obtained is consistent with the Θ_F obtained for Ce:YIG on silica substrates [22]. The noise of ±150 °/cm is due to mechanical vibrations of the Faraday rotation measurement setup and backside scattering from the sample because the back side of the substrate was not polished.

Faraday rotation values for Ce:YIG/YIG (2 Hz) are -1400 ± 150°cm^{-1}, -1800 ± 25°cm^{-1}, and -2100 ± 150°cm^{-1} for YIG grown at 500°C, 560°C and 640°C respectively. Corresponding Faraday rotation values for Ce:YIG/YIG (10 Hz) grown at 500, 560 and 640°C are -340 ± 100°cm^{-1}, -650 ± 200 °cm^{-1}, and -980 ± 250 °cm^{-1}, respectively. The Faraday rotation increased with saturation magnetization.

Optical transmission measurements, as shown in Fig. 3-15(b), indicate that total optical propagation loss was similar for 760 nm thick Si_3N_4 coated silicon wafers with and without Ce:YIG/YIG (except for the shift in the thickness fringe positions). The optical loss was therefore dominated by the silicon nitride, not the garnet films, and the loss of the garnet bilayer could not be determined by this method.

In summary, we demonstrated a growth method for integrating onto silicon nitride a transparent magnetooptical oxide, Ce:YIG, with bulk or near-bulk M_s and Faraday rotation. Due to the reactivity of the nitride surface which oxidized during the garnet growth process,

one needs to account for the 10-20 nm of lossy silicon oxynitride layer when designing an integrated photonic device with silicon nitride/garnet interface. Using a low deposition rate for the YIG followed by its recrystallization using RTA, a well crystallized 40 nm thick YIG layer was made which served as a seed layer to grow crystalline Ce:YIG. The magnetic and magnetooptical properties of the Ce:YIG, specifically the saturation magnetization of 140 emu cm^{-3} and the Faraday rotation of up to -2650 °cm^{-1}, were equal to or close to reported bulk values, and the coercivity of the films was on the order of 80 Oe.

Growth of Ce:YIG films on Si

The monolithic integration of MO garnet materials onto Si-based photonic substrates, *e.g.* Si or Si-on-insulator (SOI), has been challenging because of thermal and lattice mismatch and the formation of undesirable non-garnet phases. Previously, Gomi *et. al.* [33,43,53] sputtered CeYIG on garnet and thermally-oxidized Si substrates. CeYIG with a Ce substitution of $x = 1$ ($x = 1$ in $Ce_xY_{3-x}Fe_5O_{12}$) could be grown on garnet substrates, but on non-garnet substrates the films were polycrystalline and x was limited to 0.7 before other phases appeared [53,29].

A two-step-deposition method using pulsed laser deposition (PLD) was demonstrated in which a thin YIG buffer layer was used as a seed layer for growth of polycrystalline CeYIG on non-garnet substrates [1-3] and used this process to make an integrated isolator based on a ring resonator. The YIG seed layer provides a virtual substrate on which CeYIG can grow, lessening the tendency for unwanted phases such as CeO_2 to form, even for high Ce contents such as $x = 1$. This process produced films with Faraday rotation angle of –800 °·cm^{-1} and figure-of-merit (FOM) of 20 °·dB^{-1}, but required processing at high temperatures during the three steps of YIG growth (550˚C), a subsequent rapid thermal anneal (850˚C), and then the CeYIG growth (650˚C). From the point of view of integration with other on-chip optical components, it is important to minimize the thermal budget of the film deposition and annealing processes. In the second part of section 3.1.2, the structural, magnetic and magnetooptical performance of YIG and CeYIG are presented when these films were grown

under conditions that minimize the thermal budget of each of the three process steps, to produce CeYIG/YIG bilayers on SOI. The Faraday rotation angle, refractive index, extinction coefficient and FOM of polycrystalline YIG and CeYIG are reported and compared with data from single crystal films.

The films were deposited using PLD and specific for this study, the distance between the target and the substrate was 60 mm. Specific for this study, the targets were also polished by sandpaper before each deposition because the laser erosion caused changes in the surface target composition. The YIG films were deposited on SOI substrates that have Si (220 nm)/ SiO_2 (3 μm)/Si (0.4 mm), where the parentheses show the thicknesses, at 100°C in 1.5 × 10^{-6} Torr without any added gas flow. This condition was chosen to minimize the thermal budget of the YIG deposition step because as-deposited films were amorphous, regardless of whether the substrate temperature was at 550°C or 100°C, with or without oxygen. The deposition rate was ~1.2 nm·min^{-1} to form a 350 nm thick YIG film on the SOI substrate.

The YIG films were then annealed using RTA at various temperatures for 3 minutes in 5 standard liters per minute (slpm) oxygen flow. The substrate temperature was rapidly ramped from room temperature (RT, 25 ˚C) to 800 °C within 30 s, held for 3 minutes, and decreased to RT within 4 minutes.

CeYIG films were then deposited onto rapid thermal annealed-YIG seed layers of various thicknesses. CeYIG was grown on the seed layer at the same condition described in Ref. [32] (at 650°C in 20 mTorr oxygen). The deposition rate of CeYIG was ~3.0 nm·min^{-1} to form a ~150 nm thick CeYIG film. The set of samples can be described as CeYIG (150 nm)/ YIG (6–136 nm)/Si substrate.

The crystalline structure of the deposited and annealed films was analyzed by XRD in ω-2θ mode. To eliminate the substrate diffraction peaks, the substrates were tilted by 1 degree during measurement as in the previous part. The composition of a thicker deposited film measured by

energy dispersive x-ray spectrometer (EDS, FEI/Philips XL30 FEG ESEM) was $Ce_{0.96\pm0.03}Y_{1.99\pm0.03}Fe_5O_{12.05\pm0.12}$, *i.e.* comparable to Ce in the target.

In addition to SOI substrates, the Ce:YIG/YIG bilayers were grown on double side polished Si for Faraday rotation measurements. In addition, optical and near infrared transmission spectra of the films were measured using a spectrophotometer. The surface roughness of a film consisting of SOI substrate/YIG (31 nm)/CeYIG (147 nm) was characterized with atomic force microscopy (AFM, Digital instruments Nanoscope). The Faraday rotation hysteresis loops of the garnet films were measured as a function of applied magnetic field at $\lambda = 1550$ nm with the oscillating polarizer method described in Ref. [53], with the field and the laser beam both perpendicular to the film plane. All characterizations were carried out at ambient temperature (25˚C).

Fig. 3-16 shows the XRD data for a set of YIG film with thickness of 349 nm, for different RTA temperatures. Phase-pure polycrystalline YIG was obtained when the films were annealed at more than 800°C for 3 minutes. The film annealed at 750°C showed peaks from hematite (Fe_2O_3) which can contribute large optical losses. There are no crystalline peaks from samples annealed below 700°C. These patterns suggest that the most appropriate annealing condition to crystallize the YIG of this thickness was 800°C for 3 minutes.

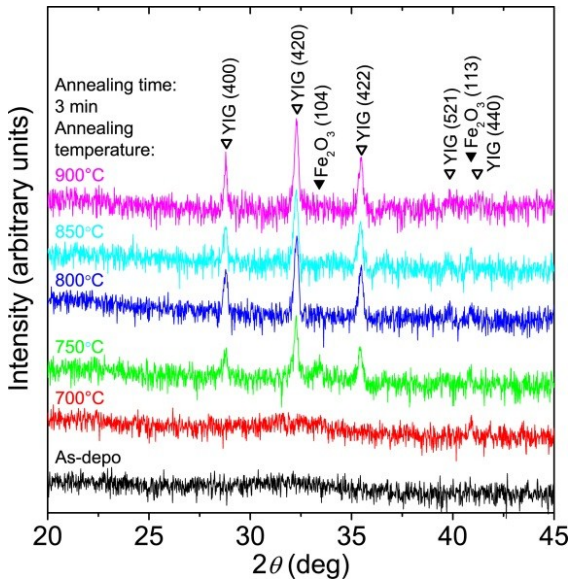

Fig. 3-16. XRD patterns of the samples of Si substrate/YIG (349 nm) annealed at various temperatures for 3 minutes. White triangles show the locations of peaks from the reference powder pattern of $Y_3Fe_5O_{12}$, while black triangles show hematite peaks.

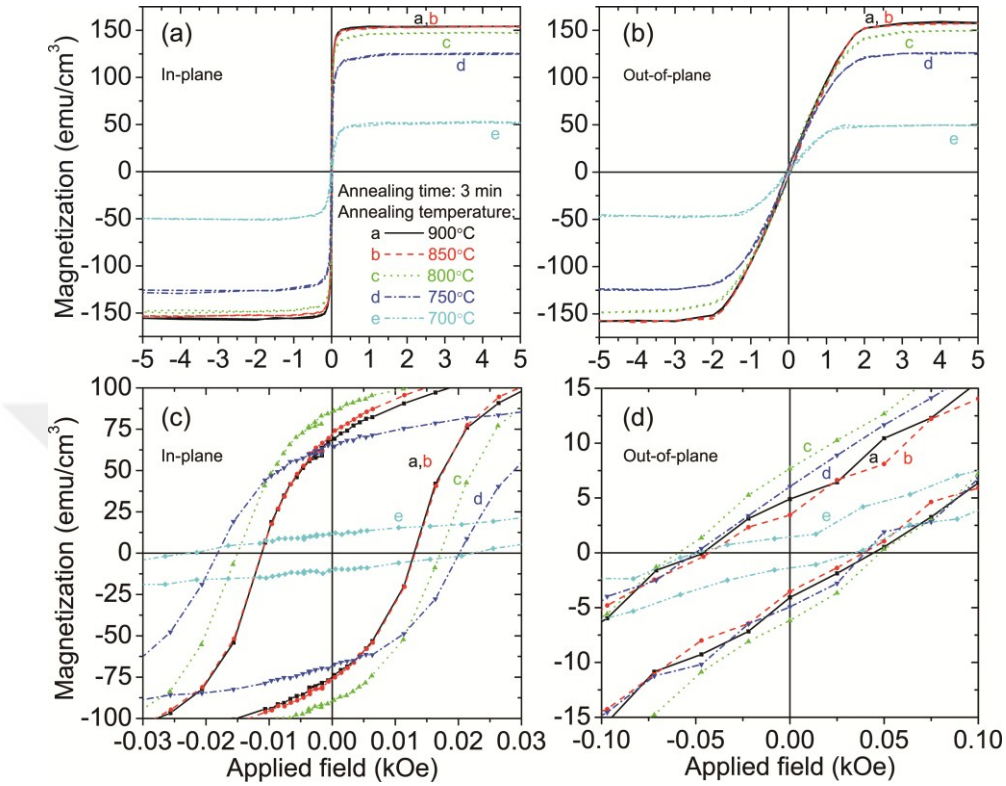

Fig. 3-17. Hysteresis loops of the samples of SOI substrate/YIG (349 nm) after RTA at various temperatures for 3 minutes. (a) and (c) are IP, (b) and (d) are OP loops. (c) and (d) are enlarged portions of (a) and (b), respectively around origin.

The different RTA temperatures also affected magnetic properties measured using VSM, as shown on Fig. 3-17. The 349 nm-thick YIG films showed in-plane magnetization with a saturation magnetization of 154 emu/cm^3 at RT (close to the value for single crystal YIG) and a hard-axis saturation field of 1.5 - 2.0 kOe. Comparing with the calculated shape anisotropy field of $4\pi M_s$ = 1.93 kOe shows that shape anisotropy was the dominant source of anisotropy in these films. The coercivity of ~15 Oe is small and comparable to that of single crystal films [29].

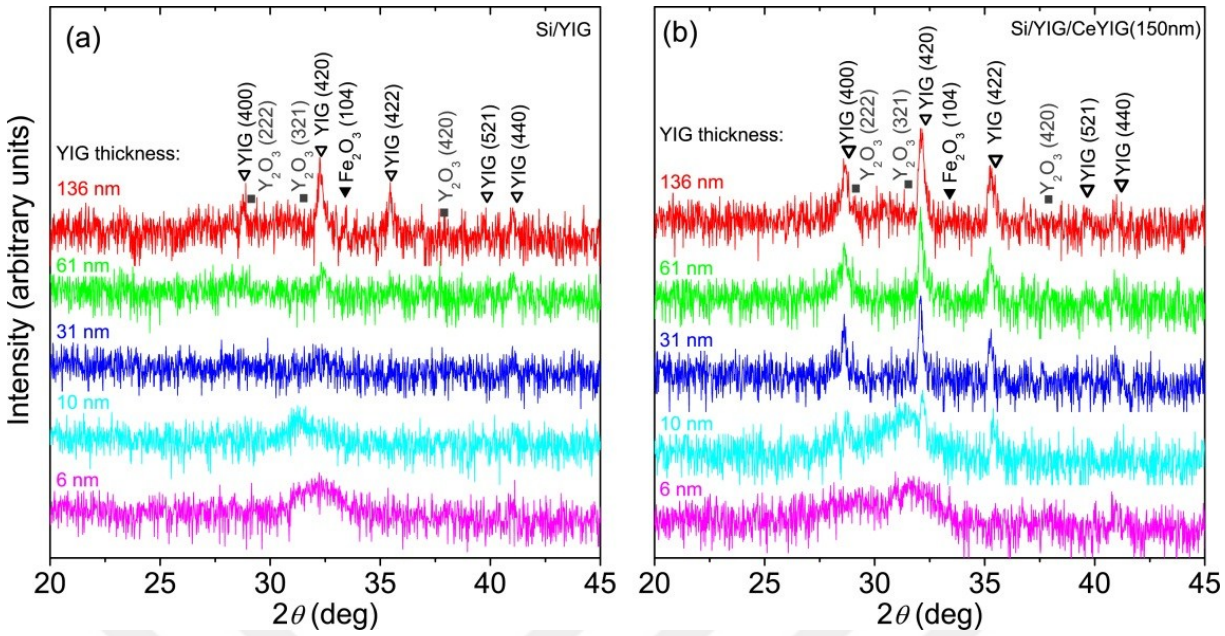

Fig. 3-18. XRD patterns of (a) the Si substrate/YIG films and (b) Si substrate/YIG/Ce:YIG. Thicknesses of the YIG layers were varied from 6–136 nm, and the thickness of Ce:YIG was fixed at about 150 nm.

Fig. 3-18 shows XRD data for YIG of various thicknesses after annealing at 800°C for 3 minutes. For YIG films with 31 nm thickness and films thinner than 31 nm, there are broad peaks indicating amorphous or nanocrystalline phases. Above 31 nm, garnet peaks are evident.

In the YIG/Ce:YIG bilayer, since the role of the YIG is to provide a crystallographic seed for the Ce:YIG, YIG structure is more critical than its magnetic properties. An annealing condition at 800°C for 3 minutes was used for the growth of the YIG seed layer in the bilayer films, since this temperature produced only garnet phases in the thicker YIG films.

XRD data for bilayers of Si substrate/YIG (6–136 nm)/Ce:YIG (~150 nm) are given in Fig. 3-19(b). Garnet peaks were apparent in Ce:YIG when the YIG thickness was 10 nm and higher. When the YIG thickness was 6 nm, peaks from yttrium oxide were visible, though the intensity was low. These results suggest that a YIG seed layer thickness of at least 10 nm was needed to promote the growth of garnet phase Ce:YIG on a Si substrate. Similar behavior was observed on the SOI substrates. The out of plane lattice constant of the Ce:YIG grown on the 31 nm thick YIG was 12.53±0.04 Å, which is slightly larger than the lattice parameter of the 136 nm thick YIG (12.51±0.03 Å).

Fig. 3-19 shows the magnetic hysteresis loops of YIG of different thickness after the 800˚C RTA. Films of 61 nm and above gave loops similar to the 349 nm thick film of Fig. 3-17, with 150 emu/cm^3 saturation magnetization, similar to bulk values. As the film thickness decreased, M_s decreased as well.

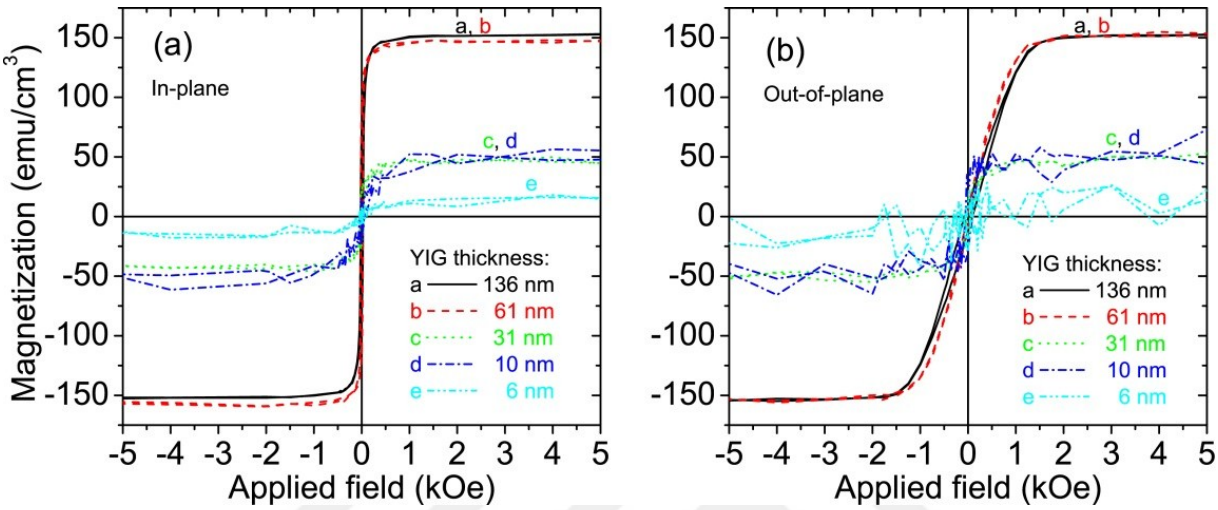

Fig. 3-19. Hysteresis loops of Si substrate/YIG with various thicknesses. The samples were annealed at 800°C for 3 minutes in 5 slpm oxygen flow. (a) IP and (b) OP magnetic hysteresis loops.

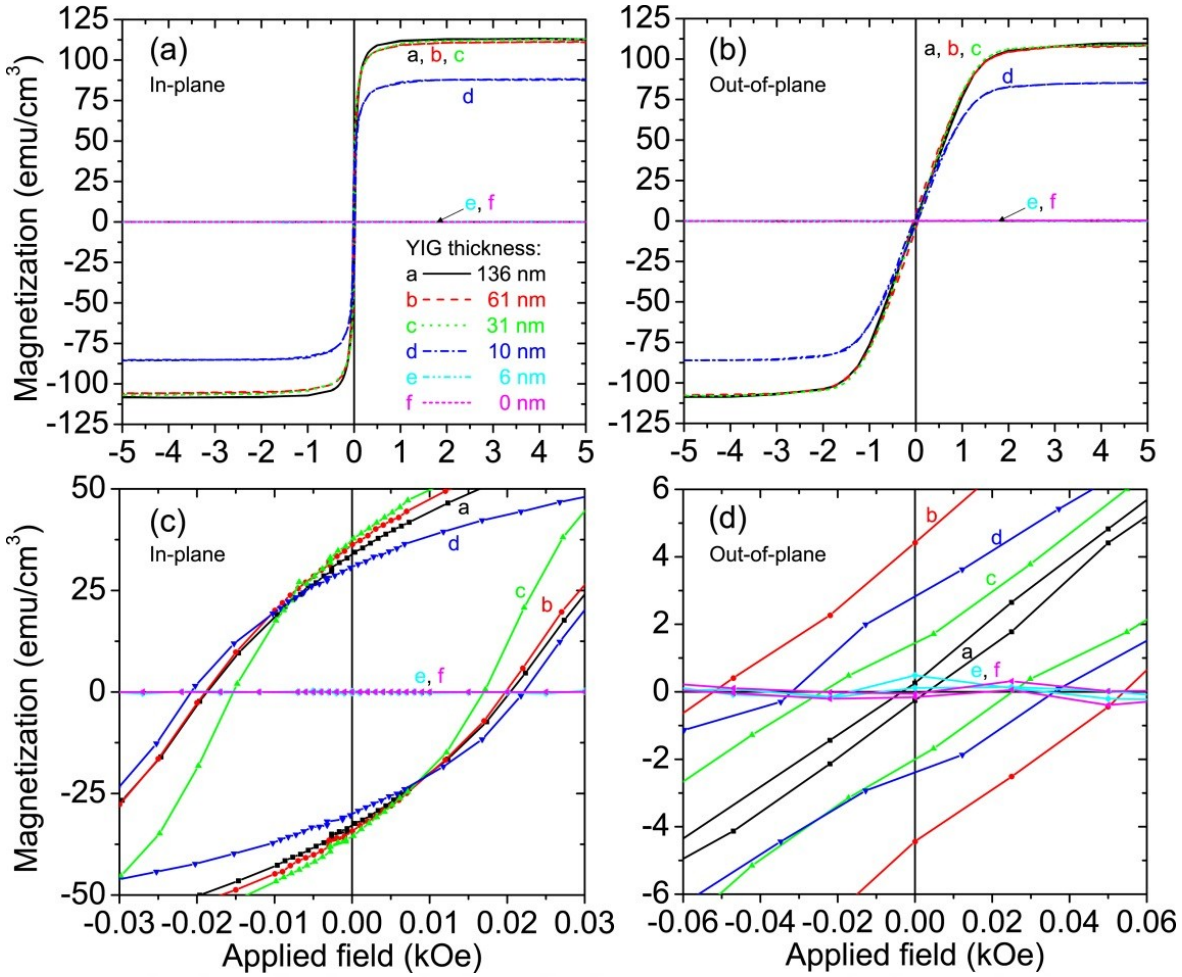

Fig. 3-20. (a) IP and (b) OP magnetic hysteresis loops of Si substrate/YIG/Ce:YIG (~150 nm) with various thickness of the YIG layer at RT. (c) and (d) are enlarged figures of (a) and (b), respectively.

Fig. 3-20 shows the magnetic hysteresis loops of the YIG/CeYIG, with the substrate and YIG contributions subtracted. The CeYIG saturation magnetization for YIG thickness of 31 nm reached 110 emu/cm^3, slightly below the value of 120 emu/cm^3 obtained for other Ce:YIG films [31].

Transmission spectra are given in Fig. 3-21. Since YIG films have a lower refractive index than the Si substrates, YIG films had antireflection effect on Si substrates. The YIG/Si samples therefore had a lower reflection and higher transmissivity compared to uncoated Si substrates, as shown on Fig. 3-21 (a). The Ce:YIG films however, had higher optical loss and lowered the transmissivity, as shown on Fig. 3-21 (b).

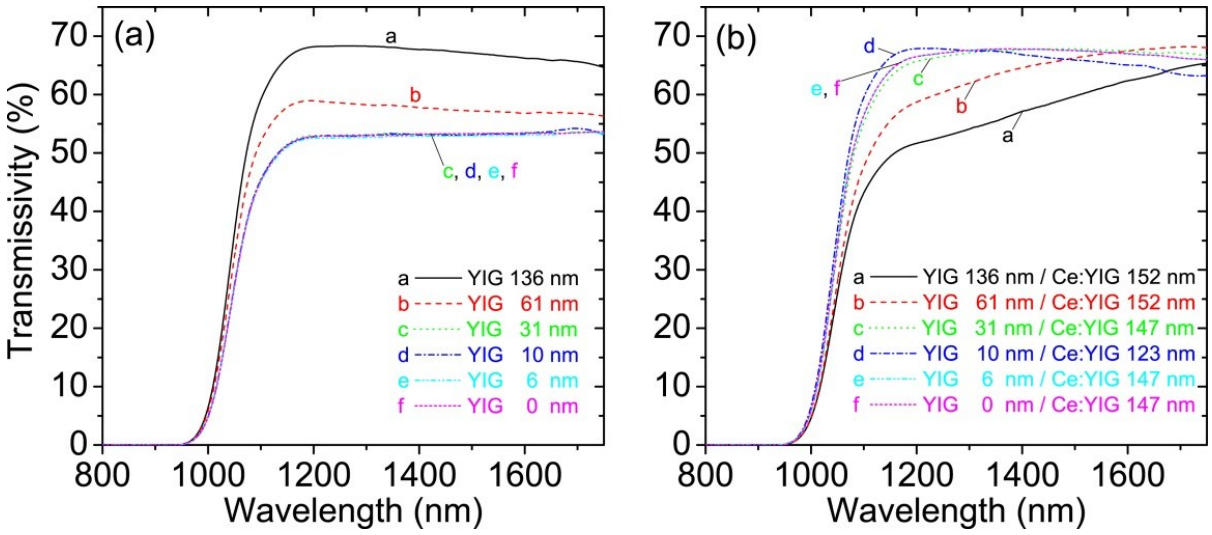

Fig. 3-21. Transmission spectra of (a) Si substrate/YIG and (b) Si substrate/YIG/Ce:YIG with various YIG film thicknesses.

Conventional Fresnel equations were used to extract the refractive indices and extinction coefficients of the Si substrate, YIG layer, and CeYIG layer from the spectra on Fig. 3-21. A thicker CeYIG film showed oscillations in the transmissivity enabling an accurate determination of optical parameters. The refractive indices and extinction coefficients at a wavelength 1550 nm are compared to values reported for bulk Si and for single crystal YIG and CeYIG grown on garnet substrates on Table 3-1. The indices show little variation with the thickness of the films. The extinction coefficient of YIG is relatively small, so a YIG seed layer does not contribute significantly to optical losses in a device.

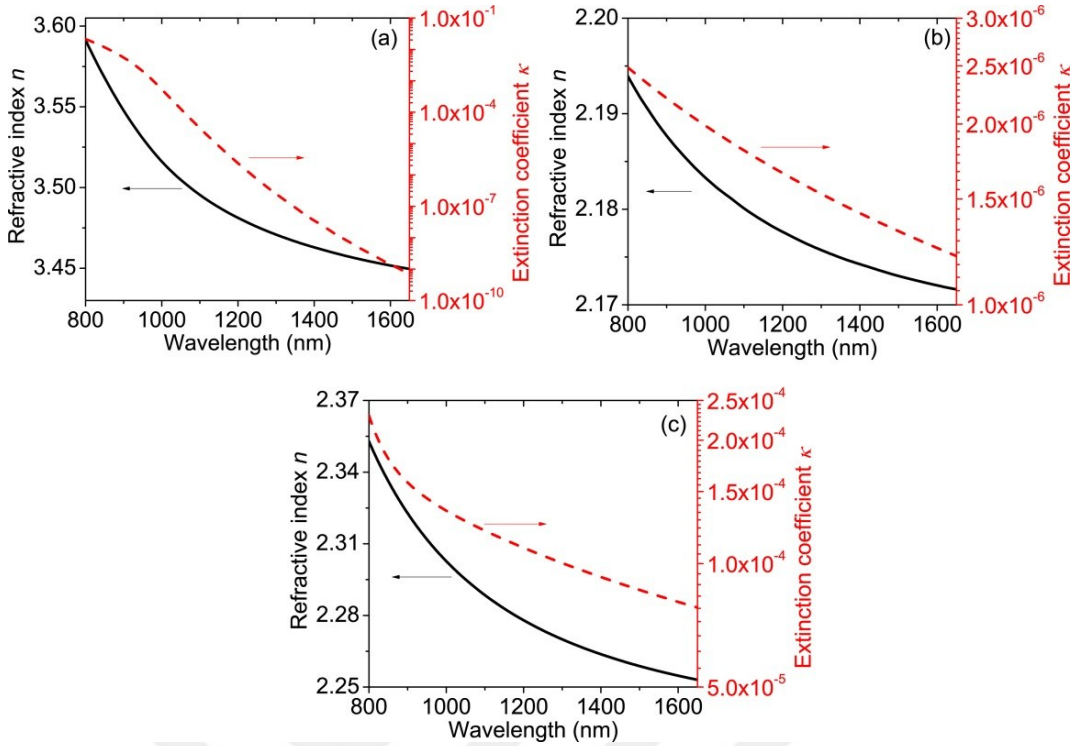

Fig. 3-22. Refractive index and extinction coefficient spectra of (a) Si substrate, (b) YIG layer and (c) and CeYIG layer derived from the transmission spectra shown in Fig. 3-21. (spectral fits were done by Prof. Taichi Goto)

Table 3-1. Refractive indices and extinction coefficients of deposited films and single crystals at the wavelength of $\lambda = 1550$ nm at room temperature.

Material	Refractive index n	Extinction coefficient k
Si substrate [54]	3.48	–
Si substrate, this study	3.45	2.9×10^{-9}
Single crystalline YIG on garnet substrate [55]	2.17	1.9×10^{-6}
Polycrystalline YIG on Si substrate, this study	2.17	1.3×10^{-6}
Single crystalline CeYIG on garnet substrate [32]	2.21	2.8×10^{-5}
Polycrystalline CeYIG on Si substrate, this study	2.25	8.3×10^{-5}

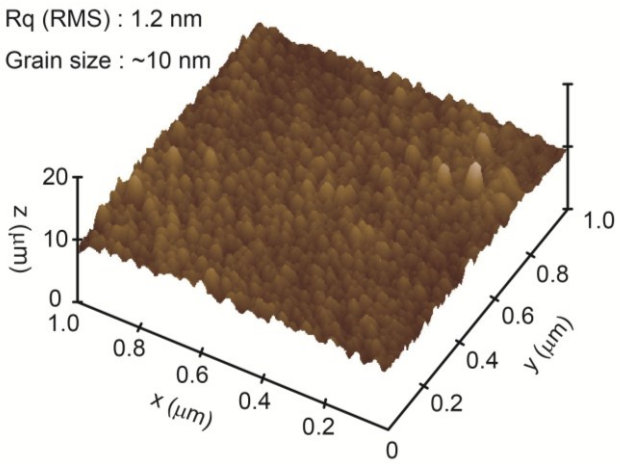

Fig. 3-23. AFM surface profile of Ce:YIG(147 nm)/YIG (31 nm)/SOI substrate over 1x1μm^2 area. (AFM imaging done by Prof. Taichi Goto)

Fig. 3-23 shows a 3D atomic force microscope (AFM) image of Ce:YIG (147 nm)/ YIG (31 nm) on SOI substrate. The grain sizes were found to be ~ 10 nm with an RMS roughess of 1.2 nm. The smooth surface is important in optical devices to reduce scattering.

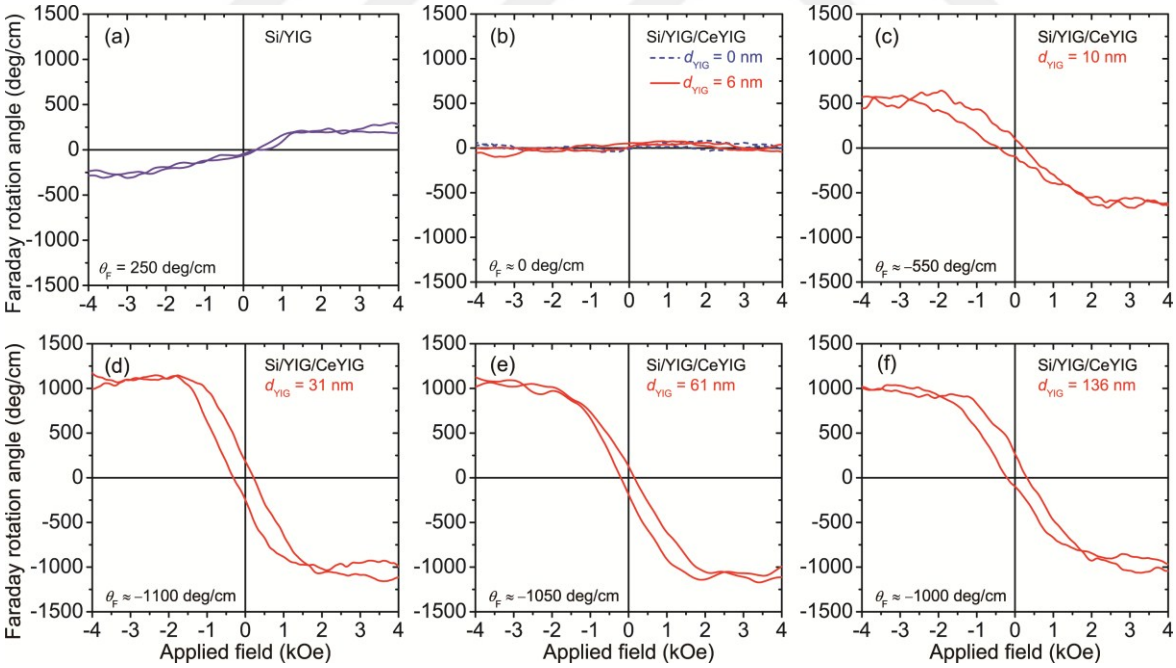

Fig. 3-24. Faraday rotation hysteresis loops of (a) YIG on Si (b-f) Ce:YIG/YIG/Si films with the indicated YIG thicknesses d_{YIG}. The loops were measured at λ = 1550 nm and at RT.

The saturation Faraday rotation of the YIG layer on Si was ~250 °·cm^{-1} at 1550 nm wavelength, Fig. 3-24 (a). This magnitude is similar to single crystal values (273 °·cm^{-1} at

λ = 1100 nm in Ref. [36], 250 °·cm^{-1} at λ = 1150 nm in Ref. [56]). The Faraday loops for the Ce:YIG/YIG bilayers are given on the same figure (after subtracting the substrate contributions). The Ce:YIG films have opposite sign of Faraday rotation than does YIG. The Faraday loops also have the same hard-axis shape as the OP magnetization loops. The bilayer has a maximum Faraday rotation of –1100 °·cm^{-1} when YIG thickness is 31 nm. The Faraday rotation angle was smaller than that of single crystals, which may be a result of defects or the presence of Ce^{4+}, which is a more stable state than Ce^{3+} and does not contribute to the enhancement in Faraday rotation. Since the garnet films are polycrystalline, partial crystallization and grain boundary scattering also contribute to reduced Faraday rotation and higher optical absorption with respect to the Faraday rotation of bulk or epitaxial thin film MO garnet crystals.

From the extinction coefficient and Faraday rotation, one can obtain a magnetooptical figure of merit which describes the quality of the MO material for non-reciprocal devices in photonic integrated circuits. Here, the figure of merit is defined as Faraday rotation angle/extinction coefficient (deg/cm) or loss (deg/dB). Table 3-2 shows the figure of merit of two-step-deposited CeYIG on Si substrate/YIG seed layer compared to single crystalline CeYIG on a garnet substrate, as well as to the earlier data for CeYIG on YIG deposited at higher temperatures [1].

Table 3-2. Figure of merit of polycrystalline Ce:YIG on non-garnet substrates and single crystalline CeYIG on garnet substrates (λ = 1550 nm, at RT)

Material	Faraday rotation θ_F (deg/cm)	Optical loss		Figure of merit	
		k [a]	α (dB/cm)[b]	$\lvert\theta_F/k\rvert$ (deg/cm)	$\lvert\theta_F/\alpha\rvert$ (deg/dB)
Single crystalline CeYIG on garnet substrate [32]	–3300	2.8×10^{-5}	9.7	1.2×10^{8}	340
Single crystalline epitaxial Ce:YIG on GGG substrates (previous section)	-5800	10^{-5}	1.5	5.75×10^{8}	379-401
Polycrystalline CeYIG on YIG deposited at 550°C on Si substrate [3]	–800	1.1×10^{-4}	40	7.8×10^{6}	20
Polycrystalline CeYIG on YIG deposited at 100°C on Si substrate, this study	–1100	8.3×10^{-5}	29	1.3×10^{7}	38

[a]Extinction coefficient k.

[b]Absorption coefficient α (dB/cm) = $10\times\log_{10}(-4\pi k \times 0.01 / \lambda)$

Two-step-deposited Ce:YIG demonstrates one order of magnitude smaller figure of merit than single crystalline epitaxial Ce:YIG films on GGG substrates. This indicates that there is a significant room for improvement of Faraday rotation and optical transmission of the Ce:YIG films on Si. In order to improve Faraday rotation, a more efficient garnet crystallization method other than RTA (such as laser annealing) can be used. By improving long range crystallinity in Ce:YIG, one can also reduce optical scattering losses due to grain boundaries or amorphous regions of garnet. Improved long range crystallinity also reduces Ce^{4+} fraction (which is responsible for higher absorption and reduced Faraday rotation [57]). Despite these limitations, the polycrystalline Ce:YIG film is still a good material for integrated MO devices. Comparing the FOM with, The Ce:YIG films presented in this section have superior figure of merit than

that of polycrystalline CeYIG on YIG deposited at the higher temperature [1], even though the films discussed in this section were deposited with a lower total thermal budget.

The growth study presented in this section demonstrates that a reduced thermal budget for growth can be used to achieve good enough MO figure of merit for integrated nonreciprocal photonic devices. A YIG seed layer with optimized thickness grown using PLD at 100ºC and with optimized rapid thermal annealing temperature serves as a crystallographic template for good quality MO Ce:YIG films on Si or SOI substrates. The YIG films initially grown at were amorphous, but RTA at 800ºC for 3 minutes in 5 slpm oxygen crystallized the films into pure garnet phases. The magnetic properties, refractive index, extinction coefficient and Faraday rotation angle of the YIG films are comparable to single crystal YIG.

Polycrystalline Ce:YIG films grown at 650ºC the (30 nm or thicker) YIG seed layers exhibited Faraday rotation higher than that for YIG and with opposite sign. The optical absorption, saturation magnetization and Faraday rotation angle were not as high as those for single crystal values. The figure of merit was 38 deg/dB, about 10x less than that of single crystal CeYIG. One can further enhance the Ce:YIG figure of merit by enhancing crystallization efficiency and long range order. Increasing grain sizes can reduce grain boundary scattering. Larger grains with smaller uncrystallized fractions of garnet are going to yield a reduced overall optical absorption.

These results enable formation of functional Ce:YIG on non-garnet substrates for integrated device demonstrations. This two-step deposition process can provide a route to monolithic integration of MO devices while reducing the thermal budget of the process.

3.1.3 Comparison of magneto-optical properties of garnet films

The optical and magneto-optical properties of YIG-based garnets studied in the first half of Chapter 3 and in the literature are presented and compared on Table 3-3. Epitaxial thin film MO garnets achieve 379-401°·dB^{-1} figure of merit, while polycrystalline garnet films reach 20-56°·dB^{-1}. The loss of the polycrystalline films are typically one order of magnitude higher than the loss of the epitaxial films. These losses are attributed to partial crystallization of garnets on nongarnet substrates, grain boundary scattering, growth-induced losses due to oxygen deficiency of garnets.

Table 3-3. Comparison of MO figure-of-merit values for polycrystalline Ce:YIG on non-garnet substrates, single crystalline Ce:YIG on garnet substrates (λ = 1550 nm, at RT) and bulk Ce:YIG garnets and semiconductors.

MO Material and Substrate [Reference]	MO Figure-of-merit (°·dB^{-1})	Refractive index (n)	Extinction coefficient (k)	Faraday rotation (°·cm^{-1})	Optical Loss (dB·cm^{-1})
$Y_{2.82}Ce_{0.18}Fe_5O_{12}$ (no substrate, bulk crystal) [58]	1420	(Not available)	1.48e-6	-740	0.12
Single crystalline epitaxial Ce:YIG on GGG substrates [this thesis, part 3.1.1]	379, 380, 401	2.26	1e-5	-5800	1.5
Single crystalline CeYIG on $Gd_3Sc_2Ga_3O_{12}$ [32]	340	2.21	1.7e-5*	-3300	5.8
$Ce_1Y_2Fe_5O_{12}$ on (111) doped-$Gd_3Ga_5O_{12}$ [59]	321	(Not available)	1e-5	-4500	14
Polycrystalline CeYIG on YIG deposited at 550°C on Si substrate [3]	20	(Not available)	1.1e-4	-800	40
Polycrystalline CeYIG on YIG deposited at 100°C on Si substrate [5]	38	2.17	8.3e-5	-1100	29
$Ce_1Y_2Fe_5O_{12}$ (Ce:YIG) on Silica [22]	56	2.3	1.5e-5	-2700	48
Ce:YIG on Si [1]	21.8	2.2	(not available)	-1263	58
Fe:InP [60]	27.1	(not available)	(not available)	1485	54.8
Fe:InGaAsP [61]	23	(not available)	1.23e-5	100	4.34

*Optical loss was presented as 5.8 dB/cm for 0.5 μm-thick film. Extinction coefficient was calculated using: Opt. loss (dB/cm) $=-10\times\log_{10}(\exp(-4\pi k/\lambda_0\times t))$, where t is the propagation distance or film thickness

3.2 YIG top seed layer and magneto-optical isolator demonstrations

3.2.1 YIG top seed layer

In this part, we focus on growing Ce:YIG directly on top of Si waveguides using a YIG seed layer from the top of Ce:YIG. In the second part (3.2.2), we apply this growth method to demonstrate a promising example of an integrated MO isolator using Ce:YIG. Garnet growth methods have been developed by Xueyin Sun and Mehmet Onbasli. Device fabrication has been done by Prof. Taichi Goto. Device characterization has been done by Qingyang Du. There have been several demonstrations of on-chip optical isolators made out of Ce:YIG by several groups [4,5,6,13,63,64]. While these demonstrations represent an important step towards on-chip optical isolation, it is mandatory that both MO material/device integration technology and MO film quality (in terms of MO figure of merit) are further improved to fulfill the demanding requirements of photonic integration.

As presented previously in this chapter, on-chip integration of YIG and Ce:YIG materials has been challenging because they cannot be grown heteroepitaxially on classical semiconductor substrates. This is because of the large thermal budget required for garnet growth as well as lattice and thermal expansion coefficient (CTE) mismatch between garnets and common semiconductors. Due to the large CTE mismatch, a low growth temperature is desired in order to prevent garnet film cracking. A reduced thermal budget is also critical to on-chip device integration. YIG and substituted garnet films have been integrated on photonic substrates using wafer bonding,[13] metal-organic chemical vapor deposition (MOCVD),[7] sputtering [15-22] and pulsed laser deposition (PLD) [1,2,3,5,29,48,49]. Wafer bonding capitalizes on the excellent MO properties of single crystal bulk garnet. This hybrid integration approach, however, adds to processing complexity and reduces throughput. The other methods mentioned allow monolithic integration of garnets on semiconductors, despite the fact that the resulting films suffer from reduced MO figure of merit compared to bulk garnet. As presented in section 3.1.2, a two-step PLD growth method was demonstrated in which a thin YIG buffer layer was grown then crystallized by rapid thermal annealing

(RTA), serving as a seed layer for subsequent growth of polycrystalline Ce:YIG on Si and silica.[1,5] On silicon nitride, slow growth of the YIG seed layer improved the magnetic properties and Faraday rotation of Ce:YIG grown on top of it.[6] Sputtering was also used to grow garnets in a similar two-step process in which a YIG layer was deposited, annealed and utilized as a seed layer for Ce:YIG or Bi:YIG growth.[65]

In this section, a PLD growth method is demonstrated for making Ce:YIG films on a variety of substrates (Si, quartz, GGG) in which the YIG layer this time acts as an *in situ* seed layer for Ce:YIG *during* the crystallization of both YIG and Ce:YIG. Layers of both YIG and Ce:YIG are deposited in one PLD step followed by an anneal. Crystallization of the Ce:YIG during RTA is facilitated by YIG layer(s) on top or at the bottom of the stack. This simplification reduces the thermal budget and increases throughput by reducing the number of PLD steps from two to one and also yields films with good magnetic and MO properties. From photonic device design point of view, this simplification actually has an other advantage: A YIG overlayer can promote Ce:YIG crystallization from the top as well as a conventional YIG underlayer enables Ce:YIG to be grown directly on a waveguide. By having the YIG seed layer crystallize Ce:YIG from the top, one can grow Ce:YIG directly on the silicon waveguide, maximize MO phase shift accumulated on the guided light and avoid the spacing loss caused by a weakly magnetooptical YIG underlayer. An integrated optical isolator device with improved performance characteristics is demonstrated using this approach in this section.

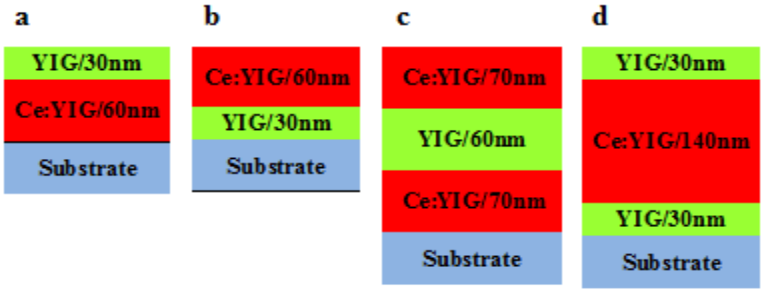

Fig. 3-25. Pulsed laser deposition sequence schematic of the films on different substrates (Si, quartz and GGG) made with one-step deposition followed by annealing. (a), (b) two-layer garnet film with 90 nm

total thickness; (c), (d) three-layer garnet films with 200 nm thickness.

Fig. 3-25 shows the layer structures of the Ce:YIG and YIG samples prepared on (001) silicon (Si) and Z-cut (0001) quartz (Qz) using PLD, followed by annealing. Identical layer sequences were also grown on (100) GGG substrates as references. The films were deposited on (001) Si, (100) GGG, Z-cut quartz (0001) substrates and silicon-on-insulator waveguides using pulsed laser deposition (PLD) at 10 Hz repetition rate, fluence of 2 J cm^{-2}, at substrate temperature at 650°C throughout the deposition, target-substrate distance of 6 cm, and an oxygen pressure of 25 mTorr during growth (5×10^{-6} Torr base pressure). Specific to this

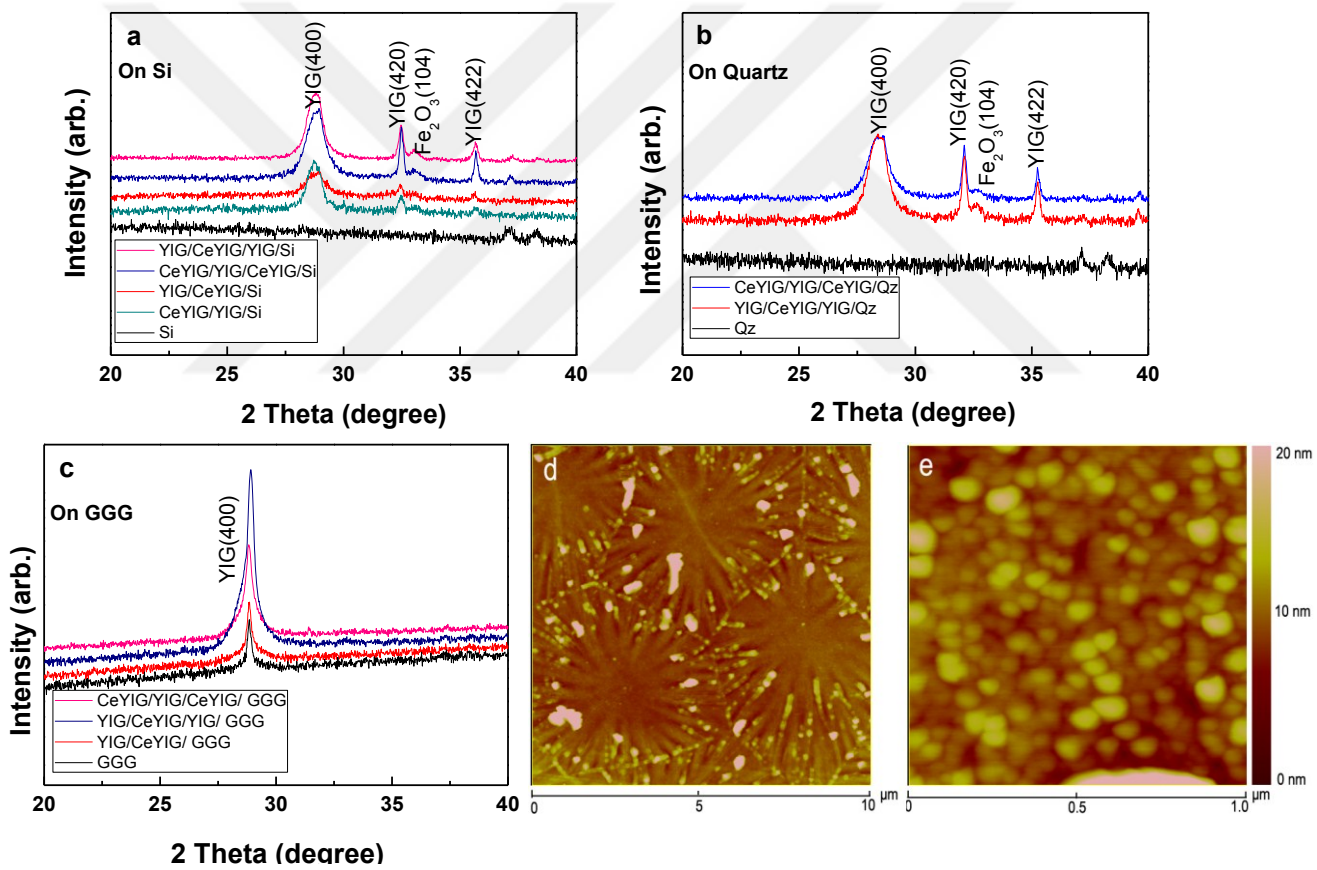

project, the samples were kept after deposition at 650°C for 15 min at 500 Torr oxygen pressure, and then cooled to 200°C at a ramping rate of 5°C min^{-1} under 500 Torr oxygen pressure. The films were subsequently rapid thermal annealed (Modular Process Tech, RTP-600S) at 800°C for 5 min.

Fig. 3-26. (a), (b) XRD ω-2θ scans for the garnet films on (a) Si, (b) quartz; (c) XRD ω-2θ scans for the films on GGG (100) substrates; (d), (e) AFM images of (d) YIG/Ce:YIG/Si, 10 × 10 μm^2 area and (e)

Ce:YIG/YIG/Si, 1 × 1 μm^2 area. All films were rapid thermal annealed.

Fig. 3-26 shows the XRD diffraction patterns for the bilayer YIG/Ce:YIG/substrate and Ce:YIG/YIG/substrate (total film thickness: 90 nm) and trilayer YIG/Ce:YIG/YIG and Ce:YIG/YIG/Ce:YIG (total film thickness: 200 nm), after RTA[19] at 800°C for 5 minutes. The YIG (400) peak has the highest intensity among all peaks of the films films as shown on Fig. 3-26(a) and (b). Based on the powder diffraction peak intensities, the films have a preferred (100) orientation. The OP lattice constant of the films are 12.39 Å, similar to that of YIG films (12.38 Å) [1]. The weak peak at 33.1˚ ± 0.05˚ for films on Si and Qz is attributed to antiferromagnetic hematite, α-Fe_2O_3 [5]. The XRD ω-2θ patterns for the films grown and rapid thermal annealed on GGG are shown on Fig. 3-26(c). The garnet films on GGG are epitaxial single-crystals for all layer sequences without any secondary phases.

Fig. 3-26 (d) and (e) show the surface topography for YIG/Ce:YIG/Si and Ce:YIG/YIG/Si, respectively. For the YIG/Ce:YIG/Si the grain size at the top surface was up to 5 μm, and the grains showed a radiating pattern, consistent with the grain sizes and shapes found for garnet films on Si_3N_4, Fig. 3-11(e). On the other hand, Ce:YIG/YIG/Si has dense topographic features up to ~50 nm wide. Similar large garnet grains have also been seen in single layer YIG grown on other substrates such as diamond (supplied by Prof. Amir Yacoby from Harvard University for another project). Fig. 3-27, 28 and 29 shows the XRD ω-2θ pattern, scanning electron micrograph (SEM) and AFM scan of the surface topography of 50 nm-thick YIG film on diamond grown with a similar PLD growth recipe and annealed with RTP. Grains as large as 5-10 μm are observed on both SEM micrographs and AFM images. These large grains are as wide as 5-10 μm on diamond and Si_3N_4. In addition, the circular grain morphologies are similar with outward radial patterns. The radial patterns suggest that the YIG layers first grow as islands and radially outward and then combine.

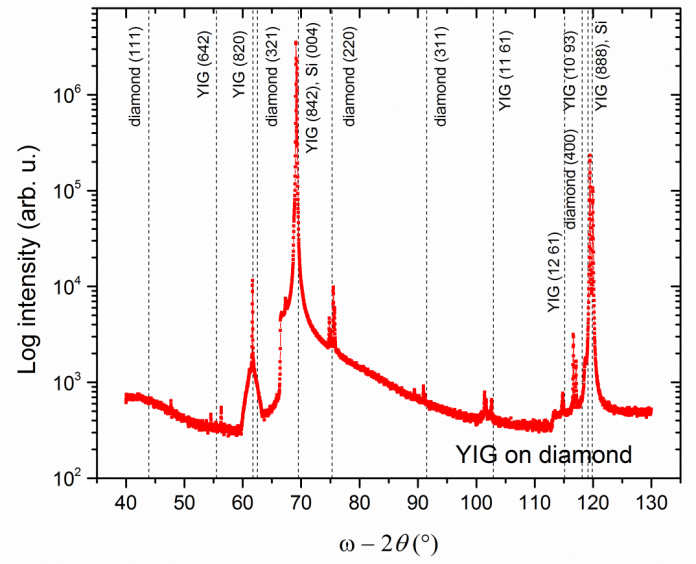

Fig. 3-27. X-ray diffraction pattern of a polycrystalline YIG film crystallized on a diamond substrate (2 × 2 mm^2 × 50 µm) which was mounted on a silicon wafer.

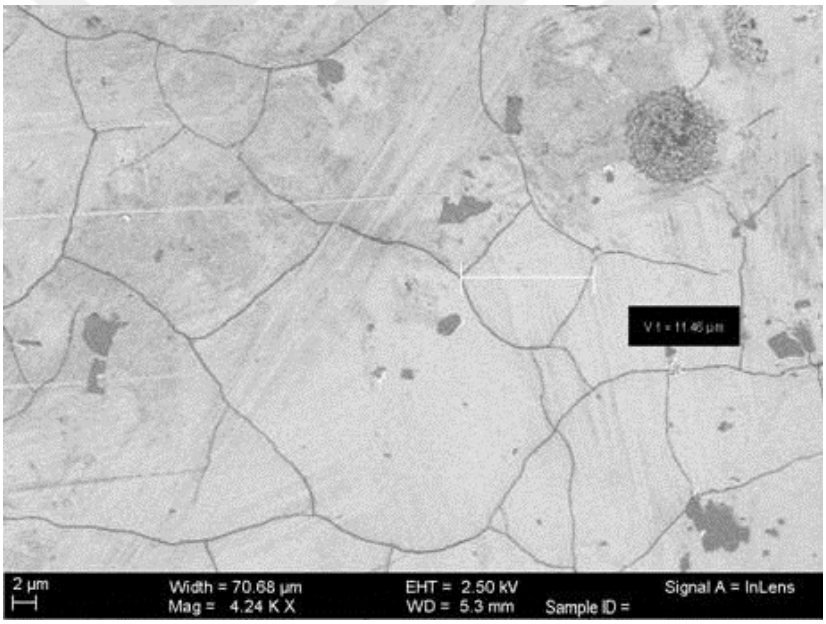

Fig. 3-28. Scanning electron micrographs of YIG (50 nm)/diamond after rapid thermal annealing.

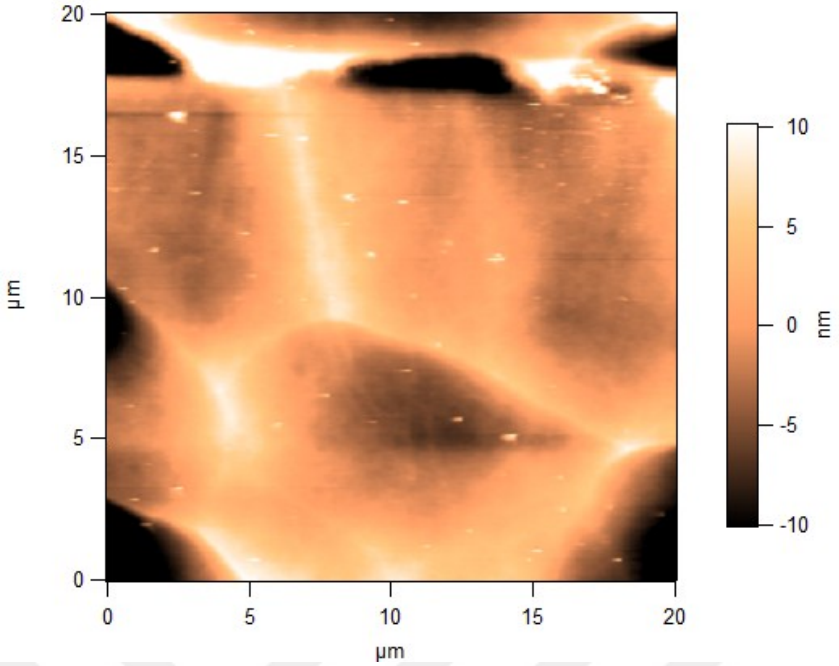

Fig. 3-29. AFM scan of a 50 nm-thick YIG on diamond after rapid thermal annealing. (AFM imaging done by Dr. Huiliang Zhang from Harvard University)

Fig. 3-30 shows the TEM and elemental mapping images of YIG (30nm)/CeYIG (60 nm)/Si (Fig. 3-30(a, c, e)) and YIG (30nm)/CeYIG (60 nm)/YIG (30nm)/Si (Fig. 3-30(b, d, f)). In both samples the grain size in the Ce:YIG layer was less than 20 nm, but the YIG layer consisted of much larger grains, larger than the field of view in Fig. 3-30(a, b). High resolution (HR) TEM images of the interface between the YIG layer and the Ce:YIG layer are shown in Fig. 3-30 (c, d). The orientation of the large YIG grains was (100), while the orientations of the small grains in the Ce:YIG layer varied. Fig. 3-30(e) shows HRTEM images of the interface between film and substrate (silicon with native oxide) for YIG/Ce:YIG/Si. The Ce:YIG layer in contact with the amorphous SiO_x was crystalline, with a ~1 nm thick layer of amorphous Ce:YIG at the interface. In contrast, in the trilayer YIG/Ce:YIG/YIG/Si sample, the YIG in contact with the Si was a large fully crystallized grain with (100) orientation, Fig. 3-30 (f). The elemental map in Fig. 3-30 (g) of the YIG/CeYIG/Si illustrates uniform distribution of Y throughout the layers and localization of Ce in the Ce:YIG layer. Fe, however, showed a less uniform distribution in the Ce:YIG layer than in the YIG.

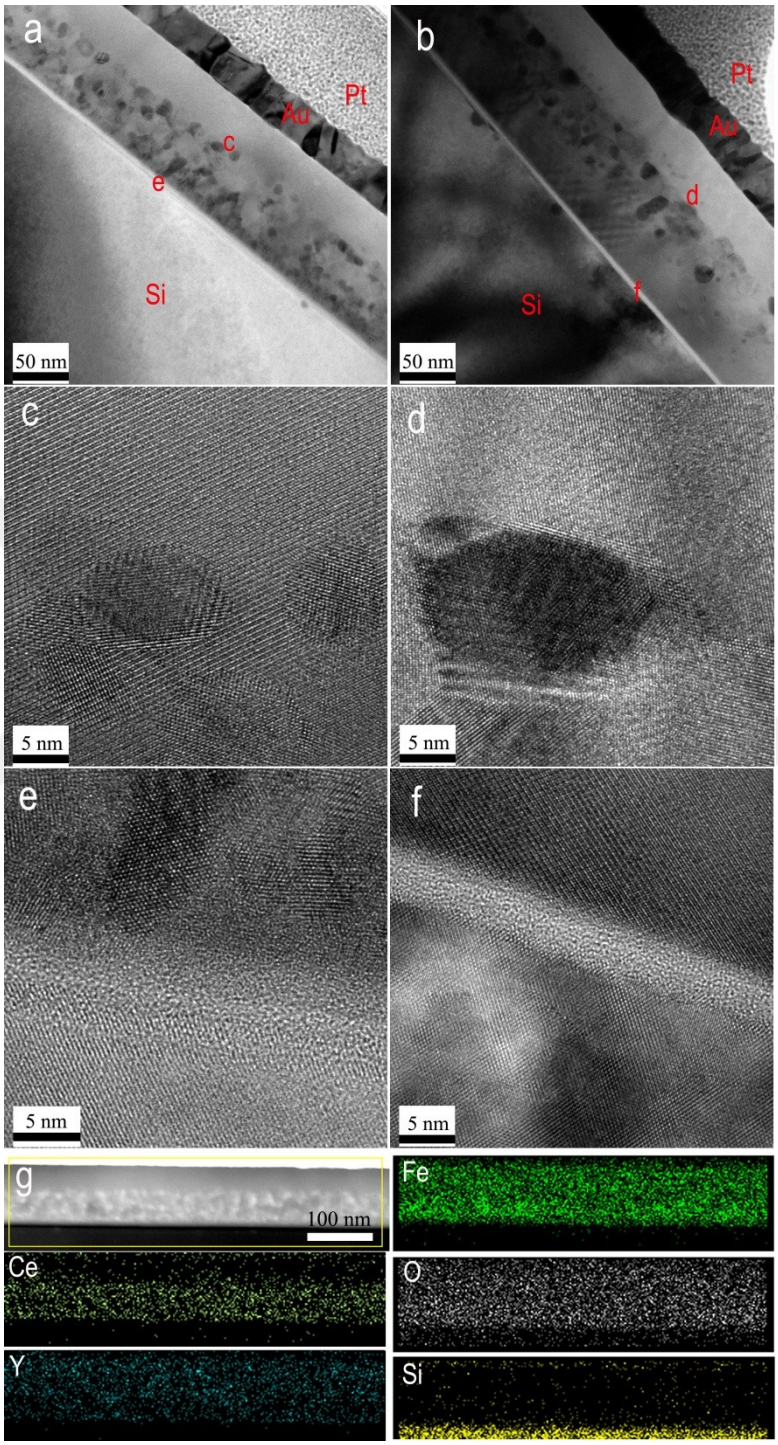

Fig. 3-30. TEM images and element mapping of films on Si. (a, c, e): YIG/Ce:YIG/Si; (b, d, f): YIG/Ce:YIG/YIG/Si (YIG ~30 nm, CeYIG ~60 nm). (a, b) Bright field TEM cross-section images. (c, d) HRTEM images of the interface between the YIG and Ce:YIG layer. (e), (f) HRTEM images of the interface between the substrate (Si) and the films. (g) STEM image and STEM-EDX element mappings of the YIG/Ce:YIG/Si film. (TEM analysis was done by Dr. Xueyin Sun).

Growing a Ce:YIG film directly on Si or Si_3N_4 and annealing under the same conditions did not yield garnet-structured films on non-garnet substrates. Prior work also showed that in the absence of the YIG layer, crystallization of the Ce:YIG layer is impeded [1,5,22,24,65]. The present results extend this result to show that the templating effect of YIG on Ce:YIG growth exists even if both layers are simultaneously crystallized. The YIG is assumed to crystallize first, providing a large-grained layer that promotes crystallization of Ce:YIG, even if the YIG is placed on top of the Ce:YIG.

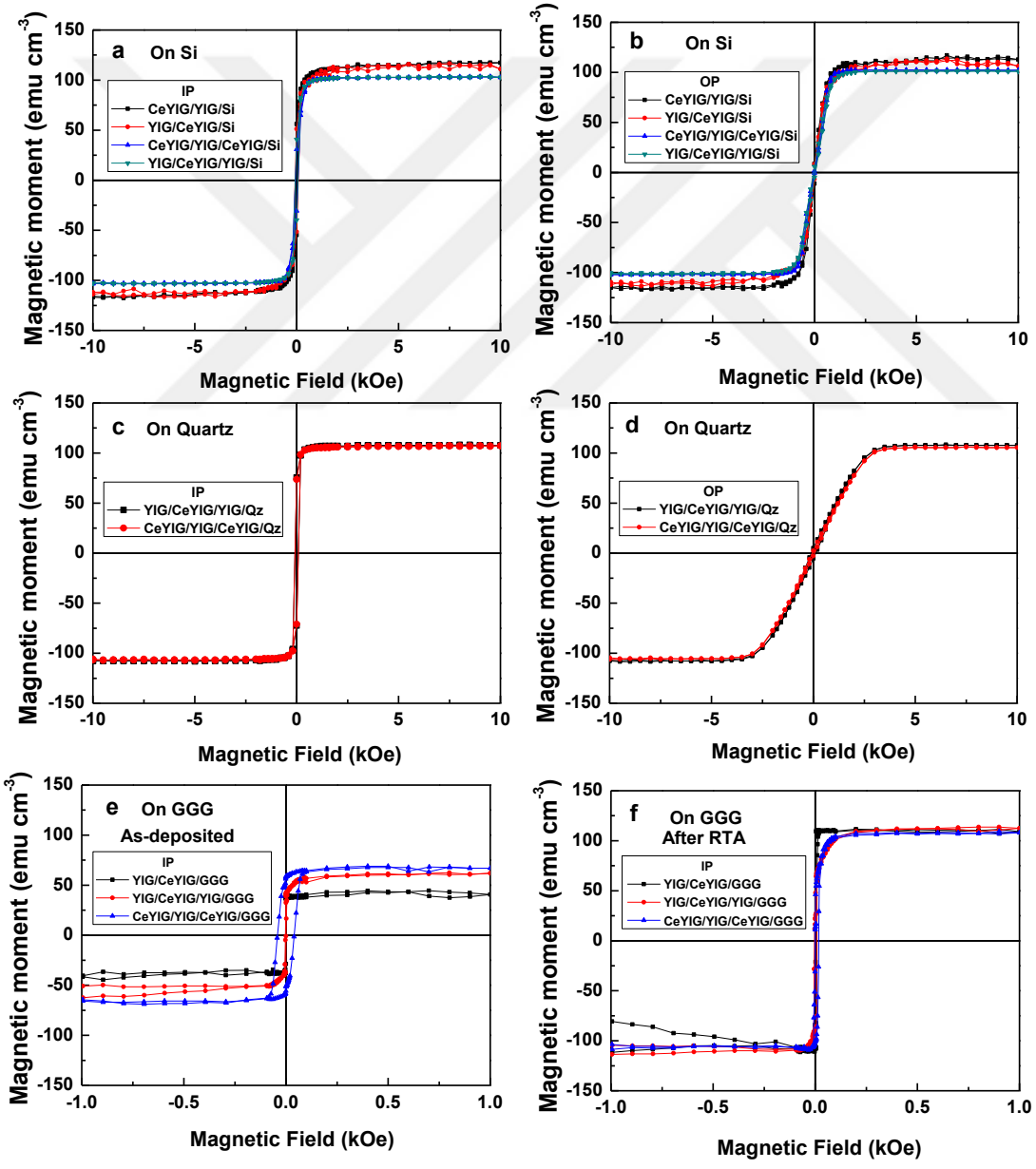

Fig. 3-31. (a) IP and (b) OP magnetic hysteresis loops of films on Si after RTA. (c) IP and (d) OP magnetic

hysteresis loops of films on quartz after RTA. (e), (f) IP magnetic hysteresis loops of films on the single crystal GGG (100) before and after RTA, respectively.

IP and OP magnetic hysteresis loops of Ce:YIG films were measured at room temperature using a VSM and are shown on Fig. 3-31. Fig. 3-31 (a) and (b) show the IP and OP hysteresis loops of YIG/Ce:YIG bilayer on Si, respectively. The saturation magnetic moments M_s (averaged over bilayer or trilayer garnet films) of the films are 115 emu cm^{-3} (with ~5% error estimate) for the Ce:YIG/YIG/Si and 113 emu cm^{-3} for the trilayer films on Si was 103 emu cm^{-3}. The M_s of the films on Qz is about 108 emu cm^{-3}, as shown on Fig. 3-31 (c, d). M_s of the films on GGG after RTA is 110 emu cm^{-3} as shown on Fig. 3-31 (f). The hysteresis loops of the garnet films on GGG before RTA are shown on Fig. 3-31 (e). The coercivity H_c of single crystal multilayer films on GGG was <10 Oe, and it was a few times larger for films on Si. These results are consistent with the samples being primarily garnet phase, without significant magnetite or maghemite spinel phases.

The bulk saturation magnetization at room temperature of YIG is about 140 emu cm^{-3} [51], and for Ce:YIG 120 emu cm^{-3} [31], slightly higher than that of the films made in this study. The seed layer deposition conditions, in particular deposition rate [6] and the annealing temperature [86] have an important effect on the magnetic properties, for example via their effect on oxygen content and cation ratios. Growth parameters were not explored in this study in detail, and it is expected that the M_s could be increased by further optimization to be closer to bulk values.

The films all have high remanence in plane with an OP hard axis, but the magnitude of the net anisotropy differs between the films grown on different substrates. The net anisotropy can be estimated from the hard axis (i.e. the OP) saturation field, H_K which was 1400 Oe for films on Si and 3500 Oe for films on Qz. The anisotropy K_{tot} consists of the sum of shape anisotropy (producing $H_K = 4\pi M_s$, in cgs units), magnetocrystalline and magnetoelastic contributions. For YIG, the shape anisotropy of 1.2×10^5 erg cm^{-3} is the dominant factor leading to H_K = 1760 Oe in unstrained polycrystalline YIG films with bulk M_s. The room

temperature magnetocrystalline anisotropy is small (~10^4 erg cm^{-3}) and the magnetostriction coefficient is small, $\lambda_{100} = -1.3 \times 10^{-6}$. [67] The magnetocrystalline anisotropy of Ce:YIG is not well known, but will be neglected here due to the polycrystallinity of the Ce:YIG layers. The room temperature magnetostriction coefficient of $Ce_3Fe_5O_{12}$ (extrapolated from small concentrations of Ce) has been given as $\lambda_{100} = +120 \times 10^{-6}$ and $\lambda_{111} = +50 \times 10^{-6}$ [68]. Data on $Ce_xY_{1-x}Fe_5O_{12}$ in the range of x = 0–0.125 [69] also show that Ce contributed a positive magnetostriction, suggesting that the x = 1 composition used here should have a positive magnetostriction. If we extrapolate from [69], we obtain $\lambda_{100} \sim +10 \times 10^{-6}$ at x = 1, smaller than the x = 1 extrapolation from [68]. Considering that the Ce:YIG occupies only about half the volume of the film the effective magnetostriction of the film will be reduced from this value but is expected to still be positive. An estimate of the magnetoelastic anisotropy is $(3/2)\lambda_{100}E\varepsilon_z$, with ε_z the out of plane strain and E the Young's modulus, 200 GPa [70]. The in-plane thermal mismatch strain $\varepsilon_x = -\varepsilon_z/2$ is determined by the product of the difference in thermal expansion coefficients and the temperature change. For garnet films on Si the film will experience tensile strain after cooling from 800˚C, with $\varepsilon_x \sim 6 \times 10^{-3}$ (neglecting temperature dependence of the thermal expansion coefficients), whereas for films on crystalline quartz, with an in-plane thermal expansion coefficient of 13.7×10^{-6} [71] the films will experience compressive strain, $\varepsilon_x \sim -8 \times 10^{-3}$. These thermal mismatch strains, combined with the positive magnetostriction, would suggest that the films on Qz would be easier to magnetize in the out-of-plane direction than those on Si, but the out-of-plane saturation field, H_K was higher for the films on Qz, not lower. This suggests that the thermal mismatch may not be the only source of strain in the films, i.e. the films were not fully relaxed at the annealing temperature.

3.2.2 Magneto-optical isolator demonstration

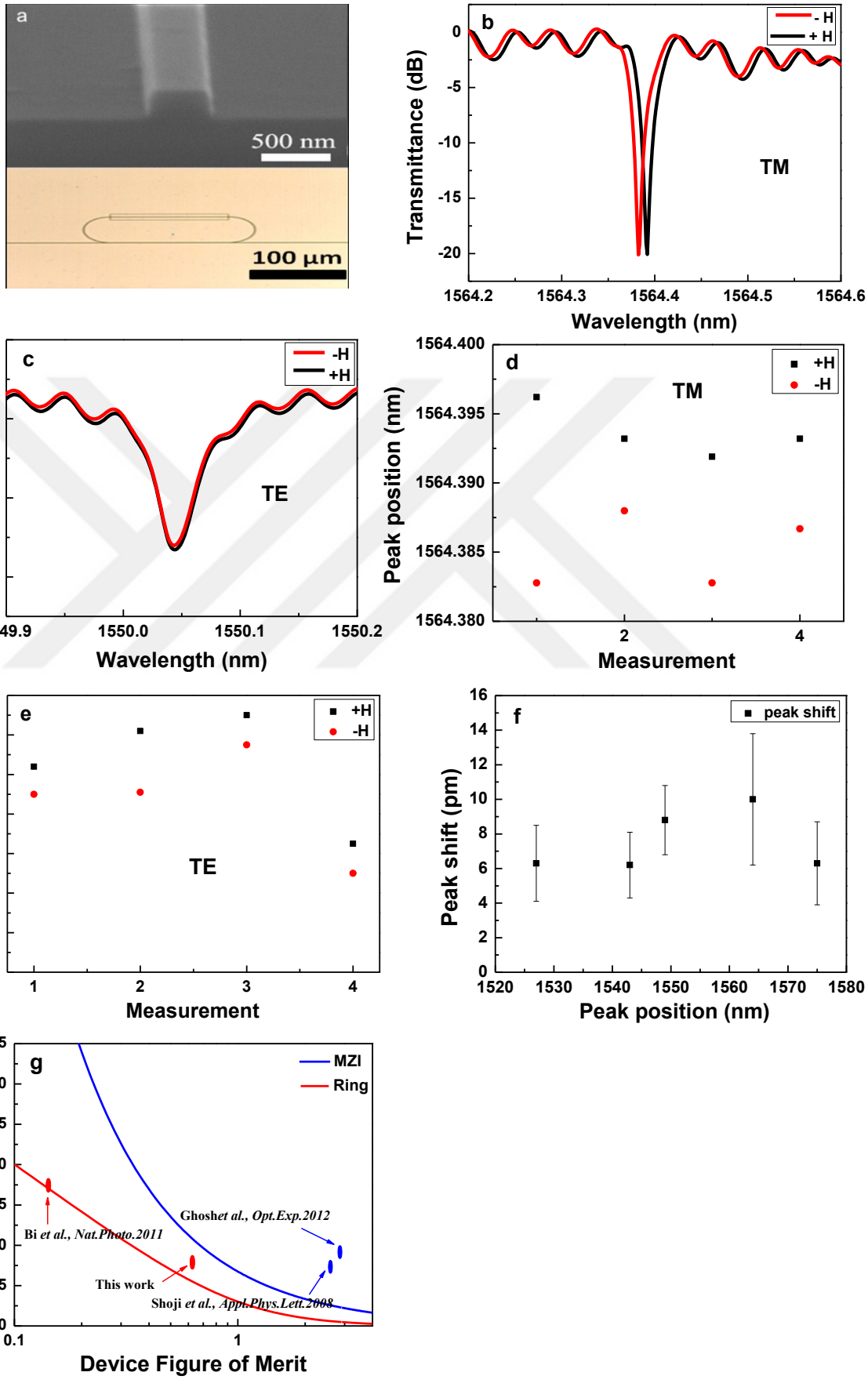

Fig. 3-32. (a) A tilted view SEM micrograph of the silicon-on-insulator waveguide (top) and an optical micrograph of the resonator (bottom). (b) Transmission spectra of TM mode under applied magnetic fields of opposite directions. Insertion loss measured from the figure is 7.4 dB. (c) Transmission spectra of TE mode under applied magnetic fields of opposite directions. (d) TM mode resonant peak positions measured when the magnetic field direction was reversed ten consecutive times. (e) TE mode resonant peak positions measured when the magnetic field direction was reversed eight consecutive times. (f) Measured wavelength dependence of non-reciprocal resonant peak shift. (g) Insertion losses of isolators: the solid lines are simulated performance of ideal micro-ring and MZI devices, whereas the dots correspond to experimental measurement results in this report and literature. (Waveguide measurements were done by Qingyang Du)

To quantify the magneto-optical behavior of the films on an integrated device, we fabricated integrated optical isolator devices by depositing YIG (30 nm)/CeYIG (60 nm) films on top of silicon-on-insulator racetrack resonators using the device fabrication recipe described in section 2.1.3 and ref. [9]. The YIG (30 nm)/CeYIG (60 nm) films on the optical isolator were grown at the same deposition run with the TEM sample YIG (30 nm)/CeYIG (60 nm)/Si, shown in Fig. 3-30(a). Therefore their deposition parameters are the same.

Fig. 3-32(a) shows a tilted-view SEM micrograph of the SOI waveguide and a top view of the isolator, which consists of a racetrack resonator adjacent to a waveguide. [1] The total length of the racetrack resonator is 682 μm, and the oxide window is 200 μm in length. Details of the fabrication process are described in [9]. Fig. 3-32(b) and (c) show the transmission spectra of quasi-transverse magnetic (TM) and quasi-transverse electric (TE) modes through the isolator, respectively, measured for positive and negative magnetic fields applied IP and perpendicular to the garnet-clad section of the resonator. A resonant peak shift arising from non-reciprocal phase shift (NRPS) in the waveguide is clearly visible for the TM mode, whereas the TE mode exhibits negligible resonant peak shift, consistent with our magnetic field configuration. The device insertion loss is estimated to be 7.4 dB, and the isolation ratio is 13 dB according to the definition given in Ref. [1]. The Faraday rotation of the Ce:YIG film was estimated to be 1,100 $^{\circ}cm^{-1}$ using perturbation theory.[1]

The resonant wavelengths obtained from the measurements are plotted in Fig. 3-32(d) and (e). The average peak shift from four separate measurements is (9.6 ± 4.1) pm for the TM

mode and (1.7 ± 0.4) pm for the TE mode. The small drift over repeated measurements is likely a result of temperature change. Fig. 3-32(f) plots the wavelength dependence of the non-reciprocal resonance shift.

To benchmark the performance of our device, we simulated the insertion losses of ideal isolator devices based on micro-ring resonator and Mach-Zehnder interferometer (MZI) geometries, respectively, using procedures detailed in the Supporting Information. We choose insertion loss rather than isolation ratio as the performance benchmark here, since it is directly correlated with the magneto-optical figure of merit of the non-reciprocal device, defined as: $FOM = \Delta\beta/\alpha$, where $\Delta\beta$ denotes the nonreciprocal phase shift (NRPS), i.e. the propagation constant difference of forward and backward propagating modes in the waveguide, and α gives the waveguide loss. In contrast isolation ratio is not an intrinsic parameter reflecting the magneto-optical figure of merit of the isolator devices, because it can be maximized by approaching the critical coupling condition in micro-rings, or tuning the power splitting ratio in two interferometer arms in the case of MZI.

The simulated insertion losses are plotted in Fig. 3-32(g) as solid lines, and the points denote the device insertion loss demonstrated in this study as well as values quoted from the literature.[1,64,72] The improvement of the device performance compared to earlier results is mainly attributed to reduced garnet material loss, and further device and material processing improvement will enhance the MO characteristics of integrated optical isolators.

YIG layers grown either above or below the Ce:YIG serve as effective seed layers to promote crystallization of the MO Ce:YIG layers. Templating Ce:YIG crystallization from the top eliminates the need for a YIG layer between the waveguide and the Ce:YIG. Growth of the Ce:YIG directly in contact with the waveguide increases optical coupling into the Ce:YIG. The top-down crystallization of the Ce:YIG provides more flexibility for optical isolator designs. The top-seeding approach may also be applicable in other materials systems where a seed layer is needed to ensure correct phase formation in a functional layer. The films were compared to single crystal films grown on GGG substrates and had similar

magnetization. An integrated resonator optical isolator was fabricated on a Si waveguide showing an insertion loss of 7.4 dB and an isolation ratio of 13.0 dB at the 1520–1590 nm wavelength range, which represents significant performance improvement over previously demonstrated on-chip isolators.

3.3 Summary

In this chapter, we first focused on growing 14 nm and 80 nm-thick Ce:YIG films on GGG (100), (110) and (111) substrates and characterizing their structural, magnetic, optical and magneto-optical properties. Faraday rotation and absorption spectra yielded high MO figures of merit of *379, 380, and 401 deg · dB^{-1}* for Ce:YIG (100), (110) and (111) at $\lambda = 1550$ nm. These figure-of-merit values provide upper limits for how much MO functionality one might expect from polycrystalline MO films on nongarnet substrates. Since figure of merit at $\lambda = 1550$ nm is not too sensitive to crystallographic orientations of garnet films, one needs to focus on (i) improving the crystallization efficiency of garnet on nongarnet substrates such as Si, SOI or Qz, and on (ii) minimizing grain boundary scattering by promoting the growth of larger garnet grains.

Based on these insights, three different garnet deposition methods were explored: Ce:YIG/YIG growth on Si_3N_4 with a two-step PLD and a one step RTA process, Ce:YIG/YIG growth on SOI and Si with a two-step PLD (lower thermal budget) and a one step RTA process, YIG/Ce:YIG growth on Si waveguides with a one-step PLD and a one step RTA process. In the first method, effect of the structural quality of the YIG seed layer has been explored. The growth rate (optimum: 2 Hz) and temperature (650°C) of the YIG seed layer have been found to maximize the MO response of Ce:YIG layer which was grown on the YIG seed layer. In the second method, the thermal budget of garnet deposition was improved by depositing the YIG seed layer at 100°C. In addition, a minimum YIG seed layer thickness (31 nm) and the RTA step were found to be essential in forming crystalline and functional MO Ce:YIG. In the third method, the thermal budget of garnet deposition was reduced even

further by eliminating one of the PLD steps. YIG has been found to promote Ce:YIG crystallization as a top-layer. This functionality enables direct growth of Ce:YIG on Si waveguides and higher nonreciprocal phase shift accumulation on the waveguide mode. One demonstration proved that optical isolator performance, in particular the insertion loss, can be improved using this garnet deposition method (down to insertion loss of 7.4 ± 1.8 dB and an isolation ratio of 13.0 ± 2.2 dB).

References

[1] L. Bi, J. Hu, P. Jiang, D. H. Kim, G. F. Dionne, L. C. Kimerling, and C. A. Ross, *Nat. Photonics* **5**, 758 (2011).

[2] L. Bi, J. Hu, L. Kimerling, and C. A. Ross, *Proc. SPIE* **7604**, 760406 (2010).

[3] L. Bi, J. Hu, G. F. Dionne, L. Kimerling, and C. A. Ross, *Proc. SPIE* **7941**, 794105 (2011).

[4] T. Mizumoto, R. Takei, and Y. Shoji, *IEEE J. Quantum Electronics* **48**, 252 (2012).

[5] T. Goto, M. C. Onbasli, and C. A. Ross, *Opt. Express* **20**, 28507 (2012).

[6] M. C. Onbasli, T. Goto, X. Sun, N. Huynh, C. A. Ross, *Opt. Express* **22**, 25183 (2014).

[7] B. Stadler, K. Vaccaro, P. Yip, J. Lorenzo, Y. –Q. Li, and M. Cherif, *IEEE Trans. Magn.* **38**, 1564 (2002).

[8] T. Soma, J. Satoh, and H. Matsuo, *Solid State Commun.* **42**, 889 (1982).

[9] M. A. Gilleo and S. Geller, *Phys. Rev.* **110**, 73 (1958).

[10] R. E. Nahory, M. A. Pollack, W. D. Johnston, Jr., and R. L. Barns, *Appl. Phys. Lett.* **33**, 659 (1978).

[11] B. E. A. Saleh and M. C. Teich, *Fundamentals of Photonics, second edition*, Wiley-Interscience, Weinheim, Germany, **1997**

[12] T. Mizumoto, R. Takei, and Y. Shoji, *IEEE J. Quantum Electronics* **48**, 252 (2012).

[13] M.-C.Tien, T. Mizumoto, P. Pintus, H. Kromer, and J. E. Bowers, *Opt. Express* **19**, 11740 (2011).

[14] B. Stadler, K. Vaccaro, P. Yip, J. Lorenzo, Y. –Q. Li, and M. Cherif, *IEEE Trans. Magn.* **38**, 1564 (2002).

[15] M. Gomi, T. Tanida, and M. Abe, *J. Appl. Phys.* **57**, 3888 (1985).

[16] Q.-H. Yang, H.-W. Zhang, Q.-Y. Wen, and Y.-L. Liu, *J. Appl. Phys.* **108**, 073901 (2010).

[17] Q. Yang, Z. Huaiwu, L. Yingli, and W. Qiye, *IEEE Trans. Magn.* **43**, 3652 (2007).

[18] S. Sung, X. Qi, and B. J. H. Stadler, *Appl. Phys. Lett.* **87**, 121111 (2005).

[19] T. Suzuki, *J. Appl. Phys.* **69**, 4756 (1991).

[20] T. Suzuki, G. Zaharchuk, G. Gorman, F. Sequeda, and P. Labun, *IEEE Trans. Magn.* **26**, 1927 (1990).

[21] M. Vasiliev, P. C. Wo, K. Alameh, P. Munroe, Z. Xie, V. A. Kotov, and V. I. Burkov, *J. Phys. D: Appl. Phys.* **42**, 135003 (2009).

[22] T. Goto, Y. Eto, K. Kobayashi, Y. Haga, M. Inoue, and C. A. Ross, *J. Appl. Phys.* **113**, 17A939 (2013).

[23] X. Y. Sun, Q. Du, T. Goto, M. C. Onbasli, D. H. Kim, N. M. Aimon, J. Hu, C. A. Ross, "Single-step deposition of cerium substituted yttrium iron garnet for monolithic on-chip optical isolation", (under review)

[24] T. Goto, M. C. Onbasli, D. H. Kim, V. Singh, M. Inoue, L. C. Kimerling, and C. A. Ross, *Opt. Express*

22, 19047 (2014).
[25] M. Levy, *IEEE J. Sel. Top. Quantum Electron.* **8**, 1300 (2002).
[26] D. Dai, J. Bauters, and John E Bowers, *Light: Science & Applications* **1**, e1 (2012).
[27] B. Sepulveda, G. Armelles, L.M. Lechuga, *Sensor Actuat A-Phys.* **134**, 339 (2007).
[28] A. Kehlberger, K. Richter, G. Jakob, M. C. Onbasli, D. H. Kim, T. Goto, C. A. Ross, G. Gotz, G. Reiss, T. Kuschel, and M. Klaui, "Enhanced magnetooptic Kerr effect and magnetic properties of epitaxial CeYIG thin films," (under review)
[29] M. C. Sekhar, M. R. Singh, S. Basu, and S. Pinnepalli, *Opt. Express* **20**, 9624 (2012).
[30] M. Huang, S.-Y. Zhang, *Appl. Phys. A* **74**, 177 (2002).
[31] S. Mino, A. Tate, T. Uno, T. Shintaku, and A. Shibukawa, *Jpn. J. Appl. Phys.* **32**, L994 (1993).
[32] T. Shintaku, A. Tate, and S. Mino, *Appl. Phys. Lett.* **71**, 1640 (1997).
[33] M. Gomi, H. Furuyama, and M. Abe, *J. Appl. Phys.* **70**, 7065 (1991).
[34] M. Lang, M. Montazeri, M. C. Onbasli, X. Kou, Y. Fan, P. Upadhyaya, K. Yao, F. Liu, Y. Jiang, W. Jiang, K. L Wong, G. Yu, J. Tang, T. Nie, L. He, R. N Schwartz, Y. Wang, C. A Ross, K. L Wang, *Nano Lett.* **14**, 3459 (2014).
[35] B. Jiang, Z. Zhao, X. Xu, P. Song, X. Wang, J. Xu, P. Deng, *J. Cryst. Growth* **277**, 186 (2005).
[36] W. Wettling, B. Andlauer, P. Koidl, J. Schneider, and W. Tolksdorf, *Phys. Stat. Sol. (b)* **59**, 63 (1973).
[37] S. Visnovsky, N. P. Thuy, J. Stepanek, V. Prosser, and R. Krishnan, *J. Appl. Phys.*, **50**, 7466 (1979).
[38] F. J. Kahn, P.S. Pershan, and J.P. Remeika, *Phys. Rev.* **186**, 891 (1969).
[39] S. H. Wemple, S. L. Blank, J. A. Seman, W. A. Biolsi, *Phys. Rev. B*, **9**, 2134 (1974).
[40] E. Jakubisova-Liskova, S. Visnovsky, H. Chang, M. Wu, *J. Appl. Phys.* **117**, 17B702 (2015).
[41] G. J. Diercks, Jr., S. Samuelson, *IEEE Trans. Magn.* **31**, 3328 (1995).
[42] M. Gomi, H. Furuyama, and M. Abe, *Jap. J. Appl. Phys.* **29**, L99 (1990).
[43] M. Gomi, K. Satoh, and M. Abe, *Jap. J. Appl. Phys.* **27**, L1536 (1988).
[44] M. Gomi, H. Furuyama and M. Abe, *J. Appl. Phys.* **70**, 7065 (1991).
[45] Y. Xu, J. H. Yang, and G. Zhang, *J. Phys.: Cond. Mat.* **5**, 8927 (1993).
[46] M. Kucera, J. Bok, K. Nitsch, *Solid State Commun.* **69**, 1117 (1989).
[47] S. Wittekoek, T. J. A. Popma, J. M. Robertson, and P. F. Bongers, Phys. Rev. B **12**, 2777 (1975).
[48] S. Leitenmeier, T. Korner, J. Griesbauer, M. Herbort, A. Heinrich, B. Stritzker, *J. Cryst. Growth* **310**, 5392 (2008).
[49] E. Popova, N. Keller, F. Gendron, M. Guyot, M.-C. Brianso, Y. Dumond, and M. Tessier, *J. Appl. Phys.* **90**, 1422 (2001).
[50] M. Huang, Z-C. Xu, *Thin Solid Films* **450**, 324 (2004).
[51] M. Huang, S.-Y. Zhang, *Appl. Phys. A* **74**, 177 (2002).
[52] G. Dionne, Magnetic Oxides, Springer, New York, **2009**.
[53] M. Gomi, K. Satoh, H. Furuyama, and M. Abe, *J. Magn. Soc. Jpn.* **13**(2), 163 (1989).
[54] D. E. Aspnes and J. B. Theeten, *Phys. Rev. Lett.* **43**(14), 1046 (1979).
[55] T. Nakano, H. Yuri, and U. Kihara, *IEEE Trans. Magn.* **20**(5), 986 (1984).
[56] W. A. Crossley, R. W. Cooper, J. L. Page, and R. P. van Stapele, *Phys. Rev.* **181**(2), 896 (1969).
[57] Y. Xu, J. H. Yang, and X. J. Zhang, *Phys. Rev. B Condens. Matter* **50**(18), 13428 (1994).
[58] S. Higuchi, Y. Furukawa, S. Takekawa, O. Kamada and K. Kitamura, *Jpn. J. Appl. Phys.* **38**, 4122 (1999).
[59] T. Shintaku, *Appl. Phys. Lett.* **73**, 1946 (1998).

[60] T. R. Zaman, X. Guo, and R. J. Ram, "Faraday rotation in semiconductors for photonic integration," in Proc. Conf. Lasers Electro-Optics, San Francisco, CA, May 2004, p. 2.
[61] T. R. Zaman, X. Guo, and R. J. Ram, *Appl. Phys. Lett.* **90**, 023514, (2007).
[62] L. Bi, "Magneto-optical Oxide Thin Films and Integrated Nonreciprocal Photonic Devices," PhD Thesis, Massachusetts Institute of Technology (2011).
[63] Y. Shoji, M. Ito, Y. Shirato, T. Mizumoto, *Opt. Express* **20**, 18440 (2012).
[64] S. Ghosh, S. Keyvavinia, W. Van Roy, T. Mizumoto, G. Roelkens, R. Baets, *Opt. Express* **20**, 1839 (2012).
[65] A. D. Block, P. Dulal, B. J. H. Stadler, N. C. A. Seaton, *IEEE Photonics Journal* **6**, 0600308 (2014).
[66] T. Boudiar, B. Payet-Gervy, M.-F. Blanc-Mignon, J.-J. Rousseau, M. Leberre, H. Joisten, B. Canut, *Proc. SPIE* **5250**, 263 (2004).
[67] Landolt-Bornstein New Series, Group II, Vol. 12, "Magnetic and other properties of oxides and related compounds part a: Garnets and perovskites", (Eds: K.H. Hellwege and A.M. Hellwege), Springer-Verlag, Berlin Germany **1978.**
[68] R. L. Comstock and J. J. Raymond, *J. Appl. Phys.* **38**, 3737 (1967).
[69] K. P. Belov, N. V. Volkova, V. I. Raitsis, A. Ya Chervonenkis, *Soviet Phys-Solid State (English transl.)* **1972**, 14, 1607.
[70] D. F. Gibbons and V. G. Chirba, *Phys. Rev.*, **110**, 770 (1958).
[71] MTI Corp. data sheet, http://www.mtixtl.com/sio2singlecrystalquartz.aspx, accessed: December, 2014
[72] Y. Shoji, T. Mizumoto, H. Yokoi, I. Hsieh, R. M. Osgood, *Appl. Phys. Lett.* **92**, 071117 (2008).

Chapter 4.
Room Temperature Magnonic Materials

Ferrimagnetic insulators such as iron garnets ($Re_3Fe_5O_{12}$, Re: rare-earth metal), and in particular $Y_3Fe_5O_{12}$ (YIG), are unique materials that can offer an environment for testing new magnetic phenomena such as propagation of pure spin currents (but not charge currents), (inverse) spin-Hall effect (when brought in contact with a metal contact that has high atomic mass and spin-orbit coupling) [1], spin-Seebeck effect [2,3], ultra-low Gilbert damping [4], phase control of spins [5], tunability of magnetic anisotropy from in-plane to even perpendicular magnetic anisotropy at room temperature with the appropriate choice of rare-earth element [6], high magneto-optical figure of merit [7-13]. On the device side, the iron garnet compounds (especially YIG) offer unprecedented design capabilities such as magnon propagation (collective oscillations of spin waves, magnons are bosons and obey Bose-Einstein statistics) over a few hundred μm to almost cm long distances on chip

[4,14,15], spin wave amplification [16], all-magnon transistors [17], magnon logic circuits, spin injectors and detectors [14,15]. To be able to demonstrate all of these capabilities, one needs to first demonstrate that the garnet films grown have high-quality and bulk-like magnetic and spin-wave transport properties.

In this chapter, we focus on the PLD growth and characterization structural, magnetic and damping properties of bulk-like YIG films. We also study the effect of substrate orientation as well as Cerium substitution on magnetic and damping properties of YIG films. In the final part, we study the demonstration of a room temperature perpendicular magnetic anisotropic iron garnet (Thulium iron garnet, $Tm_3Fe_5O_{12}$, TmIG). FMR measurements done by A. Kehlberger and help on PLD target preparation by A. Tang are acknowledged.

4.1 Magnonic materials

Thickness dependence of Gilbert damping of high-quality epitaxial YIG films on GGG (100) (done in collaboration with A. Kehlberger and Prof. M. Kläui from University of Mainz, Germany)

For applications that require magnetic insulators, magnetic garnets are useful materials both in bulk and in thin film forms. Due to YIG's intrinsically low magnetic damping, radar and microwave applications were the first major applications that used bulk YIG crystals for early experiments in magnonics. During and after World War II, bulk YIG crystals were used for studying magnonics at the micrometer to millimeter length scales needed for microwave devices. In the past decade, with the development of PLD systems that can achieve good stoichiometry transfer of complex oxides from bulk target to thin films; YIG and spin wave applications such as integrated spintronic, magnonic or magnetooptical devices started becoming accessible for researchers. The performances of these devices critically depend on the high structural and magnetic quality of YIG. In particular, very low damping in thin film YIG is a critical enabler for fabrication of magnonic logic devices to transport, store and process microwave and digital information for the post-CMOS (complementary metal-oxide-semiconductor) era. Applications include integrated multi-modal spin-wave devices, delay lines, filters, resonators, generators, multi-channel receivers, directional

couplers and Y-junctions [4,14]. In addition, low damping (high Q-factor of 200 to 30000) can be utilized for spin-based resonant sensing applications [18].

Both pulsed laser deposition (PLD) and sputtering of complex oxides have enabled excellent control of film thickness, stoichiometry, surface roughness and magnetic properties of magnetic oxide thin films. Previous reports on YIG films grown using liquid phase epitaxy, PLD or sputtering have found damping parameters ranging from 1.6×10^{-4} to 4.3×10^{-3}, summarized in Table 4-1 [19-28]. These damping parameters were extracted from ferromagnetic resonance measurements at comparable resonance frequencies (3-24 GHz). The intrinsic damping in bulk YIG has been reported to be $\alpha = 3 \times 10^{-5}$ [29]. In this section, we present the PLD growth and characterization of epitaxial YIG thin films grown on Gadolinium Gallium Garnet ($Gd_3Ga_5O_{12}$, GGG) substrates, with saturation magnetization close to bulk and low damping parameters. The processes developed for ceramic YIG target preparation and film growth by PLD are presented. We characterized the crystalline structure, phase purity and lattice parameters of YIG films with different thicknesses using high-resolution x-ray diffraction (HRXRD). The thickness dependence of magnetic properties (saturation moment and Gilbert damping) and structural properties (out-of-plane lattice parameter and surface roughness) were investigated.

Table 4-1. Damping parameters published for YIG thin films.

Growth method [Reference]	**Thickness (nm)**	**ΔH, (Oe) FWHM**	**Frequency, GHz**	**ΔH_0 (Oe)**	**α**	**M_s (emu cm^{-3})**
PLD [19]	9	7.5 (14)	24	5 (8)	0.7×10^{-3}	156
PLD [20]	9				0.5×10^{-3}	156
PLD [21]	11	6.5	10	5	3.2×10^{-4}	133
PLD [22]	4	26	10		3.8×10^{-3}	135
LPE [23]	200	1.9	10	0.4	2.0×10^{-4}	139
PLD [24]	20	1.9	10	0.35	2.2×10^{-3}	129
	200	2.8	10	1.2	1.6×10^{-4}	141
PLD [25]	19		9.5	3	3.5×10^{-4}	104
Sputtering [26]	26	9	9.5	3	1×10^{-3}	139
Sputtering	5100	3	5	3	10^{-4}	139

[27]						
LPE [28]	100	2	3.5	1.6	$2.8x10^{-4}$	144
PLD (this study)	79	3	10	1.4	$2.2x10^{-4}$	137

The YIG target preparation recipe is presented in chapter 2. The films were grown using PLD as described in chapter 2. Here, we presented the growth parameters specific to YIG films. The surface of the 10 mm x 10 mm GGG (100) substrates, which were purchased from MTI Crystals Inc., were cleaned by ultrasonicating in acetone and then in isopropanol for 10 minutes each. YIG films were grown with 400 mJ pulses at 10 Hz PLD pulse rate while the substrates were held at 650°C under 20 mTorr oxygen pressure ($5x10^{-6}$ Torr base pressure). The growth rate was about 3 nm · min^{-1}. The growth chamber was cooled in oxygen ambient at 5°C · min^{-1} rate until the substrate reached 200°C, when the heater was switched off. After growth, the films were ex situ annealed at 800°C for 120 seconds *ex situ* using a rapid thermal annealer (RTA). YIG films with 17, 34, 49, 64, 79, 92, 97, and 190 nm thicknesses (measured using XRR and profilometry) were grown on GGG substrates in separate deposition runs using the recipe described above. The target-substrate distance was kept at 85 mm for all samples. The correct target stoichiometry, oxygen pressure, temperature and a low deposition rate are critical for achieving bulk-like magnetization and high crystal quality YIG films on GGG substrates. The structural (out-of-plane, OP, lattice parameter, film thickness, surface roughness, substrate quality in terms of rocking curve full-width at half-maximum), magnetic (magnetic saturation moment, remanence, saturation field, coercivity), and damping properties of YIG films were characterized after RTA and are presented on Table 4-2 and 4-3.

Table 4-2. YIG lattice constants and thicknesses extracted from XRD.

YIG thickness from XRR (nm)	**OP lattice parameter from (800) peak position (Å)**	**OP lattice parameter from Laue Oscillations (Å)**	**Thickness derived from Laue Oscillations (nm)**	**Thickness Error (nm)**	**Rocking Curve FWHM (°)**	**Error in FWHM (°)**
17 ± 1	-	12.395 ± 0.01	19	3	-	
34 ± 1	-	12.4 ± 0.005	34	3	-	
49 ± 2	-	12.4 ± 0.005	47	3	-	
64 ± 2	12.391	12.395 ± 0.005	63	3	-	
79 ± 2	12.406	12.402 ± 0.005	78	3	0.02595	0.0007

92 ± 2	12.408	12.405 ± 0.005	89	4	0.02552	0.0007
97 ± 2	12.407	12.403 ± 0.005	96	5	0.02364	0.0002
190 ± 2*	12.399	12.398 ± 0.005	186	6	0.0181	0.0002

*(this sample's thickness was obtained using profilometer)

HRXRD (Bruker D8 Discover), X-ray reflectivity (HRXRR) and atomic force microscope (AFM Nanoscope IV, tapping mode operation at 2 Hz scan rate) were used to measure the microstructure, lattice parameter, thickness and surface roughness of the YIG films. Fig. 4-1(a) shows the HRXRD 2θ plot near the YIG (800) and GGG (800) peak for the 97 nm thick YIG film. A Ge-monochromator was installed to filter out the $K\alpha_2$ and to only observe the $K\alpha_1$ (1.5406Å) peaks. The (800) substrate peak of GGG shows up on this figure as the HRXRD peak with the highest intensity at 2θ=59.70° and corresponds to the (giving a lattice parameter of 12.381 Å). The second peak on the left shoulder of the substrate peak corresponds to the (800) peak of the YIG film at 2θ=59.56°. The oscillations to left and right of the substrate peak are called *Laue oscillations*, or thickness fringes of the YIG film, which indicate the periodic and high-quality crystallographic layers and high ordering. These oscillations were observed for the scans for each sample and could be fitted to derive the film thickness, lattice parameter and strain even for films with weak intensity YIG peaks. We assumed an in-plane coherent interface for this fit but allowed for a variation of the out-of-plane lattice constant as function of thickness, which is expected due to relaxation from the residual stress at the interface.

The mean out-of-plane lattice parameter resulting from this fit of the thickness fringes is shown in Table 4-2, column 3 and agrees with that determined from the (800) peak maximum (Table 4-2, column 2) within the error estimation. The data suggest that the in plane and out of plane lattice parameters of the YIG differed by less than 0.2%. The rocking curves of the YIG (800) peak were also measured for the thicker films, which showed a narrow single symmetric peak (typically 0.0025°, see Table 4-2, column 7), indicating a good crystallographic texture and no significant mosaicity within the films.

HRXRR data measured at grazing incidence were also fitted to extract film thickness from the period of the low angle oscillations, seen in Figure 1(b), which yielded values slightly larger than those from the Laue oscillations. As XRR probes electron density, while XRD probes crystal coherence, the XRR measurement should yield an upper bound.

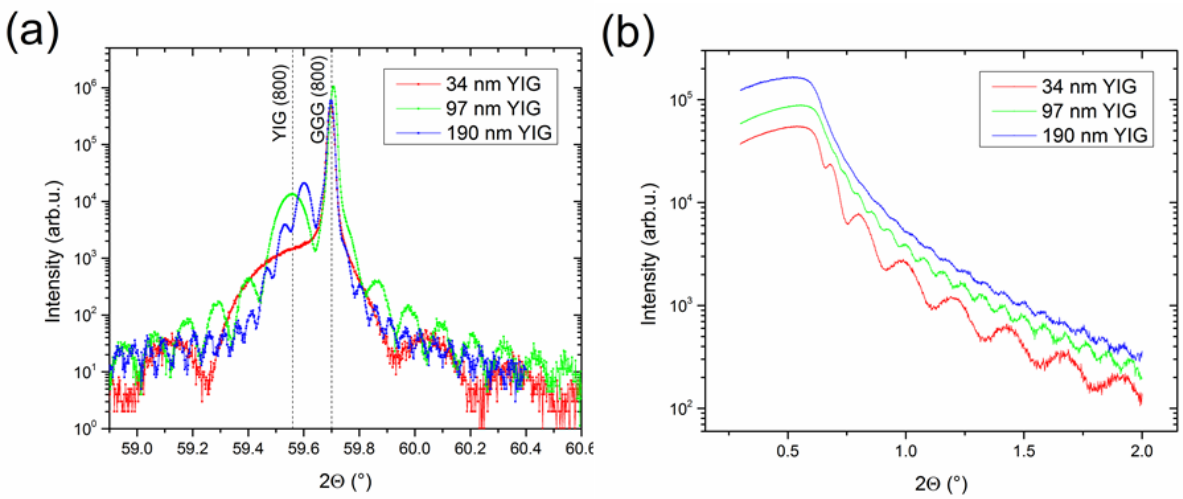

Fig. 4-1. (a) HRXRD 2θ plot around YIG (800) and GGG (800) peaks, dashed lines indicate (800) peaks of bulk YIG and GGG. FWHM of substrate (800) rocking curve is around 0.008°. (b) HRXRR plot for 34, 97 and 190 nm thick YIG films. HRXRD and HRXRR plots for other thicknesses were similar except for the period of the oscillations, which was shorter for thicker films.

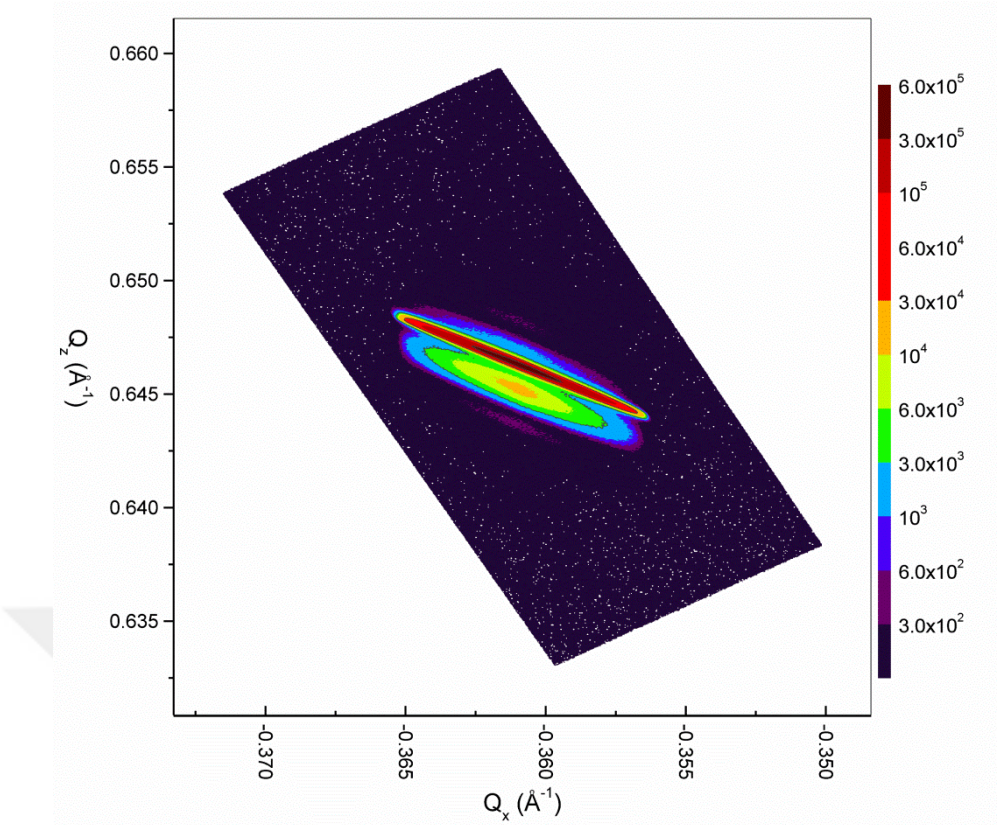

Fig. 4-2. Reciprocal space map for 79 nm thick YIG film on GGG (100) near the (248) peak measured in grazing incidence configuration.

High-resolution RSM measurements of the 79 nm thick film indicates that the film is lattice matched to the substrate (q_x (film) = q_x (substrate)). There was also no x-ray evidence of the growth of other crystalline phases based on measurements of the thickest (190 nm) film. The RSM given here belongs to the (248) peak of 79 nm thick YIG film on GGG (100) (substrate) measured at grazing incidence configuration. The plot is in log intensity scale. The strong peak near (q_x, q_z) = (0.3610, 0.647) $Å^{-1}$ belongs to the (248) peak of the GGG (100) substrate. The peak near (q_x, q_z) = (0.3610, 0.646) $Å^{-1}$ belongs to the (248) peak of the YIG (100) film. The RSM demonstrates that the q_x of both film and the substrate are identical, indicating that the film is lattice matched to the substrate.

Table 4-3. Damping values derived from the VNA-FMR measurements of the YIG (100) samples

YIG thickness (nm)	Gilbert damping	Gilbert damping error	FWHM @ 10 GHz (Oe)	FWHM @ 10 GHz error (Oe)	ΔH_0 (Oe)	ΔH_0 Error (Oe)	M_s (emu cm^{-3})

17	7.0×10^{-4}	0.7×10^{-4}	9.0	0.8	4.0	0.4	126 ± 3
34	5.8×10^{-4}	0.5×10^{-4}	5.3	0.5	1.2	0.3	135 ± 3
49	4.1×10^{-4}	0.5×10^{-4}	4.8	0.5	1.8	0.3	135 ± 3
64	3.8×10^{-4}	0.2×10^{-4}	4.4	0.3	1.6	0.1	133 ± 4
79	2.2×10^{-4}	0.2×10^{-4}	3.0	0.2	1.4	0.1	137 ± 3
92	3.4×10^{-4}	0.3×10^{-4}	3.7	0.4	1.2	0.2	137 ± 3
97	2.6×10^{-4}	0.3×10^{-4}	4.2	0.3	2.4	0.1	135 ± 3
190	4.1×10^{-4}	0.5×10^{-4}	4.4	0.6	1.5	0.3	133 ± 3

Fig. 4-3 shows AFM surface profiles of (a) 17 and (b) 79 nm thick YIG films. The RMS surface roughnesses of the films were 0.14 and 0.20 nm, respectively. The surface roughness increased slightly for the thicker YIG films but RMS roughness was smaller than 0.5 nm for all films presented on Table 4-3, which is less than the lattice parameter. The target-substrate distance of around 85 mm led to a slow growth rate of YIG (3 nm/min) increasing adatom diffusion distances at the high growth temperature. The rapid thermal annealing step after film growth had the following effects: (i) YIG coercivity was not changed (within the 2 Oe measurement step size), (ii) the RMS surface roughness decreased by ~0.03 nm on average and (iii) the saturation magnetic moment increased by up to 10 emu cm^{-3}. The annealing step improves the saturation magnetic moment slightly.

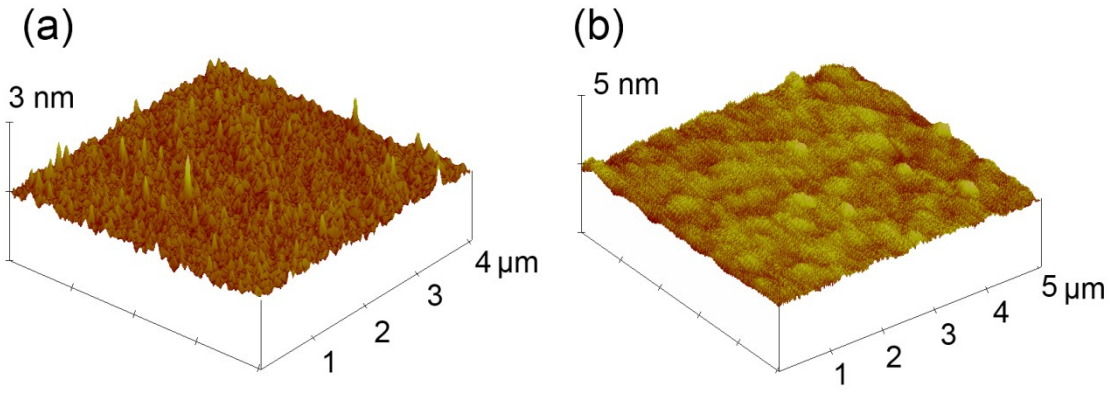

Fig. 4-3. AFM surface profiles of (a) 17 nm and (b) 79 nm thick YIG films. RMS surface roughness was 0.14 nm and 0.20 nm, respectively.

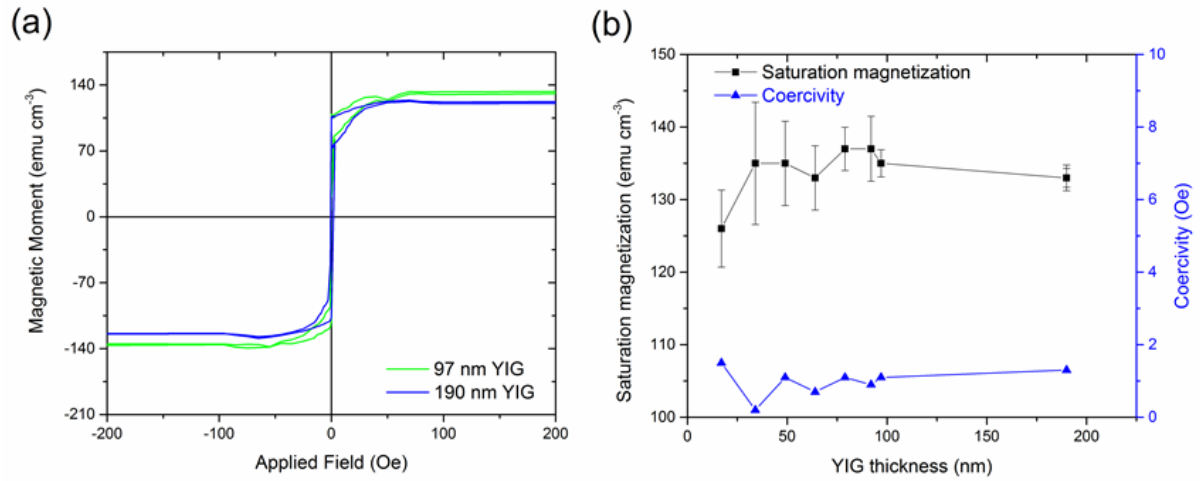

Fig. 4-4: ΔH as function of the resonance frequency. The inset shows one example of the measurement for a resonance frequency of 10.704 GHz. All these data were recorded for the 92 nm thick YIG film. Damping (α) is 3.4×10^{-4} and $\Delta H_0 = 1.2$ Oe for this sample.

Magnetic hysteresis loops of YIG films measured at room temperature (22 ˚C) using VSM are shown in Fig. 4-4(a) for magnetic fields applied parallel to the sample plane (in-plane measurement with H-field along [100]). Saturation moments were also extracted from ferromagnetic resonance measurements described below and were used to calibrate the VSM data. SQUID magnetometry measurements (done in Mainz, Germany) confirmed the saturation moments determined from FMR (ferromagnetic resonance). The coercivity of the samples was below 2 Oe, with the 17 nm sample at 5 Oe, but the accuracy of these values is limited by the step size of 2 Oe.

The YIG films were found to have in-plane easy axis for all thicknesses due to the dominant shape anisotropy and their saturation moments were $M_s = 137$ emu · cm^{-3}, with less than 5% measurement error. The bulk room temperature saturation moment for YIG is (M_s = 140 emu · cm^{-3}) [30] as shown in Table 4-2 and on Figure 4-4(b). The error bar on the saturation moment is mostly attributed to the error in film thickness measurement and any minor differences in the background substraction between each film. The saturation moments of the films were very consistent (except for the thinnest film). The thinnest sample yielded a slightly lower value, but considering the error estimate, we estimate that this difference may not be significant. The growth time for the thinnest films was < 4 min and the target or substrate may not have reached a steady state temperature during the deposition. Several of

the thinnest films were grown and they showed more variability in magnetization than the thicker films. The M_s for the thinnest film reported here is the averaged value over multiple samples grown for each thickness. Hard-axis (out-of-plane, OP hysteresis results not shown) saturation fields near 2 kOe were consistent with shape anisotropy being the dominant anisotropy.

To determine the suitability of the epitaxial YIG films for spintronics applications we measured Gilbert damping parameter α by FMR. Signal stripe and external magnetic field are oriented parallel to the in-plane [100] direction of the sample. The measurements were performed by recording absorption of the S_{21} signal emitted by the VNA in the frequency range of 7 GHz to 13 GHz. For one measurement the frequency was swept over a suitable range, while the applied magnetic field was kept constant. The inset of Figure 4-5 shows an example of one of these measurements for the 92 nm thick film. Each resonance dip was fit with a Lorentz model to determine the frequency linewidth Δf of each resonance. Since shape anisotropy dominates the magnetization orientation, the frequency linewidth Δf was converted into the ΔH H-field linewidth by using the Kittel formula (without an anisotropy term):

$$\Delta H = \left(\partial f_{\text{Kittel}} / \partial H\right)^{-1} \Delta f = \Delta f \left(2\sqrt{H^2 + H M_S}\right) / \left(\gamma\mu_0 / 2\pi \,(2H + M_S)\right), \qquad (1)$$

where H is the magnetic field during the measurement and $\gamma/2\pi \cong 28\ (\text{GHz}/10\ \text{kOe})$ is the gyromagnetic ratio [4]. The M_s values were extracted from the resonance frequency as function of the applied field by fitting the Kittel equation (without magnetocrystalline or magnetoelastic anisotropy terms) and are given in Table 4-3. Using the ΔH obtained, the Gilbert damping parameter α was extracted as the slope of ΔH vs. the applied driving frequency, as shown in Fig. 4-5(a). In the Landau-Lifshitz model the relation between ΔH and excitation frequency is given by $\Delta H = \Delta H_0 + \frac{4\pi\alpha}{\gamma} f$, where ΔH_0 describes the inhomogeneous broadening for zero frequency. The damping values are given in Table 4-3

and on Fig. 4-5(b).

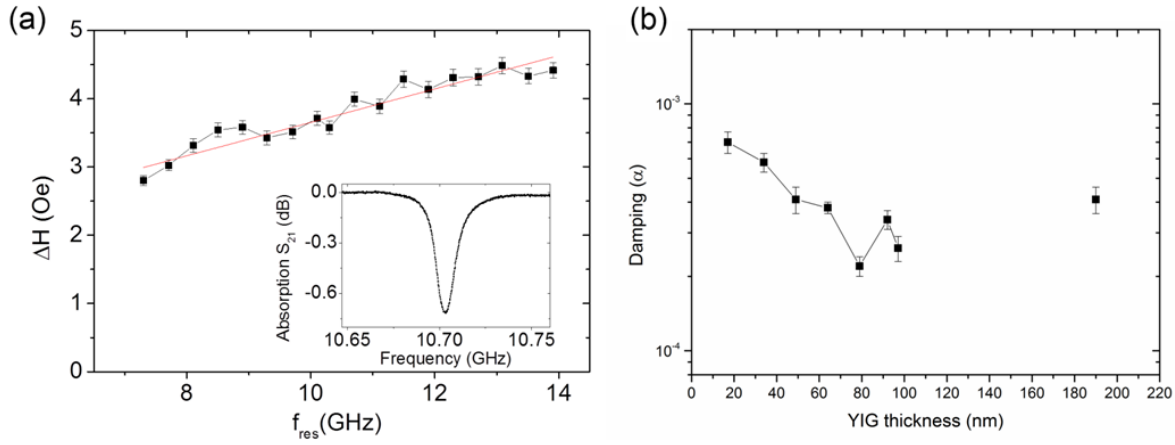

Fig. 4-5: (a) Magnetization as a function of applied in plane magnetic field for YIG films with different thicknesses showing typical hysteresis loops. The normalized Ms varies within 4%. (b) Ms and coercivity are shown as functions of YIG film thickness. (c) Damping parameter of YIG films as a function of film thickness. (FMR measurements were done by Dr. Andreas Kehlberger)

The damping parameters are low compared to other YIG thin films reported previously [19-28], and they all exceed the value reported for bulk YIG [29]. Magnetic moment and damping parameters are independent of film thickness (within the error bars). The thinnest YIG film is an exception, since it is affected by surface and interface effects and its M_s and α depend on thickness. As the films were grown under similar growth conditions, the damping is mostly independent of film thickness. The bulk YIG damping, $\alpha = 3x10^{-5}$ [29], is still an order of magnitude lower than damping values found in the thin films prepared for this study. This difference indicates that there is room for improving YIG film quality even further, although the current quality of the films is enough to improve the performance most spin wave devices reported in the literature. The difference between the damping values of the thin film and bulk YIG films can arise from thin film effects (i.e. confinement along the through-thickness dimension) as well as possible contributions from nanoscale inhomogeneities in of the stoichiometry. One may also need a systematic study of oxygen partial pressure dependence of film damping in order to minimize the damping with respect to oxygen partial pressure during growth. Growing films with a slower deposition rate such as 1 nm · min^{-1} may also reduce the defect density in the films and reduce the damping. As shown on Fig. 4-2, the substrate quality also needs to be improved significantly until the

substrate peak is narrow in both q_x and q_z axes. An improved substrate quality can directly lead to reduced damping values.

The YIG films on GGG (100) substrates presented here are single-phase, smooth films (measured RMS roughness ~ 20% of YIG lattice parameter) with bulk-like magnetic properties and ultra-low damping (α = 2.2 - 7 x 10^{-4}). The large target-substrate distance enabled the growth of smooth YIG films. Low surface roughness helps reduce magnon scattering and overall damping value. YIG films with thicknesses ranging from 17 nm to 200 nm had saturation magnetization 137 emu cm^{-3} (5% error) with in-plane easy axis and coercivity ~ 2 Oe. The resonances obtained 7-13 GHz for a range of film thicknesses have linewidths narrower than those commonly reported in the previously.

The quality of the YIG films presented in this study alone is sufficiently superior to most other YIG films, such that simply fabricating the spin wave devices again with the YIG film growth recipe presented here is going to improve the device performance. We expect magnonic logic devices, sensors, and other devices that transport, store and process microwave and digital information with low power and at high density [5,14-17,31] may benefit from this study. In addition, fundamental magnetic phenomena such as spin-Seebeck effect, magnetization dynamics, domain wall dynamics, or on-chip quantum teleportation mechanisms can be investigated more precisely [18].

Substrate orientation dependence of Gilbert damping of YIG films
(done in collaboration with A. Kehlberger and Prof. M. Kläui from University of Mainz, Germany)

In this part, we present the substrate orientation dependence of structural, magnetic and damping properties of YIG and Ce:YIG ($Ce_1Y_2Fe_5O_{12}$) films grown. YIG films were grown on GGG (001) and GGG (111) substrates at the same time inside the same chamber using the recipe presented in the previous part. Ce:YIG films were grown on GGG (001) and GGG (111) substrates at the same time inside the same chamber using the recipe presented in the

previous part, except that the oxygen pressure during growth was 5 mTorr.

Table 4-4. Structural properties of YIG and Ce:YIG films measured using HRXRD, XRR and SQUID magnetometry

Sample	OP lattice constant (Å) ± 0.01 Å	Film peak FWHM (mdeg) ± 0.2 mdeg	Thickness (XRR) (nm) ± 1 nm	Surface roughness (XRR) (nm)	M_s ($kA \cdot m^{-1}$ or $emu \cdot cm^{-3}$)
YIG/GGG (001)	7.0×10^{-4}	0.7×10^{-4}	9.0	0.8	4.0
YIG/GGG (111)	5.8×10^{-4}	0.5×10^{-4}	5.3	0.5	1.2
Ce:YIG/GGG (001)	4.1×10^{-4}	0.5×10^{-4}	4.8	0.5	1.8
Ce:YIG/GGG (111)	4.1×10^{-4}	0.5×10^{-4}	4.4	0.6	1.5

XRD was used to determine if there are secondary phases inside the crystals and to measure the OP lattice constants. XRD does not indicate any secondary iron oxide or ceria phases. XRR was used to measure the film thicknesses within ± 1 nm. The surface roughnesses were extracted from XRR and compared with surface roughness results from atomic force microscopy. Table 4-4 lists the OP lattice parameters of the films with ± 0.01 Å error, which were extracted from coupled ω - 2θ scans shown on Fig. 4-6. In addition, the full-width at half-maxima of the film peaks were also measured as a comparison of the relative relaxation of the films. Atomic force microscopy indicates that the RMS surface roughnesses of the films are 0.3 nm for both orientations of Ce:YIG, even less than the roughness prediction made using the model that fits the XRR measurement. Magnetic hysteresis loops and saturation moments were measured using SQUID magnetometry and listed on Table 4-4. Magnetic saturation moments of the films grown on GGG (111) are slightly higher than the films on GGG (001) substrates. In addition, Ce:YIG films have about 10% higher net magnetic saturation moment than YIG films. Y^{3+} ions are not magnetic. Ce^{3+} ions distort the octahedral coupling of Fe^{2+} and Fe^{3+} ions, leading to an increase of the magnetic moment.

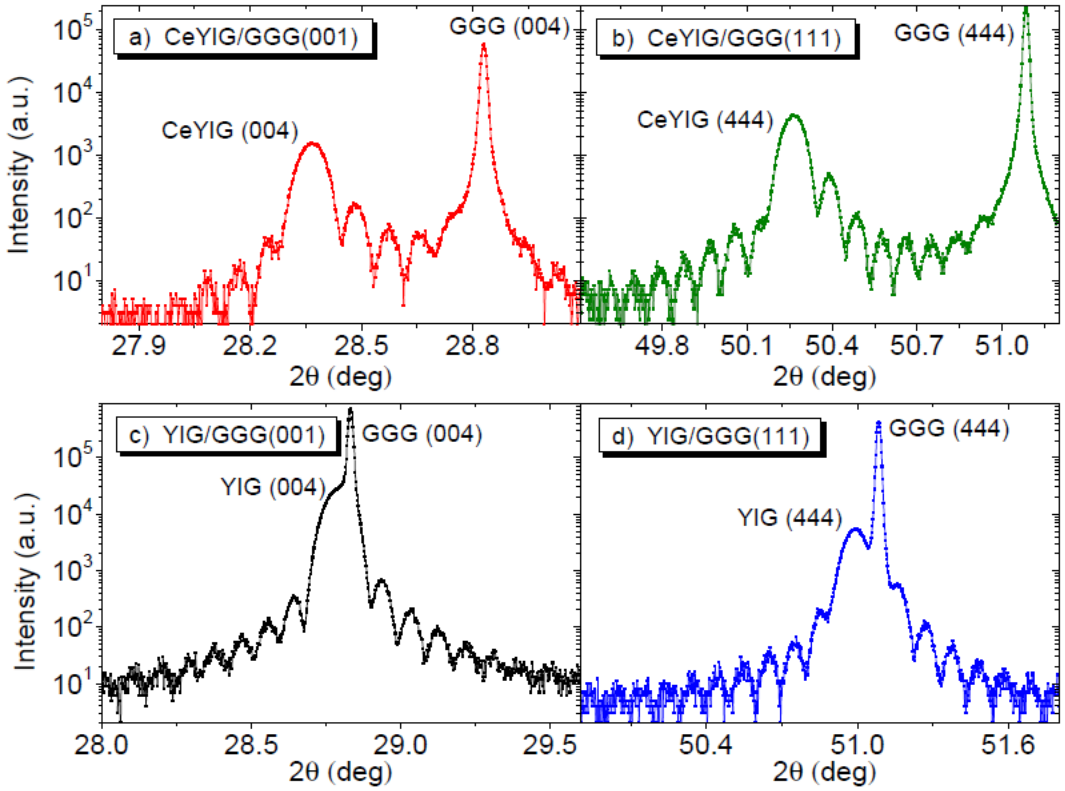

Fig. 4-6: Coupled ω - 2θ scans for each sample: Ce:YIG films on (a) GGG (001) and (b) GGG (111), YIG films on (c) GGG (001) and (d) GGG (111). (XRD measurements were done by Dr. Andreas Kehlberger).

Table 4–5 indicates the FMR linewidths and damping values extracted for YIG and Ce:YIG films on GGG (001) and GGG (111) substrates. Compared with the linewidths presented in the previous section (YIG thickness dependence of α), here, linewidths of YIG films are similar. YIG on GGG (111) has a twice as high a linewidth and a damping compared with YIG films. This difference can be due to the difference spin wave scattering properties of different terminations of the YIG crystal. The Ce:YIG films on GGG (001) have 2 orders magnitude wider linewidth and higher damping compared with YIG on GGG (001). These properties indicate that Cerium substitution enhances spin wave scattering significantly. In addition, the damping of the Ce:YIG on GGG (111) is about a factor of 2 higher than that for Ce:YIG on GGG (001). Since damping increases by a factor of 2 when YIG or Ce:YIG is grown on GGG (111) instead of GGG (001), one can estimate that the crystalline orientation is responsible for this increase. As spin waves need to traverse the garnet octahedra diagonally, short range coupling is weaker and the spin wave may decay faster (to yield

higher α). More precise atomic-scale spin-wave simulations need to be done to describe the effect of substrate orientation precisely.

Table 4-5. Linewidth and damping of YIG and Ce:YIG films on GGG (001) and (111)

Sample	$\mu_0\Delta H_0$ (mT)	α (10^{-4})
YIG/GGG (001)	0.24 ± 0.04	2.6 ± 0.4
YIG/GGG (111)	0.41 ± 0.06	4.4 ± 0.7
Ce:YIG/GGG (001)	22 ± 4	200 ± 40
Ce:YIG/GGG (111)	-2.9 ± 3	480 ± 70

Fig. 4-7 shows the ferromagnetic S_{21} resonances for (a) Ce:YIG films and (b) YIG films on GGG (111) and GGG (001) substrates. There is two orders of magnitude difference between the linewidths of Ce:YIG resonances and YIG resonances as shown on Fig. 4-7(a) and (b). This difference is an indicator of two orders of magnitude damping difference, as analyzed in Fig. 4-7(c). Ce:YIG has Gilbert damping on the same order as permalloys (~$2\text{-}5\cdot10^{-2}$). Therefore, Ce:YIG is simply not very advantageous in terms of damping properties, however, Ce:YIG has a different advantage with respect to YIG films: Ce:YIG has a strong magneto-optical Faraday and Kerr effect response. As a result, one can use magneto-optical Kerr effect microscopy to study domains in Ce:YIG *in situ* while the magnons propagate.

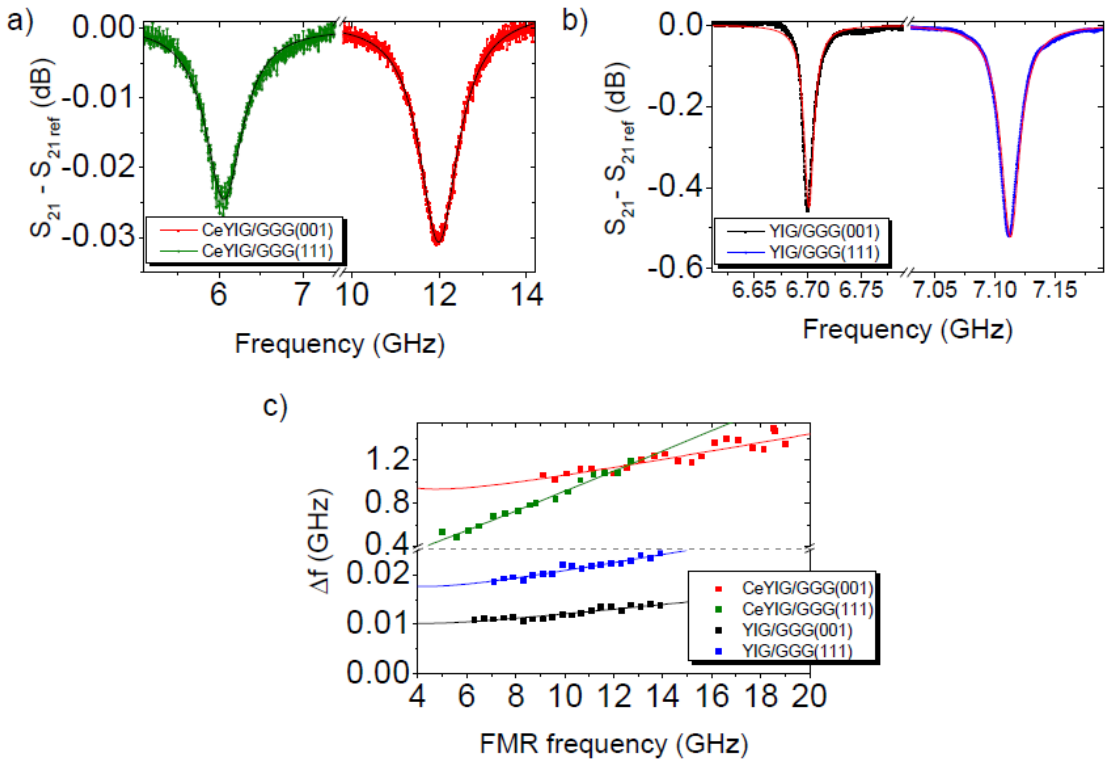

Fig. 4-7: Ferromagnetic resonance S_{21} dips for (a) Ce:YIG and (b) YIG films on GGG (111) and on GGG (001). (c) Δf versus FMR excitation frequency for each sample. The slope of the linear fits yields the damping α (note the change of vertical scale for Ce:YIG).

Room-temperature perpendicular magnetic anisotropic garnet ($Tm_3Fe_5O_{12}$) films on GGG (111)

In this part, we present the demonstration of a ferromagnetic iron garnet that has out-of-plane easy axis at room temperature. In most ferrimagnetic iron garnets, shape anisotropy is the strongest dominant term that determines the overall magnetic anisotropy. Typically, most iron garnets have an out-of-plane saturation field of $H_{saturation}$ (OP) = 2000 Oe, Therefore, one needs to redesign the iron garnet (i.e. YIG) such that a new anisotropy term with a negative sign is going to balance and even compensate the strong shape anisotropy. Kubota et al. previously suggested using different rare-earth ions instead of Yttrium such that the new ion with a large and negative magnetostriction constant (λ_{111}) is going to provide the necessary term for overcoming the shape anisotropy. The effective anisotropy field term, H_A, from magnetostriction of the new rare-earth element is defined as:

$$H_A = \frac{-4K_1 - 9\lambda_{111}\sigma_{||}}{3M}$$

Where K_1 is the first-order cubic anisotropy constant and $\sigma_{||}$ is the in-plane stress and M is the magnetic moment of the ion. Fig. 4-8 (from [6]) compares the magnetostriction constants of rare-earth ions. The ions with open circles have compensation temperatures near room temperature, which reduces their magnetism and usefulness. Therefore, only the ions with red dots are useful. One also needs to consider in-plane strains that are experimentally feasible (within ± 0.5%). The requirements on λ_{111} and in-plane strain eliminate all of the ions except Thulium (Tm). For Tm, H_A = +25kOe for TmIG/GGG (111)) when the in-plane strain is (+0.49%) and for stress of +1.4GPa. Since $H_A > H_{saturation}$ (OP), it is possible to overcome the shape anisotropy with reasonable in-plane strain when Tm is used instead of Y.

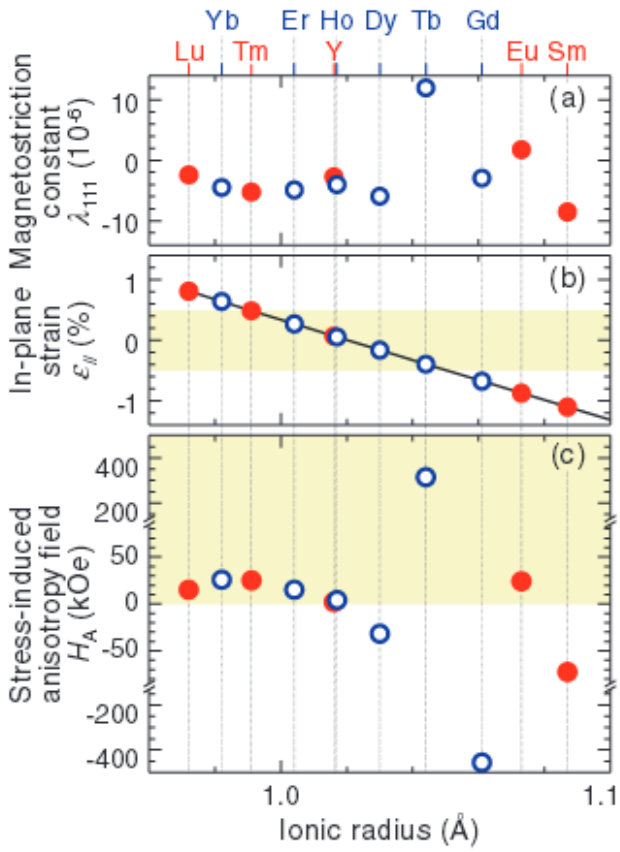

Fig. 4-8: Magnetostriction constants, in-plane strains and H_A (stress-induced anisotropy) terms for different rare-earth ions for iron garnets [6].

TmIG ($Tm_3Fe_5O_{12}$) PLD targets were fabricated to test the anisotropy of TmIG on GGG and Si substrates. The fabrication conditions for TmIG target are presented in Chapter 2 (section 2.1.2). Using the PLD target of TmIG, 19.16 nm-thick TmIG films were grown on

GGG (111) substrates at base pressure of 1 μTorr, $T_{substrate}$ = 730°C, growth rate of 0.072 nm·min^{-1} (20 nm for 500,000 laser pulses @30 Hz) under 20 mTorr oxygen pressure during growth. TmIG films on GGG (111) substrates are under in plane tension. For this sample, XRD did not indicate any secondary phases such as thulium oxide or iron oxide. Fig. 4-9 shows the room temperature IP and OP magnetic hysteresis loops of one TmIG film. The films on GGG (111) have $H_{saturation}$ (OP) ~ 400 Oe and $H_{saturation}$ (IP) near 3000 Oe. The saturation magnetic moment moment is 114 emu · cm^{-3}, which is also the M_s reported in the literature for bulk TmIG.

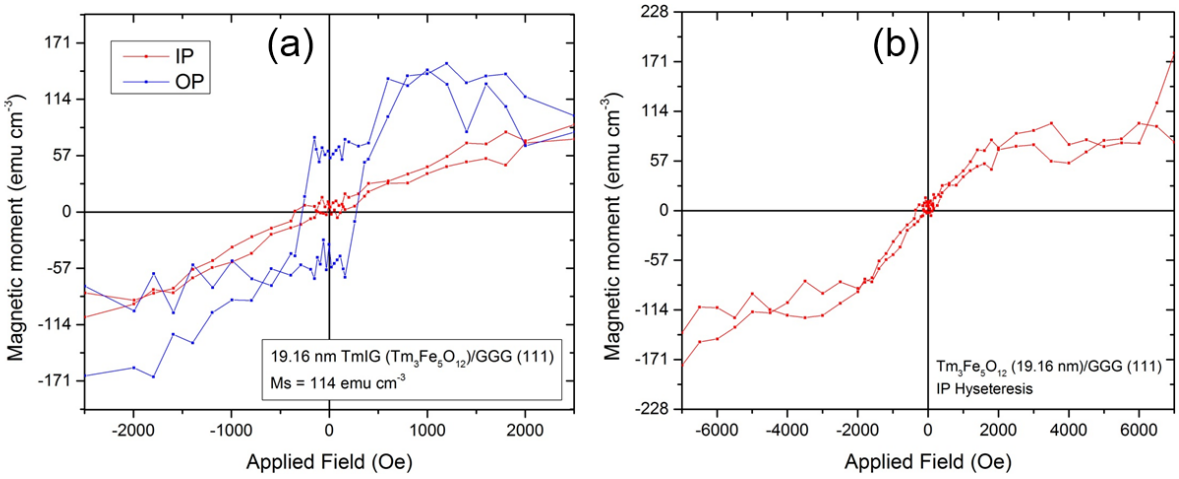

Fig. 4-9: Room-temperature magnetic hysteresis loops of $Tm_3Fe_5O_{12}$ film (19.1 nm thickness) on GGG (111), (a) in-plane and out-of-plane hysteresis loops shown together, (b) IP hysteresis.

TmIG ($Tm_3Fe_5O_{12}$) PLD targets were fabricated to test the anisotropy of TmIG on GGG and Si substrates. The fabrication conditions for TmIG target are presented in Chapter 2 (section 2.1.2). Using the PLD target of TmIG, 19.16 ± 0.1 nm-thick TmIG films were grown on GGG (111) substrates at base pressure of 1 μTorr, $T_{substrate}$ = 730°C, growth rate of 0.072 nm·min^{-1} (20 nm for 500,000 laser pulses @30 Hz) under 800 mTorr oxygen pressure during growth. For this sample, XRD did not indicate any secondary phases such as thulium oxide or iron oxide. Fig. 4-9 shows the room temperature IP and OP magnetic hysteresis loops of one TmIG film. The films on GGG (111) have $H_{saturation}$ (OP) ~ 400 Oe and $H_{saturation}$ (IP) near 3000 Oe. The saturation magnetic moment moment is 114 emu · cm^{-3}, which is also the M_s reported in the literature for bulk TmIG [33].

Magnetic properties of TmIG films are highly sensitive to oxygen pressure and substrate temperature during film growth. Since Tm is a much heavier ion than Y (Tm atomic weight: 168.9 g · mol^{-1}, Y atomic weight: 88.9 g · mol^{-1}), the PLD plume for TmIG is also much smaller than the plume of YIG (less than a third in volume). In addition, the original reference that first suggested the growth of TmIG on GGG (111) [6] demonstrated the growth of films at 800 mTorr, which decreases the growth rate even below 0.1 nm·min^{-1}. While TmIG need to be grown under high oxygen pressure to minimize oxygen vacancies and retain stoichiometry, an optimization of magnetic properties of TmIG with respect to deposition oxygen pressure can help improve deposition rate of TmIG. A lower thermal budget growth of TmIG films with thicknesses up to 200 nm (i.e. in less than 2 hours) can help improve the compability of TmIG with other materials for spin-wave devices.

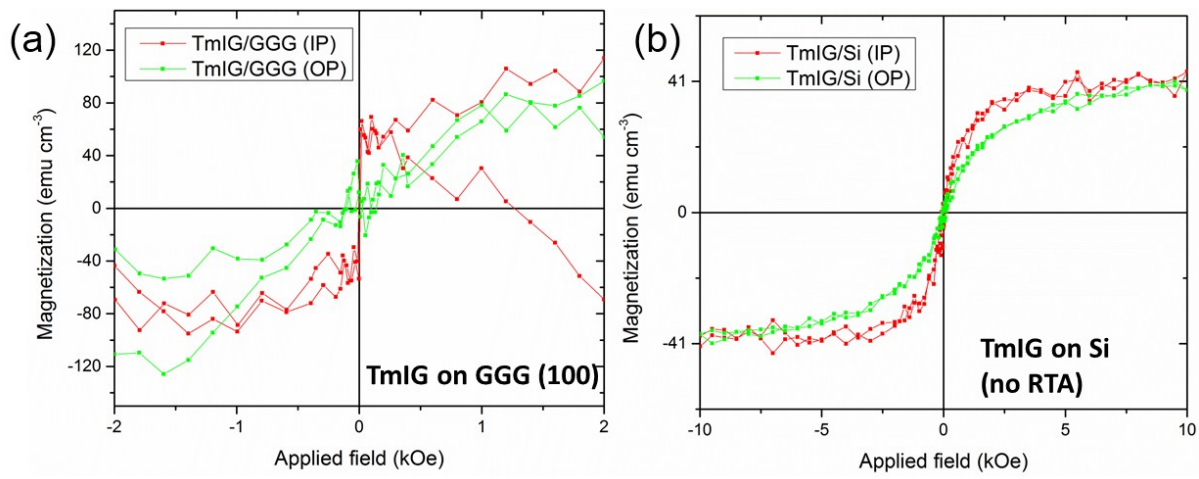

Fig. 4-10: Room-temperature magnetic hysteresis loops (IP and OP) of $Tm_3Fe_5O_{12}$ films grown on (a) GGG (100) and (b) Si.

In a separate deposition run, 30 nm thick TmIG was also grown on GGG (100) and on Si substrates and their IP and OP magnetic hysteresis loops were measured at room temperature, as shown on Fig. 4-10. The film on GGG (100) is not perpendicular magnetic anisotropy film, but instead the film prefers IP magnetization. This is an indication that λ_{100} TmIG films on Si may not be in pure garnet phase as the anisotropy properties of this film is close to isotropic. Since the measurements are noisy, there is also a need to establish a more refined VSM

measurement protocol by optimizing the measurement recipe, sample and sampleholder cleaning routines.

4.2 Summary

For spin wave propagation across long distances on spin-wave chips (several hundred μm's laterally) and without Ohmic losses at frequencies beyond 5 GHz, the development of ultralow damping garnet thin films is essential. In this chapter, we studied iron garnet growth and presented a recipe for YIG films with low Gilbert damping. In the first part, we discussed the thickness dependence of Gilbert damping of YIG films on GGG (100) substrates. The PLD-grown YIG films with thicknesses ranging from 17-190 nm have damping values of α = 2.2 - 7 x 10^{-4} at room temperature and lower than most other YIG film damping reports. While these values are already useful for enhancing spin-wave device performance, one can still improve the YIG damping further by using GGG substrates with fewer defect densities, minimizing the garnet oxygen vacancy concentration. In the second part of this section, the effect of substrate orientation (GGG (001) and GGG (111)) and Cerium substitution at Yttrium sites were investigated. When one uses GGG (111) instead of GGG (001) substrate for growing YIG or Ce:YIG films, the damping typically increases by a factor of two. This difference is attributed to weaker coupling of Fe spins across the diagonal direction of garnet unit cell and surface termination difference. Cerium substitution on Yttrium sites with $Ce_1Y_2Fe_5O_{12}$ atomic ratios broadens FMR linewidth and increases damping by two orders of magnitude with respect to YIG. Ce:YIG damping, however, is still useful and on the same order of magnitude with permalloys. As a magnetic insulator which has a usefully low damping and which enables magneto-optical Kerr microscopy imaging of domains and propagating spin waves, Ce:YIG offers testing new magnetic phenomena such as spin Seebeck effect by MOKE or other optical means of probing. In the last part, the development of TmIG, the room temperature perpendicular magnetic anisotropic (PMA) magnetic insulator, was discussed. Dominant shape anisotropy of TmIG on GGG (111) is overcome by large negative sign magnetostriction of Tm ions. An experimental room temperature PMA demonstration was presented and opportunities for further improvement are discussed.

References

[1] M. B. Jungfleisch, A. V. Chumak, A. Kehlberger, V. Lauer, D. H. Kim, M. C. Onbasli, C. A. Ross, M. Kläui, and B. Hillebrands, *Phys. Rev. B* **91**, 134407 (2015).

[2] A. Kehlberger, G. Jakob, M. C. Onbasli, D. H. Kim, C. A. Ross, M. Kläui, *J. Appl. Phys.* **115**, 17C731 (2014).

[3] A. Kehlberger, U. Ritzmann, D. Hinzke, R. Röser, G. Jakob, M. C. Onbasli, D. H. Kim, C. A. Ross, M. B. Jungfleisch, B. Hillebrands, U. Nowak, M. Kläui, "Length scale of the spin Seebeck effect", *(under review)*

[4] M. C. Onbasli, A. Kehlberger, D. H. Kim, G. Jakob, M. Kläui, A. V. Chumak, B. Hillebrands, C. A. Ross, *APL Mater.* **2**, 106102 (2014).

[5] S. Klingler, P. Pirro, T. Brächer, B. Leven, B. Hillebrands, A. V. Chumak, " Spin-wave logic devices based on isotropic forward volume magneto-static waves," arXiv:1503.04101 <http://arxiv.org/abs/1503.04101>

[6] M. Kubota, A. Tsukazaki, F. Kagawa, K. Shibuya, Y. Tokunaga, M. Kawasaki and Y. Tokura, *Appl. Phys. Express* **5**, 103002 (2012).

[7] Taichi Goto, M. C. Onbasli, C. A. Ross, *Opt. Express* **20**, 28517 (2012).

[8] L. Bi, J. Hu, P. Jiang, H. S. Kim, D. H. Kim, M. C. Onbasli, G. F Dionne, C. A Ross, *Materials* **6**, 5094 (2014).

[9] T. Goto, M. C. Onbasli, D. H. Kim, V. Singh, M. Inoue, L. C. Kimerling, C. A. Ross, *Opt. Express* **22**, 19047 (2014).

[10] M. C Onbasli, T. Goto, X. Sun, N. Huynh, C. A. Ross, *Opt. Express* **22**, 25183 (2014).

[11] X. Sun, Q. Du, T. Goto, M. C. Onbasli, D. H. Kim, N. M. Aimon, H. K. Choi, J. Hu, C. A. Ross, "One-step-deposition of cerium substituted yttrium iron garnet on an integrated optical isolator", (under review)

[12] T. Goto, D. H. Kim, X. Sun, N. M Aimon, M. C. Onbasli, J. M. Florez Uribe, K. Ackland, P. Stamenov, M. Inoue, M. Coey, G. F Dionne, C.A. Ross, "Magnetism and Faraday rotation in polycrystalline and single-crystal iron-substituted strontium titanate films deposited at different base pressures", (manuscript prepared)

[13] A. Kehlberger, K. Richter, G. Jakob, M. C. Onbasli, D. H. Kim, T. Goto, C. A. Ross, G. Götz, G. Reiss, T. Kuschel, M. Kläui, "Enhanced magnetooptic Kerr effect and magnetic properties of epitaxial CeYIG thin films", (under review)

[14] A. A. Serga, A. V. Chumak and B. Hillebrands, *J Phys. D: Appl. Phys.*, **43**, 264002 (2010).

[15] W. S. Ishak, *Proc. of the IEEE*, **76**, 171 (1988).

[16] H. Kurebayashi, O. Dzyapko, V. E. Demidov, D. Fang, A. J. Ferguson, and S. O. Demokritov, *Nat. Mater.* **10**, 660 (2011).

[17] A. V. Chumak, A. A. Serga and B. Hillebrands, *Nat. Comm.* **5**, 4700 (2014).

[18] J. R. Maze, "Nanoscale magnetic sensing with an individual electronic spin in diamond", Nature **455**, 644 (2008)

[19] B. Heinrich et al., *Phys. Rev. Lett.* **107**, 066604, (2011)

[20] C. Burrowes et al., *Appl. Phys. Lett.* **100**, 092403, (2012)

[21] Y. Sun et al., *Appl. Phys. Lett.* **101**, 152405 (2012)

[22] O. d'Allivy Kelly et al., *Appl. Phys. Lett.* **103**, 082408 (2013)

[23] C. Hahn et al., *Phys. Rev. B* **87**(17), 174417 (2013)

[24] M. B. Jungfleisch et al., arXiv:1308.3787
[25] Y. Sun et al., *Phys. Rev. Lett.* **111**, 106601 (2013)
[26] T. Liu et al., *J Appl. Phys.* **115**, 17A501 (2014)
[27] H. Kurebayashi, *Nat. Mater.,* **10**, 660 (2011)
[28] P. Pirro et al., *Appl. Phys. Lett.* **104**, 012402 (2014).
[29] M. Sparks, Ferromagnetic-Relaxation Theory (McGraw Hill, New York, 1964).
[30] B. Lax and K. J. Button, Microwave Ferrites and Ferrimagnetics (McGraw-Hill, New York, 1962).
[31] M. Lang et al., *Nano Lett.,* **14 (6)**, 3459 (2014).
[32] E. P. Wohlfarth, Ferromagnetic materials, A Handbook on the properties of magnetically ordered substances, Elsevier Science B. V., (2005) p. 42.

Chapter 5.
Room Temperature Multiferroic Materials

Perovskite oxides (ABO_3) have attracted significant research interest over the past decade since these materials offer at least two of the following functionalities inside the same material phase: ferromagnetism [1], ferroelectricity [2,3], piezoelectricity [4], thermoelectricity [5], catalysis [6], photovoltaic response [7], simultaneous transparency and conductivity [8], ultra-high melting point and the associated electronic band structure [9], lithium storage for the cathodes of batteries [10], superconductivity and 2D electron gas [11], colossal magnetoresistance [12], spin-dependent transport [13], magneto-optical activity [14], multiferroic response [15], magnetoelectric coupling [16] as a result strain state of the film (with the appropriate choice of substrate), changing the substitutional dopants, growth temperature and oxygen pressure, composite formation with spinel oxides. Perovskites typically have alkali or alkali earth metals on their A sites with a valence state of 1+ or 2+, and they have a transition metal on the B sites which can have valence state of 4+ or multivalent state. These materials can also be engineered to be oxygen-deficient, as discussed in chapter 3, in order to tune optical, magneto-optical, magnetic properties as well as electronic band structure for device functionalities.

In this chapter, we focus on the demonstration of ferroelectricity and magnetism inside the same perovskite phase. We substitutionally dope Cobalt on Ti sites of $SrTiO_3$ in order to induce magnetism. Having 30% Cobalt substitution on Ti sites is expected to distort the lattice structure of $SrTiO_3$ and cause a tetragonal distortion. In addition, Cobalt is thermodynamically more likely to have 2+ or 3+ valence states than the regular 4+ state of the B site ions. The charge neutrality requirement of each unit cell drives the formation of oxygen vacancies inside the bulk lattice to compensate for the mixed valence states of Cobalt ions. Earlier DFT simulations [17] indicate that increase in the oxygen vacancy concentration causes anisotropic expansion of perovskite lattice. This anisotropic expansion causes tetragonal crystal structure and B-site off-centering (and hence net spontaneous polarization).

This chemical strain approach helps induce tetragonal unit cell structure in the bulk $SrTi_{0.70}Co_{0.30}O_{3-\delta}$ crystal. Thus, one can avoid having to rely on substrate-induced strain effects and grow $SrTi_{0.70}Co_{0.30}O_{3-\delta}$ films with useful magnetic and ferroelectric properties on any substrate (other than polymer or paper substrates which cannot withstand high temperature growth processes). By growing films at different oxygen pressures, one can also engineer the oxygen vacancy concentration further and tune the magnetic, ferroelectric and electronic properties.

In the first part of this chapter, we focus on the unambiguous demonstration of multiferroic behavior in $SrTi_{0.70}Co_{0.30}O_{3-\delta}$ films on Si and insulating substrates (STO (100) and thick SiO_2). Next, we focus on magnetism and ferroelectricity of $SrTi_{0.70}Co_{0.30}O_{3-\delta}$ on Nb:STO substrates.

5.1 Multiferroic $SrTi_{0.70}Co_{0.30}O_{3-\delta}$ materials

5.1.1 $Sr(Ti_{0.7}Co_{0.3})O_{3-\delta}$-based multiferroic materials

As described in chapter 1, multiferroicity in perovskites is promising since this functionality can potentially offer short or long term data storage and processing operations that cannot be otherwise achieved by conventional semiconductors. A vast majority of the single-phase multiferroic materials are only multiferroic at low temperatures, or they are antiferromagnetic at room temperature reducing their usefulness significantly. In this section, we study the room temperature magnetic behavior and ferroelectricity in polycrystalline and single crystal Cobalt-substituted $SrTiO_3$ thin films ($SrTi_{0.70}Co_{0.30}O_{3-\delta}$, STCo30) on Silicon and on insulating substrates of $SrTiO_3$ (100) and thick SiO_2 films on Si. The films on Si were grown at different oxygen pressures to investigate the effect of change in the oxygen vacancy concentration on magnetism and ferroelectricity of the films.

Ferroelectric hysteresis and magnetoelectric coupling measurements, electrical resistivity,

current and capacitance vs. voltage, PUND tests, structural characterization (x-ray diffraction and photoelectron spectroscopy, transmission electron and atomic force microscopy) and density functional theory simulations indicate that STCo30 films are magnetic and ferroelectric. Magnetism originates from mixed-valence states of Cobalt ions associated with oxygen vacancies and shows an overall spin glass behavior. Within the resolution of XRD, XPS and TEM elemental mapping, no metallic Cobalt phases were observed. DFT calculations also rule out the possibility of Cobalt phases at 30% substitution, since the formation energy of metallic cobalt phases is higher than oxygen-deficient perovskite phases [17]. The oxygen vacancies and Co substitution lead to anisotropic lattice expansion, lowering the symmetry and producing net ferroelectric polarization.

Recent developments in the voltage-controlled magnetism and other magnetoelectric phenomena that can occur in multiferroic oxide thin films are promising experimental demonstrations for integrated memory and logic devices [15,18-25]. The ideal perovskite oxide material has to combine strong ferroelectricity (high saturation polarization P_s and remanent polarization P_r) with low saturation voltage (V_{sat} < 10V) and strong magnetism (high saturation magnetization M_s, remanent magnetization M_r and coercivity, H_c) with low saturation field (a few thousand Oe's) at room temperature, as well as coupling between the magnetic and ferroelectric order parameters, for integrated memory and logic applications.

Out of the wide range of multiferroic materials studied, many of them are multiferroic only at cryogenic temperatures [26], possess a less useful combination of antiferromagnetism and ferroelectricity at room temperature [27], or exhibit prohibitively high magnetic field or voltage bias points [28] for integrated device applications. As examples, $Bi_{0.75}Sr_{0.25}FeO_3$ [27] and $BiFeO_3$ and its derivatives [29,30] are both antiferromagnetic and strongly ferroelectric. Significant room-temperature multiferroicity and low-field magnetoelectric coupling has been observed in $Sr_4Co_2Fe_{36}O_{60}$ [31], $Sr_3Co_2Fe_{24}O_{41}$ [32] and Y-type $BaSrCo_{2-x}Zn_xFe_{11}AlO_{22}$ ceramics [33], and room temperature electric control of magnetism has been achieved in $SrCo_2Ti_2Fe_8O_{19}$ [34]. The ferroelectricity and magnetoelectricity of highly-insulating hexaferrites such as $Sr_3Co_2Fe_{24}O_{41}$ with spiral spin structures has been discussed in terms of

spin-current and the inverse Dzyaloshinskii–Moriya effects. In a moderate magnetic field, the transverse-conical spin component of the spin spiral leads to magnetic-field-induced polarization (magnetoelectric effect), but at higher magnetic fields, the spins become collinear and hence the polarization disappears. Multiferroic PZTFT, a solid solution of lead zirconium titanate, PZT, and lead iron tantalate, PFT) [35], showed magnetic switching of ferroelectric domains at room temperature. Cobalt-doping in small concentrations was shown to induce ferromagnetism [36] as well as magnetoelectric coupling [37] in TiO_2.

Control of magnetic substitution and oxygen stoichiometry in perovskites may offer the possibility of manipulating both ferroelectricity and ferromagnetism and a potential path towards room temperature magnetoelectrics. Substitutional doping of magnetic cations into the B sites of perovskite films has been shown to induce intrinsic magnetism without metallic precipitates, as in the case of $Sr(Ti,Co)O_{3-\delta}$ [17, 38-41] and $Sr(Ti,Fe)O_{3-\delta}$ [38,42-44]. In perovskites the magnetism depends on the oxygen vacancy concentration [45,46]. The cubic crystalline symmetry can be broken via lattice strain [47] and substitution with oxygen isotopes [48] which is expected to affect the magnetic and ferroelectric properties. Remarkably, $SrTiO_3$ (STO) films which were epitaxially grown in between conducting $SrRuO_3$ top and bottom contacts on STO (001) substrates have been demonstrated to undergo tetragonal distortion and have room-temperature ferroelectricity [49]. In that study, lower oxygen pressure during the growth of STO layer led to higher tetragonal distortion and higher remanent ferroelectric polarization, which were correlated with increasing oxygen vacancy concentration. By merging the advantages of substitutional doping of STO on the Ti sites to make the material magnetic [17, 38-44] and the advantages of chemical and epitaxial strain to induce tetragonal distortion [49], one can expect to get a room-temperature multiferroic oxide.

In this section, we demonstrate room-temperature magnetism and ferroelectricity in STCo30 thin films ($SrTi_{0.70}Co_{0.30}O_{3-\delta}$) deposited as single crystal or as polycrystalline films on Si and SiO_2. The magnetic moment was $M_s \sim 0.1 - 0.7\ \mu_B$/Co, polarization P_s up to 154 $\mu C \cdot cm^{-2}$, resistivity $\rho \sim 10^7 - 10^{11}\ \Omega \cdot cm$ at room temperature. The experimental results

on ferroelectricity and magnetism in STCo30 were quantitatively reproduced using density functional theory (DFT) simulations. The origins of magnetism and ferroelectricity in STCo30 differ from those of previously described magnetoelectric hexaferrites.

Table 5-1. Oxygen pressures, films thicknesses and properties of the samples prepared for this study. First four rows correspond to films on conducting substrates and the last 2 rows are for films on insulating substrates. All samples were grown under 1 μTorr base pressure and 650°C substrate temperature. $\rho_{effective}$ is the resistivity of films with substrate contribution.

Total Pressure at start of deposition (Torr)	**Film Thickness (nm)**	**Substrate**	**Sample name**	**$\rho_{effective}$ (Ω·cm) (V = 1V)**
1.0×10^{-6}	220	Si	STCo30/Si-1μTorr	1.54×10^{11}
3.0×10^{-6}	187	Si	STCo30/Si-3μTorr	1.04×10^{10}
6.0×10^{-6}	216	Si	STCo30/Si-6μTorr	1.02×10^{9}
1.6×10^{-3}	189	Si	STCo30/Si-1.6 mTorr	2.29×10^{8}
1.0×10^{-6}	243	STO (100)	STCo30/STO-1μTorr	3.4×10^{14}
1.0×10^{-6}	264	SiO_2	STCo30/SiO_2/Si-1μTorr	5.3×10^{14}

As described in chapter 2, the STCo films were grown by pulsed laser deposition (PLD) under different oxygen pressures from a stoichiometric STCo30 ceramic target using a 248 nm wavelength excimer laser. The target contained an atomic ratio of 30:70 Co:Ti, but the films had an atomic ratio of 23:77 Co:Ti [39]. We refer to the films as STCo30 in reference to the target composition. The STCo30 thin films were polycrystalline with native oxide of Si or on 3 μm-thick SiO_2-on-Si. Close to 30 STCo samples were made. Table 5-1 summarizes the representative samples described in this study, which were made during 5 PLD runs. The chamber was first pumped to a base pressure of 1 μTorr (this residual gas is assumed to include 20% oxygen) then growth was carried out at a substrate temperature of 650°C, and under different oxygen pressures shown in column 3 of Table 5-1. Samples were made on STO (100) with deposition pressures of 1 μTorr, and on thick SiO_2 at 1 μTorr. Samples were also grown on Si at 1, 3, 6μTorr and 1.6 mTorr pressures to experimentally test the DFT

predictions on the effect of oxygen vacancies on perovskite conductivity, ferroelectricity and magnetism. The sample thicknesses were 180 – 480 nm.

Magnetic characteristics of STCo30 films on Si and on insulating substrates

Fig. 5-1 shows room temperature (a) in plane (IP) and (b) out-of-plane (OP) magnetic hysteresis loops of the STCo30 films grown on Si under different oxygen pressures. All films show magnetic hysteresis with saturation moments (M_s) varying between 0.05 and 0.70 μ_B/Cobalt ion, and have an OP easy axis. Fig. 5-2 shows the IP and OP magnetic hysteresis loops the films on thick SiO_2, STO (100) and STO (110) substrates. These films have M_s between 0.06 – 0.50 μ_B/Co. The magnetic moment and anisotropy resemble those presented previously [39]. The magnetism occurs in films deposited at low pressures suggesting the presence of a substantial concentration of oxygen vacancies and lower-valence Co ions. The perpendicular easy axis anisotropy has been attributed to magnetoelastic effects, while the net moment suggests the presence of antiferromagnetic and ferromagnetic interactions between Co ions.

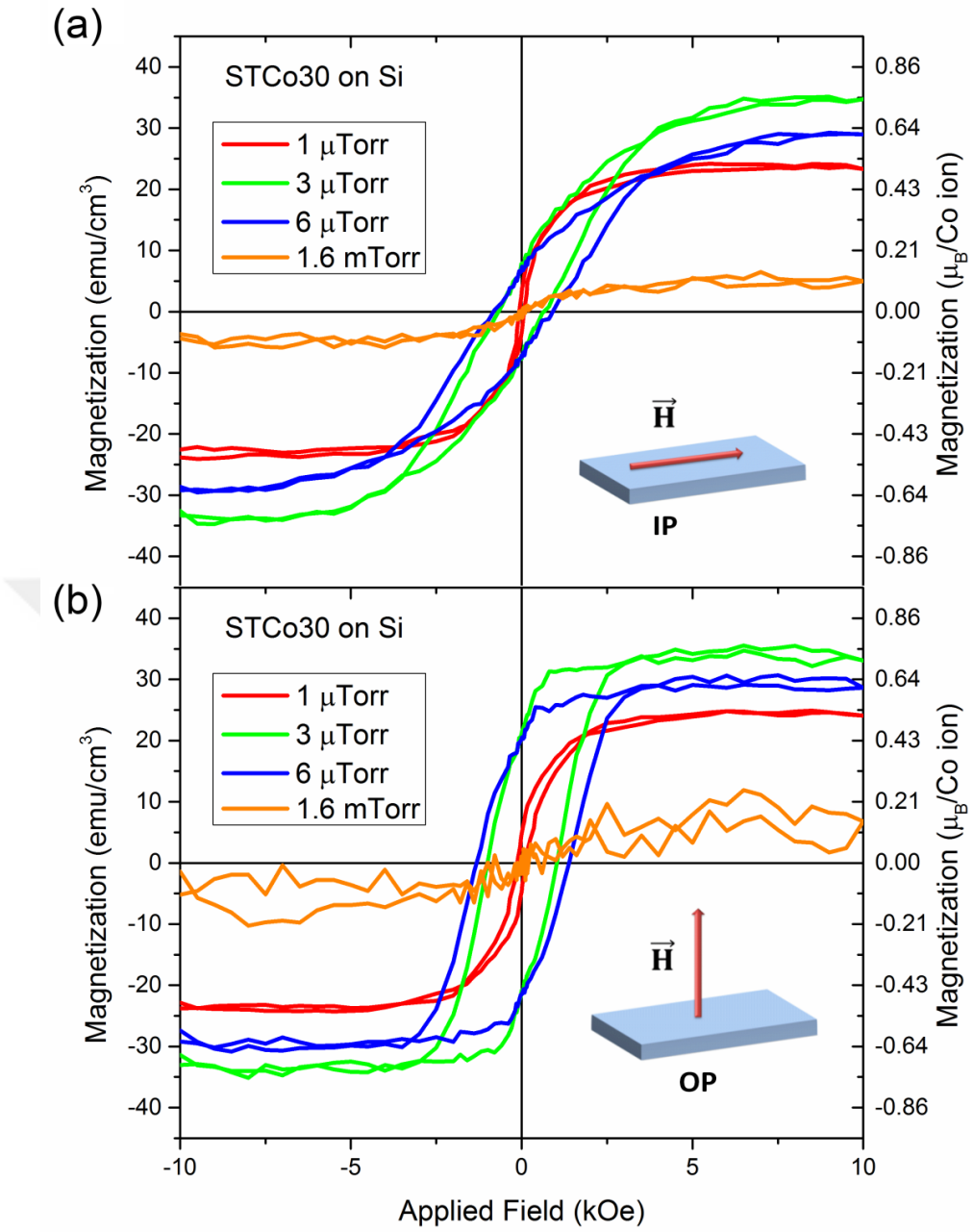

Fig. 5-1. Room-temperature magnetic hysteresis loops of STCo30 films. (a) In-plane (IP) and (b) out-of-plane (OP) magnetic hysteresis loops of STCo30 films grown at different oxygen pressures on Si.

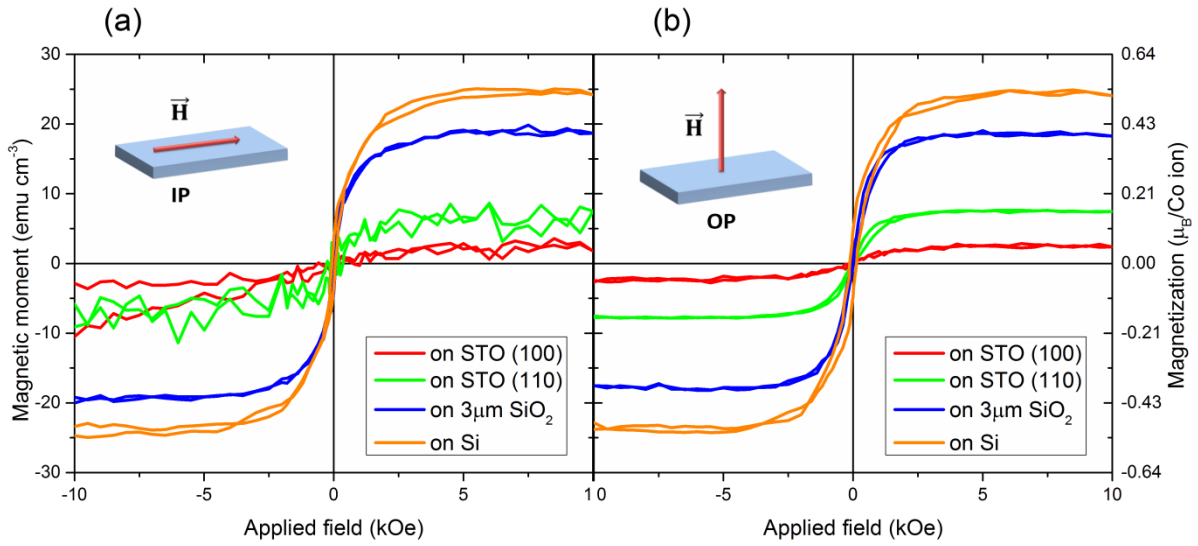

Fig. 5-2. (a) IP and (b) OP magnetic hysteresis loops of STCo30 films on STO (100) and (110), 3μm-thick SiO_2, and Si

Ferroelectric characteristics of STCo30 films on Si and on insulating substrates

Ferroelectric hysteresis loops of the samples are shown in Fig. 5-3. These hysteresis loops were measured between pairs of top contacts (V_+ and V_-, spacing: 350 μm, horizontal bias) and using a two probe measurement setup. Fig. 5-3(a) shows hysteresis loops of STCo30 films on thick SiO_2 and on STO (100) substrate. The saturation behavior, coercive voltage and ferroelectric saturation polarizations of STCo30 films resembles the room-temperature ferroelectric hysteresis loops of STO films presented previously [49]. The loops saturate properly with a linear dielectric substrate contribution. The dielectric component of STCo30, measured as $\varepsilon_r = 245$ (compared to $\varepsilon_r(SrTiO_3) = 300$), contributes a linear background to the P-V loop. The difference between the permittivity constants of the films and bulk $SrTiO_3$ is attributed to oxygen vacancies in the films. With higher oxygen pressure, the coercive voltage decreases, while saturation polarization increases.

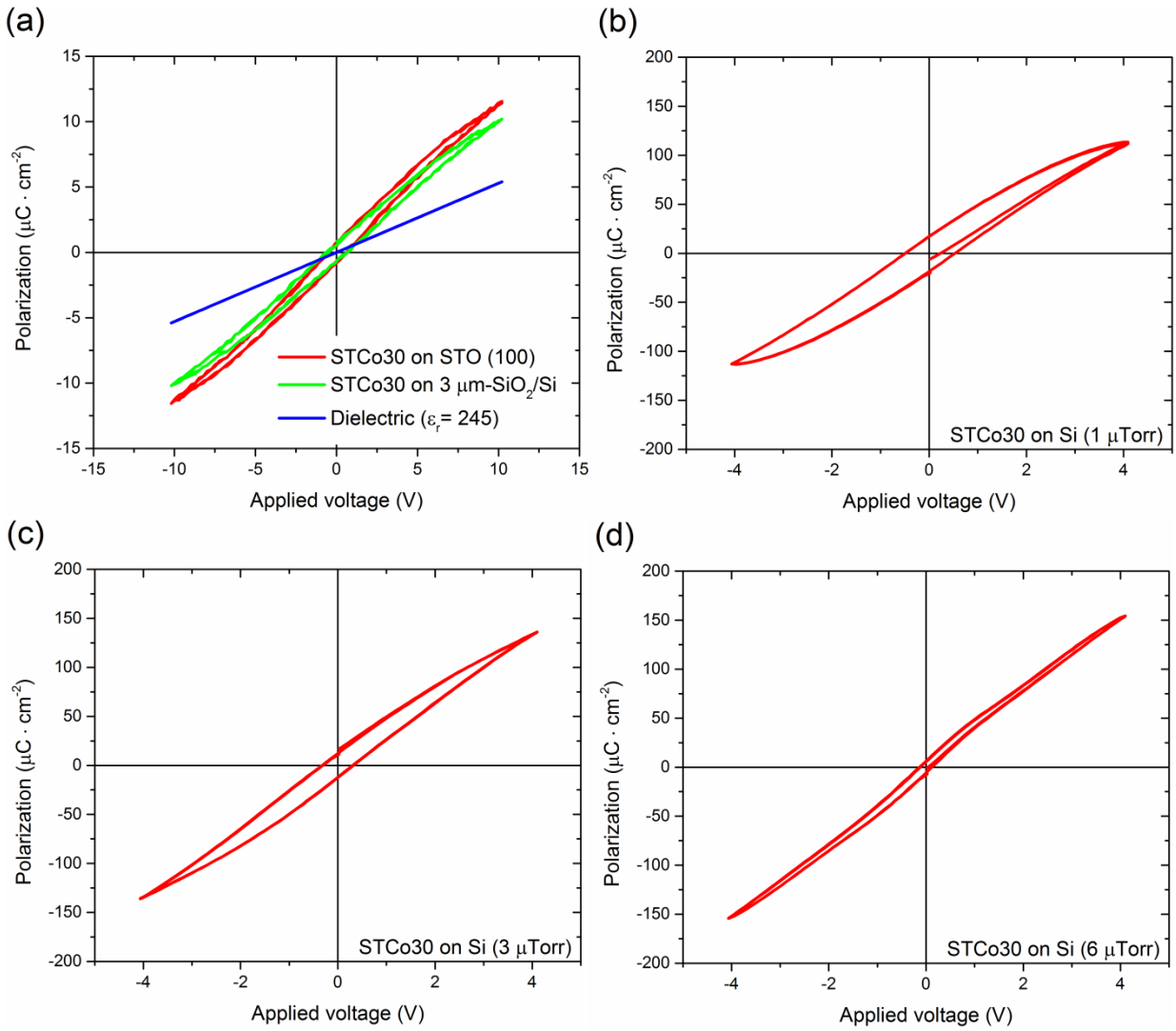

Fig. 5-3. Room-temperature ferroelectric hysteresis loops of STCo on (a) STO (100) and 3-μm-thick SiO_2-on-Si, and on (b) Si substrates grown at 1, 3 and 6 μTorr pressures (PO_2 = 0.2, 2.2 and 5.2 μTorr), respectively.

Capacitance-voltage (C-V) loops of these films indicate the characteristic ferroelectric switching behavior with minimal resistive leakage (less than 1 nA). An example C-V hysteresis loop is shown on Fig. 5-4. Due to the symmetric switching peaks near ±1.3V (similar to saturation voltages Fig. 5-3), we rule out any Schottky behavior. The measured ferroelectricity does not originate from Schottky contacts, because current-voltage characteristics (I-V curves) of each sample are linear and resistivities do not depend on voltage. Au/Ti work functions enable the formation of Ohmic contacts.

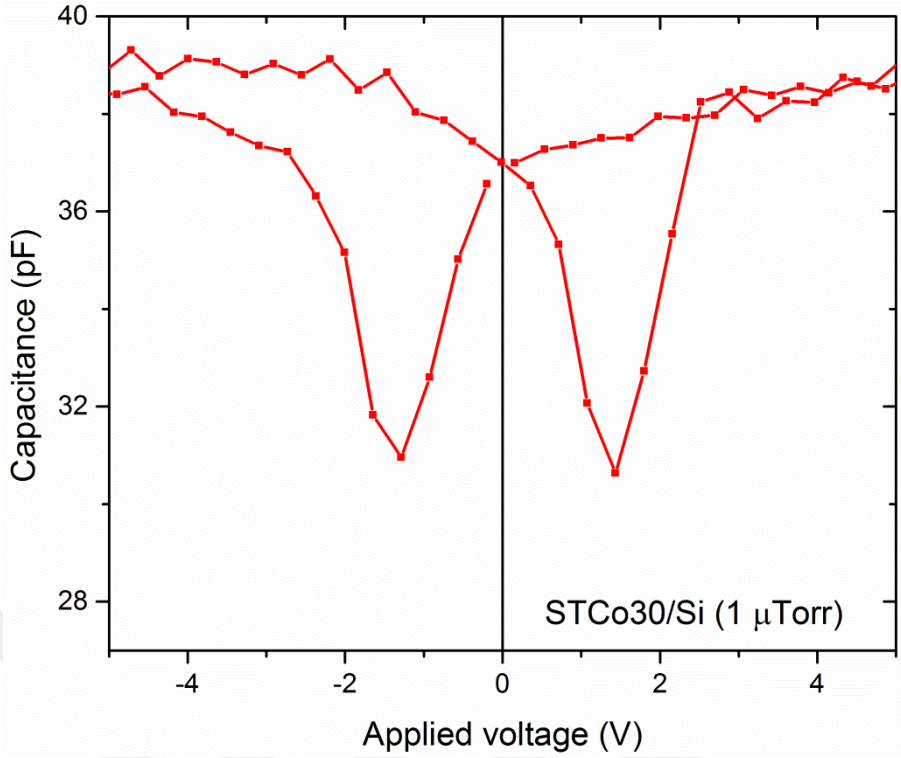

Fig. 5-4. Capacitance vs. voltage scan for STCo30 film grown on Si at 1 μTorr. Symmetric switching dips indicate ferroelectric behavior, low slope of the background indicates low resistive or capacitive leakage currents. (This measurement was done by Dr. Enno Lage).

In order to test the repeatability of the voltage cycling of polarization, PUND tests (positive up negative down) were done on the STCo30/Si samples. Fig. 5-5 shows the measured polarization and applied voltage as a function of time for each STCo30 film grown at 1, 3, 6μTorr and 1.6 mTorr. On the right hand column, the hysteresis loops corresponding to these samples are also presented. Polarization behavior of each sample on Fig. 5-5 shows that there is non-zero P_r (remanent polarization) and charge can be retained in the remanent state over periods (~35 ms) much longer than characteristic ionic diffusion times.

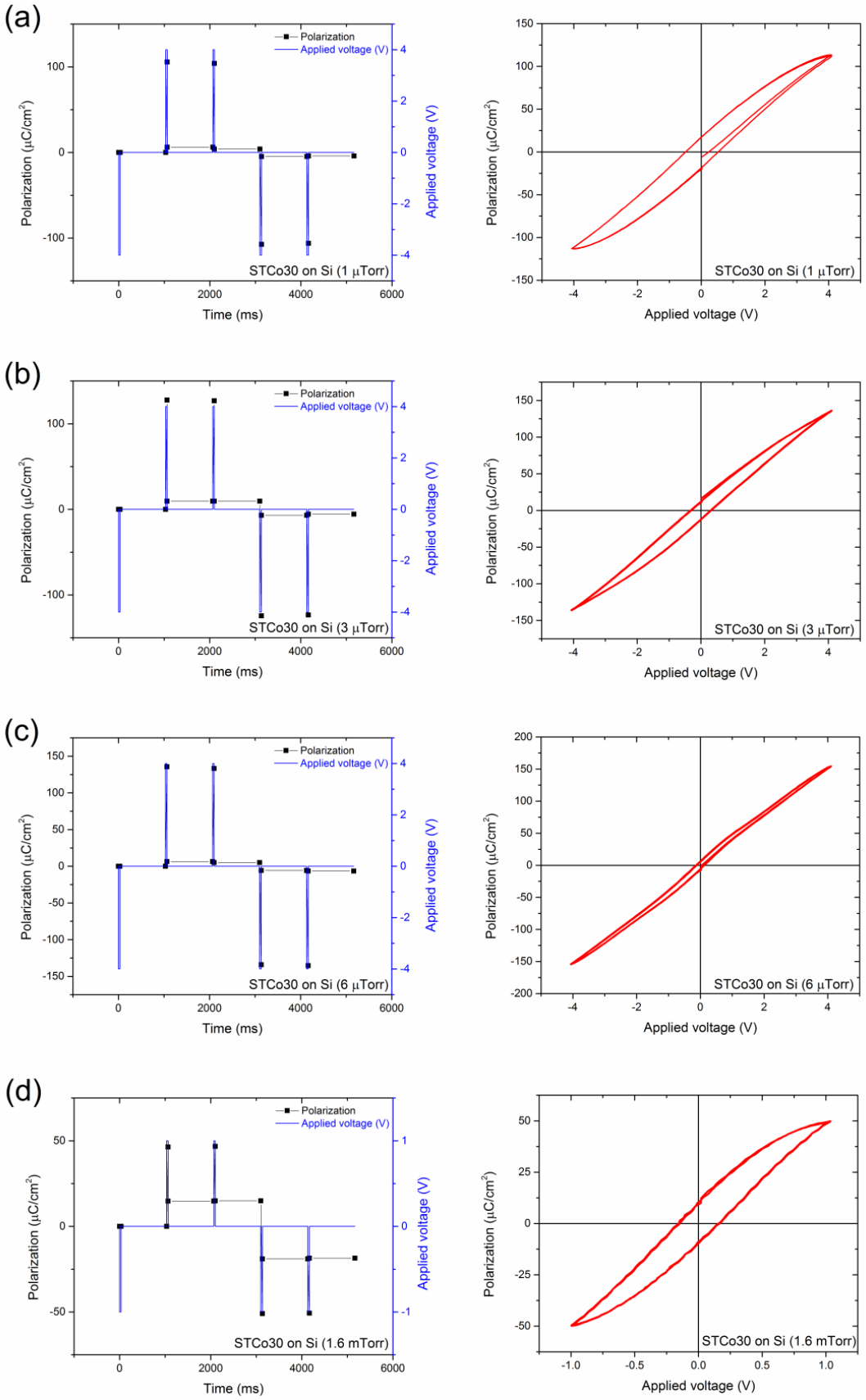

Fig. 5-5. PUND (positive up negative down) tests of STCo30 films on Si. PUND test plots for STCo30 films on Si grown at (a) 1, (b) 3, (c) 6 μTorr and (d) 1.6 mTorr with ferroelectric loops accompanying each PUND plot. Ferroelectric polarization is retained for periods much longer than a Schottky or a

back-to-back diode would retain.

Similarly for STCo30 films on SiO_2 and on STO (100), in order to test the repeatability of the voltage cycling of polarization, PUND tests were done. For films on SiO_2 and on STO (100), the overall film resistivities were measured to be $\rho_{STCo30} \sim 10^{14}$ Ω·cm. Fig. 5-6 shows the measured polarization and applied voltage as a function of time for STCo30 films grown on SiO_2 and on STO (100). On the right hand column, the hysteresis loops corresponding to these samples are also presented. Polarization behavior of each film on the insulating substrate shows that there is a repeatable non-zero P_r and charge can be retained in the remanent state over periods much longer than characteristic ionic diffusion times for films on insulating substrates as well.

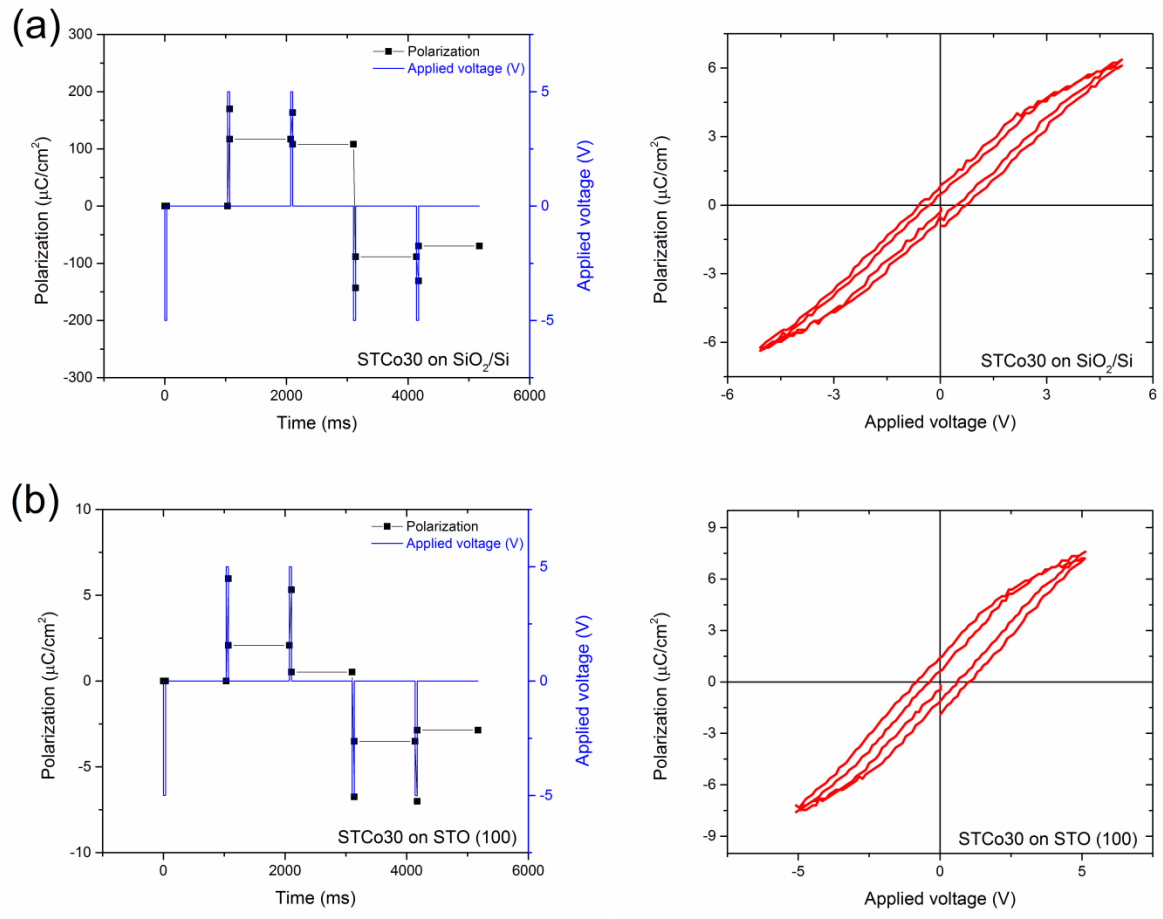

Fig. 5-6. PUND (positive up negative down) tests of STCo30 films on insulating substrates: (a) SiO2-on-Si, (b) STO (100). Ferroelectric polarization is retained for periods much longer than a Schottky or a back-to-back diode would retain.

In order to retain ferroelectric polarization for as long as possible, the resistivity of the

films must be maximized. Table 5-2 compiles the resistivity measurements of STCo30 films on Si, Nb:STO and on insulating SiO_2 and STO substrates. Since the resistivities of the film are ~10^7-10^{14} Ω·cm, the films are highly insulating.

Table 5-2. Oxygen pressures, films thicknesses and the magnetic, ferroelectric and electrical properties of the samples prepared for this study.

#	**Oxygen Pressure (Torr)**	**Thickness (nm)**	**Substrate**	**M_s (emu·cm^{-3})**	**P_s (μC·cm^{-2})**	**$2P_r$ (μC/cm^2)**	**Resistivity (Ω·cm) at 3V**
1	**< 1.0 x 10^{-6}**	220	Si	24.9	72	25.2	1.92 x 10^9
2	**< 1.0 x 10^{-6}**	220	Nb:STO	44.6	122.7	90	3.79 x 10^8
3	**3.0 x 10^{-6}**	187	Si	37	41.6	13	6.14 x 10^9
4	**3.0 x 10^{-6}**	187	Nb:STO	11.5	119.5	85	1.83 x 10^7
5	**6.0 x 10^{-6}**	216	Si	26.4	19	14.6	~10^9
6	**6.0 x 10^{-6}**	216	Nb:STO	41.8	106.8	94	2.40 x 10^7
7	**1.6 x 10^{-3}**	189	Si	5.6	50	20	~10^9
8	**1.6 x 10^{-3}**	189	Nb:STO	4.9	270	139	1.56 x 10^7
9	**< 1.0 x 10^{-6}**	243	STO (100)	18.5	8.6	1.36	3.47x 10^{14}
10	**< 1.0 x 10^{-6}**	530	STO (110)	7.5	28.5	22	1.22x 10^{10}
11	**< 1.0 x 10^{-6}**	264	SiO_2	2.6	5.8	1.67	5.32x10^{14}

Substrate contributions on magnetic and polarization switching characteristics

In addition, one also needs to characterize the substrate contibutions to magnetism, resistivity and ferroelectricity. Fig. 5-7 shows the polarization v. voltage hysteresis loop measurements for bare substrates. Since Si is a semiconductor, it has an imperfect leaky resistance behavior as shown on Fig. 5-7(a). Nb:STO substrates are conducting, however, these substrates also show a complicated saturated switching behavior that requires further investigation. Fig. 5-7(c) and (d) indicate the pure linear dielectric response in the polarization loops of the SiO_2/Si substrates and STO (100) substrates. Fig. 5-7(e) shows the polarization vs. voltage loop for STO (110). This substrate has a polar termination which contributes an intrinsic ferroelectric polarization.

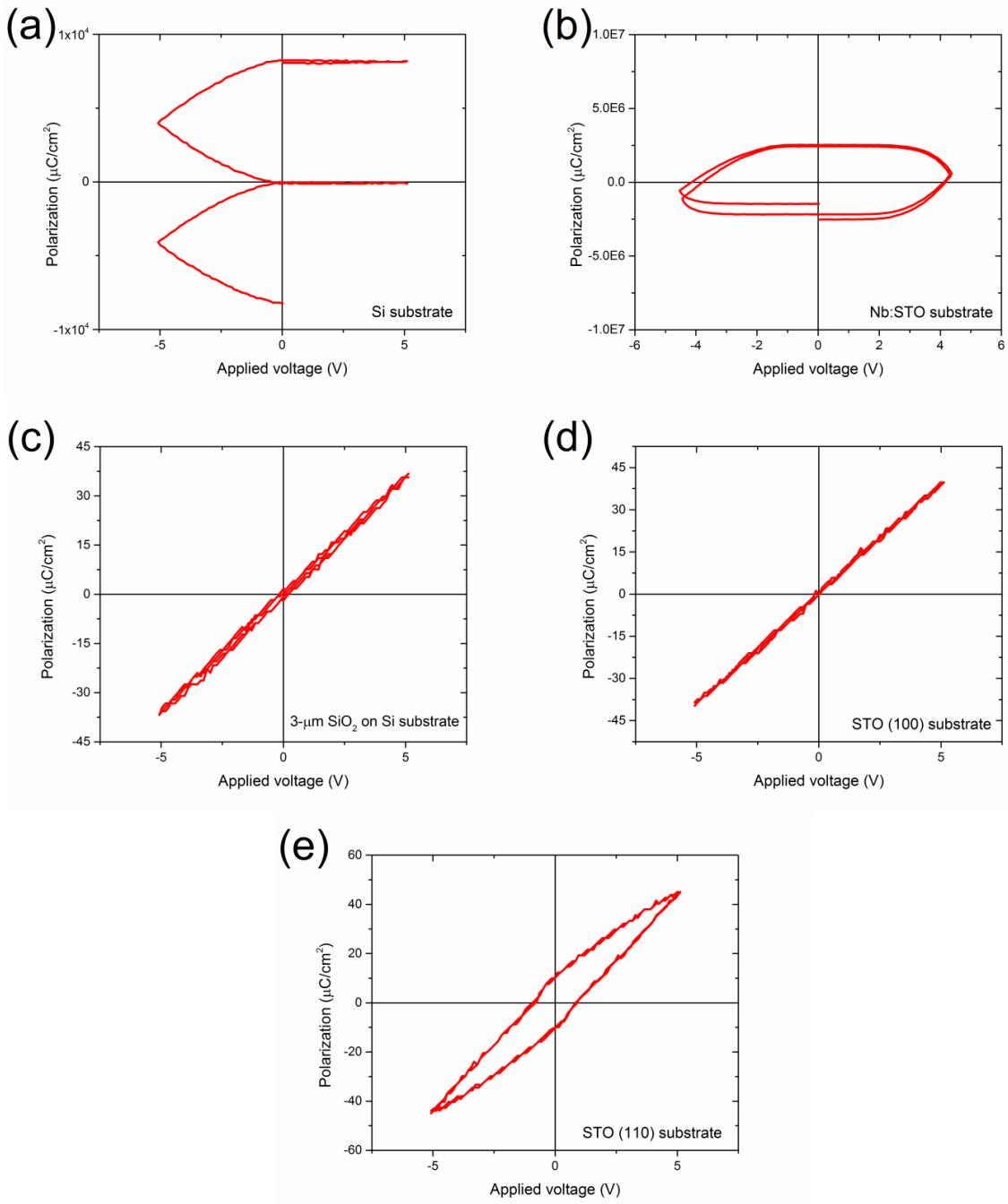

Fig. 5-7. Ferroelectric hysteresis loops of (a) Si, (b) Nb:STO, (c) SiO_2 on Si, (d) STO (100), (e) STO (110) each biased between up to 5V. Silicon is resistive and because of its conductivity, the loop does not close on itself. Nb:STO is a leaky oxide with ferroelectricity below 0.35V. SiO_2 on Si and STO (100) substrates are dielectric materials with linear P-V curves. STO (110) yields ferroelectric hysteresis due to its polar surface.

In another experiment, the substrate contribution to magnetism was investigated after annealing the bare substrates at high temperature and in vacuum with the same PLD recipe used for depositing STCo30 films, except that the films were this time not deposited. Bare

STO, Si, SiO_2 and Nb:STO substrates were loaded into the PLD chamber and the chamber was pumped down, heated up, pumped down again to the base pressure (heating causes outgassing at high temperatures), annealed for as long as the deposition time and then cooled down. Fig.5-8 and Fig. 5-9 show the IP and OP magnetic hysteresis loops of the STO (100) and STO (110) substrates. Fig. 5-10 shows the IP magnetic hysteresis loops of the Nb:STO substrates before and after annealing. The magnetization changes or the change of the substrate background signals are negligible and at least two orders of magnitude lower than the magnetic moments of the films. Therefore, the substrate contribution to magnetism is also ruled out.

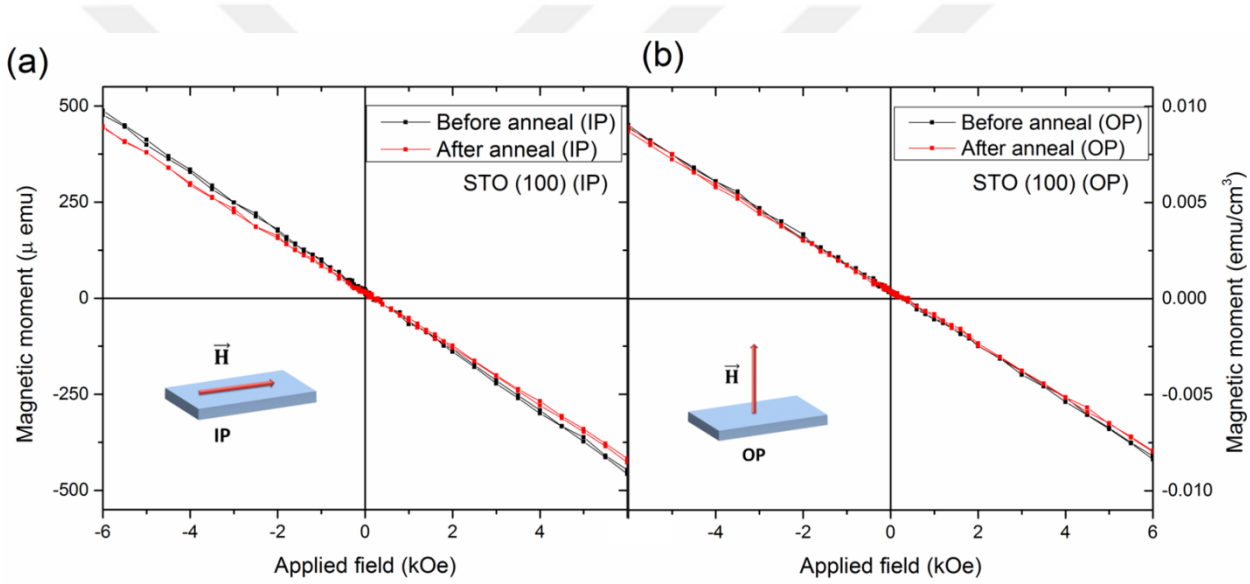

Fig. 5-8. (a) IP and (b) OP magnetic hysteresis loops of STO (100) substrate before and after annealing in the PLD chamber with the same chamber parameters as in STCo30 (except that the film was not grown). The vertical axis is in units of 10^{-6} emu.

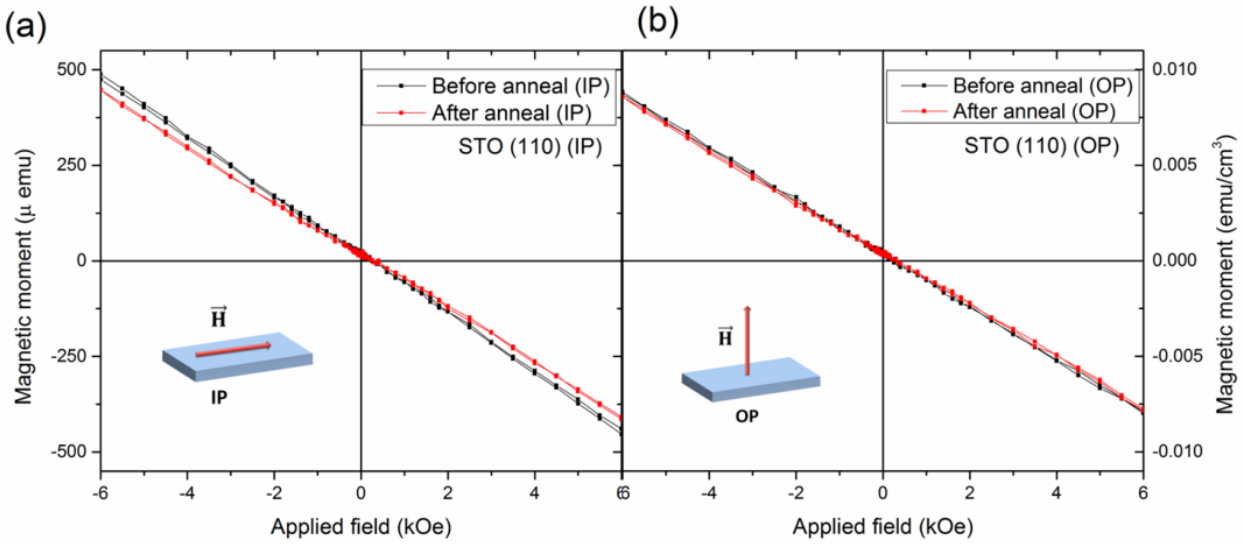

Fig. 5-9. (a) IP and (b) OP magnetic hysteresis loops of STO (110) substrate before and after annealing in the PLD chamber with the same chamber parameters as in STCo30 (except that the film was not grown). The vertical axis is in units of 10^{-6} emu.

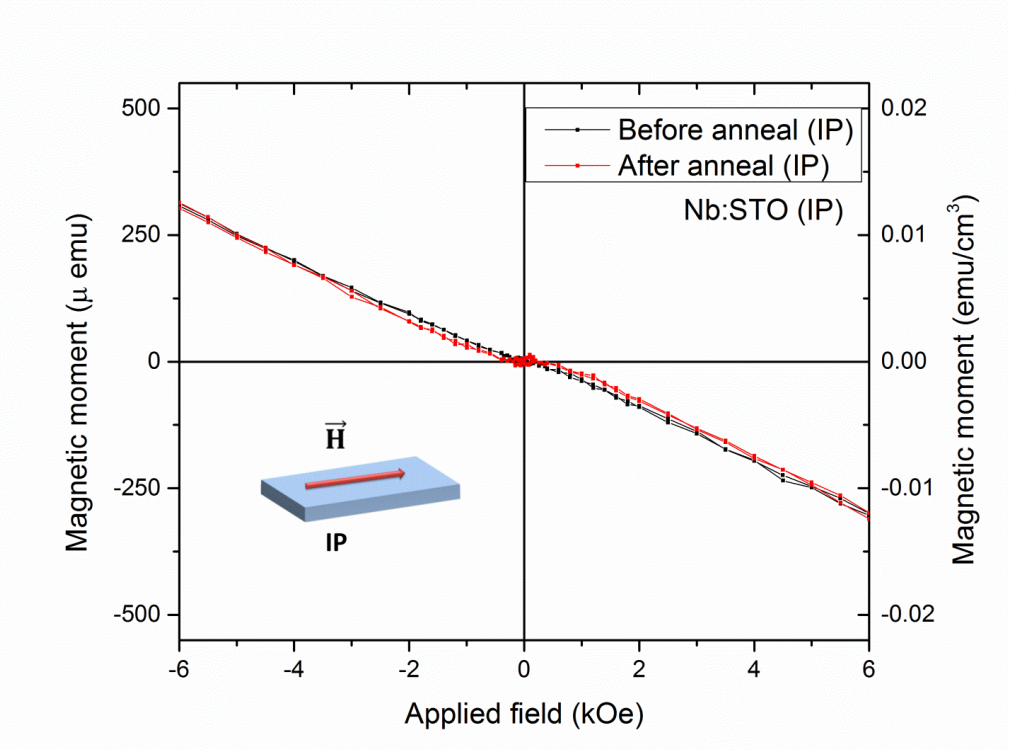

Fig. 5-10. IP magnetic hysteresis loops of Nb:STO substrate before and after annealing in the PLD chamber with the same chamber parameters as in STCo30 (except that the film was not grown). The vertical axis is in units of 10^{-6} emu.

In order to quantify the contributions of Cobalt substitution and oxygen vacancies into the magnetism of STCo30 films, pure $SrTiO_3$ (STO) films were grown on Si, SiO_2, STO (100), STO (110) and on Nb:STO substrates using the same growth recipe. Fig. 5-11 shows (a)

IP and (b) OP room temperature magnetic hysteresis loops of STO films. Comparing with Fig. 5-1 and 5-2, the magnetic saturation moment of STO films are one order of magnitude lower than STCo30 films on all substrates except STCo30 on STO (100) and (110). In addition, STO films are almost isotropic. Therefore, Cobalt contribution is indeed critical in inducing magnetic anisotropy. Since Cobalt ions and oxygen vacancies are coupled [17], one needs to consider the coupled Co-oxygen vacancy interaction (rather than 'a linear sum' of contributions to magnetism) that distorts the STCo30 unit cell. This interaction is going to be discussed in the DFT simulations part.

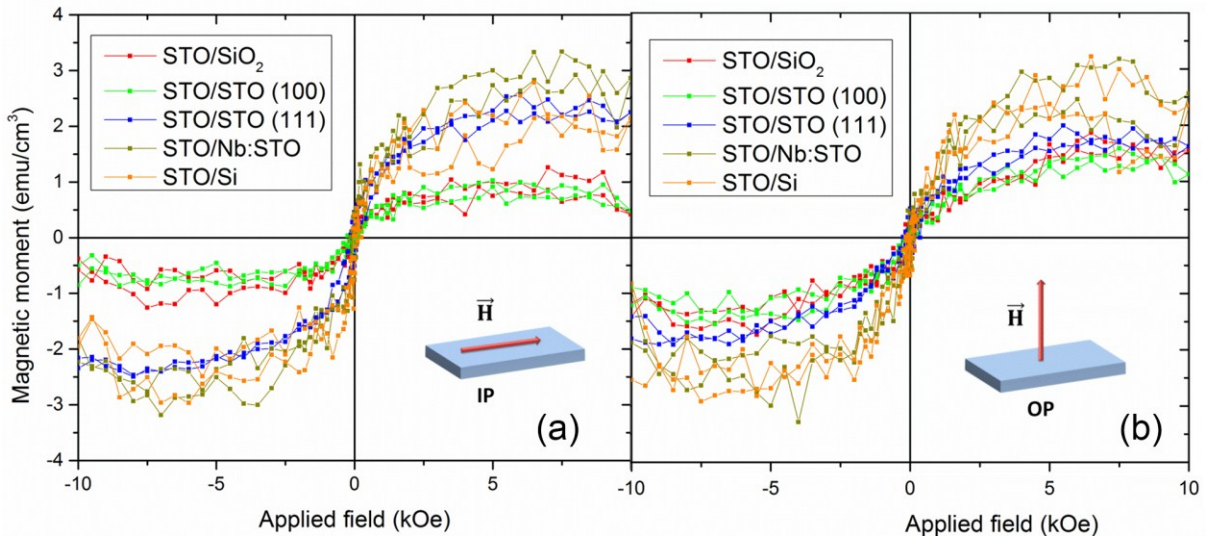

Fig. 5-11. (a) IP and (b) OP magnetic hysteresis loops of $SrTiO_3$ (STO) films on SiO_2, STO (100), STO (110), Nb:STO and on Si.

The resistivity of the films grown directly on Si native oxide have been measured to be $\rho_{STCo30} \sim 10^9 - 10^{11}$ Ω·cm. Once the films are thick enough (t > 200 nm), leakage to the substrate can be suppressed. In addition, before growth, the PLD chamber was pumped down to 1μTorr at room temperature, then heated up to about 650°C and then pumped down to 1μTorr again. During the high-temperature pump down which takes longer than 5 hours for our PLD chamber, we estimate that the native oxide grew as thick as 15-20 nm. The high-temperature pump down served the dual purpose of minimizing substrate leakage with thicker native oxide as well as enhancing STCo30 perovskite lattice distortion through increase in the oxygen vacancy concentration, which will be discussed later in the section.

The ferroelectric saturation polarization increased, but voltage required for ferroelectric saturation and remanent ferroelectricity decreased with higher oxygen pressure. Among all samples prepared for this study, the largest P_{sat} (saturation ferroelectric polarization) observed was 154 $\mu C \cdot cm^{-2}$ for 6 μTorr STCo30/Si sample, Fig. 5-3(c) and the largest $2P_r$ (remanent polarization) was measured to be 35 $\mu C\ cm^{-2}$ for the 1μTorr STCo30/Si sample, Fig. 2(b). The dielectric constants of the STCo30 1μTorr films reached as low as $\varepsilon_r = 203$ and this constant increased with oxygen pressure during deposition as the oxygen vacancy concentration decreases.

Microstructure of STCo30 films

In order to understand the microstructure of the STCo30, transmission electron microscope (TEM, JEOL 2010F field emission) imaging, elemental mapping, and x-ray diffraction analysis (XRD, (PANalytical X'Pert PRO MPD with Cu K_α source, wavelength 0.1541 nm) ω-2θ scans and reciprocal space mapping (RSM, Rigaku SmartLab XRD) were carried out. Fig. 5-12(a) shows a cross-section TEM micrograph and Fig. 5-12(b) shows the corresponding elemental mappings for Sr, Ti, Co and O ions of the STCo30 film on Nb:STO (1 μTorr). TEM indicates the polycrystalline nature of the film. Within the resolution of elemental mapping, metallic cobalt clusters were not observed, and there was an approximately homogeneous distribution of the Co except for a Co-rich layer at the top surface of the film. If this layer had contributed to magnetism strongly as a metallic Cobalt layer, the average magnetic moment of the film would have been much higher than found in Fig. 5-1. In comparison, TEM of the STCo30/STO shows epitaxial growth with misfit dislocations and phases with (111) orientations.

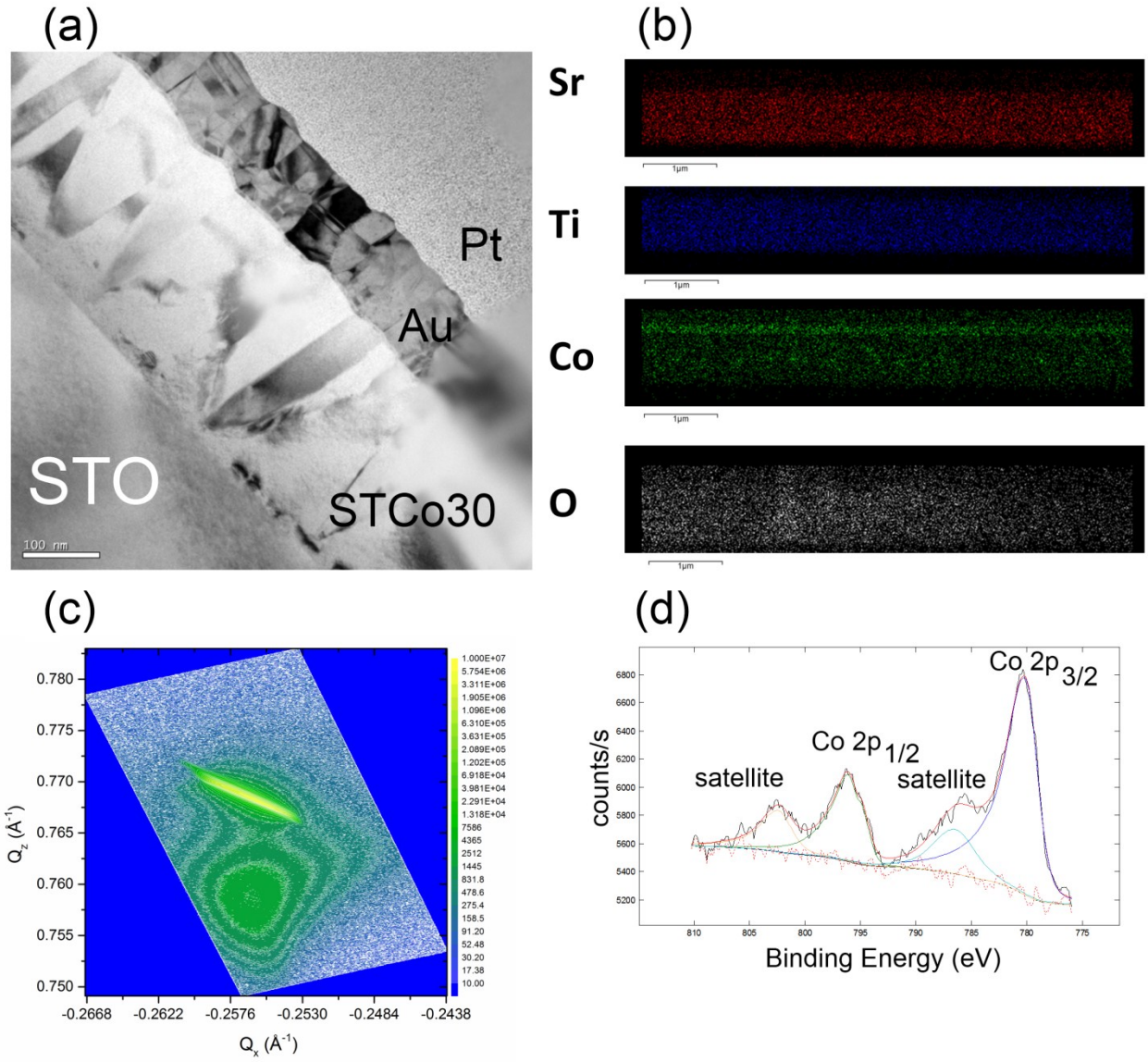

Fig. 5-12. (a) High resolution TEM micrograph (scale bar: 100 nm) of STCo30/Nb:STO (1 μTorr) and its (b) elemental mapping of Sr, Ti, Co and O across the film, (c) reciprocal space map of STCo30/STO-1 μTorr indicating tetragonal distortion, (d) Cobalt 2p photoelectron spectra of STCo30/STO-3 μTorr, demonstrating mixed valence of Co ions. (TEM imaging and XPS measurements were done by Dr. Xueyin Sun and Elisabeth Shaw, respectively.)

XRD (ω-2θ) scans for phase identification identified each peak as a signature of STCo30. Within the resolution of the x-ray diffractometer, no metallic cobalt peaks were observed. Fig. 5-12(c) shows the RSM of STCo30 on Nb:STO. The substrate and film peaks are aligned at the same q_x, i.e. the STCo in-plane was lattice matched to the substrate with in-plane lattice parameter a_{STO} = 3.905 Å. The OP lattice parameter of the film c exceeds that of the substrate, and for the film c = 3.953 Å, and c/a = 1.011, i.e. a tetragonal distortion very similar to the

values reported in [49].

In order to identify the valence states of Cobalt ions in the films, x-ray photoelectron spectroscopy (XPS) analysis was done on STCo30/STO (100) sample. Fig. 5-12(d) shows the XPS spectrum which has binding energies peaks at 780.4 and 796.2 eV, which correspond to the Co $2p_{3/2}$ and $2p_{1/2}$ doublets originating from spin-orbit interaction. If there had been metallic Cobalt particles within the region probed by XPS, the spectra would be expected to show $2p_{3/2}$ and $2p_{1/2}$ peaks at 777.3 and 792.4 eV, respectively [39]. As these peaks are not present on Fig. 5-12(d), the possibility of having metallic Co clusters has been precluded (at least for the film surface). Two satellite peaks exist around 786 and 803 eV, which are 7 eV above the principal peaks. This binding energy separation of 7 eV between the principal and satellite peaks is comparable with that of Co^{2+} or Co^{3+} ions in previous reports [39]. The strong satellite peak is a characteristic of Co^{2+}, as in La_2CoO_4 [50], compared to the very weak satellite peaks observed for Co^{3+} and Co^{4+} ions in $La_{1-x}Sr_xCoO_3$ [51] or STCo bulk samples [52] fabricated under high oxygen pressure. The strong satellite peak in the XPS spectrum indicates that the film contains Co^{2+}. Since the binding energy of the Co $2p_{3/2}$ peak is smaller than that of pure Co^{2+} perovskites (781.3 eV) [39], Co is in a mixed valence state also containing Co^{3+}. Based on the measured XPS spectra of Co in $LaCoO_3$, $SrCoO_3$ and La_2CoO_4 [39], and earlier DFT predictions [17] estimate that Co^{2+} and Co^{3+} are the major valence states of Co. The lower valence Co ions are larger than the Ti^{4+} explaining the larger unit cell volume compared to STO.

Co^{+2} is the most common valence state due to strong XPS peak, but the relative concentration of Co^{2+}:Co^{3+} depends on the oxygen vacancy concentration (and hence the oxygen vacancy parameter δ) due to charge neutrality of the unit cell. The earlier studies on the stoichiometry of our STCo30 films show that Cobalt is at around at. 23% [39]. Approximating the stoichiometry of the films as $SrTi_{0.75}Co_{0.25}O_{3-\delta}$ and assuming that the films contained purely Co^{2+} valence state (with Sr^{2+} and Ti^{4+}), charge neutrality of the unit cell requires that $\delta = 0.25$. If $SrTi_{0.75}Co_{0.25}O_{3-\delta}$ contained purely Co^{3+} valence state (with Sr^{2+} and Ti^{4+}), δ must be 0.125. As XPS results show that Co^{2+} constitutes a greater fraction of the Cobalt ions than Co^{3+}, one

can estimate that δ is closer to 0.25 than 0.125 (δ > 0.1875). Since Co ions in the films have lower valence than Ti^{4+} ions, the lattice volume of STCo30 films are larger ($3.961 \cdot 3.905^2$ $Å^3$) compared than STO (3.905^3 $Å^3$).

As shown on Fig. 5-1 and Fig. 5-2, the saturation magnetic moments of the films grown at different oxygen pressures are between 0.06 and 0.6 μ_B/Co ion, which is an indication that all of the STCo30 films have some antiferromagnetic coupling. The films are magnetic and magnetization decreases with higher oxygen pressure during growth. With higher oxygen pressure, oxygen vacancy concentration inside STCo30 film lattice is reduced and hence, a greater fraction of Cobalt ions are coupled antiferromagnetically to nearest Cobalt ions via oxygen. DFT predictions on this system suggested that increasing oxygen pressure (and decreasing oxygen vacancy concentration) reduces M_s and causes lattice volume to undergo anisotropic lattice expansion [17]. DFT results also suggest that Co ions adjacent to oxygen vacancies have higher moment [17]. Due to the mixed valence states of Co ions, there is a mixture of ferromagnetic and antiferromagnetic interactions and net spin glass behavior is expected.

STCo30 films are oxygen-deficient, compressively strained by the substrate in plane and contain Co^{2+} and Co^{3+} mixed valence states. The total magnetic anisotropy energy of films has contributions from shape and magnetoelastic anisotropies, which leads to uniaxial anisotropy (OP easy axis). Previous DFT predictions concluded that Co adjacent to oxygen vacancies has higher spin state [17], which is also consistent with the magnetoelastic Jahn-Teller or spin-orbit stabilization of Co2+ ions. In a previous study, the behavior of high spin and low spin Co^{2+}, Co^{3+} and Co^{4+} ions were modeled [38]. The lattice parameters and the mismatch strains (~ $(a_{out\text{-}of\text{-}plane} - a_{STO})/a_{STO}$) also decrease with higher oxygen pressures due to the reduction in the magnetoelastic Co^{2+} ion concentration.

Density-functional theory simulations on the electronic band structure, magnetic and ferroelectric properties of STCo30 films

In order to better understand the origins of magnetism and ferroelectricity in STCo, density functional theory calculations were done by Prof. Juan Manuel Florez (a post-doc in Prof. Ross group). The focus here is on the influence of the oxygen deficiency on the macroscopic magnetic and ferroelectric properties and therefore its role in multiferroicity. As presented in chapter 2, the electronic structure was calculated for each of the possible Co-Co ion arrangements in a supercell of 2x2x2 perovskite unit cells using GGA+U. The supercell contained one or two Co ions depending on whether Cobalt concentration x = 0.125 or 0.25 or zero, one or two oxygen vacancies [17]. The simulated stoichiometries correspond to bulk compositions of $SrTi_{0.875}Co_{0.125}O_{3-\delta}$ and $SrTi_{0.75}Co_{0.25}O_{3-\delta}$ with δ = 0, 0.125 or 0.25. Technical details about the DFT calculations can be found in chapter 2. In our previous DFT studies of $SrTi_{0.75}Co_{0.25}O_{3-\delta}$ [17] using a hybrid functional for δ = 0 and 0.125, we found that when δ = 0, the ground state contained low spin $t_{2g}^5e_g^0$ Co^{4+}, but when δ = 0.125, the ground state consisted of Co^{3+} with a high spin state ($t_{2g}^4e_g^2$) for the Co^{3+} adjacent to the oxygen vacancy and a low spin state ($t_{2g}^6e_g^0$) in the fully-coordinated Co^{3+}. The next-lowest energy state consisted of high spin Co^{2+} adjacent to the vacancy and low spin Co^{4+} in the fully-coordinated site, with ferromagnetic coupling but weak exchange interactions. Both energy states yielded an average of ~1.6 μ_B/Co. In an actual STCo30 film, a VSM measurement averages over many random configurations of Co-oxygen vacancy pairs. The presence of the vacancy led to greater lattice expansion, tetragonal distortion and increased optical band gap.

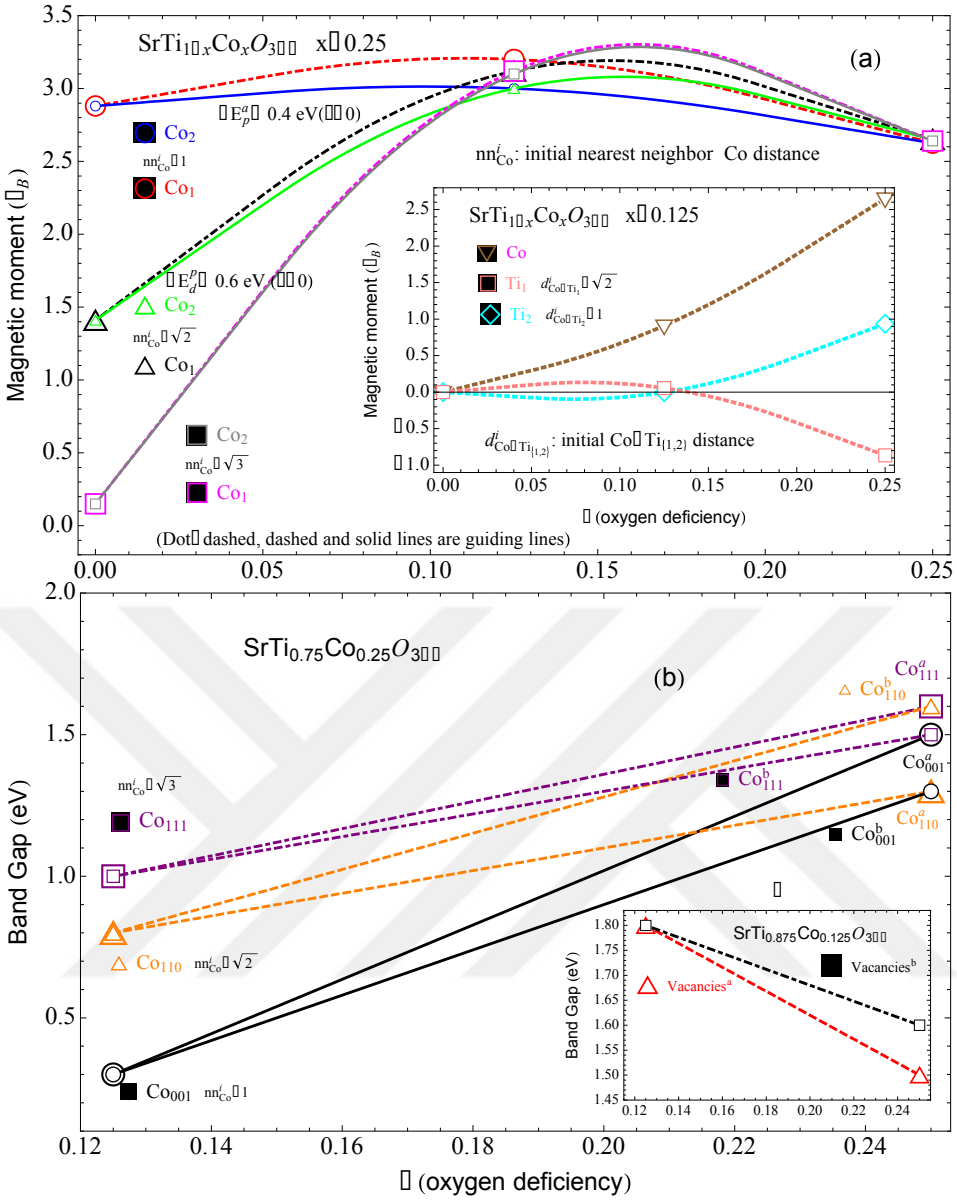

Fig. 5-13. (a) Magnetic moments (in units of μ_B) calculated per formula unit using DFT as a function of different oxygen vacancy concentrations δ in STCo25 (x = 0.25 Cobalt concentration). Circular, triangular and square data points correspond to cases where nearest-neighbor Co distances are 1, $\sqrt{2}$, or $\sqrt{3}$ unit cells. The inset corresponds to similar calculations for STCo12.5 (x = 0.125 Cobalt concentration). (DFT simulation results provided by Prof. Juan Manuel Florez)

As shown on Fig. 5-13(a), magnetic moment is maximized for oxygen vacancy concentraions of about δ = 0.125. Fig. 5-13(a) inset shows for lower Co concentration (x = 0.125) that high δ leads to changes in the valence state of a Ti ion adjacent to the oxygen vacancy. The Ti magnetic moment is antiparallel to the Co moment, which produces a ferrimagnet in the ground state and lowers the net moment. This result is consistent with the

experimental results on Fig. 5-1, which presents that the magnetic moment of the STCo30 3μ Torr film on Si is maximized. Since the STCo30 films are polycrystalline and they do not have any substrate strain effects, one can compare these experimental results with the DFT calculations. The magnetic moments of the STCo30 films presented on Fig. 5-1 first increase from 1 to 3μTorr. The magnetic moments then decrease with higher oxygen pressure.

In comparison, for $x = 0.125$, the inset of Fig. 5-13(b), the second vacancy is not adjacent to the Co ion, and it leads to a reduced valence Ti ion and a decrease in the bandgap. This occurs because the Ti coordinated by the second vacancy loses an empty t_{2g} state, narrowing the gap and yielding a plausible Ti^{+3} state with $1\mu_B$. For the $\delta = 0.25$ (two-vacancies in the superlattice), there is less effect of nn_{Co} on the bandgap and magnetic moment, so the details of the Co and vacancy positions are not critical and one might expect a material with disordered Co and vacancy sites to follow the same general behavior as predicted by the DFT model.

Fig. 5-13(b) shows the oxygen-deficiency dependence of electronic band gap (eV) for Cobalt concentration x = 0.25 and x = 0.125 (inset). The oxygen vacancy parameter $\delta = 0.25$ cases were formed by adding a vacancy to the ground state configurations at $\delta = 0.125$. The $\delta = 0$ cases are semi-metallic with narrow gaps, in agreement with hybrid DFT results [17]. When x = 0.25, a higher optical band gap is predicted by DFT with high oxygen vacancy concentration, as shown on Fig. 5-13(b). When x = 0.125, a lower optical band gap is predicted by DFT with higher oxygen vacancy concentration.

The presence of a vacancy opens notable band gaps. This suggests that those electrons generated by the missing oxygen are contributing to the t_{2g} orbitals more easily when the Co are closer together, localizing empty e_g states closer to the Fermi energy, which in turn decreases the spin from high to low. The gaps increase by a further 0.5-1.0 eV when the second oxygen vacancy is added, and the moment of both Co ions is high because both Co ions are adjacent to a vacancy.

The band gap predictions are experimentally and quantitatively confirmed by Fig. 5-14, which shows the optical and near-infrared transmission spectra of STCo30 films grown on double-side polished STO substrates under similar oxygen pressures. The DFT predictions indicate that as oxygen vacancy concentration is increased (i.e. lower oxygen pressure during growth), the band edge moves from 0.3 eV (λ_g = 4132 nm) to about 1.6 eV (λ_g = 775 nm). On Fig. 5-14, the band tail of films grown at high oxygen pressures extend into the midwave infrared region and the band tail gradually moves to less than 870 nm (E_g > 1.45 eV) for STCo30 1μTorr sample. Aside from band gap and magnetism predictions, the quantitative agreement between DFT and the experiment extends into ferroelectricity, as discussed below.

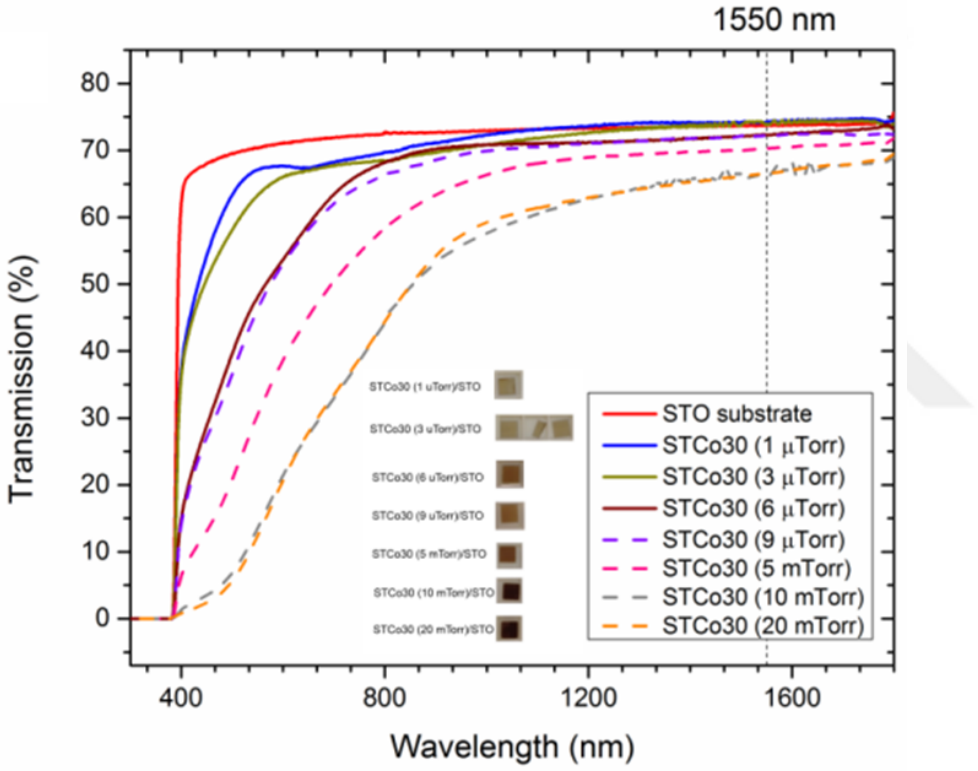

Fig. 5-14. Oxygen partial pressure dependence of optical transmission spectra of STCo30 films.

Fig. 5-15 shows the DFT predictions for the net ferroelectric polarization per unit cell for Cobalt concentrations of x = 0.25 and x = 0.125 (inset) calculated as a function of oxygen vacancy number δ. The net polarization varies between 50 upto 250 μC cm^{-2} (except for one configuration that does not yield ferroelectricity). Remarkably, the predicted values for polarization are very similar in magnitude to the experimental polarizations presented in Fig. 5-3 and Fig. 5-5, supporting the experimental conclusions despite the fact that the experimental

films average out over a random distribution of different Cobalt-oxygen vacancy configurations.

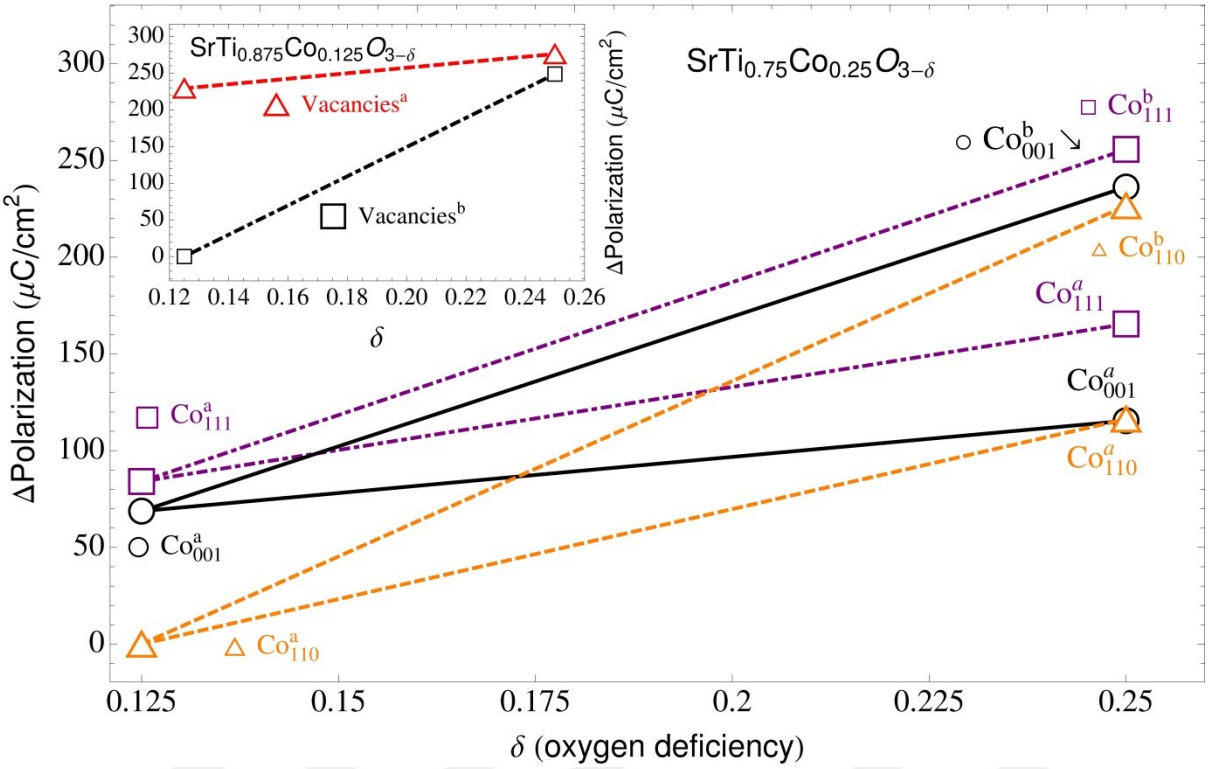

Fig. 5-15. (a) Co magnetic moments of the global lowest-energy configuration (gle) for x=0.25 ($Co^{a}_{\{111, 110, 001\}}$); Inset: Co and Ti magnetic moments of the gle for x=0.125. (b) Band gaps of gle for x=0.25, and of gsle for x=0.25 with δ=0.25; Inset: Band gaps of gle (Vacancies a) and gsle (Vacancies b) for x=0.125. (c) Macroscopic polarization of gle in (a), and of the global second lowest-energy configuration (gsle) for x=0.25 with δ=0.25 (Co^{b}{111, 110, 001}); Inset: Macroscopic polarization of gle (Vacancies a) and gsle (Vacancies b) for x=0.125.

Fig. 5-16 shows 9 cartoons of the 2x2x2 simulated supercells that visually describe formation mechanism of net spontaneous polarization. Supercells on the first column depict $SrTi_{0.75}Co_{0.25}O_{3-\delta}$ with δ = 0.125. Dark blue circles represent Cobalt atoms, red circles represent oxygen atoms, green circles represent Strontium atoms. For the first columns, oxygen octahedras tilt, and Ti and Co ions are off-centered. DFT calculations also predict that Ti ions also off-center as a result of the Cobalt substitution and contribute to net ferroelectric polarization. When δ = 0.25, octahedral tilt is further enhanced and off-centering of Ti and Co ions start occurring for most of the B-site ions.

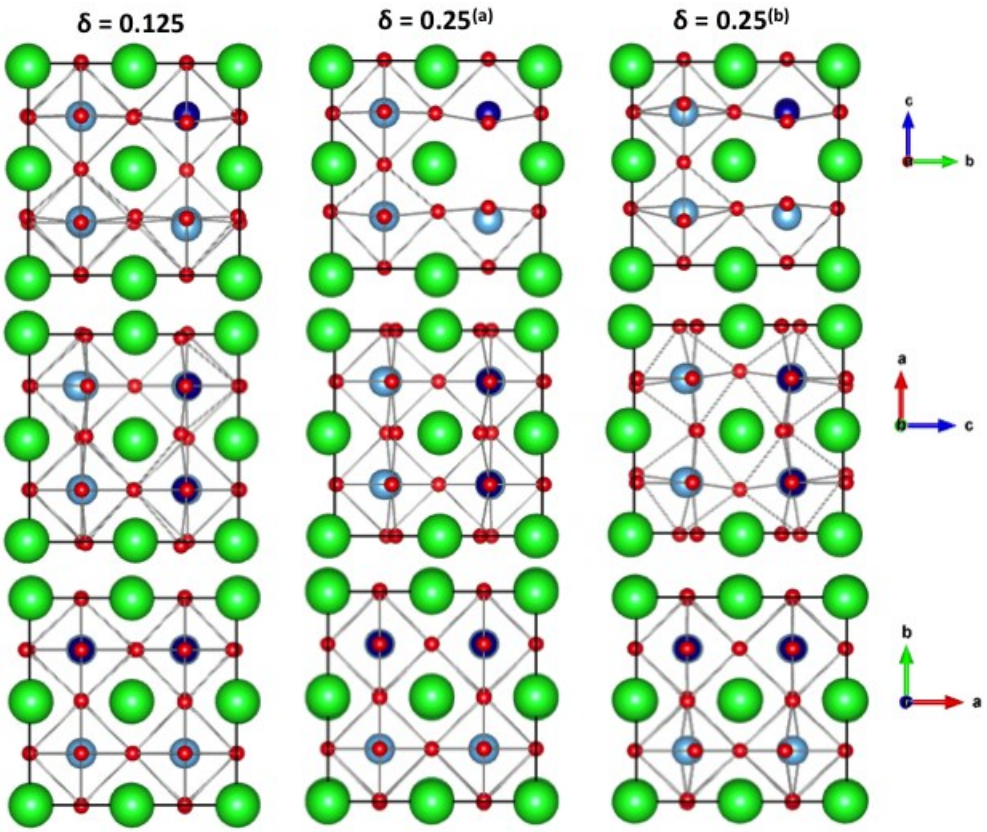

Fig. 5-16. Unit cells of $SrTi_{0.75}Co_{0.25}O_{3-\delta}$ for $\delta = 0.125$ and $\delta = 0.25$. Dark blue circles represent Cobalt atoms, red circles represent oxygen atoms, green circles represent Strontium atoms. The configurations Co^{a}_{001} and Co^{b}_{001} have been displayed for the last case. Upper row: view from {001} direction. Middle row: view from {100}. Lower row: view from {010}.

These DFT results indicate that the concentrations of Co and oxygen vacancies provide separate handles to manipulate the magnetization, bandgap and polarization of STCo. One can change the target composition to change Cobalt concentration and the oxygen pressure and temperature during deposition, which together influence the oxygen stoichiometry. The oxygen deficiency promotes insulating states, helping to fulfill the requirement for the presence of ferroelectricity as well as promoting high magnetic moment Co ions.

5.1.2 Magnetism and ferroelectricity in STCo30 films on Nb:STO substrates

As mentioned in the previous section, the STCo30 films on Nb:STO substrates require separate investigation since the Nb:STO substrate has a resistive switching behavior. The first step into investigation of the magnetic and ferroelectric properties of the STCo30 films on

Nb:STO substrates is the demonstration of magnetism in the films on Nb:STO substrates. Fig. 5-17(a) and (b) indicate the IP and OP magnetic hysteresis loops of the films grown on Nb:STO at different oxygen partial pressures, respectively. The STCo30 films prefer OP anisotropy with a saturation field of about 4000 Oe. In addition, the magnetic moments of the films are within 0.4-1.7μ_B/Co ion. Similar to STCo30 films on Si, the films on Nb:STO substrates also have a maximum magnetic saturation moment for STCo30 (6 µTorr)/Nb:STO. This behavior is also consistent with the DFT predictions, which indicate a maximum magnetic moment for Cobalt concentration x = 0.25 and δ = 0.125.

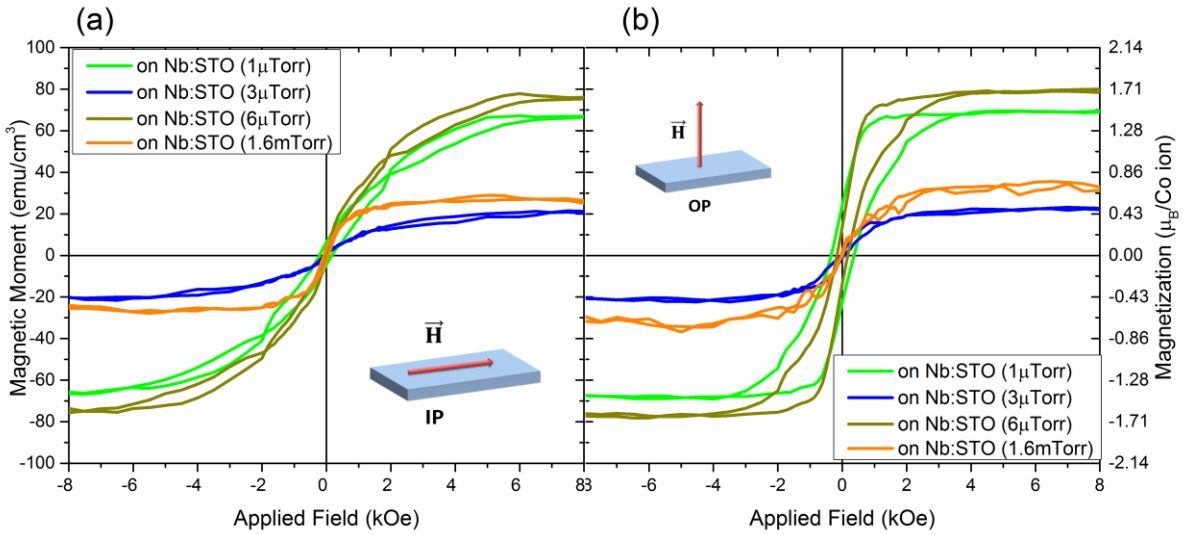

Fig. 5-17. (a) IP and (b) OP magnetic hysteresis loops of the STCo30 films grown on Nb:STO substrates under different oxygen pressures.

The temperature dependence of magnetic saturation moment of the STCo30 on Nb:STO substrates was investigated in order to probe if there is a metallic Cobalt behavior. Fig. 5-18 shows the SQUID measurements of the IP magnetic saturation moment of the (1µTorr)/Nb:STO sample as a function of temperature. Since the temperature dependence is a linear function (not a Brillouin-like function) and since this behavior is also consistent with the linear decrease of magnetic moment of the same material system between 300-700 K [1], a spin glass behavior is predicted. In addition, the likelihood of Cobalt metallic clusters is also precluded.

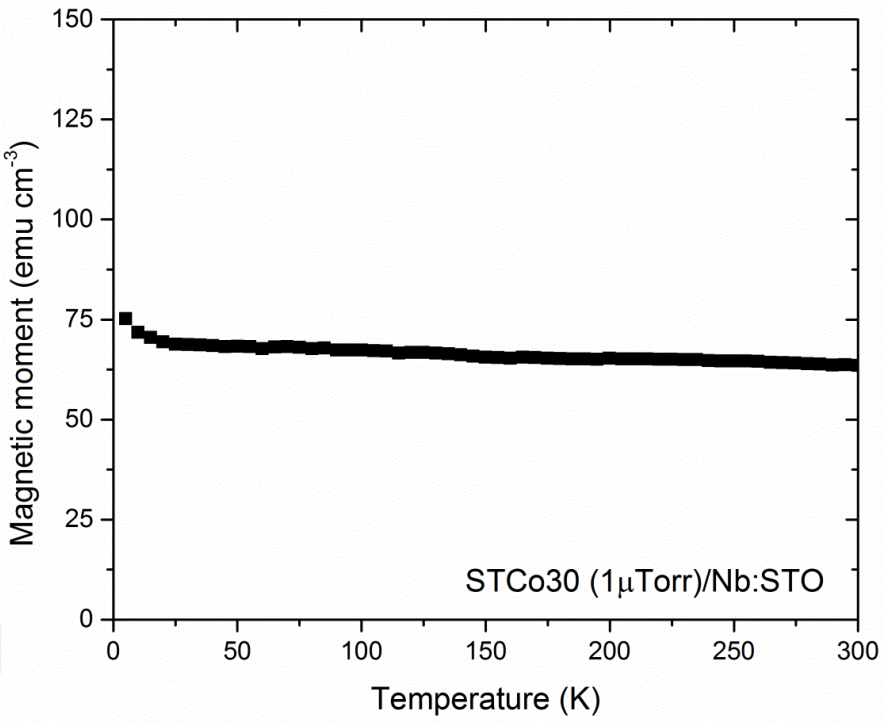

Fig. 5-18. IP saturation magnetic moment of the STCo30 (1μTorr)/Nb:STO sample as a function of temperature measured using SQUID.

The structural properties of the films on Nb:STO were investigated using HRXRD RSM measurements. XRD ω-2θ measurements did not indicate any secondary phases other than STCo30. Table 5-3 summarizes the RSM results for STCo30 films on Nb:STO and they are also compared with the RSM results for STCo30 (3 μTorr) on STO (100). The RSM results for the STCo30 (1 μTorr), (3 μTorr), (6 μTorr), (1.6 μTorr) films on Nb:STO near (013) peak of the substrate and the film are presented on Fig. 5-19 to 5-22, respectively. In addition, in-plane and out-of-plane lattice parameters of the films, well as c/a ratios and lattice volumes are presented. All films have c/a > 1, indicating that they are all strained and tetragonal with c/a ratios ranging between 1.007 (0.7% strain) up to 1.017 (1.7% strain). The films are lattice matched to their substrates. Remarkably, the lattice volume gradually increases with higher oxygen pressure up to 6 μTorr and then decreases beyond 6 μTorr. The highest magnetic moment was observed for the 6 μTorr film. The RSM of that film indicates at least 2 different STCo30 phases, both lattice-matched to the substrate, but one highly-strained and the other less strained. The lattice properties of those phases are presented on Table 5-3 as two separate columns: STCo30 phase 1 and STCo30 phase 2. This decomposition hints on the stress

relaxation mechanism of STCo30 films. Once the film reaches an upper limit for epitaxial strain, it nucleates a less strained phase of STCo30. The measured lattice parameters are within 2% of the lattice parameters predicted by DFT calculations. DFT calculations also predict the volume of the lattice volume of the films to within 5%.

Table 5-3. Lattice parameters and c/a ratios of the samples extracted from RSM data

Sample name:	**STCo30 on Nb:STO (1 µTorr)**	**STCo30 on Nb:STO (3µTorr)**	**STCo30 on Nb:STO (6µTorr) (STCo phase 1)**	**STCo30 on Nb:STO (6µTorr) (STCo phase 2)**	**STCo30 on Nb:STO (1.6mTorr)**	**STCo30 (3µTorr) on STO (100)**
Film q_x ($Å^{-1}$)	-0.2580	-0.2552	-0.2546	-0.2546	-0.2574	-0.2558
Film a	3.874	3.918	3.927	3.927	3.8845	3.9088
Film q_z ($Å^{-1}$)	0.7619	0.7601	0.7625	0.7507	0.7621	0.7590
Film c	3.937	3.947	3.934	3.996	3.937	3.953
c/a ratio	1.016	1.007	1.0017	1.017	1.013	1.011
Substrate q_x($Å^{-1}$)	-0.2580	-0.2552	-0.2546	-0.2546	-0.2574	-0.2558
Substrate q_z ($Å^{-1}$)	0.7674	0.7681	0.7681	0.7681	0.7673	0.7682
Lattice Volume ($Å^3$)	59.12	60.58	60.69	61.64	59.40	60.39

The substrates have a broad peak in both q_x and q_z axes. The broad q_x means that there is a distribution of in-plane lattice parameters of the substrate and the unit cells are not uniform. The broad q_z indicates a distribution of out-of-plane lattice lattice parameters of the substrate. A microstructure analysis is presented below with transmission electron micrographs and EDX elemental mapping of STCo30 films on Nb:STO.

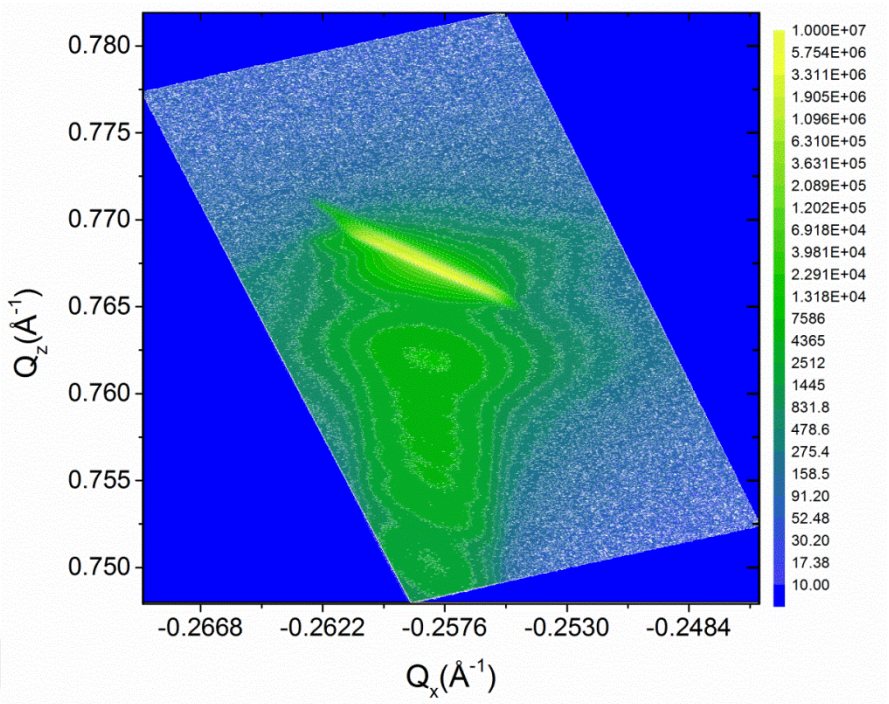

Fig. 5-19. Reciprocal space map of STCo30 film on Nb:STO (100) substrate (1 µTorr) near (013) peak of the substrate and the film.

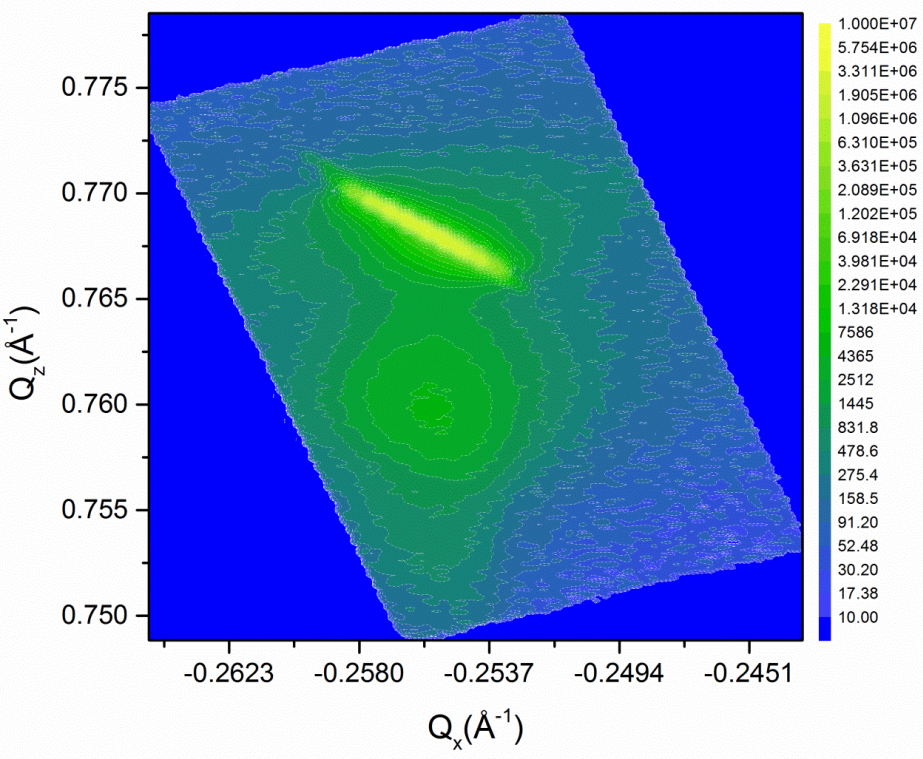

Fig. 5-20. Reciprocal space map of STCo30 film on Nb:STO (100) substrate (3 µTorr) near (013) peak of the substrate and the film.

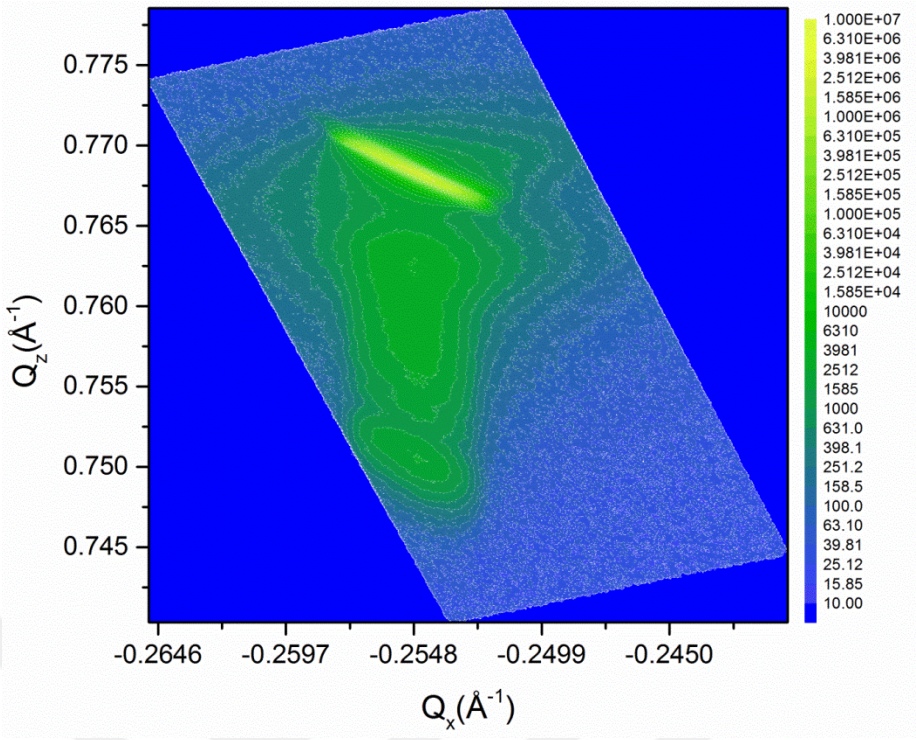

Fig. 5-21. Reciprocal space map of STCo30 film on Nb:STO (100) substrate (6 µTorr) near (013) peak of the substrate and the film.

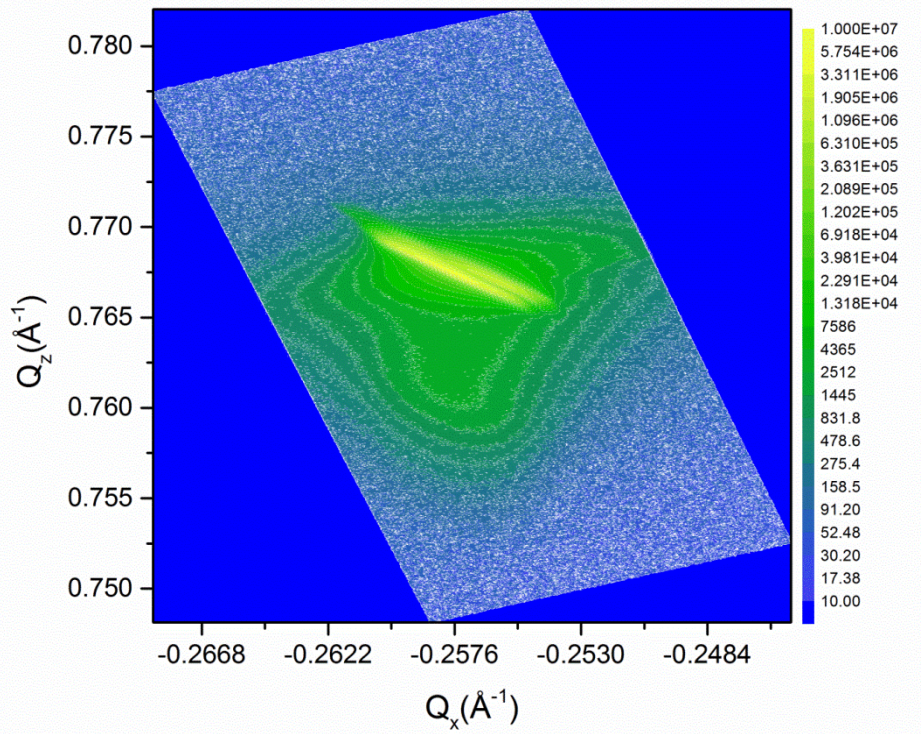

Figure 5-22. Reciprocal space map of STCo30 film on Nb:STO (100) substrate (1.6 mTorr) near (013) peak of the substrate and the film.

In order to investigate whether metallic Cobalt clusters have nucleated inside the films,

cross-section transmission electron microscopy (TEM) analysis and elemental mapping across STCo30 films on Nb:STO (1 μTorr) were done. Fig. 5-23 shows the TEM micrographs of STCo30 on Nb:STO (1 μTorr) sample. Fig. 5-24 shows the EDX elemental mapping of the film shown in Fig. 5-23. Cobalt is distributed evenly across the film and clustering cannot be observed. Since magnetic saturation moment of samples are lower than the magnetic moment of Cobalt metal (1.7 μB/Cobalt), since XPS results indicate no metallic Cobalt peaks, and since EDX elemental mapping does not show cluster phases, we rule out the possibility of having metallic cobalt secondary phases.

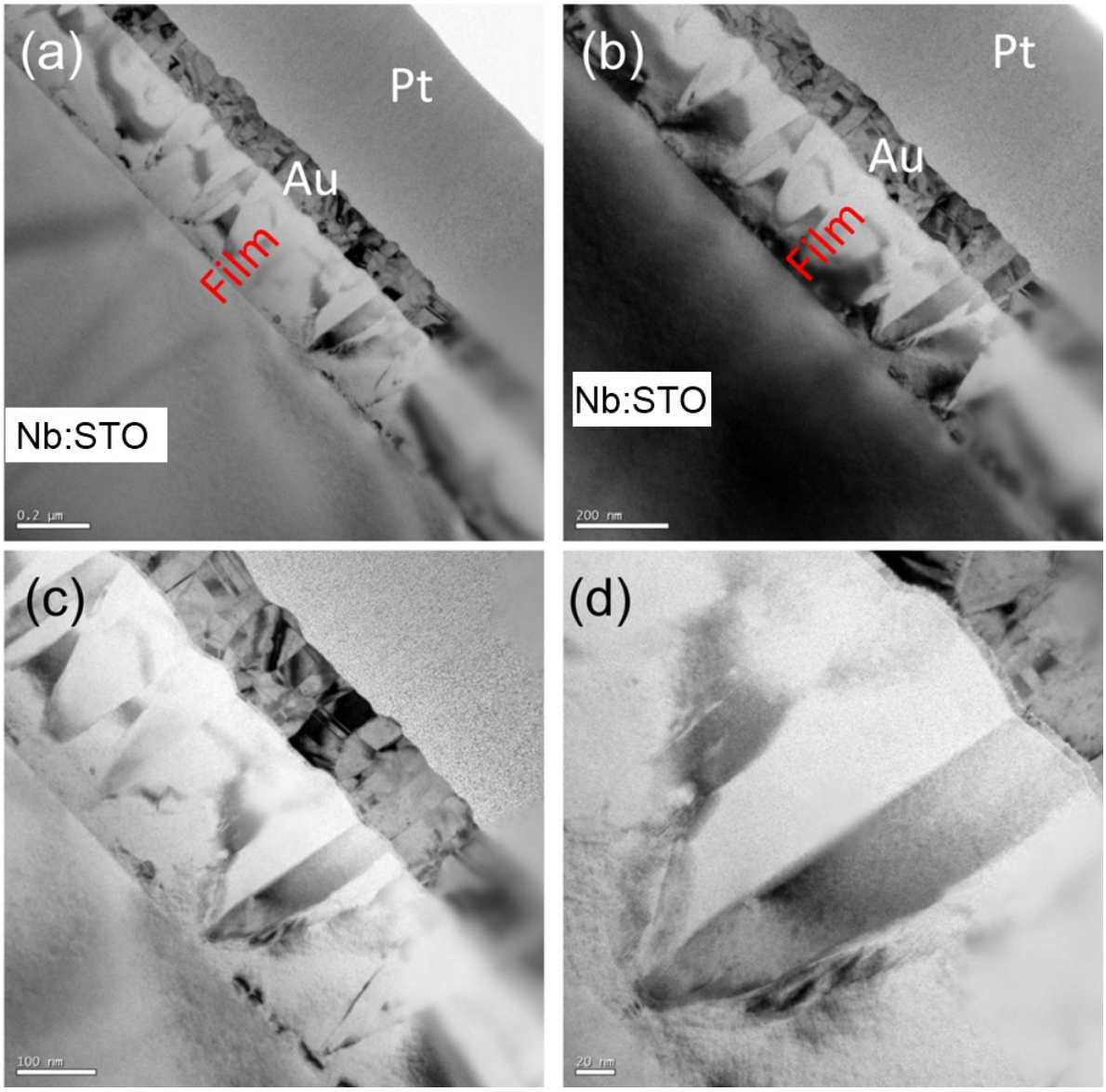

Fig. 5-23. Transmission electron micrographs of STCo30 film on Nb:STO (100) substrate (1 μTorr). The microstructure shows (100) and (110) film orientations of the same STCo30 phase. (TEM imaging by Dr.

Xueyin Sun).

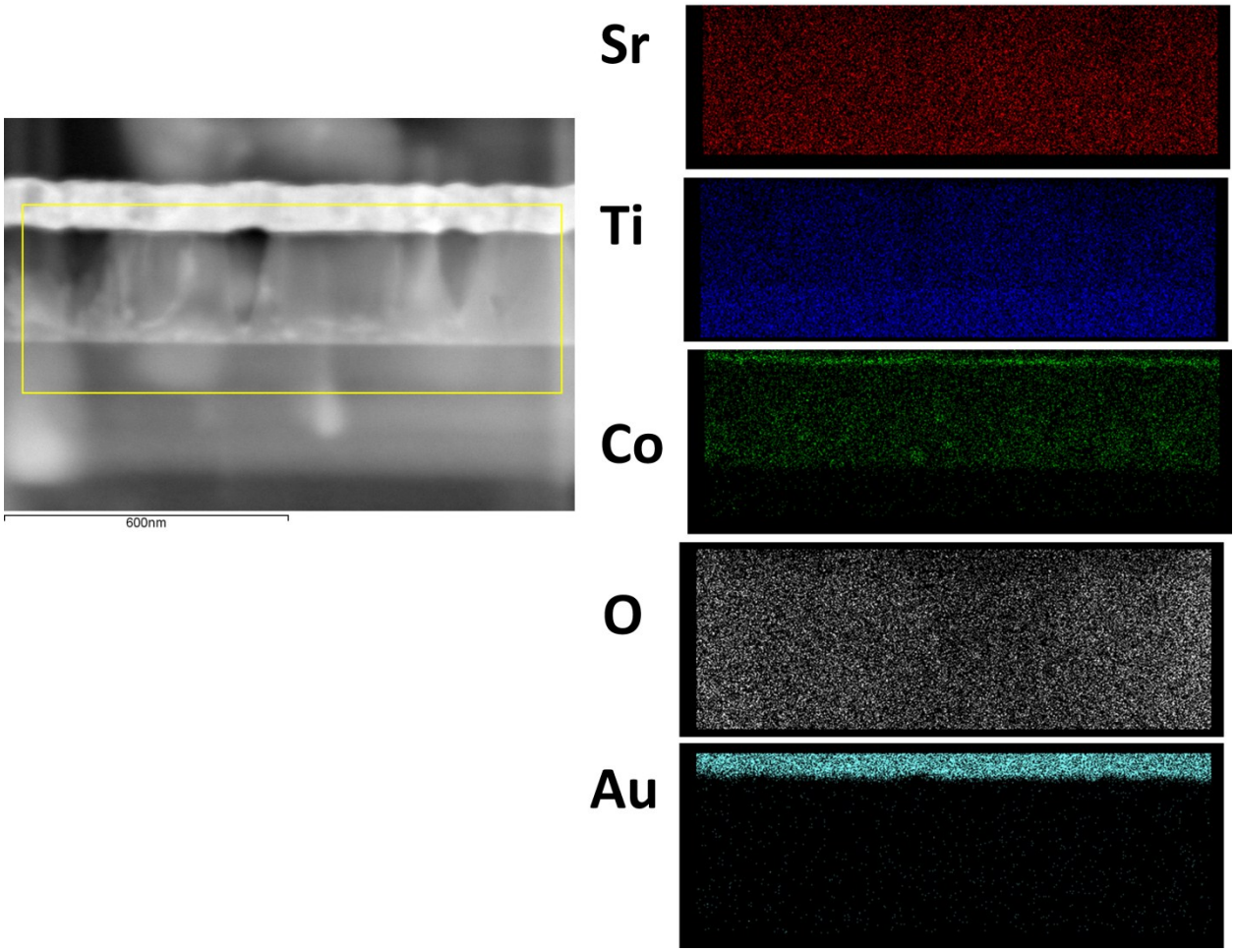

Fig. 5-24. Transmission electron micrographs and EDX elemental mapping of STCo30 film on Nb:STO (100) substrate (1 μTorr). There are no clusters, the scale bar is 600 nm. (TEM imaging by Dr. Xueyin Sun).

Finally, the ferroelectric and resistive switching characteristics of the films on Nb:STO are investigated. First, the resistivity of the Nb:STO substrate is measured as a function of voltage. The resistivity of the Nb:STO substrate has been found to be ~$8 \cdot 10^2$ Ω · cm and the resistivity decreases with voltage. Fig. 5-25 shows the voltage dependence of Nb:STO substrate. In addition, polarization hysteresis loops were measured on the same substrate. Depending on the voltage range of cycling, very strong polarization (200-400 $\mu C \cdot cm^{-2}$) responses were obtained. Fig. 5-25 insets include the leaky polarization hysteresis loops of the bare substrate when the cycling voltage ranges were (i) ±0.09 V, (ii) ±0.15 V, (iii) ±0.20 V, (iv) ±0.25 V, (v) ±0.30 V, and (vi) ±0.35 V. Nb:STO has intrinsic switching below 0.35 V. Beyond 0.35V, perfect leaky hysteresis behavior similar to the lower right hand inset is

shown.

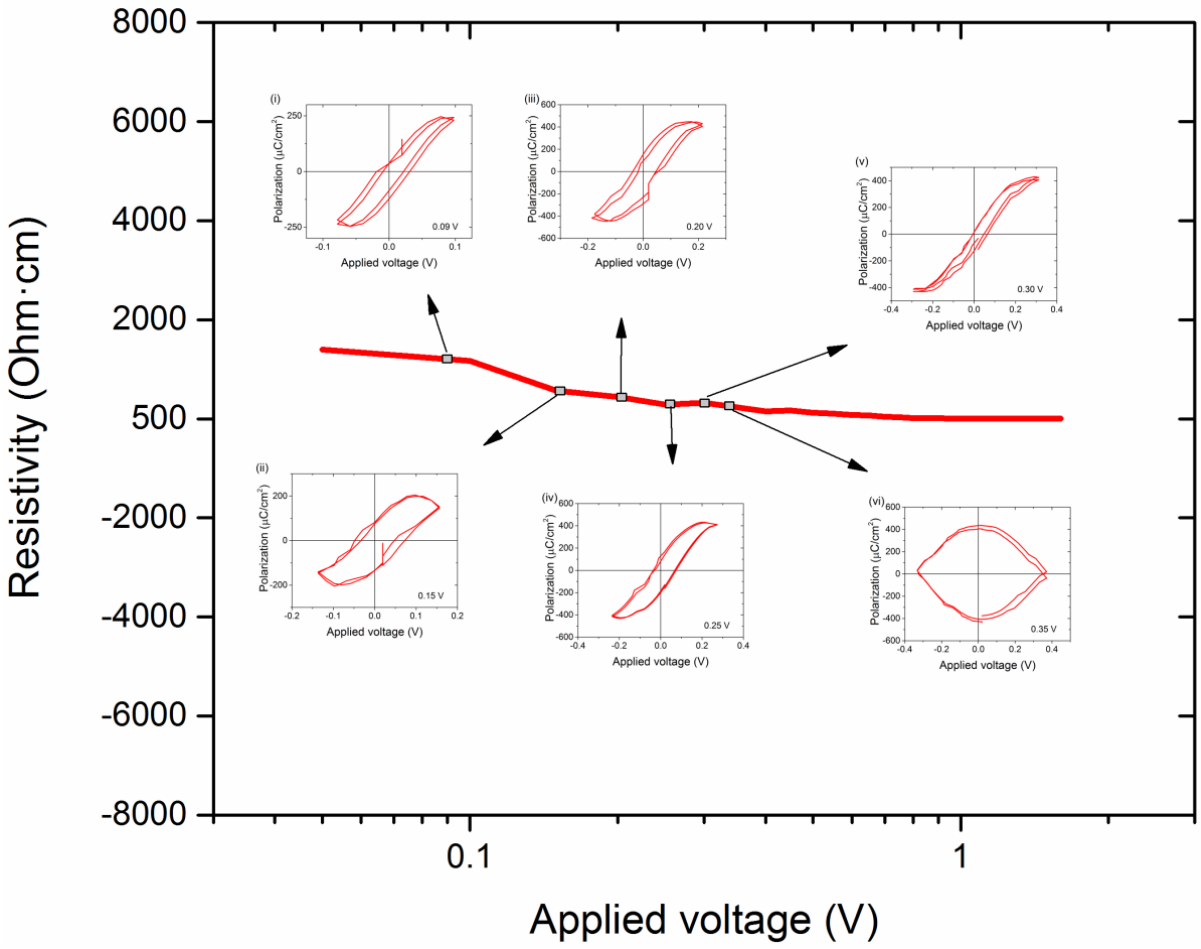

Fig. 5-25. Voltage dependence of the conductivity of Nb:STO substrate with hysteresis loops of Nb:STO substrate at (i) 0.09 V, (ii) 0.15 V, (iii) 0.20 V, (iv) 0.25 V, (v) 0.30 V, and (vi) 0.35 V. Nb:STO has intrinsic switching below 0.35 V.

Fig. 5-26 (a)-(d) show the PUND tests and ferroelectric switching measurements for the STCo30 films grown under (1, 3, 6 μTorr and 1.6 mTorr) on Nb:STO substrates with Au/Ti contacts on STCo30 and with horizontal bias configuration (V+: top and V-: top contacts), respectively. Although PUND tests indicate highly-reproducible strong remanent polarization states ($2P_r$ within 50-400 $\mu C \cdot cm^{-2}$), polarization loops do not fully saturate. The polarization loops do not fully saturate and this behavior may be due to leakage along oxygen vacancy-rich film surface, leakage along grain boundaries that shunt the film from surface to substrate as cross-section TEM shows in Fig. 5-23 and leakage along the conductive substrate.

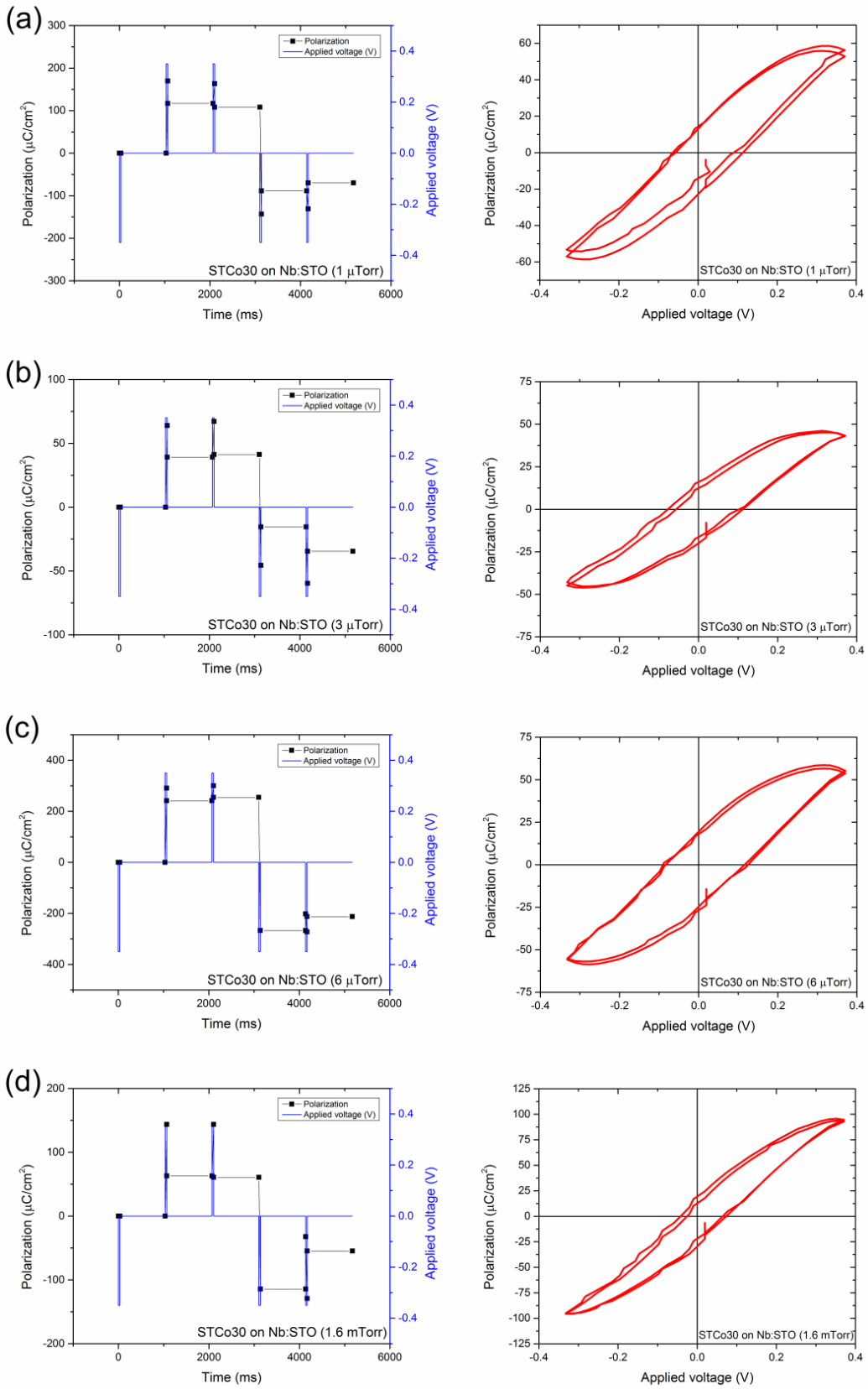

Fig. 5-26. PUND (positive up negative down) tests of STCo30 films on Nb:STO. PUND test plots for STCo30 films on Nb:STO grown at (a) 1, (b) 3, (c) 6 μTorr and (d) 1.6 mTorr with ferroelectric loops accompanying each PUND plot. Ferroelectric polarization is retained for periods much longer than a Schottky or a back-to-back diode would retain.

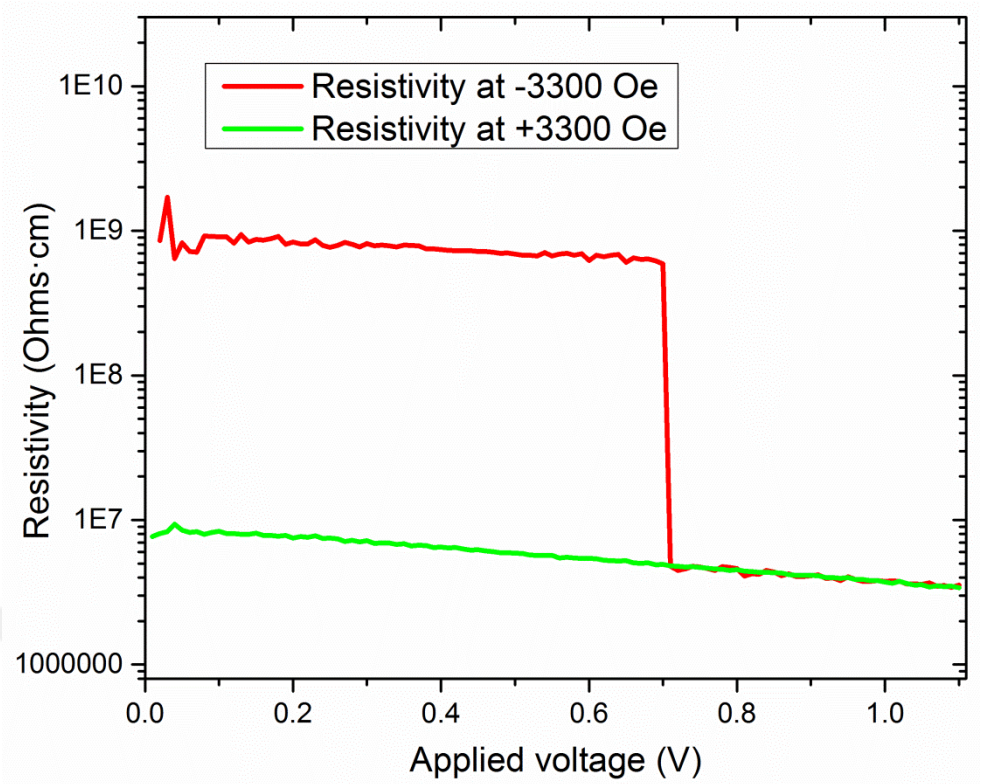

Fig. 5-27. Voltage and magnetic field-dependent resistivity measurements of STCo30 (1 μTorr) film on Nb:STO. Red (green) curve corresponds to a voltage-dependent resistivity scan when the applied magnetic field is -3300 Oe (+3300 Oe).

A remarkable and a very reproducible resistive switching behavior was observed for STCo30 (1μTorr) on Nb:STO (but not for other STCo30 films on Nb:STO) under applied magnetic field of ±3300 Oe within $V_{applied}$ < 1V. Each resistivity point on Fig. 5-27 was measured by 100-ms long voltage pulse and then recording the current output and then calculating resistivity from contact spacing and film thickness. Fig. 5-27 shows the results of 220 such measurements. When resistivity was measured under -3300 Oe OP bias (on a permanent NdFeB magnet, field measured using a Gaussmeter), resistivity was within $7x10^8$-$1x10^9$ Ω·cm for as long as $V_{applied}$ < 0.7V. When the applied voltage was increased to beyond 0.7V, resistivities measured decrease to ~$4x10^6$ Ω·cm. When the applied voltage is reduced to below 0.7V, resistivity increased by two orders of magnitude again and the resistivity results retraced the red curve back. When the magnet was flipped, resistivities decreased to 5-$9x10^6$ Ω·cm and the green curve was obtained. When voltage was reversed, the green curve was retraced. Next, the magnet was flipped again and resistivities obtained were found to retrace the red curve back and forth again. This behavior is unique to the films

on the Nb:STO substrates. Given the voltage-dependent substrate resistivity (Fig. 5-25), one can correlate the substrate switching behavior with the electroresistive and magnetoresistive switching behaviors. Clearly, a more systematic study needs to be done to model and ideally engineer this effect to fabricate magnetoresistive/electroresistive switches. The polarization and resistive switching behavior presented for STCo30 films on Nb:STO shows that the substrate participates significantly to the overall sample characteristics. As the films are highly more resistive than the Nb:STO substrates ($\rho_{STCo30}/\ \rho_{Nb:STO} > 10^4$), the surface and substrate leakage contributions significantly alter the overall resistivity. In addition, due to the substrate switching effects below 1V, the STCo30/Nb:STO (substrate) samples do not yield conclusive results on the individual polarization switching properties of STCo30 film or the Nb:STO substrate.

5.1.3 Magneto-optical properties of $SrTi_{0.70}Co_{0.30}O_{3-\delta}$ films

In this section, we study the magneto-optical properties of Cobalt-substituted $SrTiO_3$ ($SrTi_{0.70}Co_{0.30}O_{3-\delta}$, STCo30). In the following paragraphs, the structural, magnetic, optical and magneto-optical properties of STCo30 films grown on double side-polished STO under different oxygen pressures ranging from 1μTorr upto 20 mTorr using PLD are presented. In this section, we focus on perovskite-based MO materials, because these materials have the potential to be MO [1] as well as piezoelectric [53], which can be used to fabricate voltage-controlled magneto-optical modulators.

$SrTiO_3$ (STO) is a wide indirect band gap perovskite oxide (E_g = 3.2 eV) with that is transparent to visible and near-infrared telecommunication wavelengths [54,55]. Transition metal substituted STO films, such as $Sr(Ti,Co)O_{3-\delta}$ [1], $(La,Sr)(Ti,Co)O_{3-\delta}$ [56-58], and $Sr(Ti,Fe)O_{3-\delta}$ (STF) [38,43,59-60], exhibit room temperature magnetic and magneto-optical (MO) properties which can be engineered by using substrates, substituent types and concentrations, buffer layers and film growth conditions. Faraday rotation of substituted STO films make these films attractive for integrated non-reciprocal photonic device applications [1]

such as isolators and circulators as well as for fundamental investigations of the spectral origins of MO properties and superexchange effects [61]. Substituted STO films can be grown both as polycrystalline films on Si or as single crystals (with multiple orientations) on perovskite substrates. In addition, STF films grew with two different epitaxial orientation on CeO_2/yttria-stabilized zirconia buffered Si, forming so-called "double-epitaxial growth" in which the (100)-oriented film contained (110) crystals which formed to relieve strain [62].

In an earlier study, the structural, magnetic and magneto-optical properties of $Sr(Ti,Co)O_{3-\delta}$ (STCo) films on $LaAlO_3$ substrates were characterized [1]. The lattice constant of the STCo films increased with Co concentration and STCo films showed IP compressive strain as well as a tetragonal unit cell with c-axis along the OP direction (c/a ~ 1.028 for Co 37.5%). OP lattice parameter c increased by ~1.39% (3.960 to 4.015Å) as Co concentration was increased from 0% to 37.5%. As Co concentration increased, the magnetic moment increased for Co up to ~30% Co and then decreased. Saturation moments up to 0.5 μ_B per Cobalt ion and an OP easy magnetization axis were observed at RT. Faraday rotations up to -500 $deg \cdot cm^{-1}$ at $\lambda = 1550$ nm were demonstrated. The MO hysteresis of these films also showed an out-of-plane easy magnetic axis. At 1550 nm, the optical constants for STCo were n=2.34 and $k=1.1\times10^{-3}$ and the MO figure-of-merit was 0.57 $deg \cdot dB^{-1}$.

These results suggest that Co- or Fe-substituted STO may be useful in magneto-optical devices, although their MO performance to date is not as good as that of iron garnets. Ref. [1] indicated that the base pressure prior to deposition had a significant effect on the magnetic properties of STCo films, though this was not explored in depth. The base pressure during growth is expected to affect the oxygen vacancy concentration, altering properties such as optical absorption and magnetism [17]. Oxygen vacancies have many fundamental effects on perovskites, for instance, electromigration of oxygen vacancies was able to induce reversibly-switchable diode and photovoltaic effects in $Bi_{0.9}Sr_{0.1}FeO_{3-\delta}$ thin films [63]. Blue light was emitted from Ar^+-irradiated STO thin films due to radiative recombination of conduction electrons and holes stabilized within the band gap of STO [64]. In another study,

the resistivity of $La_{0.67}Ba_{0.33}MnO_z$ was enhanced about four orders of magnitude at room temperature by reducing oxygen content from z = 2.99 to 2.80 [65]. The control of oxygen stoichiometry in perovskites opens the possibility of electrical control of carrier density, optical, magnetic and MO properties.

STCo30 films were grown on STO substrates under different oxygen pressures and changes in their structural, magnetic, optical and MO properties as a function of oxygen pressure during growth are investigated. In ref. [1], 30 at.% Co concentration was found to maximize magnetic moment and Faraday rotation, therefore this concentration was used for the ceramic target and for the perovskite films grown. Each film was grown on a double-side polished STO (001) substrate at 650°C substrate temperature under various oxygen pressures (base pressure: $1x10^{-6}$ Torr). Assuming the base pressure gas contains about ~20% oxygen (atmospheric fraction of oxygen), the oxygen partial pressure before setting the oxygen flow is assumed as ~$2x10^{-7}$ Torr. After reaching the base pressure at 23°C, the oxygen partial pressure was set manually to the values ranging from less then 1μTorr upto 20 mTorr, as indicated on Table 5-4.

Table 5-4. STCo sample list, structural, optical and MO properties.

Sample Name	**Film Thickness (nm)**	**Out-of-plane lattice parameter (Å) Error: ±0.005 Å**	**Lattice volume ($Å^3$)**	**Oxygen Pressure (Torr)**	**Faraday rotation at 1550 nm ($°\cdot cm^{-1}$)**	**Optical Loss at 1550 nm ($x10^3$) ($dB\cdot cm^{-1}$)**	**Figure-of-merit ($x10^{-3}$) ($°\cdot dB^{-1}$)**
1 μTorr	270	3.956	60.33	< $1x10^{-6}$	-75	37.8	1.99
3 μTorr	280	3.961	60.40	< $3x10^{-6}$	-220	23.6	9.33
6 μTorr	281	3.931	59.94	$5x10^{-6}$	-80	33.4	2.39
9 μTorr	250	3.915	59.70	$8x10^{-6}$	-92	6.8	13.5
5mTorr	260	3.926	59.87	$5x10^{-3}$	-27	14.2	1.88
10mTorr	237	3.901	59.49	$1x10^{-2}$	-31	21.1	1.47
20mTorr	256	3.908	59.59	$2x10^{-2}$	-25	0.390	64

For lower pressure samples (1-9 μTorr), the growth rate was 2.8 $nm\cdot min^{-1}$. For for higher oxygen pressure samples (5, 10 and 20mTorr), the growth rate was 1.76 $nm\cdot min^{-1}$. A previous

study indicates that the cation stoichiometry is $SrTi_{0.77}Co_{0.23}O_{3-\delta}$ [1] (oxygen deficiency of the film: δ). After deposition, the chamber was cooled at a rate of 5°C min^{-1}. Films with similar thicknesses were grown at the same processing conditions indicated on Table 5-4.

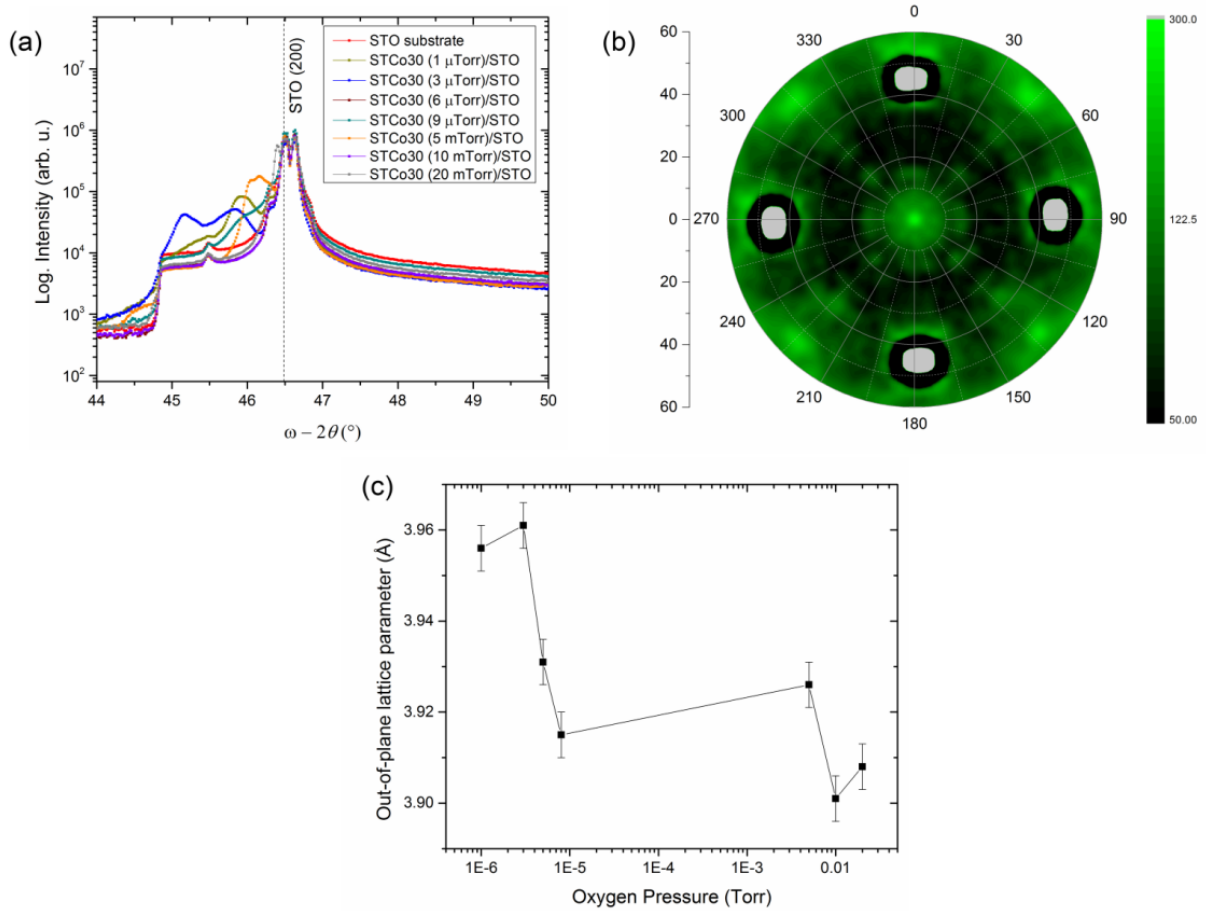

Fig. 5-28. (a) X-ray diffraction patterns (ω-2θ plots) indicate the phases present for films grown at different oxygen pressures. The strongest peaks are from the STO substrate, as well as a step at 44.8˚ and a small peak at 45.5˚. (b) Two-dimensional XRD scan of 9 μTorr STCo30 film about the 101 peak shows two four-fold symmetric peak sets (0, 90, 180, 270°) and (45, 135, 225, 315°) which correspond to (100) and (111) epitaxial orientations, respectively. The center peak shows 101 oriented crystal. Pole figure was acquired by A. Tang. (c) Oxygen partial pressure dependence of the OP lattice parameters of the films.

Fig. 5-28(a) shows the XRD ω-2θ plots near STO (200) substrate peak for identifying the phases and OP lattice parameters of the STCo30 films as a function of oxygen partial pressure. The STO substrate without film shows strong STO peaks at 2θ = 46.5˚ and additionally a small

peak at 45.5˚ and a step at 44.8˚. The STCo30 (200) films peaks are found to the left of the STO peak, broader and lower intensity than the STO peak. A reciprocal space map measurement done on the STCo30 (1 μTorr)/STO sample (not shown) indicated that even when the films were about 200 nm thick, the in-plane lattice parameter of the films and the substrate were identical, therefore the films were epitaxial with the substrate.

OP lattice parameters extracted from the ω-2θ scans are listed on Table 5-4. In some cases, e.g. 3 μTorr, the peak was split suggesting relaxation of part of the film, as seen in $Sr(Ti,Ga,Fe)O_{3-\delta}$ films [66]. The smaller OP lattice parameter (less strained) was calculated and shown on Table 5-4. The more strained fraction of the 3 μTorr film has 4.012Å for OP lattice parameter (2.7% strain on STO substrate, unit cell volume: a $\cdot 3.905^2$ $Å^2$ = 61.18 $Å^3$). The films grown at lower oxygen partial pressures (1-9 μTorr films) had OP lattice parameters *c* larger than the IP lattice parameter of the STO substrates (*a* = 3.905 Å), i.e. the *c/a* ratio was up to 1.014 assuming the film is lattice matched to the substrate in plane. STCo30 films prepared for the multiferroic project discussed in chapter 5 also have a similar relaxation into highly-strained and less-strained fractions of the same perovskite phase (STCo30 (6 μTorr) films on Niobium-doped STO substrates, Table 5-4 and the reciprocal space map in Fig. 5-21). An upper limit for c/a ~ 1.017 was observed for all films. All films contained perovskite phases, but metallic Cobalt or Co oxide peaks were not observed for any of the films.

For all films, STCo30 (101) and (111) peaks were also observed. This is reminiscent of a similar system, $Sr(Ti,Fe)O_{3-\delta}$, which demonstrated a double-epitaxial microstructure consisting of (100) film containing (110) crystals, [70] where each crystal type had a specific orientation with respect to the substrate. A 2D XRD (pole figure) scan about the 101 peak was done on the 9 μTorr STCo30/STO film. The 9 μTorr STCo30 film was chosen because this sample yielded the strongest STCo (101) peak near 32.4° during the ω-2θ scans. Diffraction angle α was varied from 0° to 90° with a step size of 3° and β was varied from 0° to 360° with a step size of 3° at a speed of 150° per minute. Fig. 5-28(b) displays the pole figure, which shows the cubic four-fold symmetry in the film. The center peak indicates the presence of (101)-oriented STCo30. The set of four peaks at α=45° correspond to the (111) peaks and indicates the

presence of (111)-oriented crystals. The remaining set of four-fold symmetric peaks at (0, 90, 180, 270°) indicate the (100)-orientated film. This film therefore had three sets of crystal orientations in the film with specific orientations with respect to the substrate, so could be described as 'triple-epitaxial'. Cross-section transmission electron micrographs (shown on Fig. 5-12(a)) obtained for another STCo30 sample on Nb:STO (grown at 1μTorr) showed wedge-shaped features nucleating near the film-substrate interface and growing wider as the film thickness increased. These represent crystals other than (100) which are presumed to nucleate to relieve film strain. According oxide thin film growth models, XRD scans and cross-section TEM images we observed, we believe that the STCo30 films initially grew with cube-on-cube epitaxy on the (100) STO, and the other crystal orientations formed to lower strain as the film grew thicker, leading to the splitting evident in the (200) peak of some of the samples.

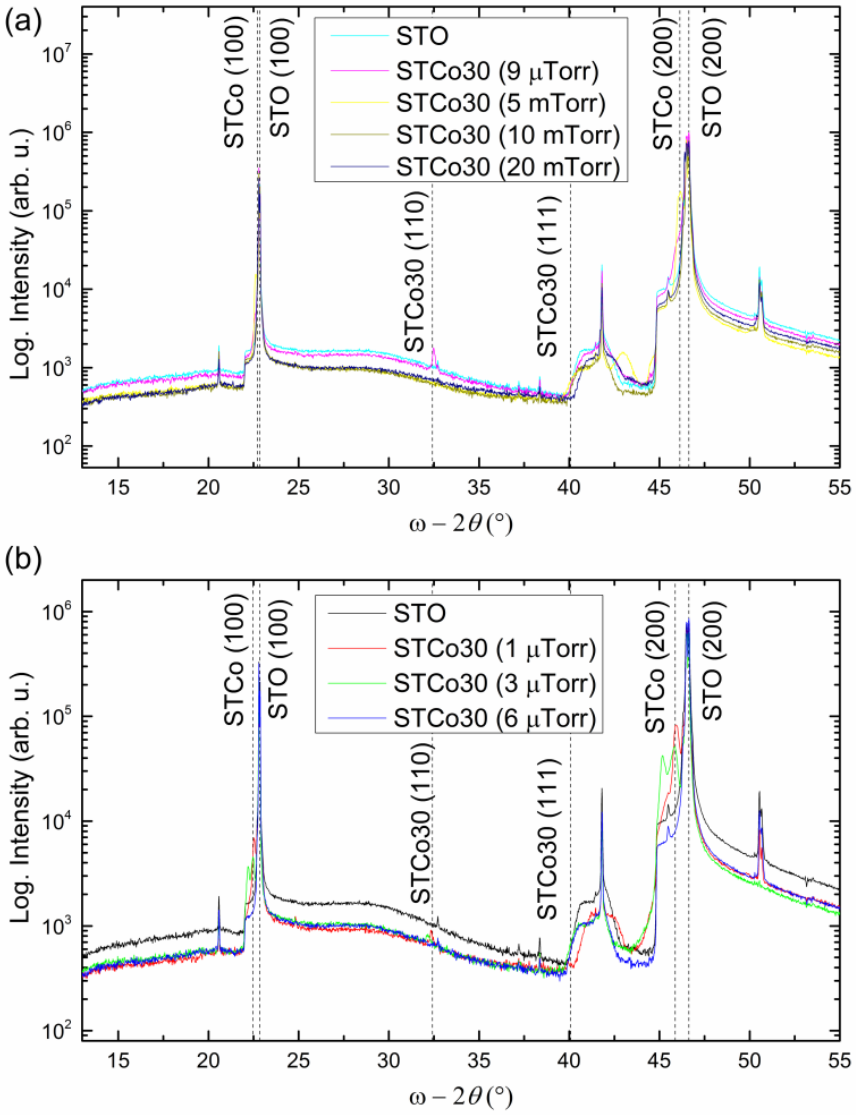

Fig. 5-29. X-ray diffraction patterns (ω-2θ plots) indicate the phases present for films grown at different oxygen pressures for films grown under (a) 9 μTorr, 5 mTorr, 10 mTorr and 20 mTorr, and under (b) 1, 3 and 6 μTorr. Both plots include the diffraction patterns for bare STO substrate for comparison.

Phases present inside the films are investigated with larger angular range ω-2θ XRD scans as shown in Fig. 5-29(a) for the 9 μTorr, 5 mTorr, 10 mTorr and 20 mTorr films and Fig. 5-29(b) for 1, 3 and 6 μTorr films. ω-2θ scans of an STO substrate were included with both plots to distinguish the film and substrate peaks. The peaks without labels originate from the substrate. An XRD reference pattern for a very similar 30 at.% Cobalt-substituted perovskite bulk powder of $SrTi_{0.70}Co_{0.30}O_{2.9}$ (powder diffraction reference number: 00-053-1216) indicates STCo30 (101) and (111) peaks at 2θ = 32.509 and 2θ = 40.078°. All of the peaks are either from the substrate or from the epitaxial film peaks immediately adjacent to the major

substrate peaks or from the (110) or (111)-oriented perovskite phases., i.e. there were not detectable amounts of other phases.

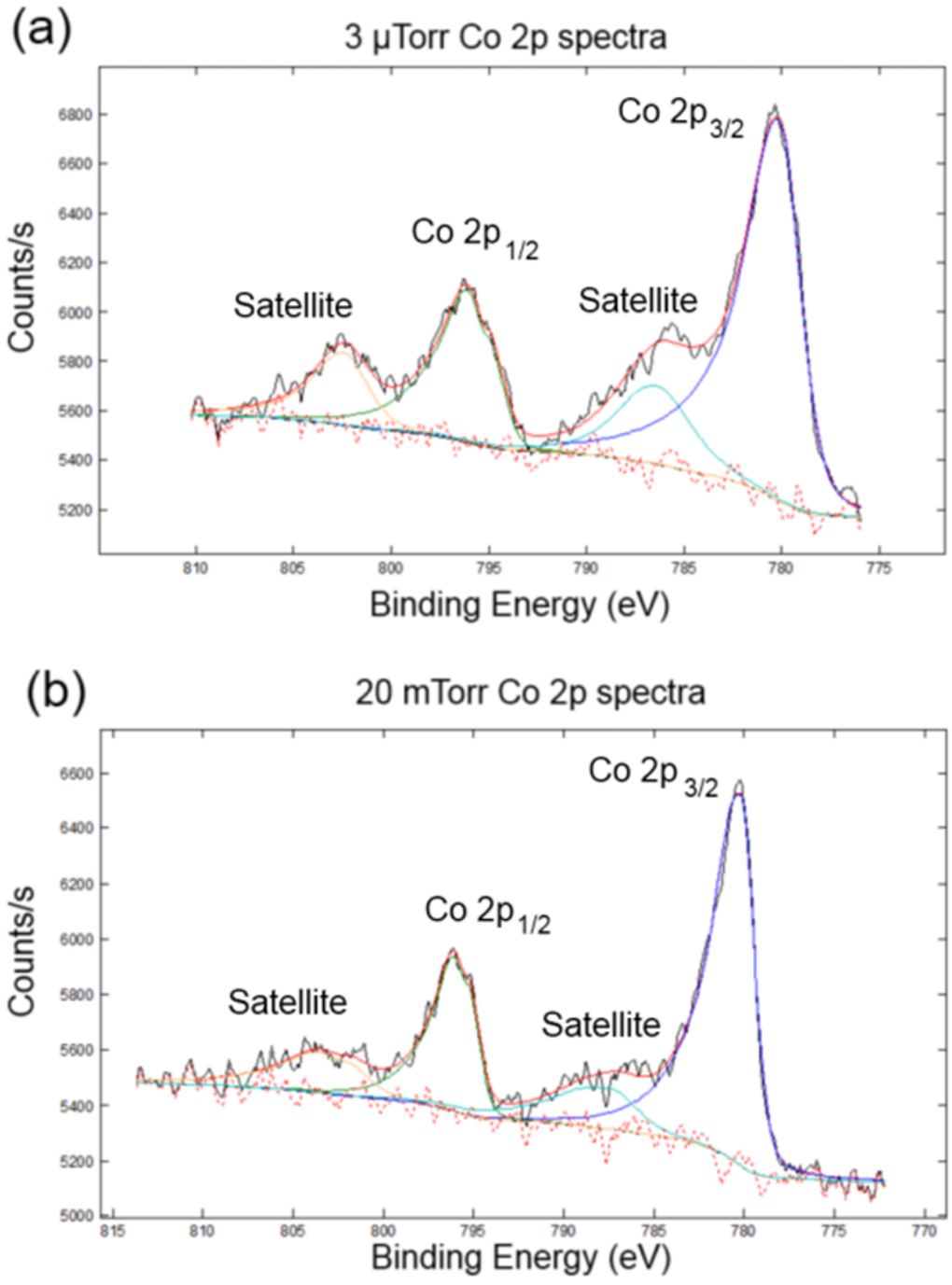

Fig. 5-30. Cobalt 2p x-ray photoelectron spectra for STCo films grown under (a) 3 µTorr and (b) 20 mTorr oxygen. The Co $2p_{3/2}$ and Co $2p_{1/2}$ doublets for both spectra indicate mixed-valence states for the Co ions. (XPS data acquired by Elizabeth Shaw)

X-ray photoelectron spectroscopy (XPS) was carried out to investigate the valence states of the cobalt in perovskite films. Fig. 5-29(a) and 5-29(b) show the XPS spectra for STCo30 (3 μTorr) and STCo30 (20 mTorr) films, respectively. Both spectra show peaks at 780.4 and 796.2 eV, which are the binding energies of Co $2p_{3/2}$ and $2p_{1/2}$ doublets originating from spin-orbit interaction. Cobalt metal is not present according to these spectra, because if metallic Co clusters had formed, the $2p_{3/2}$ and $2p_{1/2}$ peaks would be at 777.3 and 792.4 eV, respectively [1]. The lack of metallic Co peaks in the XRD and XPS spectra indicate that there are no significant amounts of Co metal. Near 786 and 803 eV, the satellite peaks for Co $2p_{3/2}$ and $2p_{1/2}$ doublets are observed. Each satellite peak is 7 eV beyond its principal peak. A 7 eV difference between the principal and satellite peaks is similar to the binding energy differences for Co^{2+} or Co^{3+} ions discussed in previous studies [1]. Typical satellite peaks for Co^{3+} and Co^{4+} ions are weak, as shown for $La_{1-x}Sr_xCoO_3$ [51] and for STCo bulk samples [24] fabricated under high oxygen pressure. In the spectra shown here, the satellite peak is strong, as a characteristic of Co^{2+} ion, as discussed for La_2CoO_4 [50]. The strong satellite peak in the XPS spectrum therefore indicates that the film contains Co^{2+}. In addition, DFT predictions on oxygen-deficient STO with 25% Co substitution, close to the composition of STCo30, [17] also support the presence of Co^{2+}. The binding energy of the Co $2p_{3/2}$ peak is smaller than that of pure Co^{2+} perovskites (781.3 eV) [1], suggesting that Co is in a mixed valence state also containing Co^{3+}. This result is also consistent with the DFT predictions [17]. We therefore believe that Co^{2+} and Co^{3+} are the major valence states of Co within the STCo30 films, both for STCo30 (3 μTorr) and STCo30 (20 mTorr) films. The difference is that in the STCo30 (20 mTorr) film, Co $2p_{1/2}$ peak has lower intensity and hence the Co^{2+} fraction relative to Co^{3+} is lower than in the STCo30 (3 μTorr) film.

Oxygen vacancies are expected to be present for all deposition pressures because $\delta = 0$ would require the Co to be quadrivalent. The reduction in the fraction of Co^{2+} with increasing oxygen partial pressure is expected from a reduction in oxygen vacancy concentration. This also reduces the average size of the Co ion and the lattice volume (assuming $V_{STCo30} = a_{out\text{-}of\text{-}plane} \cdot 3.905^2$ Å^3) as indicated on Table 5-4. Since earlier studies show that Cobalt is at

around 23 at.% [1], the Sr, Ti and Co ionic concentrations are close to those in the the DFT study of STCo [17]. A comparison with DFT results for unit cell volume enables an estimate to be made of the bounds for δ for the films prepared for this study. DFT studies for 25% Cobalt-substituted STO with δ = 0 ($SrTi_{0.75}Co_{0.25}O_3$) and δ = 0.125 ($SrTi_{0.75}Co_{0.25}O_{2.875}$) have unit cell volumes of 57.56 $Å^3$ and 58.50 $Å^3$, respectively [17]. The δ = 0.125 case would correspond to Co^{3+} average valence state whereas δ = 0.25 corresponds to Co^{2+} average valence state, with Sr^{2+} and Ti^{4+} present. Since XPS showed that Co^{2+} constitutes a greater fraction of the Cobalt ions than Co^{3+}, we can estimate that δ is closer to 0.25 than 0.125. The unit cell volume of all the films is larger than the DFT prediction for δ = 0.125 for all samples, which suggests δ > 0.125 even for films grown in oxygen.

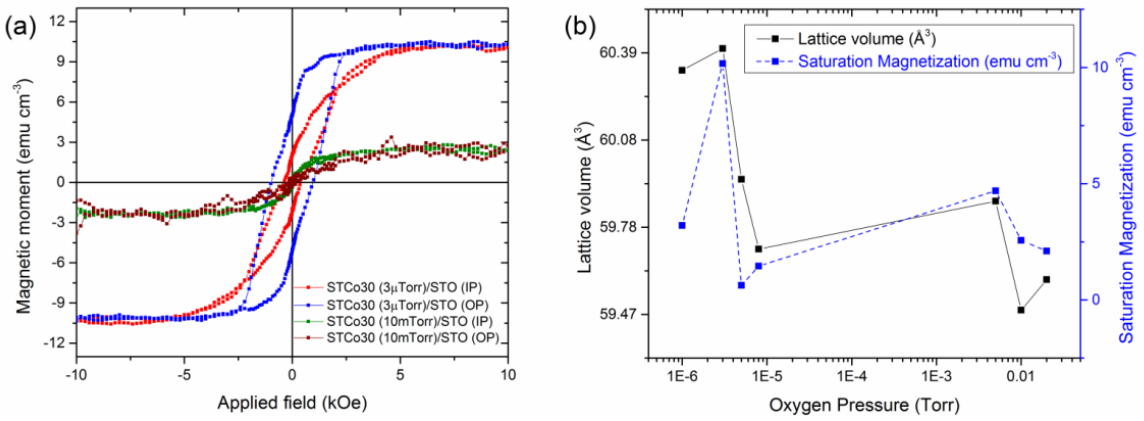

Fig. 5-31. Oxygen pressure dependence of magnetism and out-of-plane lattice parameter. (a) In-plane and out-of-plane magnetic hysteresis loops of STCo30 (3μTorr) and STCo30 (10mTorr) films. (b) Oxygen partial pressure dependence out-of-plane lattice parameter of the films and saturation magnetization.

In order to investigate how the oxygen partial pressure affects magnetic properties of the films, room temperature magnetic hysteresis loops of the films were measured using VSM. Fig. 5-31(a) indicates the IP and OP hysteresis loops for STCo30 (3 μTorr) and STCo30 (10 mTorr) films. Magnetic saturation moments (M_s) for the films were 10.6 emu·cm^{-3} (~0.23 μ_B/Co ion) and 2.8 emu·cm^{-3} (~0.06 μ_B/Co ion) for STCo30 (3 μTorr) and STCo30 (10 mTorr) films, respectively. M_s of the films grown at oxygen pressures at or above 6 μTorr were lower than 0.1 μ_B/Co ion, indicating that all of the STCo30 films have a substantial amount of antiferromagnetic coupling between neighboring Co ions. Experimental results on oxygen

pressure dependence of M_s are presented in Fig. 5-31(b) and the M_s shows a strong positive correlation with the lattice parameter. Consistent with DFT predictions [17], increasing oxygen pressure (and decreasing oxygen vacancy concentration) reduces M_s and the lattice volume.

The OP easy axis evident in the loops of Fig. 3-31(a) for the 3 μTorr sample is assumed to originate from magnetoelastic anisotropy. With higher oxygen pressure, the films become more isotropic. Octahedrally coordinated Co^{2+} is a highly magnetoelastic ion, and the compressive strain state of the film is assumed to provide magnetoelastic stabilization to align the magnetic moments within the film.

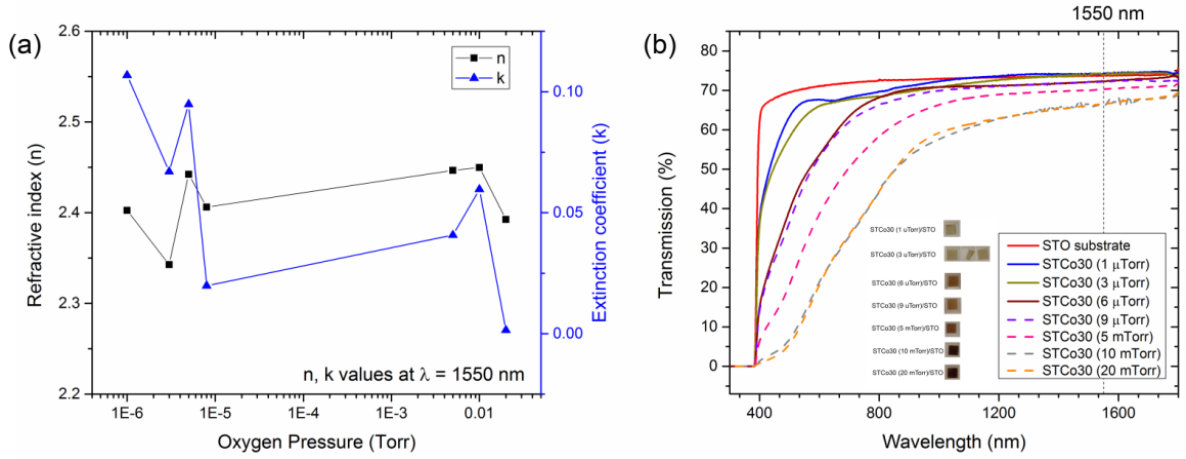

Fig. 5-32. Optical properties of STCo films. (a) Refractive indices (n) and extinction coefficients (k) at λ = 1550 nm. (b) Transmission spectra of the films (inset: sample photos, in the same order in the legend).

The effect of oxygen pressure during growth on refractive index and extinction coefficient is shown in Fig. 5-32. Using a spectroscopic ellipsometer, Ψ and Δ were measured and a thin film model fit was used to extract the refractive indices and extinction coefficients of the films at λ = 1550 nm with a mean square error in each fit is less than 10^{-3}. The film thicknesses were measured using a profilometer. The refractive index of the STCo30 films was in the range 2.42 ± 0.03 at λ = 1550 nm, except the 3 μTorr sample has a refractive index of 2.34 at λ = 1550 nm, as shown in Fig. 5-32(a). The lower refractive index is consistent with the presence of the smaller, less polarizable Co^{2+} ions. The optical absorption and extinction coefficients, also shown in Fig. 5-32(a), generally decreased with higher oxygen pressure. The fits are best

around 1550 nm. Fig. 5-32(b) shows optical transmission data for the films as a function of wavelength, from which the band gap can be estimated. Bare STO substrate has an indirect band gap near 3.2 eV (λ_g = 387 nm). STCo30 film band gaps are indirect with absorption tails that extend to longer wavelengths with higher oxygen pressure.

Faraday rotation of the films as a function of applied OP magnetic field was measured as shown in Fig. 5-33(a). Consistent with the OP magnetic hysteresis loops in Fig. 5-31(a), Faraday rotation was highest for 3 μTorr film and decreased monotonically with higher oxygen pressure after 3μTorr. The Faraday rotation coercivity (H_c (FR) = 1350 Oe) was greater than that of its OP magnetic coercivity (H_c = 960 Oe) for the STCo30 (3 μTorr) film. The optical loss values on Table 5-5 were calculated according to the formula: Optical loss (dB) = $-10\times\log_{10}(\exp(-4\pi k/\lambda_0\times t))$, where k is the extinction coefficient of the film at 1550 nm, λ_0 is 1550 nm, and t is the film thickness (in nm). The figures-of-merit on Table 5-5 were calculated as Figure-of-merit = (saturation FR, °·cm^{-1})/(optical loss, dB·cm^{-1}) at 1550 nm.

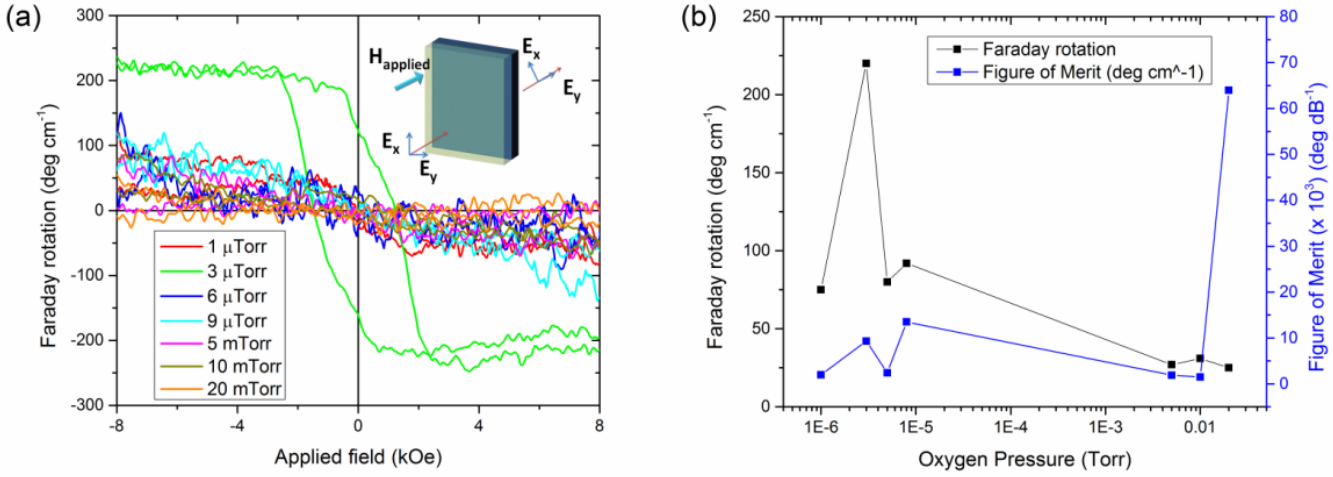

Fig. 5-33. (a) Faraday rotation loops for each oxygen pressure sample; (b) Oxygen partial pressure dependence of Faraday rotation and Figure-of-merit.

Table 5-5. Comparison of MO figure-of-merit values for garnets, perovskites and semiconductors.

MO Material and Substrate	MO Figure-of-merit (°·dB^{-1}) near λ = 1550 nm	Growth method	Optical Loss near λ = 1550 nm (dB·cm^{-1})	Other useful properties	Reference
STCo30 (20 mTorr) on STO	0.064	PLD	390.6	Perpendicular magnetic anisotropy	This study
$SrTi_{0.77}Co_{0.23}O_{3-\delta}$ on (001) $LaAlO_3$	0.57	PLD	877	Magnetic up to 1000 K	[1]
$SrTi_{0.6}Fe_{0.4}O_{3-\delta}$ on (001) $LaAlO_3$	1.11	PLD	700	Magnetic up to 1000 K	[65]
$Ce_1Y_2Fe_5O_{12}$ (Ce:YIG) on Silica	56	Sputtering	48	Grown on non-garnet substrate	[22]
Ce:YIG on Si	21.8	PLD	58	Grown on Si waveguide	[1]
$Y_{2.82}Ce_{0.18}Fe_5O_{12}$ (no substrate)	1420	Traveling solvent floating zone	0.12	Bulk crystal	[67]
$Ce_1Y_2Fe_5O_{12}$ on (111) doped-$Gd_3Ga_5O_{12}$	321	Sputtering	14	470-nm thick epitaxial film	[68]
Fe:InP	27.1	(not mentioned)	54.8	III-V semiconductor integration	[69]
Fe:InGaAsP	23	(not mentioned)	4.34	III-V semiconductor integration	[70]

For MO device applications, the optical loss of the films needs to be minimized while maximizing the Faraday rotation. In previous studies of oxides [71], optical loss was higher for films with greater Faraday rotation. The figure-of-merit may be optimized by establishing the appropriate oxygen partial pressure window. As shown in Fig. 5-33(b), Faraday rotation and figure-of-merit results at 1550 nm are presented as functions of oxygen pressure during growth. Faraday rotation was maximum in the range of 3-9 μTorr, while optical loss was minimum at 20 mTorr. The MO figure-of-merit was numerically greatest near 20 mTorr since

the optical loss of the 20 mTorr film was the lowest, but at this pressure the magnetic and MO response of the film is weak. The most plausible choice of pressure was 9 μTorr to provide the best figure-of-merit and magnetization.

The MO figure-of-merit and optical loss values found for STCo30 films and other MO films are listed on Table 5-4. Other substitutionally-doped STO-based perovskites have much higher optical loss near 1550 nm compared with the STCo30 films in this study [1,65]. The two major categories of MO materials are iron garnets and substitutionally-doped III-V films for non-reciprocal MO devices such as isolators and circulators, in which the figure-of-merit of the MO film needs to reach ~45 °·dB^{-1} [82] and the insertion loss of the device needs to be below ~1-2 dB. Substituted iron garnet films (i.e. Ce:YIG) is often used in non-reciprocal device applications [1,22,78,79] since these garnet films have very high MO figure-of-merit. Fe-doped group III-V semiconductors also achieve high MO figure-of-merit for devices integrated on a III-V substrate. The STCo30 films presented here have lower figure-of-merit than these two classes of materials, but the perpendicular magnetic anisotropy, which is also seen in polycrystalline STCo30 films grown on Si substrates (shown in chapter 5) may have a role in non-reciprocal device architectures requiring perpendicular magnetic anisotropy. This simple perovskite STCo30 film can be useful in applications requiring perpendicular magnetic anisotropy.

A remarkable aspect of this study is that the (100) STCo30 films included (110) and (111) oriented crystals assumed to form to relieve strain. As the oxygen partial pressure during growth decreased, the OP lattice parameters and unit cell volumes increased. Cobalt ions were in mixed valence states (Co^{2+} and Co^{3+}) regardless of oxygen partial pressure during growth, but the ratio of Co^{2+}/Co^{3+} decreased with higher oxygen pressure. The M_s, magnetic anisotropy, and Faraday rotation all decreased with higher oxygen pressure. The decrease in the lattice volumes presented in Table 5-4 follows trends predicted by DFT calculations of oxygen-deficient structures [17]. The MO figure-of-merit varied with oxygen pressure but was lower than that of iron garnets at 1550 nm.

5.2 Summary

The this chapter, we focused on room temperature magnetic, ferroelectric and magnetoelectric properties of STCo30 films grown on Si, STO (100), and on thick SiO_2 on Si and on Nb:STO. Ferroelectric P_{sat} and $2P_r$ reach 75 μC cm^{-2} and 32 μC cm^{-2}, respectively. STCo30 films demonstrated here are useful magnetic and ferroelectric films integrated with Si and could therefore enable low voltage and low-energy switching. We not only experimentally demonstrate multiferroic response, but also clearly prove and reproduce quantitatively most of the structural, magnetic and ferroelectric results using DFT calculations. STCo30 has OP magnetic easy axis. Ferromagnetism has been found to originate from mixed valence states of Cobalt ions and oxygen vacancies. Ferroelectricity has been found to originate from the chemical strain that Cobalt substitution imposes on the perovskite lattice and the anisotropic lattice expansion that causes B-site cation off-centering. Furthermore, substrate strain especially for the films on Nb:STO contribute to switching behavior. Oxygen vacancies, alone, cause anisotropic lattice expansion and lead to ferroelectricity in absence of strain from the substrate. This lifts the substrate strain requirement for multiferroic behavior, which significantly enhances the device design flexibility. Since STCo30 is also one of the few highly insulating ($\rho_{STCo30} \sim 10^7 - 10^{14}$ Ω·cm) multiferroic oxides, in addition to insulating magnetoelectric hexaferrites, it can enable new memory devices and can be useful in magnetic random access memories.

In addition, the oxygen partial pressure dependence of magnetic, optical, structural and MO properties of substitutionally-doped perovskite STCo30 films were also investigated. Perovskite oxides offer dynamic tunable properties such as piezoelectricity and MO or other coupled functional constitutive relations. Crystalline microstructure has been found to undergo “double-epitaxy” or “triple-epitaxy” relaxation depending on oxygen pressure during growth. Understanding and engineering these structural relaxation mechanisms can add tunability to these MO perovskites.

References

[1] L. Bi, H.-S. Kim, G. F. Dionne, and C. A. Ross, *New J. Phys.* **12**, 043044 (2010).

[2] D. Damjanovic, *Rep. Prog. Phys.* **61**, 1267 (1998)

[3] M. Dawber, K. M. Rabe, J. F. Scott, *Rev. Mod. Phys.* **77**, 1083, (2005).

[4] D. Damjanovic, "Hysteresis in Piezoelectric and Ferroelectric Materials", The Science of Hysteresis, Volume 3; I. Mayergoyz and G.Bertotti (Eds.); Elsevier (2006), 337

[5] S. Ohta, T. Nomura, H. Ohta, M. Hirano, H. Hosono, K. Koumoto, K., *Appl. Phys. Lett.,* **87**, 092108 (2005)

[6] C. H. Kim, G. Qi, K. Dahlberg, W. Li, *Science*, **327 (5973)**, 1624 (2010).

[7] Yang et. al, *Nat. Nanotechnol.* **5**, 143 (2010).

[8] E. Fortunato, D. Ginley, H. Hosono and D. C. Paine, *MRS Bull.* **32**, 242 (2007).

[9] P. E. van Keken, D. A. Yuen, A. P. van den Berg, *Science* **264 (5164)**, 1437 (1994).

[10] W. Tong, W.-S. Yoon, N. M. Hagh, G. G. Amatucci, *Chem. Mater.* ***21*** **(10)**, 2139 (2009).

[11] L. Li, C. Richter, J. Mannhart & R. C. Ashoori, *Nature Phys.***7**, 762 (2011).

[12] Millange, F., Caignaert, V., Domengès, B., and, Raveau, B., and Suard, E., *Chem. Mater.* ***10*** **(7)**, 1974 (1998).

[13] J. W. Reiner, A. M. Kolpak, Y. Segal, K. F. Garrity, S. Ismail-Beigi, C. H. Ahn, and F. J. Walker, Adv. Mater., **22**, 2919 (2010).

[14] L. Bi, J. Hu, P. Jiang, D. H. Kim, G. F. Dionne, L. C. Kimerling, C. A. Ross, Nature Photon. **5**, 758 (2011).

[15] L. W. Martin, Y.-H. Chu, R. Ramesh, Mater. Sci. Eng., R **68**, 89 (2010).

[16] C. Ederer, and N. A. Spaldin, Nat. Mater. **3**, 849 (2004).

[17] J. M. Florez, S. P. Ong, M. C. Onbasli, C. A. Ross and G. Ceder, *Appl. Phys. Lett.* **100**, 252904 (2012).

[18] J. F. Scott, Room-temperature multiferroic magnetoelectrics. *NPG Asia Mater.* **5**, 1 (2013).

[19] R. Ramesh, and N. A. Spaldin, *Nat. Mater.* **6**, 21 (2007).

[20] W. Eerenstein, N. D. Mathur, and J. F. Scott, *Nat. Mater.* **442**, 759 (2006).

[21] R. Thomas, J. F. Scott, D. N. Bose, R. S. Katiyar, *J. Phys.: Condens. Matter* **22**, 423201 (2010).

[22] L. W. Martin, S. R. Crane, Y. – H. Chu, M. B. Holcomb, M. Gajek, M. Huijben, C.-H. Yang, N. Balke, and R. Ramesh, *J. Phys.: Condens. Matter* **20**, 434220 (2008).

[23] A. P. Pyatakov, A. K. Zvezdin, *Physics - Uspekhi* **55**, 557 (2012).

[24] C. A. F. Vaz, J. Hoffman, C. H. Ahn, R. Ramesh, Adv. Mater. **22**, 2900 (2010).

[25] J. Ma, J. Hu, Z. Li, and C.–W. Nan, *Adv. Mater.* **23**, 1062 (2011).

[26] T. Kimura, T. Goto, T., H. Shintani, K. Ishizaka, T. Arima, Y. and Tokura, *Nature* **426**, 55 (2003).

[27] B. Kundys, A. Maignan, C. Martin, N. Nguyen, and C. Simon, *Appl. Phys. Lett.* **92** 112905 (2008).

[28] Y. Hamasaki, T. Shimizu, H. Taniguchi, T. Taniyama, S. Yasui, and M. Itoh, *Appl. Phys. Lett.* **104**, 082906 (2014).

[29] J. Wang, et al., *Science* **299**, 1719 (2003).

[30] D. Lee, M. G. Kim, S. Ryu, H. M. Jang, S. G. Lee, *Appl. Phys. Lett.*, **86**, 222903 (2005).

[31] K. Okumura, T. Ishikura, M. Soda, T. Asaka, H. Nakamura, Y. Wakabayashi, and T. Kimura, *Appl. Phys. Lett.* **98**, 212504 (2011).

[32] Y. Kitagawa, Y. Hiraoka, T. Honda, T. Ishikura, H. Nakamura, and T. Kimura, *Nat. Mater.* **9**, 797 (2010).
[33] S. Hirose, K. Haruki, A. Ando, and T. Kimura, *Appl. Phys. Lett.* **104**, 022907 (2014)
[34] L. Wang, D. Wang, Q. Cao, Y. Zheng, H. Xuan, J. Gao, Y. Du, Y., *Sci. Rep.* **2**, 1 (2012).
[35] D. M. Evans, et al., *Nat. Commun.* **4**, 1 (2013).
[36] Y. Matsumoto, et al., *Science* **291**, 854 (2001).
[37] Y. Yamada, et al., *Science* **332**, 1065 (2011).
[38] D. H. Kim, L. Bi, P. Jiang, G. F. Dionne, and C. A. Ross, *Phys. Rev. B* **84**, 014416 (2011).
[39] L. Bi, H.-S. Kim, G. F. Dionne, and C. A. Ross, *New J. Phys.* **12**, 043044 (2010).
[40] T. Fix, et al., *New J. of Phys.* **11**, 073042 (2009).
[41] L. Luo, et al., *Appl. Phys. Lett.* **92**, 232507 (2008).
[42] D. H. Kim, N. M. Aimon, L. Bi, G. F. Dionne, C. A. Ross, *J. Appl. Phys.* **111**, 07A918 (2012).
[43] P. Jiang, L. Bi, X. Sun, D. H. Kim, D. Jiang, G. Wu, G. F. Dionne, C. A. Ross, *Inorg. Chem.* **51**, 13245 (2012).
[44] D. H. Kim, N. M. Aimon, L. Bi, J. M. Florez, G. F. Dionne, C. A. Ross, *J. Phys.: Condens. Matter* **25**, 026002 (2013).
[45] H. Jeen et al., *Nat. Mater.* **12**, 1057 (2013).
[46] W. D. Rice, P. Ambwani, M. Bombeck, J. D. Thompson, G. Haugstad, C. Leighton, and S. A. Crooker, *Nat. Mater.* **13**, 481 (2014).
[47] J. H. Haeni, et al., *Nature* **430**, 758 (2004).
[48] M. Itoh, et al., *Phys. Rev. Lett.* **82**, 3540 (1999).
[49] Y. S. Kim, J. D. Kim, T. W. Noh, J. S. Choi, B. H. Park, J.-G. Yoon, *Appl. Rev. Lett.* **91**, 042908 (2007).
[50] T. Nitadori, M. Muramatsu M and M. Misono, *Chem. Mater.* **1** 215 (1989).
[51] T. Saitoh, T. Mizokawa, A. Fujimori, M. Abbate, Y. Takeda and M. Takano, *Phys. Rev.* B **56** 1290 (1997).
[52] S. Malo and A. Maignan *Inorg. Chem.* **43** 8169 (2004).
[53] K. Morito, Y. Iwazaki, T. Suzuki and M. Fujimoto, *J. Appl. Phys.* **94**, 5199 (2003).
[54] M. Cardona, *Phys. Rev.* **140**, A651 (1965).
[55] K. van Benthem, C. Elsässer, R. H. French, *J. Appl. Phys.* **90**, 6156 (2001).
[56] G. Herranz, R. Ranchal, M. Bibes, H. Jaffrès, E. Jacquet, J. L. Maurice, K. Bouzehouane, F. Wyczisk, E. Tafra, M. Basletic, A. Hamzic, C. Colliex, J. P. Contour, A. Barthélémy, A. Fert, *Phys. Rev. Lett.* **96**, 027207 (2006).
[57] X. S. Zhang, W. Yu, S. B. Ogale, S. R. Shinde, D. C. Kundaliya, W. Tse, S. Y. Young, J. S. Higgins, L. G. Salamanca-Riba, M. Herrera, L. F. Fu, N. D. Browning, R. L. Greene, T. Venkatesan, *Phys. Rev. B* **76**, 085323 (2007).
[58] P. Plonczak, A. Bieberle-Hutter, M. Sogaard, T. Ryll, J. Martynczuk, R. V. Hendriksen, and L. J. Gauckler, *Adv. Funct. Mater.* **21**, 2764 (2011).
[59] H. S. Kim, L. Bi, G. F. Dionne, C. A. Ross, *Appl. Phys. Lett.* **93**, 092506 (2008).
[60] D. H. Kim, L. Bi, N. M. Aimon, P. Jiang, G. F. Dionne, and C. A. Ross, *ACS. Comb. Sci.* **14**, 179 (2012).

[61] G. F. Dionne, D. H. Kim, L. Bi, C. A. Ross, *J. Appl. Phys.,* **113**, 17A927 (2013).
[62] H. S. Kim, L. Bi, H. Paik, D. J. Yang, Y. C. Park, G. F. Dionne, C. A. Ross, *Nano Lett.,* **10**, 597 (2010).
[63] Y. Guo, B. Guo, W. Dong, H. Li and H. Liu, *Nanotechnology* **24**, 275201 (2013).
[64] D. Kan, T. Terashima, R. Kanda, A. Masuno, K. Tanaka, S. Chu, H. Kan, A. Ishizumi, Y. Kanemitsu, Y. Shimakawa and M. Takano, *Nat. Mater.* **4**, 816 (2005).
[65] H. L. Ju, J. Gopalakrishnan, J. L. Peng, Q. Li, G. C. Xiong, T. Venkatesan, R. L. Greene, *Phys. Rev. B* **51,** 6143 (1995).
[66] P. Jiang, L. Bi, D. H. Kim, G. F. Dionne, and C. A. Ross, *Appl. Phys. Lett.* **98**, 231909 (2011).
[67] S. Higuchi, Y. Furukawa, S. Takekawa, O. Kamada and K. Kitamura, *Jpn. J. Appl. Phys.* **38**, 4122 (1999).
[68] T. Shintaku, *Appl. Phys. Lett.* **73**, 1946 (1998).
[69] T. R. Zaman, X. Guo, and R. J. Ram, "Faraday rotation in semiconductors for photonic integration," in Proc. Conf. Lasers Electro-Optics, San Francisco, CA, May 2004, p. 2.
[70] T. R. Zaman, X. Guo, and R. J. Ram, *Appl. Phys. Lett.* **90**, 023514, (2007).
[71] L. Bi, "Magneto-optical Oxide Thin Films and Integrated Nonreciprocal Photonic Devices," PhD Thesis, Massachusetts Institute of Technology (2011).

Chapter 6. Conclusions and Future Work

6.1 Conclusions

Recent developments in the control of pulsed laser deposition systems enabled researchers to grow bulk-quality magnetic and magneto-optical perovskites and garnet thin films on Si or Si-based substrates, GGG, STO as well as on others. The major contributions of this thesis into fundamental materials science as well as applied integrated photonics, magnonic data processing and multiferroic materials are:

In integrated nonreciprocal photonics;

1) Establishing an upper limit for the figure-of-merit of magneto-optical Ce:YIG films grown by pulsed laser deposition. As indicated in Chapter 3, the garnet quality is sufficient for low insertion loss, high bandwidth and isolation ratio integrated optical isolators. So one needs to consider grain boundary scattering, partial crystallization, and other microstructural aspects to improve garnet quality on nongarnet substrates such as Silicon.
2) Demonstration of high-quality Ce:YIG films with slow YIG seed growth (two-step growth), top YIG seed templating (one-step growth) and room temperature deposition and annealing to achieve Ce:YIG films with useful magneto-optical quality while reducing thermal budget of growth. Templating the growth from seed is also a fundamentally new growth technique.
3) Demonstration of optical isolators with reduced insertion loss and good isolation ratio by simplifying garnet growth process into a single step (growth/annealing). This demonstration highlights that reducing thermal budget of garnet growth is required for monolithic integration of isolators commercially viable.

In magnonic data processing;

1) Demonstrating epitaxial bulk-quality YIG thin films with low Gilbert damping and long propagation length for spins (i.e. dipolar magnons).
2) TmIG ($Tm_3Fe_5O_{12}$) epitaxial thin films with perpendicular magnetic anisotropy for spin injection and processing.
3) Integration of topological insulators and YIG films to achieve ultra-low energy switching.
4) Origins of spin-Seebeck effect were investigated and characteristic magnon diffusion length and the effect of film thickness on the saturation of spin Seebeck coefficient was investigated.

In multiferroic materials;

1) A rational design method of a room temperature multiferroic oxide that can be directly grown on any substrate including Si, SiO_2 or other oxide substrates without special surface treatment.
2) Making use of p-type ionic doping and oxygen vacancies for inducing ferroelectricity in magnetic perovskite oxides (demonstrated for the case of $SrTi_{0.70}Co_{0.30}O_{3-\delta}$) without having to use substrate strain. Using chemical strain (that causes anisotropic lattice expansion, tetragonal lattice distortion and B-site off-centering) helps avoid substrate strain for inducing ferroelectricity. This method can potentially simplify both silicon integration of oxides (minimize required surface treatment, expand growth window) as well as improve reliability of devices by avoiding substrate strain.

This thesis brought us a few steps closer to (i) fully-integrated photonic circuits by demonstrating different garnet thin film growth methods on Si-based photonic chips, (ii) magnonic data processors operating at 5 GHz and higher frequencies at low power, (iii) multiferroic oxide data storage elements on Silicon. While the emphasis has been on applied materials research, the contributions to the basic materials science are also fundamentally important because;

1) Magnetic anisotropy of Ce:YIG has been characterized for the first time as a function of film thickness, substrate orientation and in-plane angle. The preferred anisotropy directions for garnets have been adjusted by the substrate choice and tuning of strain.
2) The effect of mixed valence states in perovskite oxides on stoichiometry, optical and electronic properties have been identified, both in numerical modeling and experimental demonstrations consistently.
3) The requirement of satisfying "d^0 rule" for achieving multiferroic behavior inside the same phase of material has been circumvented.

Therefore this work provides material and new processing methods that enable new functionalities that would not otherwise be achievable for future nonreciprocal photonic devices, for magnonic chips, as well as for multiferroic data storage elements. We believe further exploration of the properties is going to lead to improved materials and device performance that can achieve unique functionalities described below.

6.2 Future Work

While major progress has been made in achieving high figure of merit magneto-optical materials and devices, multiferroic oxide thin films and films with low damping as magnon transport media, there is room for further studies in order to reach the ideal functional figures of merit listed in chapter 1 for data storage, processing and photonic integration. First of all, the results presented here are only proof-of-concept demonstrations. As a result, one can expect some room for further optimization in the parameter space of each of the demonstrations. On the other hand, there are more fundamental improvements that one can make in order to extend the functionality and better understand the materials and devices summarized below. Those potential improvements on materials and devices are presented below.

Future materials design and engineering work for monolithic nonreciprocal photonic

integration:

1) **Laser annealing and recrystallization of Ce:YIG:** While single crystal Ce:YIG films have been proved to provide more than enough magneto-optical figure of merit for optical isolator applications, one challenge is reducing the thermal budget of high-quality Ce:YIG growth on Si-based photonic chips. Ideally, one needs to recrystallize 100% of the Ce:YIG film without forming grain boundaries. In addition, an ideal recrystallization process for Ce:YIG funnels all the recrystallization energy into the Ce:YIG layer, not into waveguides. One way to achieve recrystallization in Ce:YIG can be via selective laser annealing of the garnet layer. Two laser sources interfering to selectively enhance recrystallization in garnet can potentially avoid a high temperature rapid thermal annealing, which is not compatible with front end or back end of the line CMOS processing. In order to eliminate the formation of grain boundaries one can prepattern a damascene structure, grow garnet films in between mesas of oxides and then do lateral overgrowth between mesas with a cyclic annealing to eliminate the dislocations and enhance recrystallization efficiency.

2) **Ce:YIG compatibility for TE-mode (transverse electric) isolator designs**: For TE-mode isolators, one needs to grow Ce:YIG films on the side of the waveguide. As a result, one needs to develop the growth methods for growing high figure-of-merit garnet films on the side of the waveguide. A potential issue is the reaction of the waveguide with garnet and degrading magneto-optical phase shift induced from the garnet layer. Another important consideration is trench coverage of garnet films: optical isolators are typically integrated in arrays on photonic circuit and one needs to fill in the trenches on the side of the isolators with high figure-of-merit garnet. Given the angular ejection of the PLD plume from the target, one needs to engineer the garnet growth conditions further (i.e. extend target-substrate distance, but grow at a slower rate) and make growth trade-offs.

3) **Establish Ce:YIG growth conditions on actual Ge-on-Si and on InGaAsP lasers.**

Future work on device engineering for monolithic nonreciprocal photonic integration:

1) **Mach-Zehnder or optical directional coupler topologies for wider bandwidth optical isolators:** An ideal optical isolator has wide bandwidth, negligible insertion loss, at least 20 dB optical isolation ratio for the wavelengths of interest (780 nm and near infrared). In order to achieve wider bandwidth with Ce:YIG devices, one needs to work with Mach-Zehnder interferometer or optical directional coupler topologies rather than a single resonator isolator. A single resonator enhances isolation ratio but reduces isolation bandwidth. On the other hand, if the loaded Q-factor of the resonator is not high (Q > a few 10^4 - 10^5), then the magneto-optical quality of the garnet layers may not be utilized properly.

2) **Reducing the overall insertion loss of an optical isolator (or any passive integrated optical component) without trading off isolation ratio or bandwidth** involves eliminating Fresnel reflections due to refractive index mismatches (pattern a tapered garnet window rather than a rectangle), sidewall roughnesses of waveguides (improved e-beam exposure and etching recipes), a more robust cleaving method (i.e. setting up a protocol with a new cleaving tool), and a more efficient fiber-to-chip and chip-to-fiber interface design (with gratings or tapered waveguides). Traditional butt-coupling from the fiber to the waveguides introduces more than 3 dB optical loss. This alone can be eliminated or at least reduced to below 1 dB by patterning a tapered waveguide coupling pattern on chip. Therefore, the overall insertion loss of optical isolators can be reduced from 7.4 dB to less than 2 dB with these improvements.

3) **Nonreciprocal superluminal communication:** Previous proposals include optical resonators engineered to produce superluminal data transfer where group velocity of data packets travels faster than the speed of light in the medium. This does not violate relativity or causality since phase velocity travels slower than speed of light. Magneto-optical superluminal communication can be a new optical isolation mechanism.

Future materials design and engineering work for garnet-based magnon devices:

1) **Reduce YIG damping further:** The Gilbert damping of bulk YIG crystal is ~10^{-5} (according to the literature), while the lowest damping achieved for our epitaxial films is $2.2 \cdot 10^{-4}$. One needs to measure the damping of a bulk YIG crystal to recognize if there is room for improvement. According to the literature value, there is still room for reducing the damping by one more order of magnitude. The difference can be due to the GGG substrate and one might need to investigate a single isolated YIG grain on a different substrate or a YIG membrane to understand if the substrate enhances damping. Other possible sources of damping may include partial relaxation of the film, surface roughness and oxygen off-stoichiometry. One might also consider trimming and slicing a YIG sheet or even a thin film membrane from a bulk YIG crystal. Then one can measure its damping and to distinguish if the YIG properties are limited from geometric confinement, or from a growth-induced strain effect or from substrate.

2) **Develop a PMA garnet with ultra-low Gilbert damping:** Achieving ultralow damping YIG enables investigations of spin-torque transfer, spin Seebeck effect, magnonic crystals and all-magnonic logic. Since YIG has in-plane easy magnetic axis, spin injection is not very efficient. In addition, spin propagation and modulation can be enhanced if YIG or another garnet can be engineered to become a perpendicular magnetic anisotropy (PMA) material. In this thesis, we grew TmIG ($Tm_3Fe_5O_{12}$) as a PMA magnetic insulator. But the Gilbert damping of these films needs to be measured. If the damping of these films are on the order of 10^{-2} (i.e. similar to permalloys) or lower, then one can consider using TmIG for magnonic logic devices as well.

3) **Grow ultra-low damping YIG on Si substrates:** Since Si CMOS logic is going to be used for at least a few more decades due to the cost advantage of Si, one needs to grow ultra-low damping YIG on Si. Since YIG crystallizes as grains with ~10-15μm

diameter on Si after rapid thermal annealing, one can either consider growing single crystal islands on Si and process magnons in those small circular YIG disks.

Future device engineering work for garnet-based magnon-based devices:

1) **Develop a magnon transistor with fan-out of more than 2**: Previous demonstrations of all-magnon transistors are valuable demonstrations to eliminate magnon-to-electric current and current-to-magnon stages. In one demonstration, a traditional source-gate-drain topology was used and a magnonic crystal pattern was fabricated between source and drain. The transmission of the magnonic crystal was modulated by magnons injected into the gate (by a nonlinear two-magnon or higher order magnon scattering process). These demonstrations are not practical because the intensity of the output magnon waves is already attenuated more than 20 dB when the transistor is switched ON. Since the attenuation of these devices are prohibitively high for any practical concatenation and logic circuit operation, one needs to engineer magnonic crystals for unity transmission for (ON) state. A more efficient way is to control the transmission spectra of the magnonic crystal by voltage. A stronger transmission for ON state is essential for concatenability and magnon logic gates.

2) **Develop magnonic logic based on phase of the wave**: Since the traditional source-gate-drain architecture for a switch does not fully utilize the advantages of magnons (waves with phases that can achieve analog or non-binary logic, modulation/demodulation for interfacing with an radio-frequency antenna), one can develop a wave interferometer structure that can act as a logic gate with high efficiency and operate at frequencies beyond 5 GHz.

3) **Increase magnon injection and detection efficiencies**: Any useful magnonic computer needs to have a "power source" which supplies magnons with high efficiency. The efficiency for magnon-to-electric current conversion (i.e. inverse spin Hall effect) needs to be improved for any practical application.

Future materials engineering work for multiferroic oxides studied for this thesis:

1) **Establish a reliable ferroelectric testing routine**: STCo30 films studied have shown ferroelectric saturation beyond a few volts in horizontal bias configuration and in capacitance-voltage loops, PUND tests and in DFT simulations. In addition, the resistivity of the films have been 10^7 Ω·cm or higher (horizontal bias). But piezoresponse force microscopy imaging and phase hysteresis measurement attempts have not been successful yet.

2) **Prepare 2D dense arrays of multiferroic STCo30 memory elements**: One can grow STCo30 on a gold bottom contact, deposit STCo30 top contact and etch a 2D array of memory elements. One can test the smallest element size that retains the functionalities presented in chapter 5.

3) **Quantify the oxygen vacancy concentration (δ in $SrTi_{0.70}Co_{0.30}O_{3-\delta}$)**: There are different methods of quantifying the oxygen vacancy concentration in STCo30. One method is thermogravimetry analysis which measures the mass change in the film upon heating the sample. Since most complex oxides lose oxygen ions from their lattices at elevated temperatures, one can expect a temperature-dependent decrease in the mass of complex oxide films, which can then be correlated with oxygen vacancy density and oxygen ionic dissociation energy. One can extract dissociation energy for oxygen ions from the lattice, assuming that the film forms oxygen vacancies with a thermally activated process. In addition, one can also calculate a refined estimate for oxygen vacancy concentrations from density functional theory simulations by fixing the simulated lattice parameter to the experimental lattice parameter.